MARS CLIMATE DATABASE v6.1
VALIDATION DOCUMENT

(ESA Contract No.4000128572/19/NL/AS)

CNES Contract ”Base de données climatique martienne”

F. Forget, E. Millour, T. Pierron, A. Bierjon (LMD)
and the MCD team

October 2022

Abstract

This is the Validation Document for version 6.1 of the Mars Climate Database (MCD). It validates some features included in the MCD and gives a systematic comparison against availables observational datasets, in order to document the ability of the MCD to predict the atmospheric state, as well as its possible biases.

Contents

1 Introduction

This document presents comparisons between available data and outputs of the Mars Climate Database version 6.1. The datasets of measurements which have been used in the comparisons detailed in this document are:

- Surface temperature, atmospheric temperature, water vapor column, water ice column and dust optical depth retrieved by Thermal Emission Spectrometer (TES) onboard Mars Global Surveyor (Smith [2004]). TES has monitored the Martian atmosphere nearly continuously for almost three full Martian years from mid-Martian year 24 (MY24) until early MY27. MGS being in a near-polar, sun-synchronous orbit, data was obtained for Local Solar times of 2 and 14 Martian hours (i.e. nighttime and daytime). The primary mode of TES data acquisition is nadir viewing. The up-to-date data used in this document was provided by M.D. Smith (NASA Goddard Space Flight Center) in april 2007. Note that the the TES data are binned in bins that are 5 degrees in L_s, 3 degrees in latitude, and 7.5 degrees in longitude.
- Atmospheric temperature and dust density-scaled opacity retrieved by Mars Climate Sounder (MCS) onboard Mars Reconnaissance Orbiter (MRO) (Kleinböhl et al. [2009]). MCS observations extend from MY28 (L_s=90°) until present. As MRO has a sun-synchronous orbit, observations are made at two mean solar local times, 3am (nighttime) and 3pm (daytime). The data used in this document was obtained from the MCS team and binned by 5 degrees in L_s, 3.75 degrees in latitude, and 5.625 degrees in longitude (Montabone et al. [2017]).
- Atmospheric temperature, water ice column and dust optical depth retrieved by Emirates Mars InfraRed Spectrometer (EMIRS) onboard Emirates Mars Mission (EMM) (Smith et al. [2022]). EMIRS observations cover only MY36 from L_s=45° to L_s=270° for now. Thanks to EMM sun-asynchronous orbit, observations cover a large spectrum of local times. The data used in this document was provided by the EMIRS team, and binned by 5 degrees in L_s, 3.75 degrees in latitude, 5.625 degrees in longitude, and 0.5 hours in Local Time.
- Surface pressure recorded by the Viking landers (MY12-MY14), InSight (MY34-MY36) (Lange et al. [2022]) and Perseverance (MY36).
- Winds recorded by InSight (MY34-MY36).

As TES, MCS and EMIRS data are binned in L_s, a major part of the day-to-day variability due to atmospheric waves is smoothed out. This makes them suitable for comparison with the MCD climatological predictions without added "perturbation". Apart from the MY25, MY28 and MY34 global dust storms periods, available data may be compared to the MCD's best guess climatology scenario, but occasional comparisons with the other scenarios designed to be representative of extreme but realistic conditions (cold, warm, storm) are also presented. Comparison with specific martian years scenario are also presented. Please note that when planetary average is done, we only take into account a certain range of latitudes (mostly -50°,50°) in order to avoid an overrepresentation of the poles. Indeed, the grid on which data and MCD are extracted are regular in longitudes and latitudes, which makes a simple average too much representative of the poles. Also there is a small delay in time for sublimation and condensation of the CO2 ice at high latitudes between the MCD and the observations. This delay makes big differences for surface temperature when averaging the field over the whole year on the entire planet. Therefore, removing poles data allows to avoid this bias.

2 Surface Pressure

2.1 Viking Lander 1

The figure below shows the comparison of the surface pressure between the measurements of Viking Lander 1 (VL1) and the MCD6.1. The comparison is done with diurnal averages of surface pressure for both VL1 measurements and the high resolution mode of the MCD. For VL1 measurements the several years of measurements (almost four martian years) were overlaid on one year and compared to the model. The seasonnal CO2 cycle is well represented in the MCD. In order to check the day-to-day variability, the RMS from the MCD is also shown on the figure. This variability seems to be a little underestimated by the model, seeing the variations of the VL1 measurements from one day to the next.

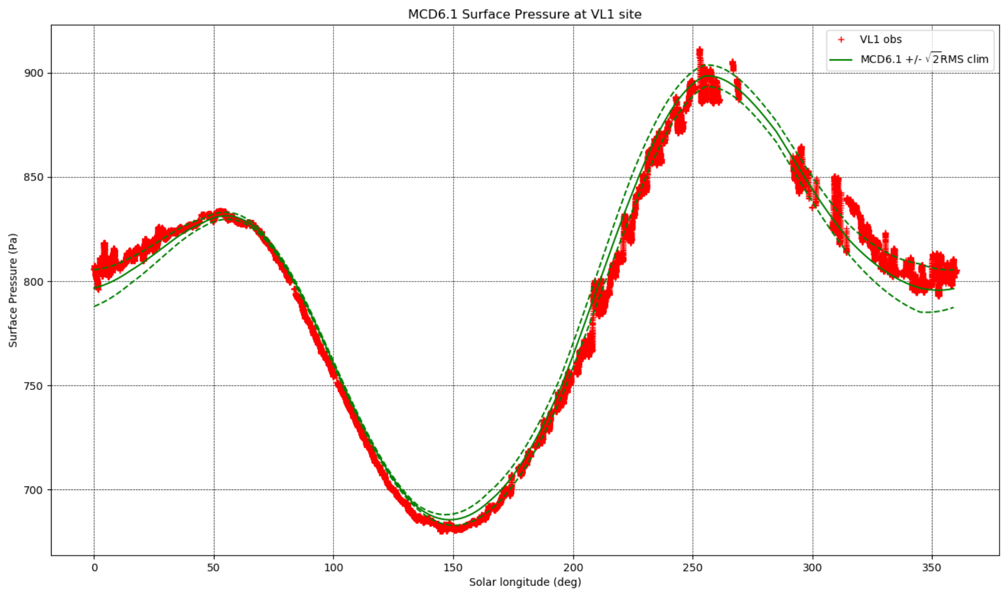

Figure 1: Surface Pressure at VL1 site, recorded by VL1 in red and MCD prediction for clim scenario in green.

The same comparison here is done except the years have not been overlaid and there is not any averaging done for the observations and the model. The MCD was called every half martian hours. This allows to check the amplitude of the diurnal cycle. It seems the amplitude of the diurnal cycle is slightly underestimated by the model all solar longitudes.

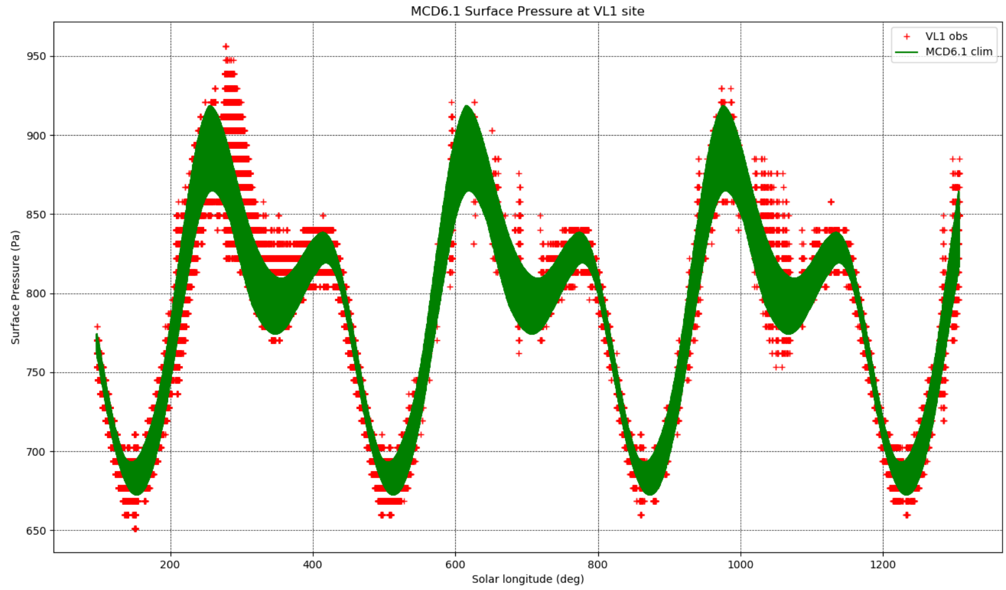

Figure 2: Surface Pressure at VL1 site, recorded by VL1 in red and MCD prediction for clim scenario in green.

2.2 Viking Lander 2

The figure below shows the comparison of the surface pressure between the measurements of Viking Lander 2 (VL2) and the MCD6.1. The comparison is done with diurnal averages of surface pressure for both VL2 measurements and the high resolution mode of the MCD. On the first year of observations, a global dust storm occured between L_s 275° and L_s 320°, which had a significant repercussion on the pressure data collected by VL2. Indeed it increased the surface pressure of several tens of Pascal. Therefore, this part of the year is directly compared to the storm case scenario of the MCD. This increase of pressure during the global dust storm is well represented by the MCD. For the other part of year, the clim scenario of the MCD was used and the surface pressure cycle simulated gives a very good fit with observations.

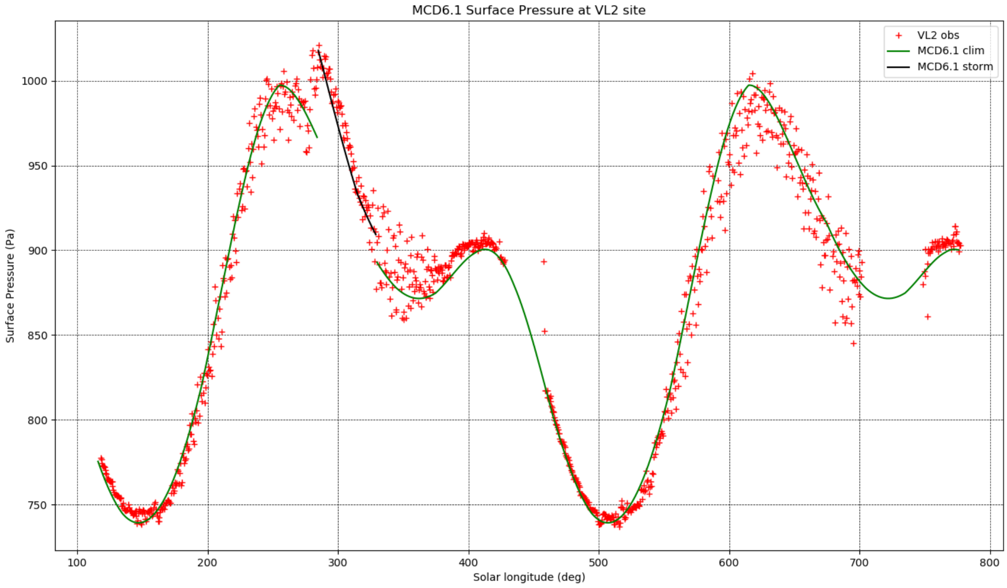

Figure 3: Surface Pressure at VL2 site, recorded by VL2 in red and MCD prediction for clim scenario in green and storm scenario in black to recover the change in behaviour recorded by VL2 during the 1977 global dust storm.

2.3 InSight

The figure below shows the comparison of the surface pressure between the measurements of Insight and the MCD6.1. The comparison is done with diurnal averages of surface pressure for both Insight measurements and the high resolution mode of the MCD. Please note that for Insight measurements, at the end of the year (after around L_s 320°), such as the beginning of the year (before around L_s 50°), both MY34 and MY35 measurements are shown. The seasonnal CO2 cycle is well represented in the MCD. In order to check the day-to-day variability, the RMS from the MCD is also shown on the figure. This variability seems to be a little underestimated by the model, seeing the variations of Insight measurements from one day to the next, which is consistent with the VL1 comparison.

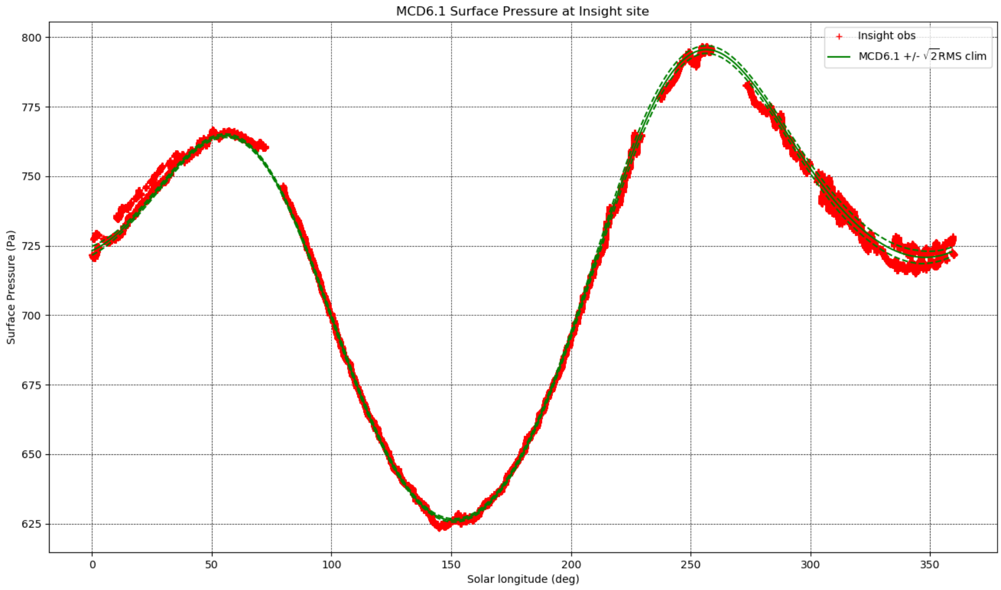

Figure 4: Surface Pressure at InSight site, recorded by InSight in red and MCD prediction for clim scenario in green.

Here the same comparison is done except there is no diurnal averaging. This allows to see the amplitude of the surface pressure diurnal cycle. Large scale perturbations scheme from MCD was added and compared directly to Insight measurements. The amplitude of the thermal tides is similar between the MCD and the observations. However arnound L_s 320°, the amplitude of the diurnal cycle measured by Insight is much bigger than the one predicted by the MCD. This may be linked to the regional C dust storm that occured at this period of the year at the equator. This dust storm was stronger this year (MY34) than the one measured the other martian years by MCS. Therefore, it is not included in the clim scenario, so this increase of the thermal tides does not appear in the MCD clim scenrario prediction.

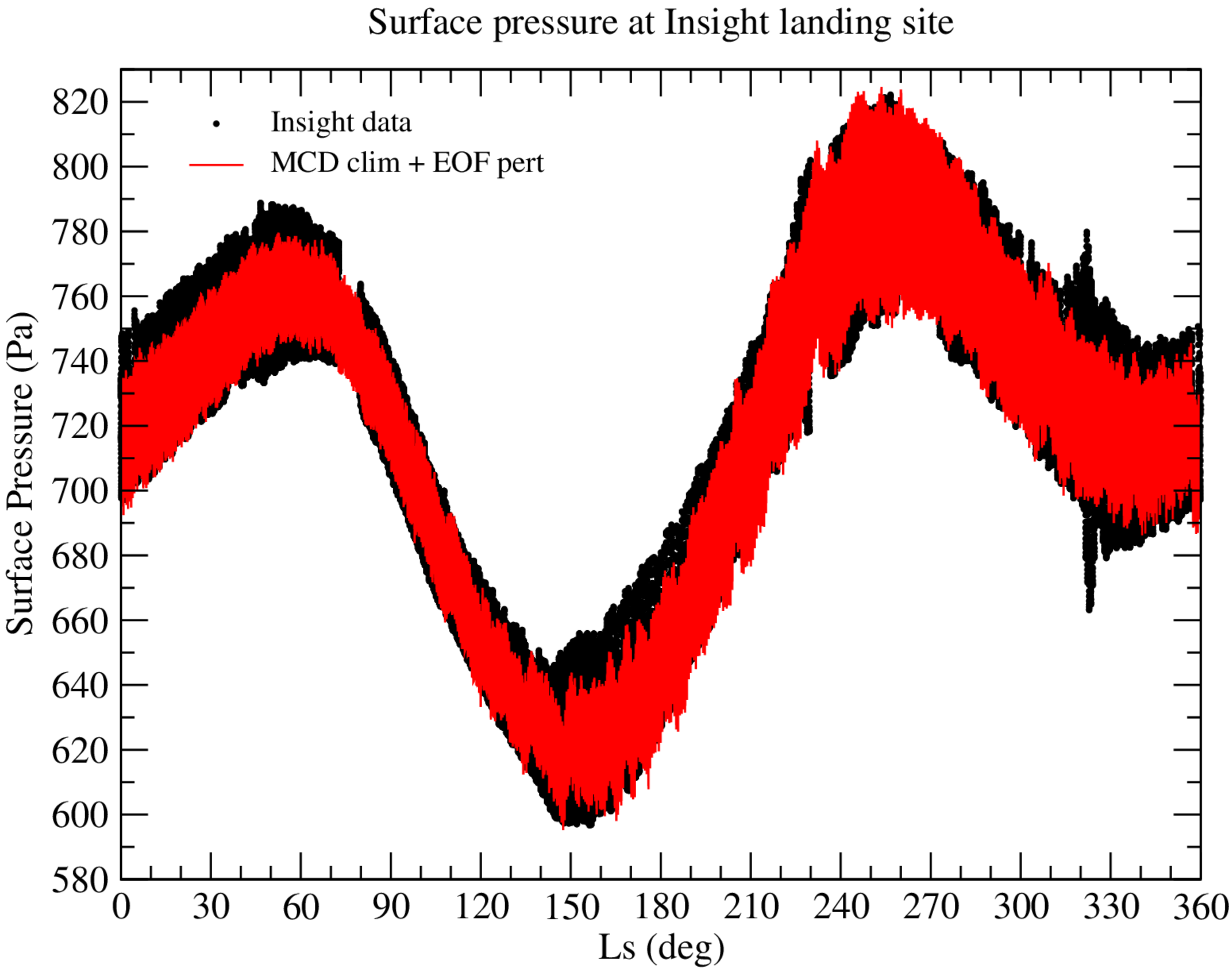

Figure 5: Surface pressure observed by Insight (first year of the mission) compared to MCD6.1 prediction (clim scenario, with large scale EOF perturbation)

Some diurnal variations are not well reproduced by the MCD even though the overall diurnal tendencies are well captured compared to Insight measurements around L_s 90°. At L_s295°the dirunal variations are very similar to the one measured by the Insight.

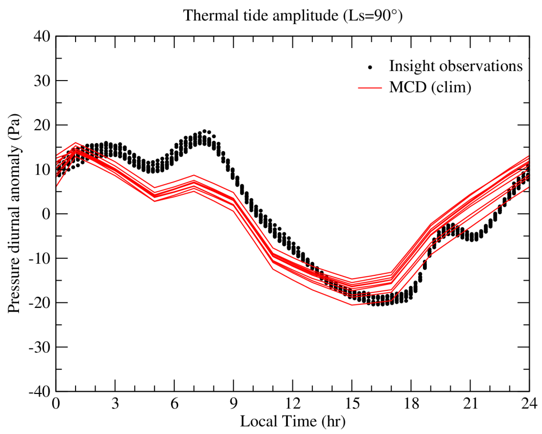

(a) L_s=90°

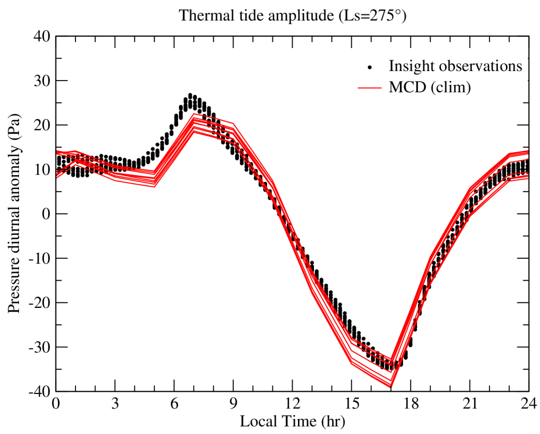

(b) L_s=295°

Figure 6: Surface pressure diurnal anomaly (i.e. signature of the thermal tides) observed by Insight during 10 sols around Ls=90° and Ls=295°, compared to the corresponding MCD6.1 prediction (clim scenario, with large scale EOF perturbation)

2.4 Perseverance

The figure below shows the comparison of the surface pressure between the measurements of Perseverance and the MCD6.1 for the first 300 mission sols (from around L_s 6° to L_s 150°). The comparison is done with diurnal averages of surface pressure for both Perseverance measurements and the high resolution mode of the MCD. The seasonnal variation is well represented by the model. A slight gap (more visible after 200 sols of mission) between the model and the measurements can be noticed. Indeed the surface pressure is underestimated of a few Pascal by the MCD.

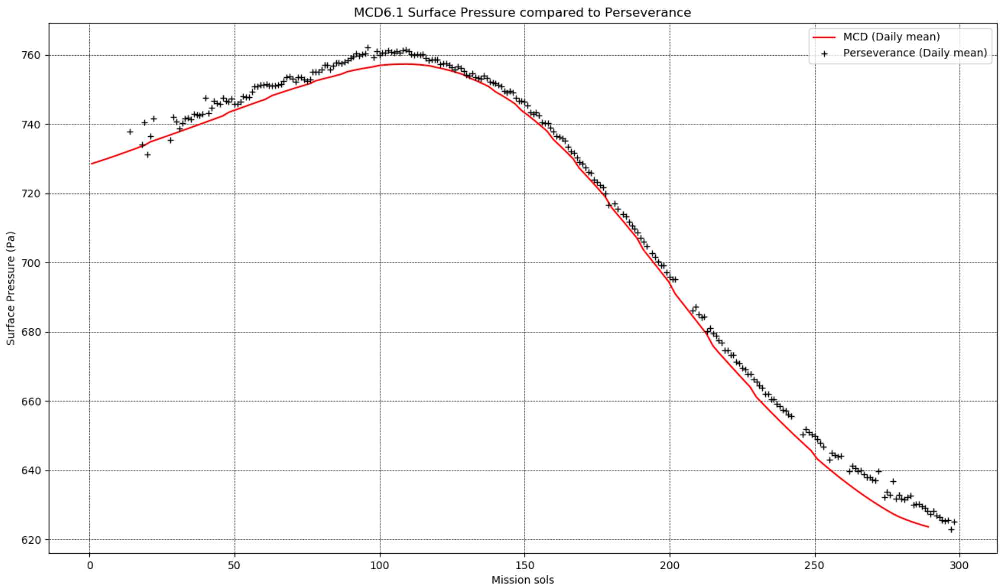

Figure 7: Surface Pressure at Perseverance site, recorded by Perseverance in black and MCD prediction for clim scenario in red.

The same comparison here is done except there is not any averaging done for the observations and the model. The MCD was called every half martian hours. This allows to check the amplitude of the diurnal cycle. The amplitude of the diurnal cycle agrees with the one measured by the rover.

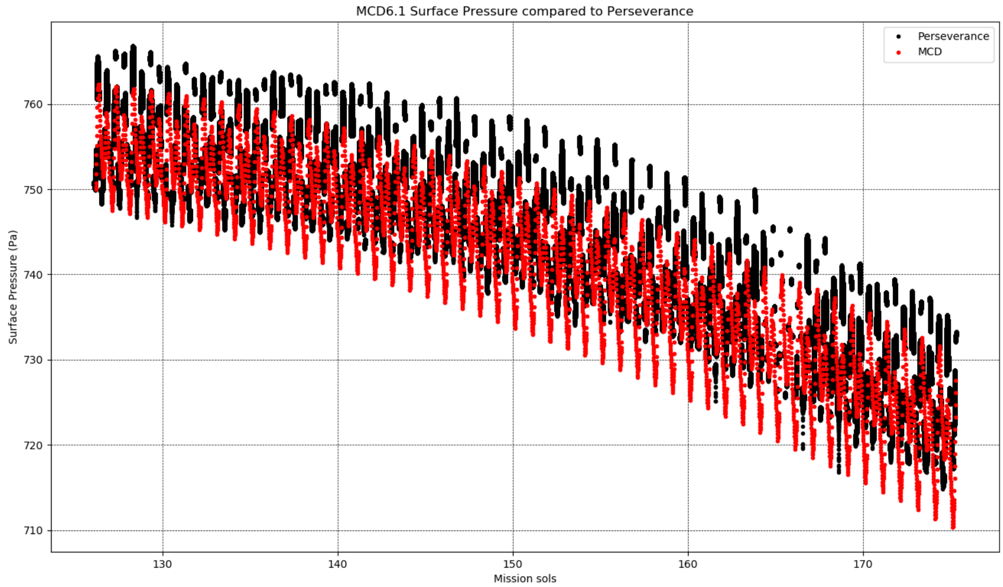

Figure 8: Surface Pressure at Perseverance site, recorded by Perseverance in black and MCD prediction for clim scenario in red.

3 Winds

3.1 InSight

The figures below show the comparison between the winds predicted by the MCD and Insight winds measurements. The amplitude of the horizontal wind and its seasonal variations are well reproduced by the MCD as seen on figure 9. In order to check the day to day variability, we add some large scale perturbations to the MCD on figure 10. The agreement between the two is good during the first part of the year. However, during the dusty season, the large scale perturbation scheme of the MCD tends to overestimate the day to day variability of the winds compared to Insight measurements.

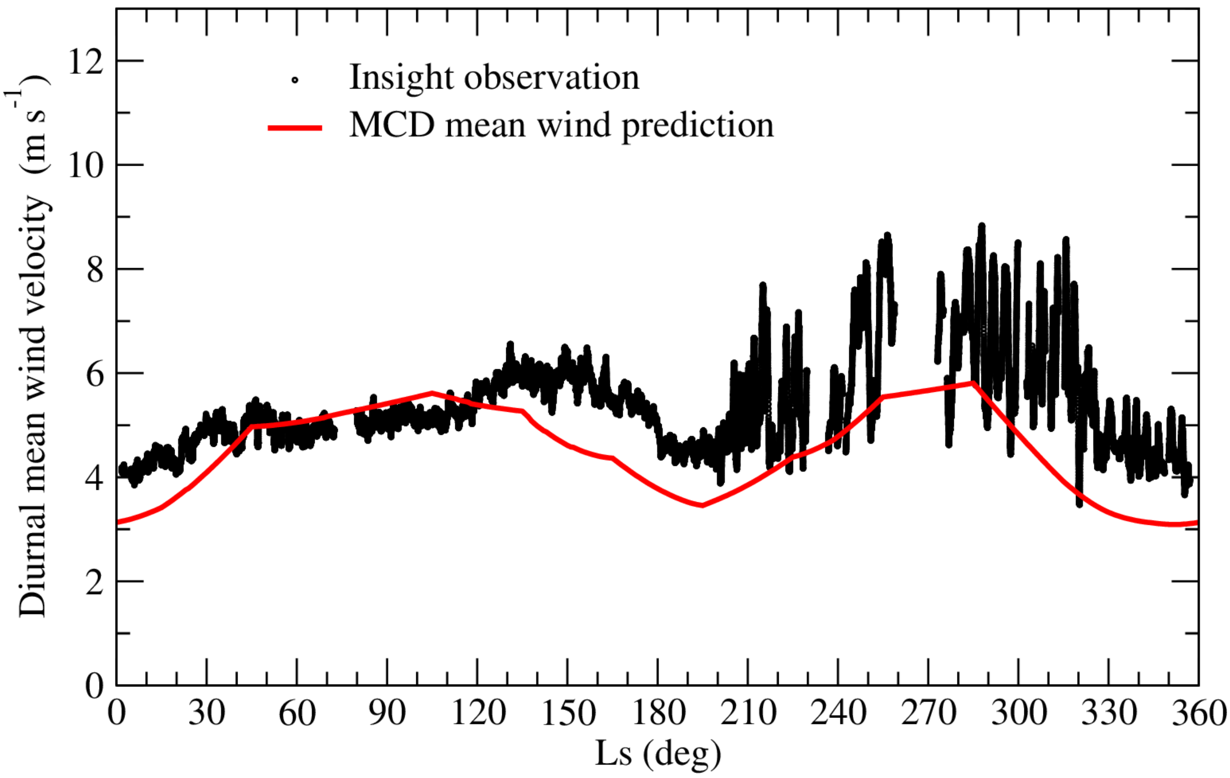

Figure 9: Diurnal mean wind velocity observed by Insight (first year of the mission) compared to MCD6.1 monthly mean predictions (clim scenario).

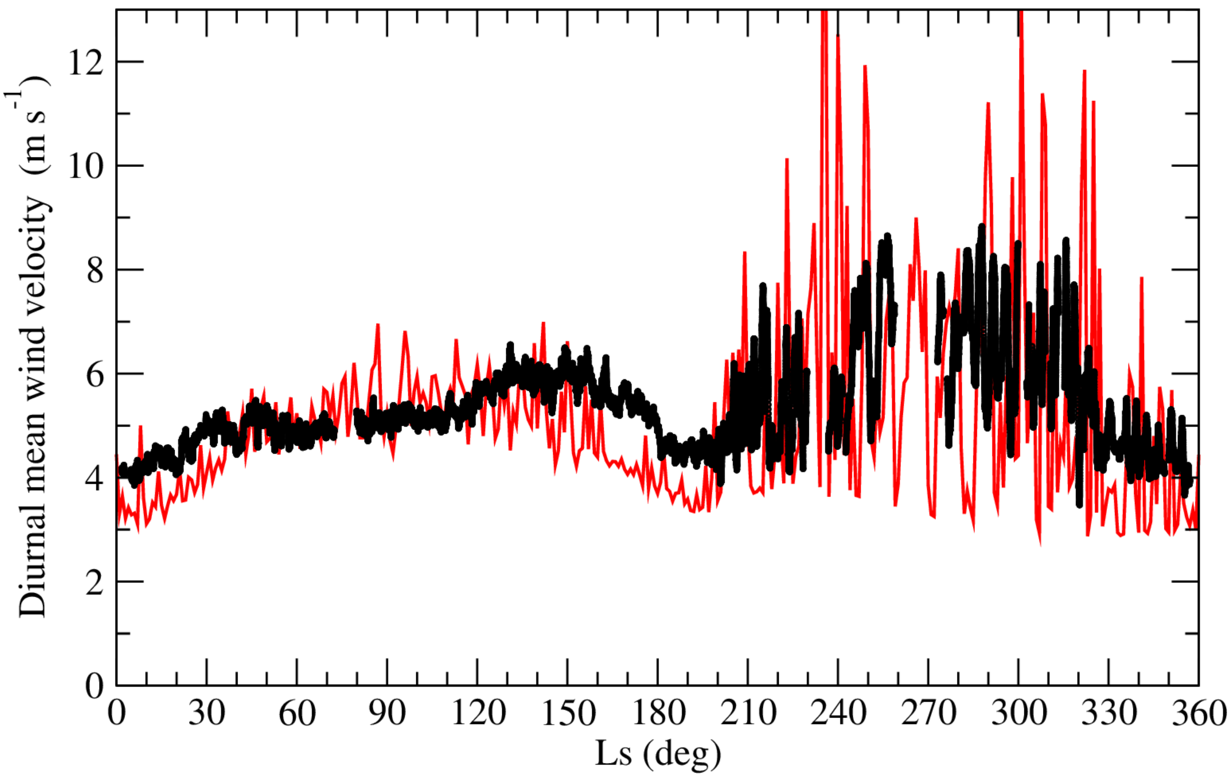

Figure 10: Diurnal mean wind velocity observed by Insight (first year of the mission) compared to MCD6.1 predictions (clim scenario) with the EOF-calculated day-to-day variability

Figure 11 shows the diurnal cycle of the wind, both in amplitude and direction, from the MCD compared to Insight measurements. For winds amplitude, the diurnal cycle is well represented by the MCD except around 5pm where the wind amplitude measured by Insight decreases abruptly contrary to the prediction of the MCD where the wind amplitude decrease more slowly. As for winds direction, both large scale winds and local slope winds effects are well reproduced by the MCD.

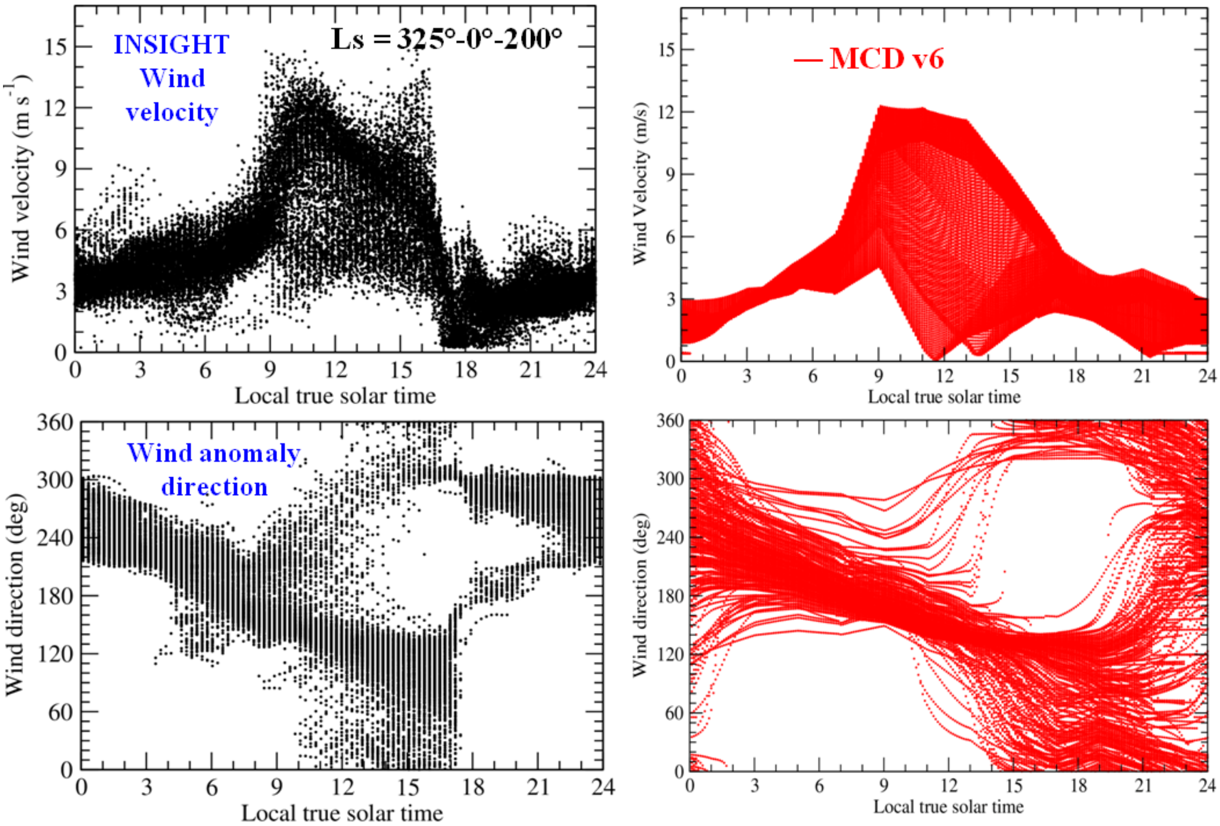

Figure 11: Wind velocities and direction (0°: southward, 90°: westward, etc.) observed by Insight (during the period Ls=325°-0°-200°) compared to corresponding MCD6.1 predictions (clim scenario)

4 Surface temperature

4.1 TES

TES records extend from mid-MY24 (L_s=102.5°) until early MY27 (L_s=85°). They are compared to the MCD directly with specific MCD scenarios (MY24 to MY27). Comparisons with clim, warm and cold scenarios are also given.

4.1.1 Day time

During day time, the zonal average of surface temperature retrieved by the MCD represents well the seasonnal variations. As for the amplitude of the surface temperature, it seems that the MCD overestimates of a few Kelvin (around 5 Kelvin) as seen on ditribution figure of MY26, which is the only complete year of TES measurements without global dust storm. During the beginning of the global dust storm of MY25 (around L_s=200°), the MCD overestimates the surface temperature compared to TES and underestimate it at the end of the dust storm. This is due to the low amount of dust in the atmosphere in the model compared to the observation at the beginning of the global dust storm, and the high one at the end of the dust storm, as developed in the 'Dust Opacity' section.

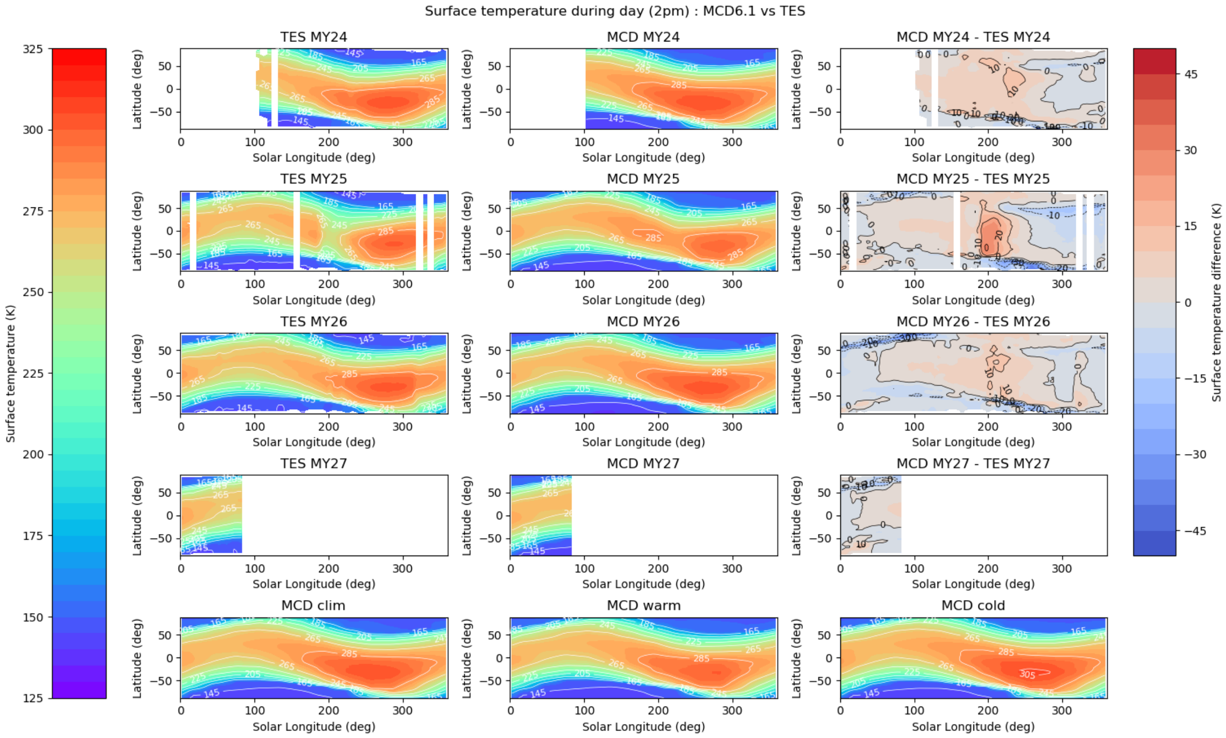

Figure 12: Zonal surface temperature over solar longitude from MY24 to MY27 (first four lines), at 2 pm (local solar time). Left : TES data. Middle : MCD data. Right : Difference MCD-TES. Last line shows clim, warm and cold scenarios.

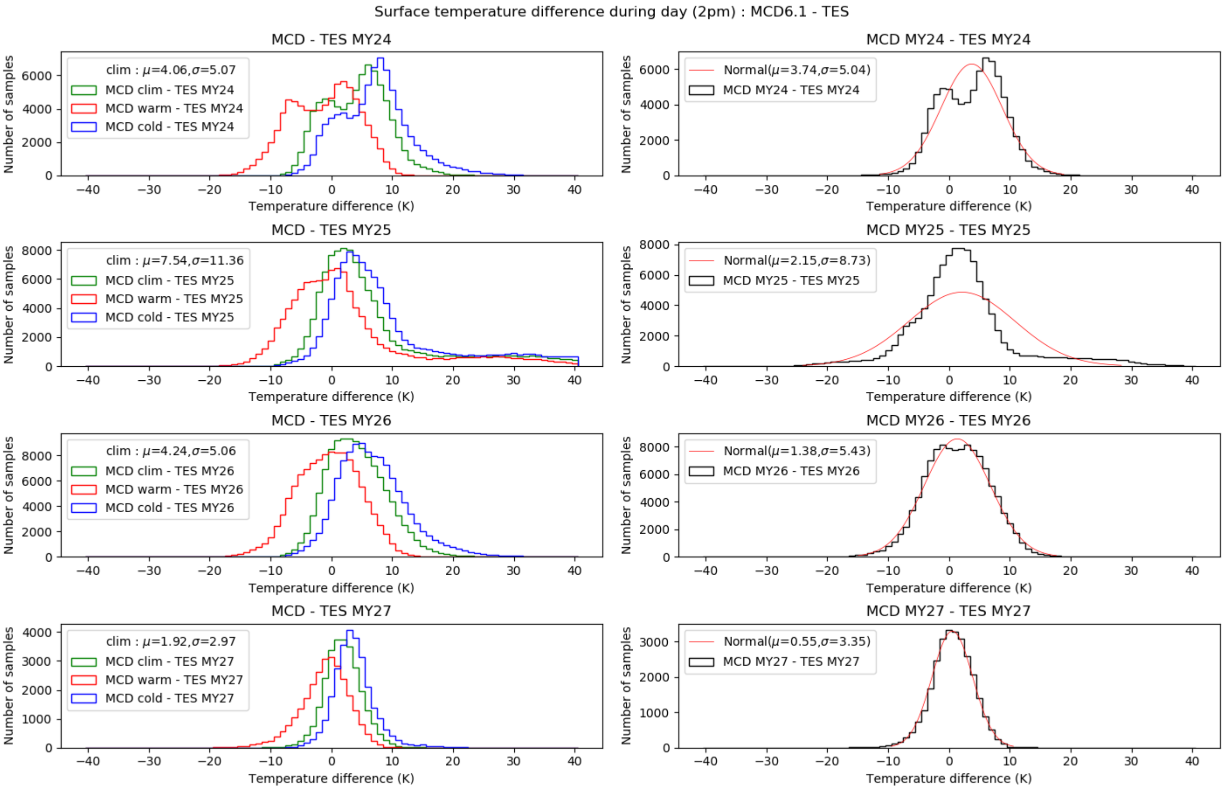

Figure 13: Distribution of surface temperature differences between MCD v6.1 and TES using bins of 1K from MY24 to MY27 (from top to bottom), at 2 pm (local solar time) in latitudes (-50,50). Left : TES compared with MCD for clim, warm and cold scenarios. Right : TES compared with MCD for specific MY scenario. The red curve on the right represents normal distributions of same mean and standard deviation.

4.1.2 Night time

During night time, the zonal average of surface temperature retrieved by the MCD represents well the seasonnal variations as seen on the figures showing the evolution over the solar longitudes, except during the global dust storm of MY25 where the surface temperature is lower in the model. Just before the dust storm, one can notice that the MCD is too warm campared to TES, this is due to the fact that the MCD interpolates field between data stored every 30° of L_s. Except during this part of the year 25, the MCD and TES surface temperature have very similar values overall (differences below 1K on average).

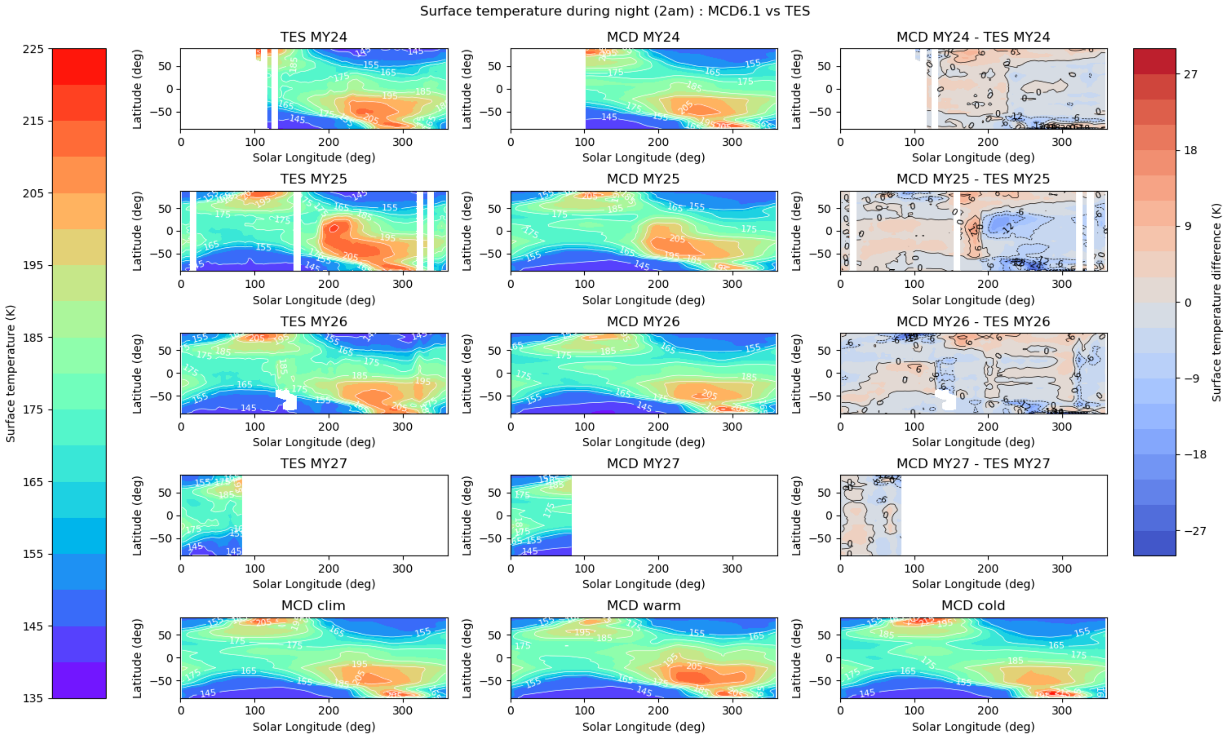

Figure 14: Zonal surface temperature over solar longitude from MY24 to MY27 (first four lines), at 2 am (local solar time). Left : TES data. Middle : MCD data. Right : Difference MCD-TES. Last line shows clim, warm and cold scenarios.

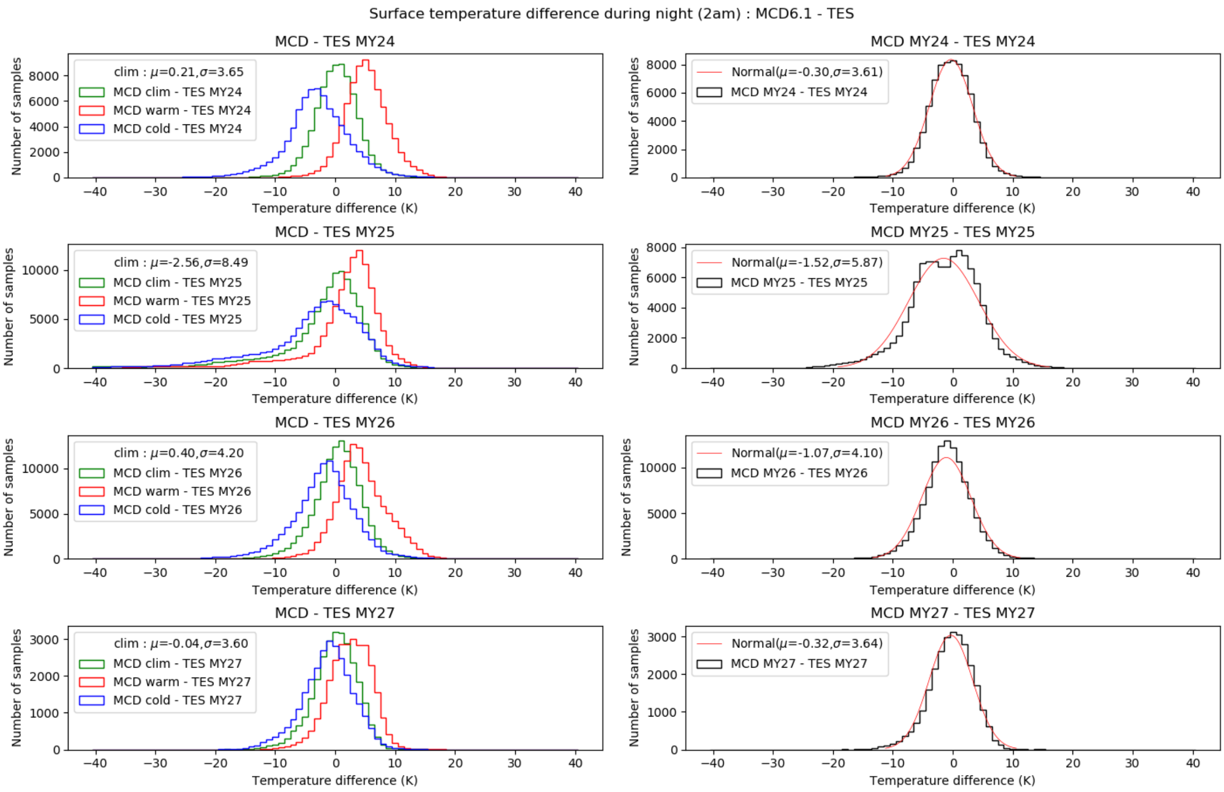

Figure 15: Distribution of surface temperature differences between MCD v6.1 and TES using bins of 1K from MY24 to MY27 (from top to bottom), at 2 am (local solar time) in latitudes (-50,50). Left : TES compared with MCD for clim, warm and cold scenarios. Right : TES compared with MCD for specific MY scenario. The red curve on the right represents normal distributions of same mean and standard deviation.

5 Atmospheric temperature

5.1 TES

TES datasets include atmospheric temperature, which we compare here to MCD predictions. Comparisons were made at 106Pa around 15-20 km altitude where TES Nadir retrieval is most accurate (peak of the weighting function). A comparison of temperature profile is also shown in order to check the agreement between the MCD and TES observations at different altitudes (from 1000Pa to 10Pa).

5.1.1 Day time

During day time, we see a good agreement between the two datasets for the seasonnal evolution of the temperature. In general the MCD is too warm near the equator, except during the dust storm of MY25 (especially at the end of it) and at the poles where the temperatures are too cold. On average over the year, the MCD over estimates the temperature at 106Pa of a few Kelvin (mean difference of 4K too warm for the MCD). Looking at the profile, we see that this warm bias is true from surface to around 40Pa (around 30km), above the MCD becomes colder than TES observation on average.

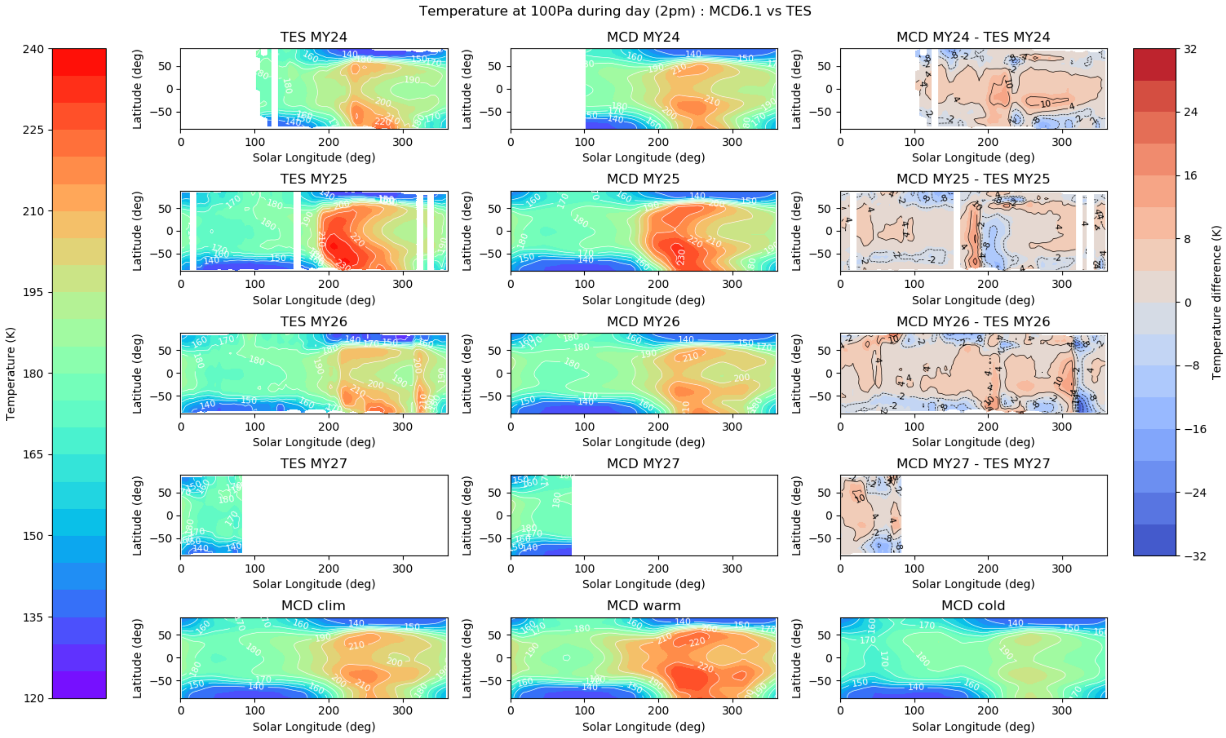

Figure 16: Zonal atmospheric temperature at 100 Pa over solar longitude from MY24 to MY27 (first four lines), at 2 pm (local solar time). Left : TES data. Middle : MCD data. Right : Difference MCD-TES. Last line shows clim, warm and cold scenarios.

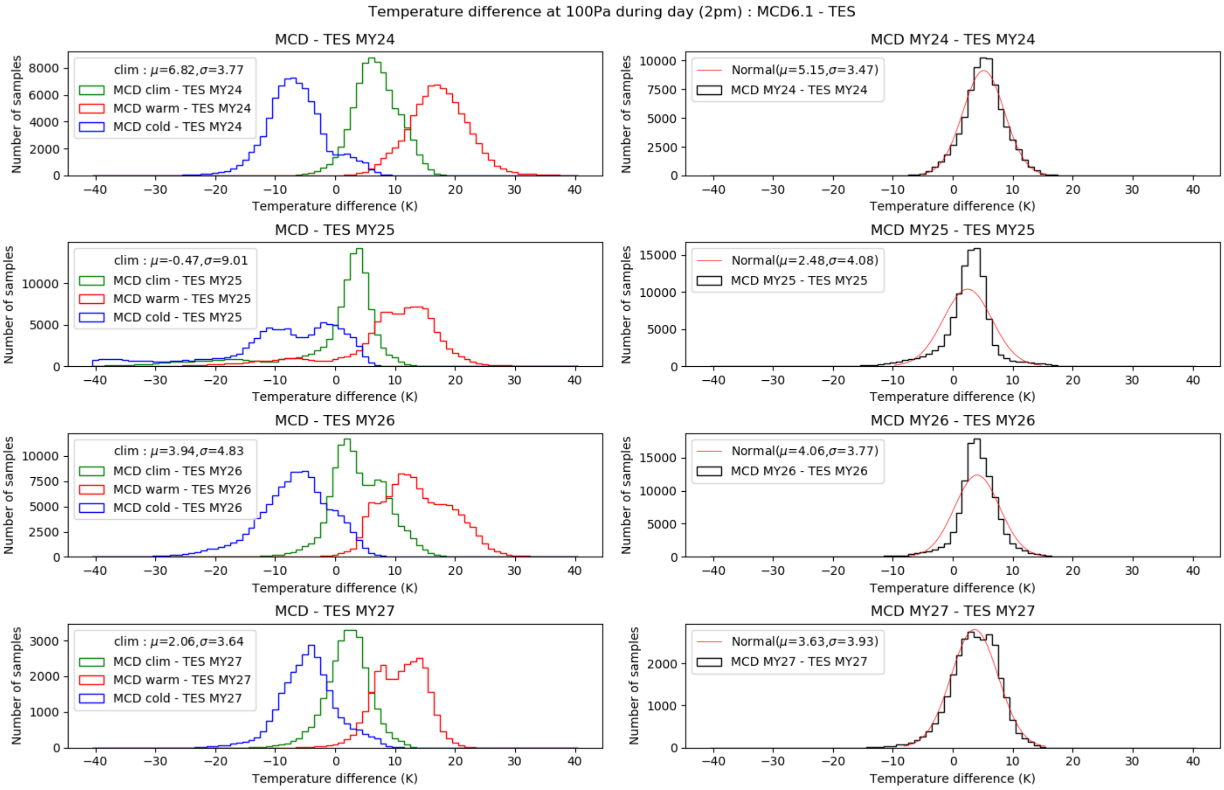

Figure 17: Distribution of atmospheric temperature at 100 Pa differences between MCD v6.1 and TES using bins of 1K from MY24 to MY27 (from top to bottom), at 2 pm (local solar time) in latitudes (-50,50). Left : TES compared with MCD for clim, warm and cold scenarios. Right : TES compared with MCD for specific MY scenario. The red curve on the right represents normal distributions of same mean and standard deviation.

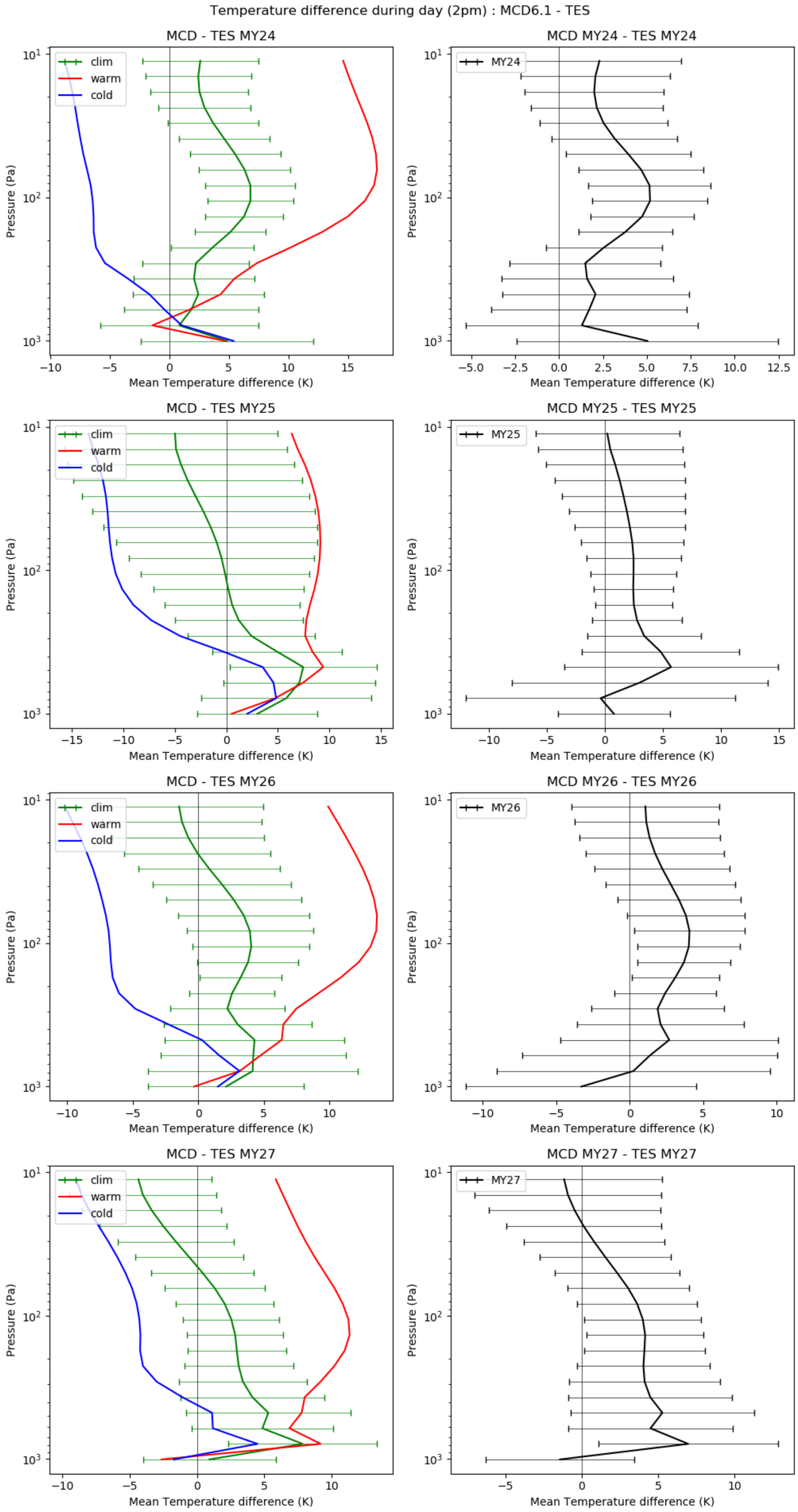

Figure 18: Profile of mean deviation for atmospheric temperature differences between MCD v6.1 and TES from MY24 to MY27 (from top to bottom), at 2 pm (local solar time) in latitudes (-50,50). Left : TES compared with MCD for clim, warm and cold scenarios. Right : TES compared with MCD for specific MY scenario.

5.1.2 Night time

During night time, we see a good agreement between the two datasets for the seasonnal evolution of the temperature. Just like during the day, at 100Pa, the MCD is mostly too warm near the equator of a few Kelvin (2 Kelvin on average). Looking at the profile, we see that this warm bias is true from 600Pa (a few km above surface) to the top of TES observations at 10Pa, which corresponds roughly to 40km. Please note that the cold bias below 600Pa corresponds to very few measurements and is therefore not very relevant.

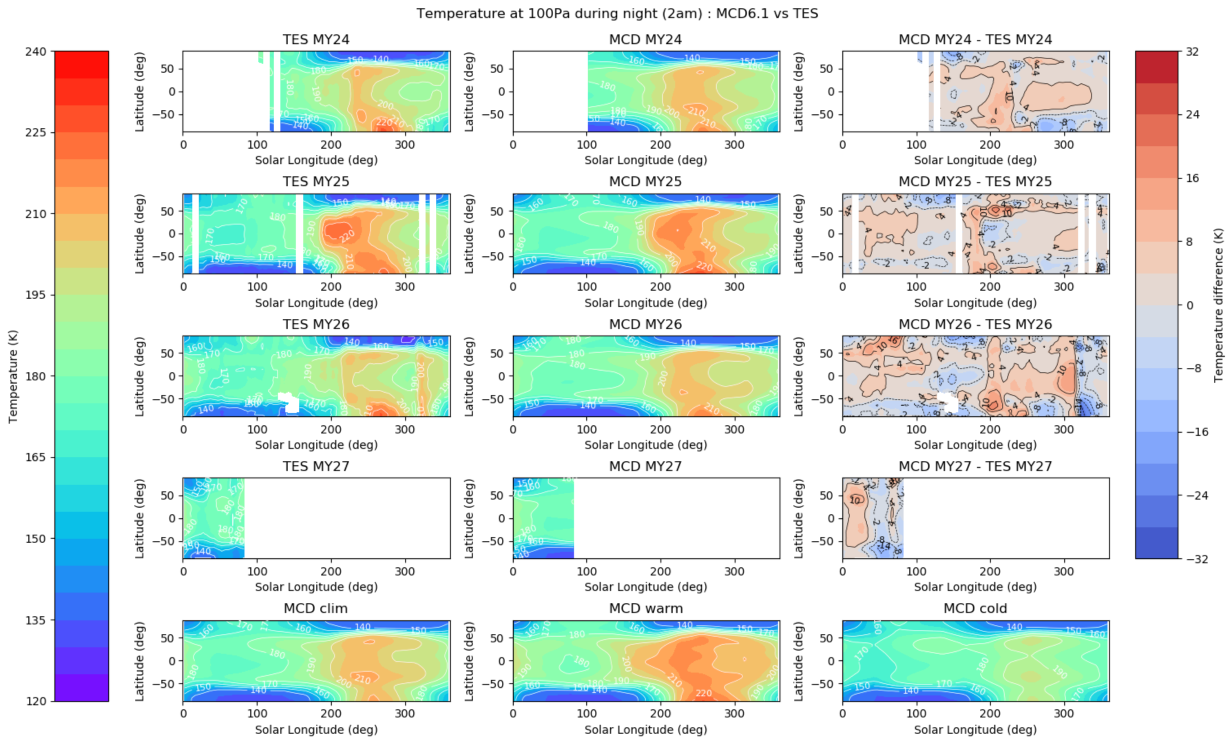

Figure 19: Zonal atmospheric temperature at 100 Pa over solar longitude from MY24 to MY27 (first four lines), at 2 am (local solar time). Left : TES data. Middle : MCD data. Right : Difference MCD-TES. Last line shows clim, warm and cold scenarios.

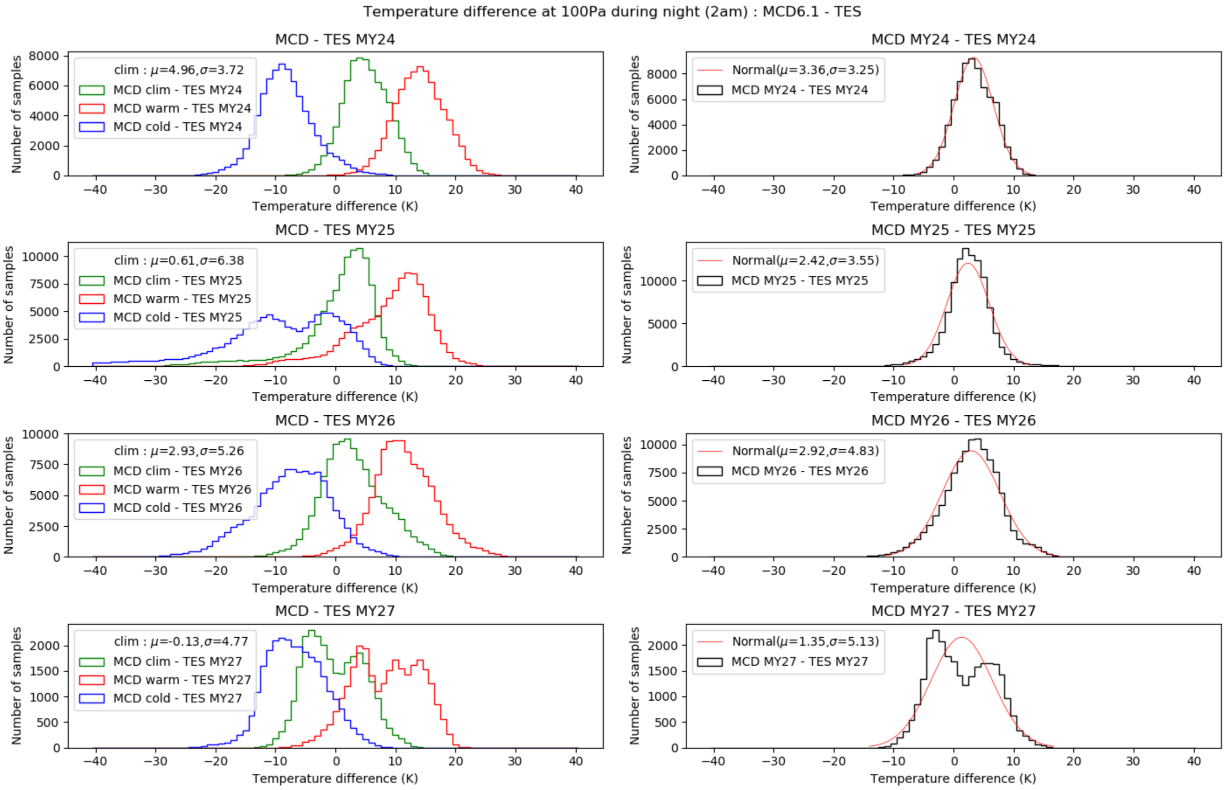

Figure 20: Distribution of atmospheric temperature at 100 Pa differences between MCD v6.1 and TES using bins of 1K from MY24 to MY27 (from top to bottom), at 2 am (local solar time) in latitudes (-50,50). Left : TES compared with MCD for clim, warm and cold scenarios. Right : TES compared with MCD for specific MY scenario. The red curve on the right represents normal distributions of same mean and standard deviation.

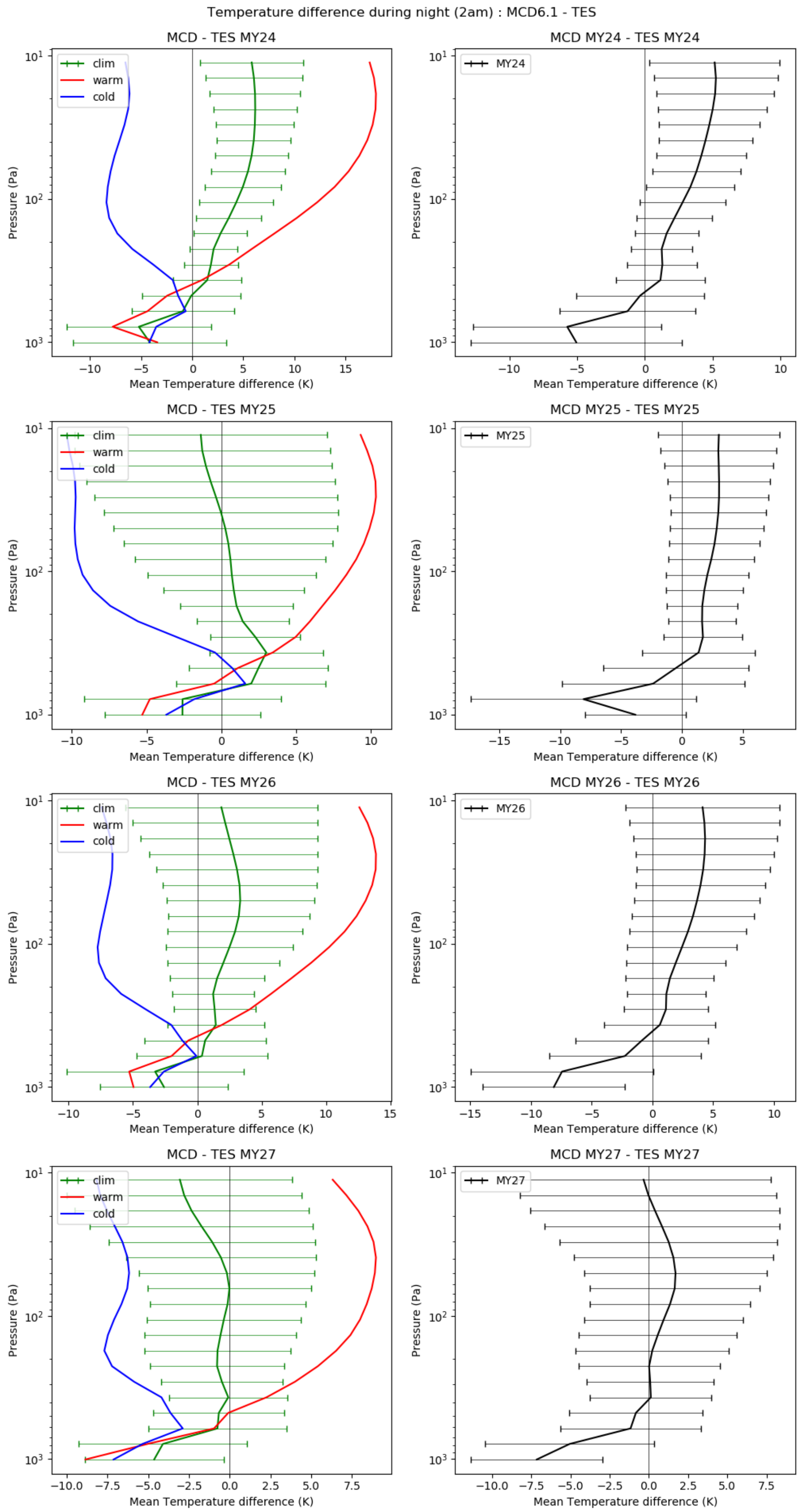

Figure 21: Profile of mean deviation for atmospheric temperature differences between MCD v6.1 and TES from MY24 to MY27 (from top to bottom), at 2 am (local solar time) in latitudes (-50,50). Left : TES compared with MCD for clim, warm and cold scenarios. Right : TES compared with MCD for specific MY scenario.

5.2 MCS

MCS datasets include atmospheric temperature, which we compare here to MCD predictions. Comparisons were made on all altitudes observed by MCS, from 1000Pa to 10^{-2}Pa, which corresponds roughly to a range from surface to 100km. The comparison is shown at different time of the year at L_s 0°, 90°, 180° and 270°. We seperate the analysis in two variables : the diurnal mean ($\frac{T_{day}+T_{night}}{2}$) and the diurnal anomaly ($T_{day} - T_{night}$).

5.2.1 Diurnal Mean

The figures below show the comparison between the MCD and MCS diurnal mean temperatures. Very close to the surface, the MCD is too cold compared to the observations but few MCS profiles reach these low altitudes. Above 600Pa, the MCD becomes slightly warmer than MCS in average, by a few Kelvins, and up to 0.1Pa. Above this altitude (80km), the MCD tends to underestimate the temperature by almost 10K. This annual trend hides a strong seasonal variability, with a warm bias always seen at L_s 90°. During MY34, the MCD overestimates the temperature just before the global dust storm. This is due to temporal interpolation made by the MCD between L_s 165° and 195°, while the global dust storm starts at L_s 190°.

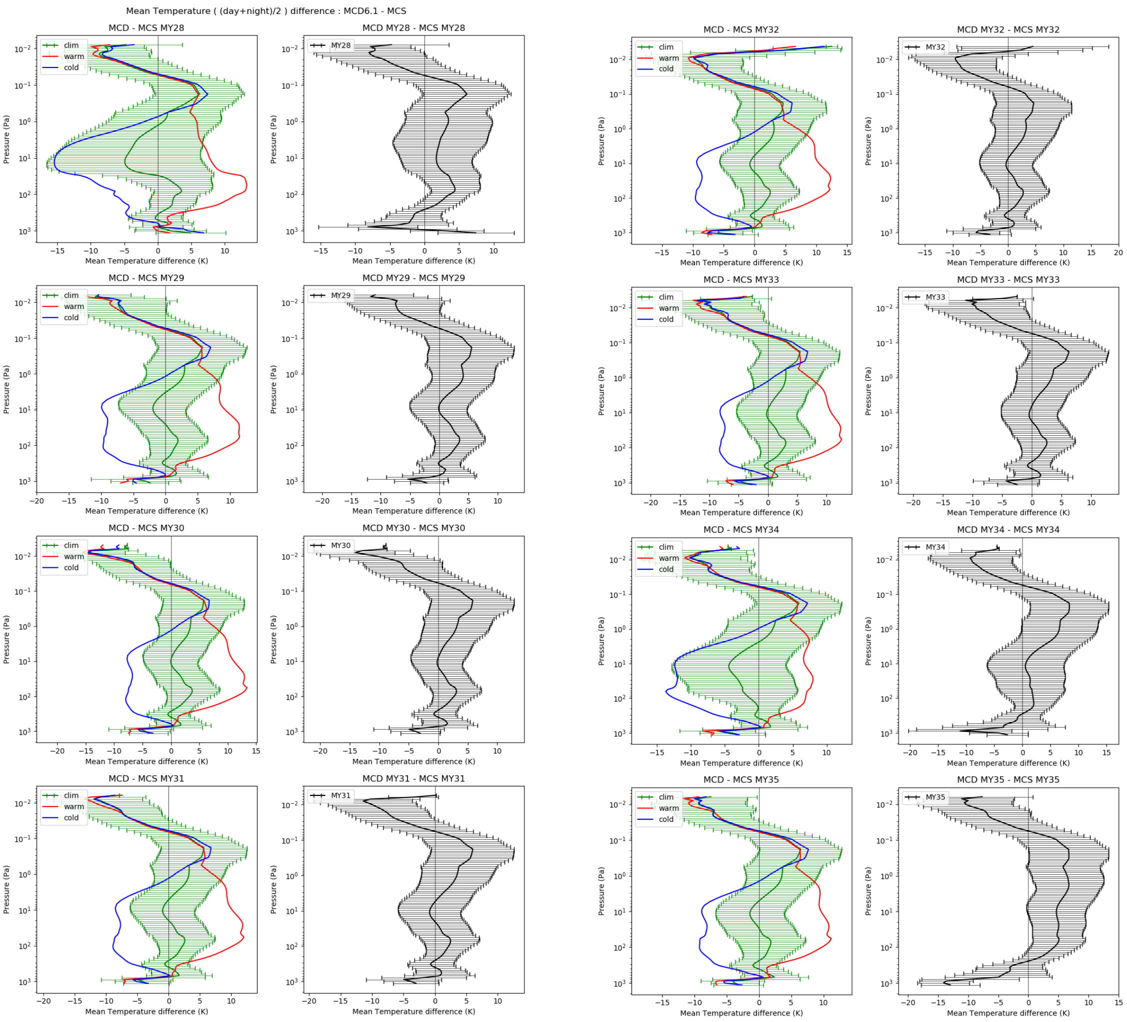

(a) MY28 to MY31

(b) MY32 to MY35

Figure 22: Profile of mean deviation for atmospheric temperature diurnal mean differences between MCD v6.1 and MCS, from MY28 to MY35 (from top to bottom), spatially averaged in latitudes (-50,50). Left : MCS compared with MCD for clim, warm and cold scenarios. Right : MCS compared with MCD for specific MY scenario.

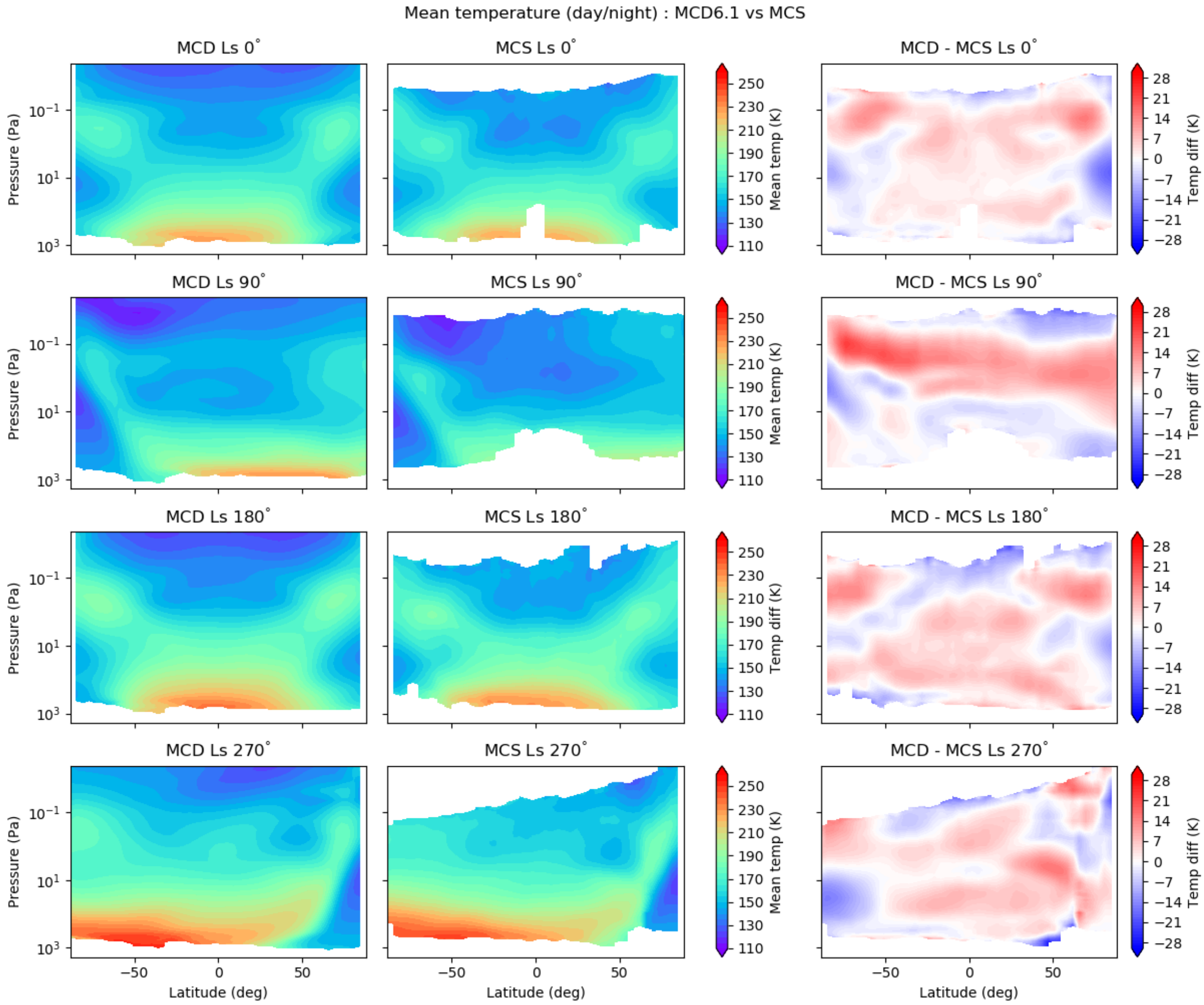

Figure 23: Cross section Pressure-latitude of zonally average mean temperature (averaged over night and day) from MCD v6.1 (left) compared to MCS (middle). The difference between MCD and MCS is shown on the right. Temperatures are shown for L_s 0°, 90°, 180° and 270° from top to bottom for MY29

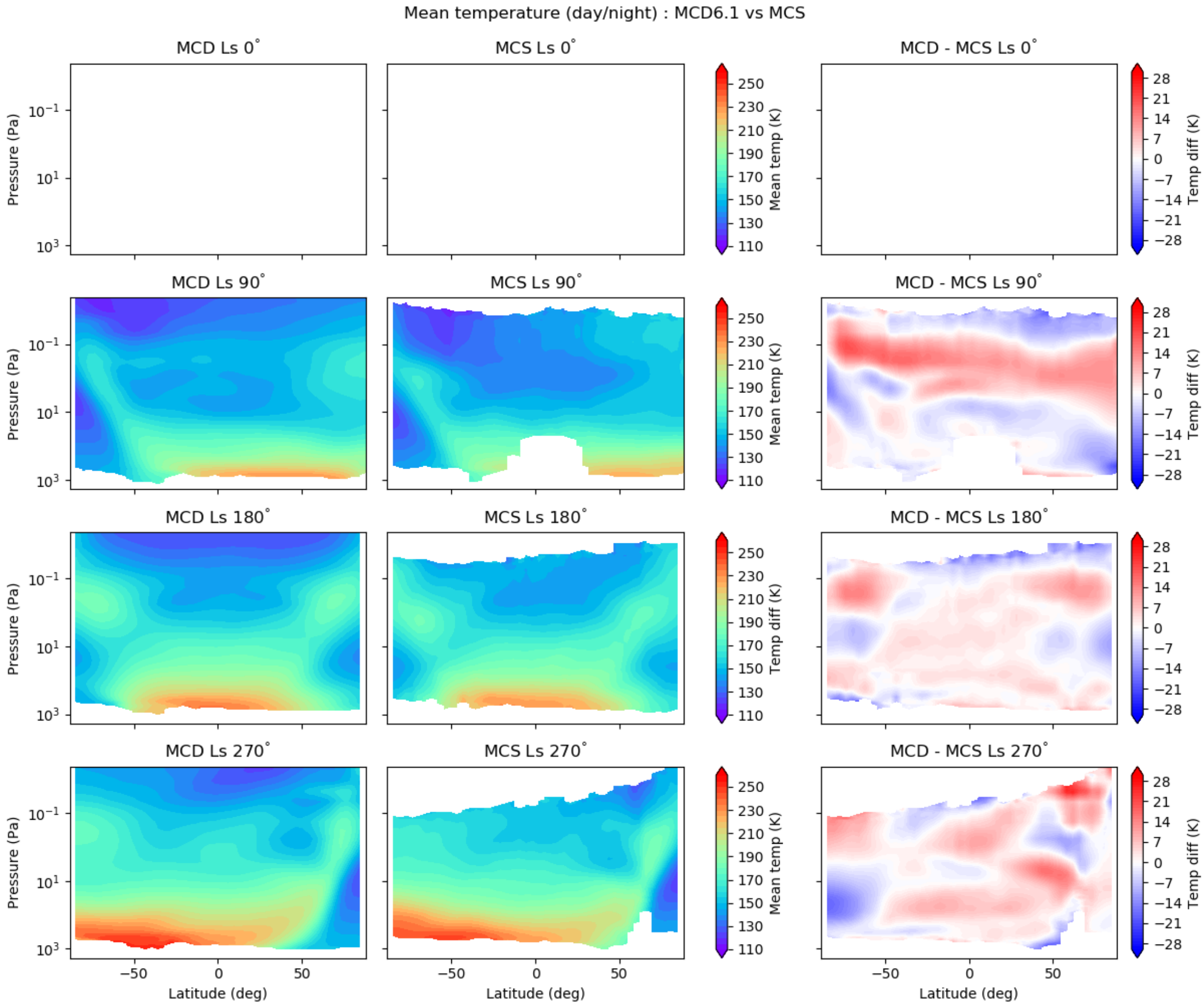

Figure 24: Cross section Pressure-latitude of zonally average mean temperature (averaged over night and day) from MCD v6.1 (left) compared to MCS (middle). The difference between MCD and MCS is shown on the right. Temperatures are shown for L_s 0°, 90°, 180° and 270° from top to bottom for MY30

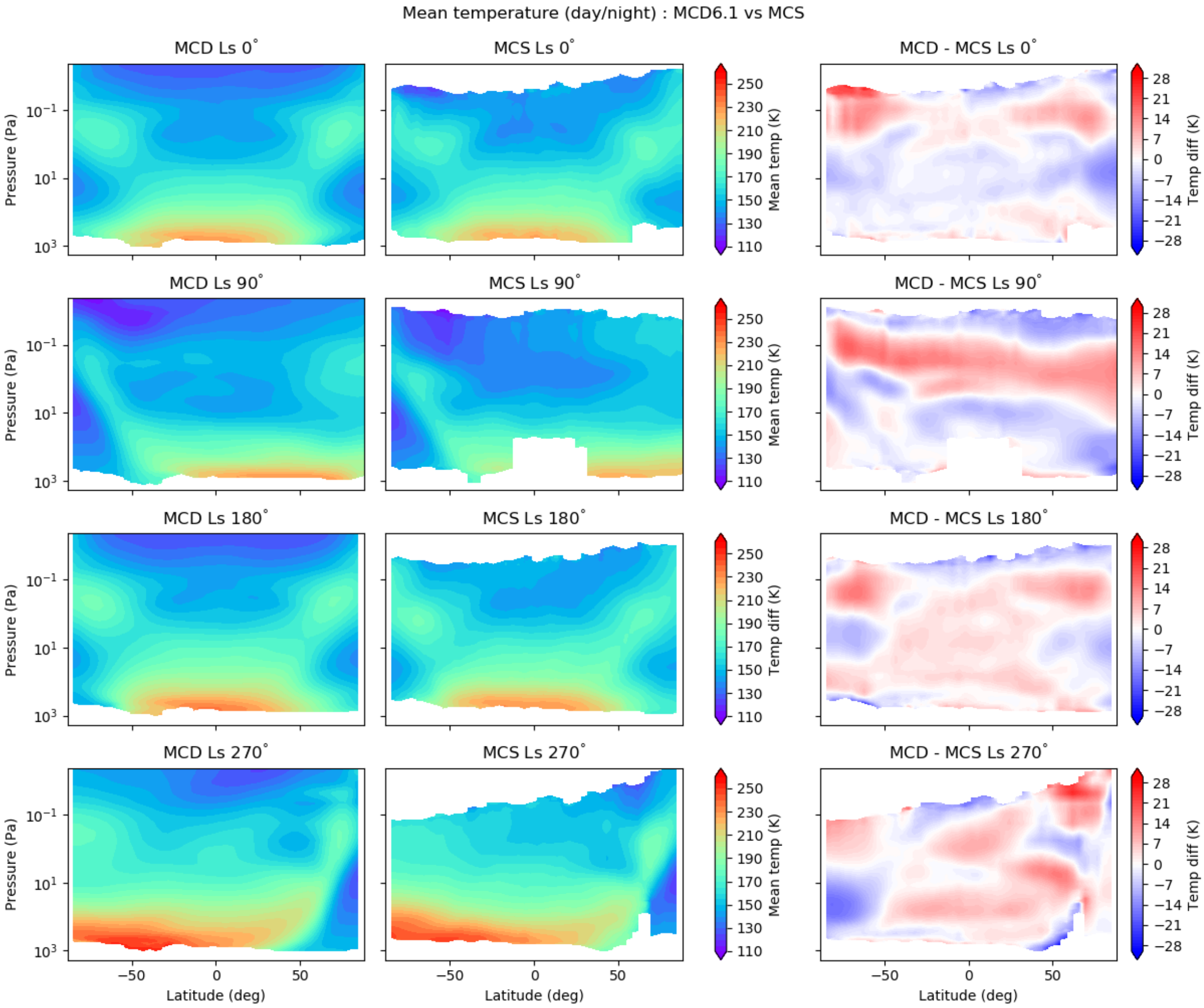

Figure 25: Cross section Pressure-latitude of zonally average mean temperature (averaged over night and day) from MCD v6.1 (left) compared to MCS (middle). The difference between MCD and MCS is shown on the right. Temperatures are shown for L_s 0°, 90°, 180° and 270° from top to bottom for MY31

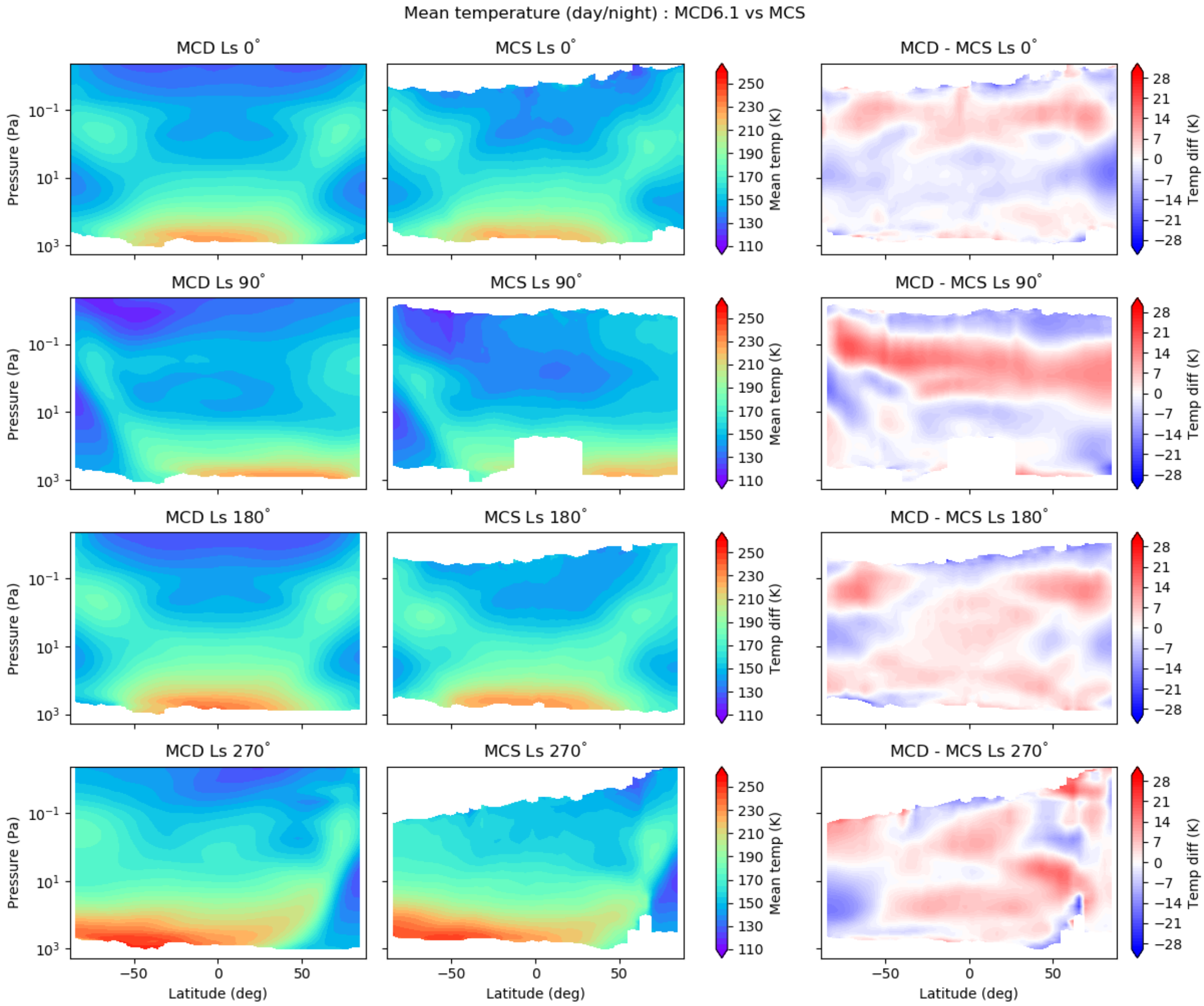

Figure 26: Cross section Pressure-latitude of zonally average mean temperature (averaged over night and day) from MCD v6.1 (left) compared to MCS (middle). The difference between MCD and MCS is shown on the right. Temperatures are shown for L_s 0°, 90°, 180° and 270° from top to bottom for MY32

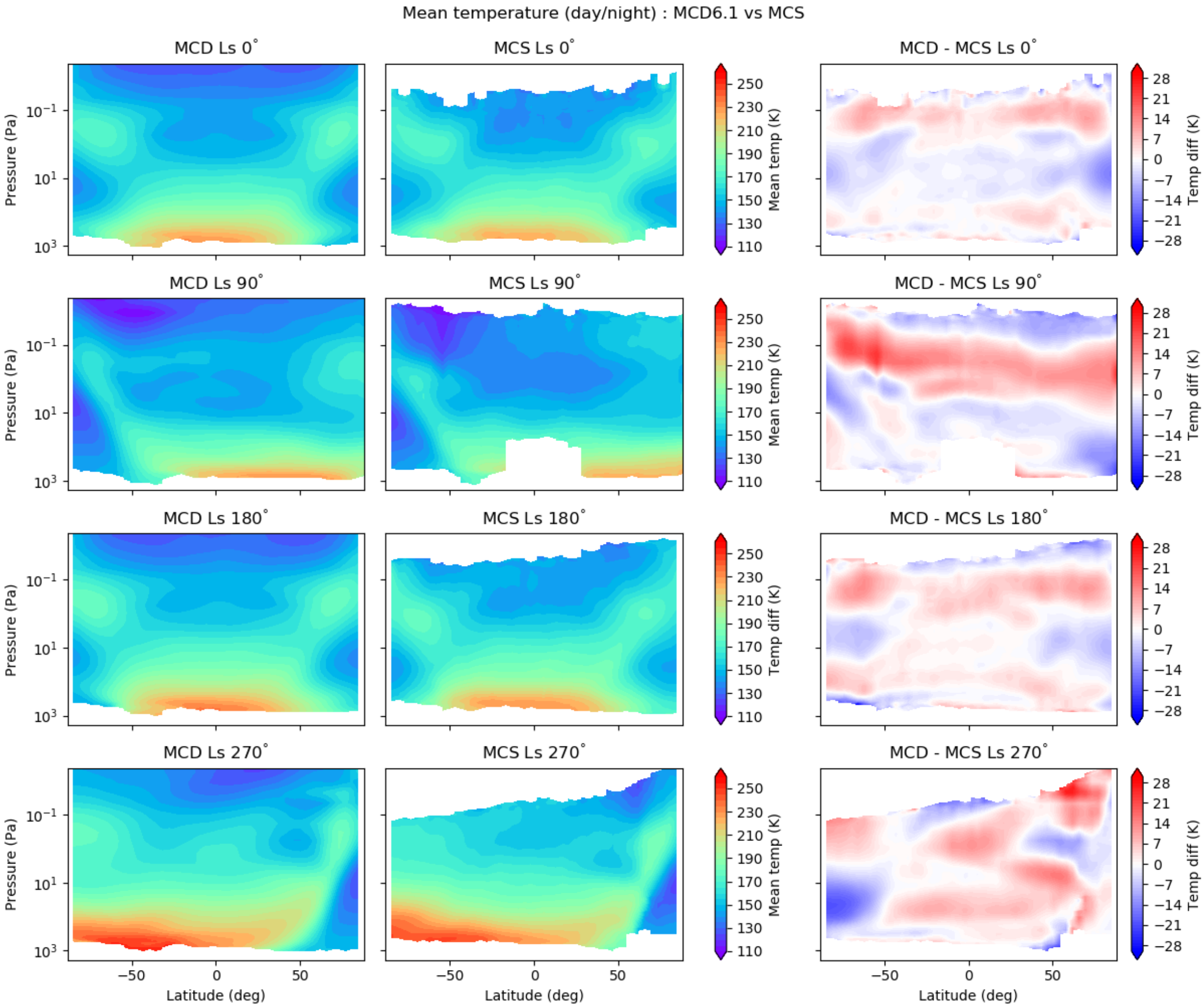

Figure 27: Cross section Pressure-latitude of zonally average mean temperature (averaged over night and day) from MCD v6.1 (left) compared to MCS (middle). The difference between MCD and MCS is shown on the right. Temperatures are shown for L_s 0°, 90°, 180° and 270° from top to bottom for MY33

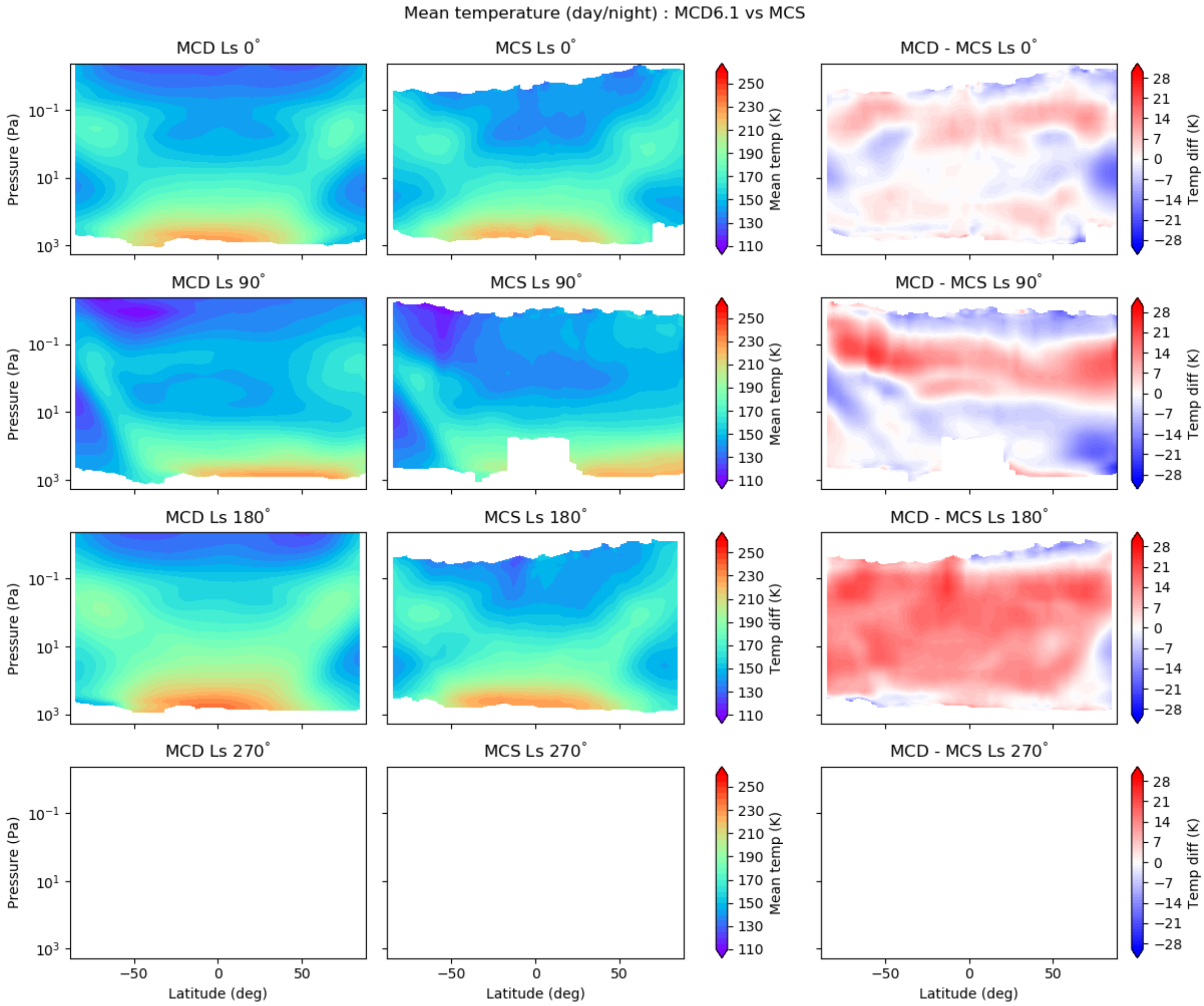

Figure 28: Cross section Pressure-latitude of zonally average mean temperature (averaged over night and day) from MCD v6.1 (left) compared to MCS (middle). The difference between MCD and MCS is shown on the right. Temperatures are shown for L_s 0°, 90°, 180° and 270° from top to bottom for MY34

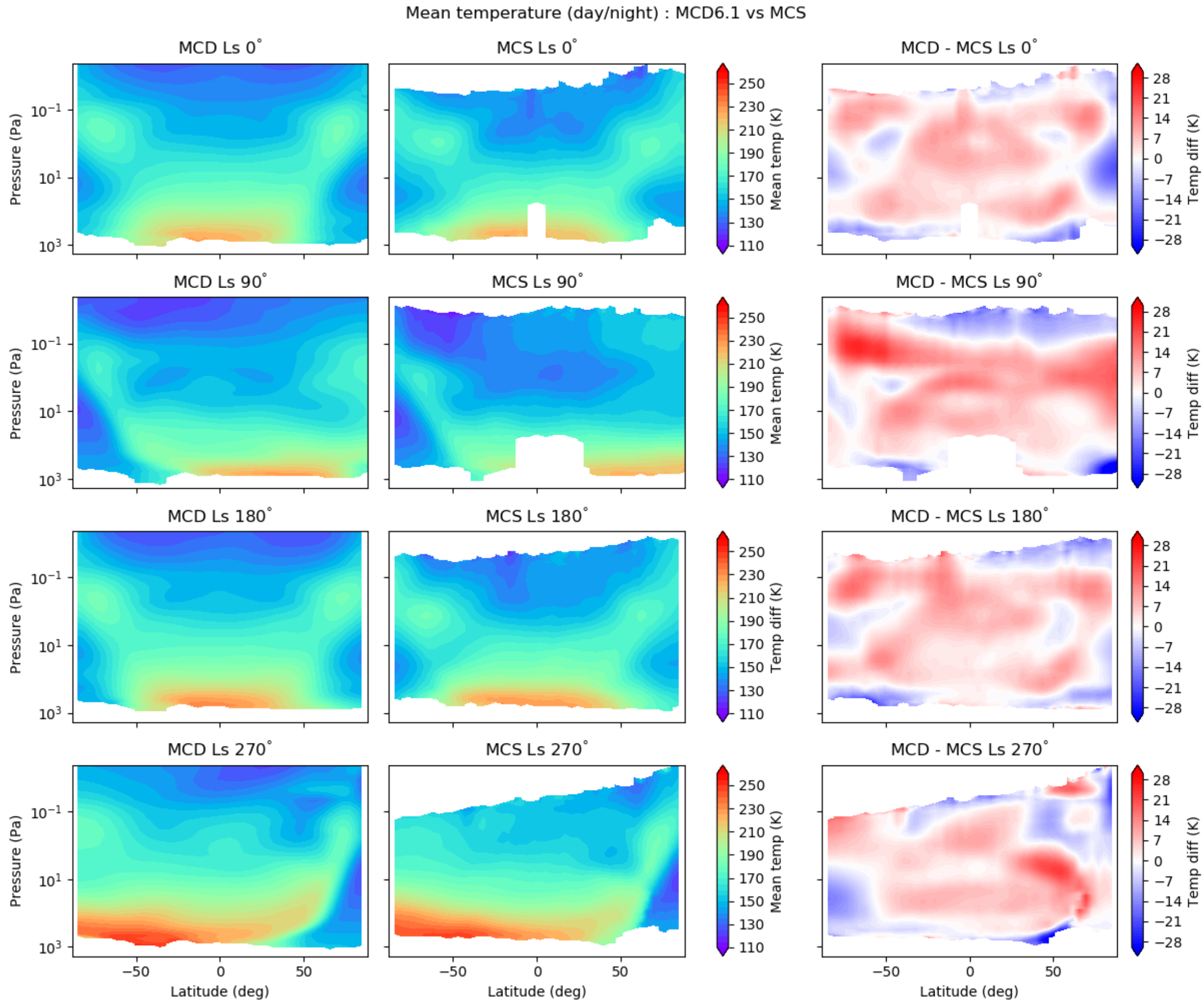

Figure 29: Cross section Pressure-latitude of zonally average mean temperature (averaged over night and day) from MCD v6.1 (left) compared to MCS (middle). The difference between MCD and MCS is shown on the right. Temperatures are shown for L_s 0°, 90°, 180° and 270° from top to bottom for MY35

5.2.2 Diurnal Anomaly

The figures below show the comparison between the MCD and MCS diurnal anomaly temperatures. These diurnal anomalies are forced by the thermal tides. Therefore, the oscillations of the datasets differences around 0 denote a difference of phase between the two. Still the spatio-temporal structure of the thermal tides and their seasonal evolution is well reproduced by the MCD as shown on the figures 31 to 37.

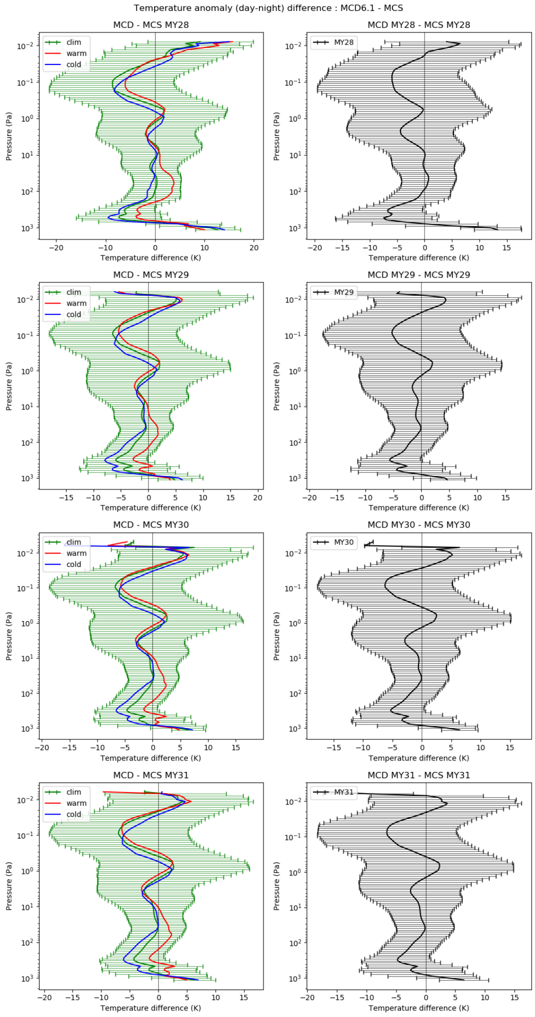

(a) MY28 to MY31

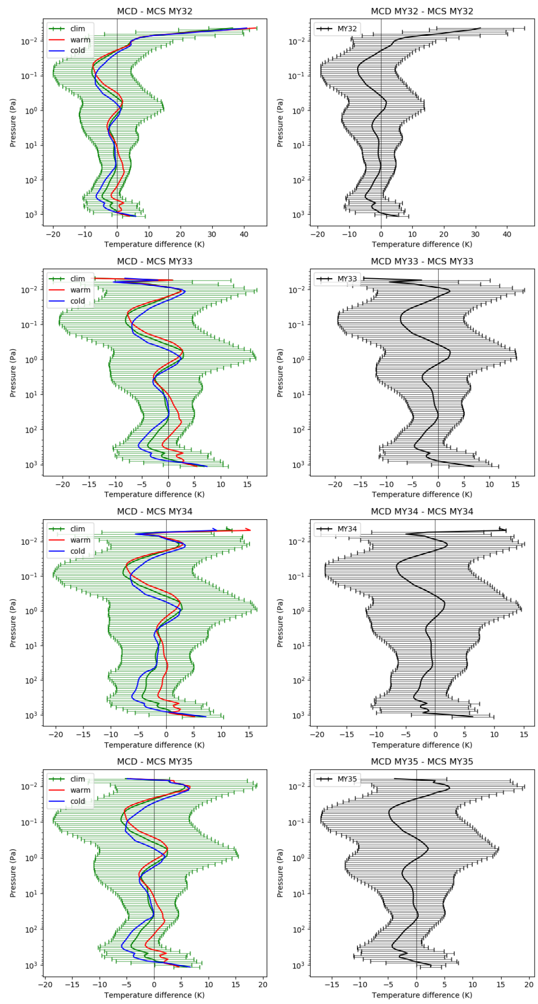

(b) MY32 to MY35

Figure 30: Profile of mean deviation for atmospheric temperature diurnal anomaly differences between MCD v6.1 and MCS, from MY28 to MY35 (from top to bottom), spatially averaged in latitudes (-50,50). Left : MCS compared with MCD for clim, warm and cold scenarios. Right : MCS compared with MCD for specific MY scenario.

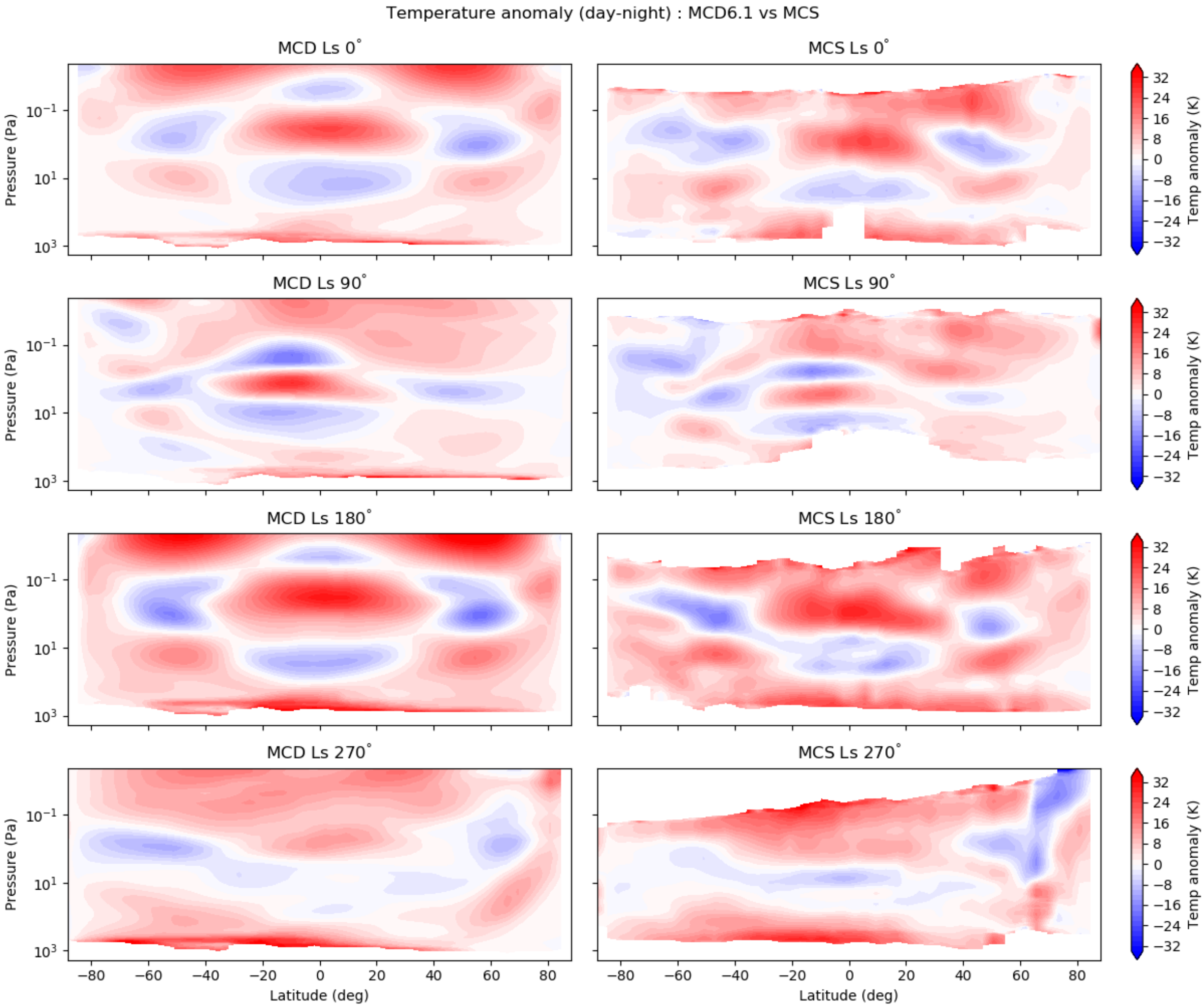

Figure 31: Cross section Pressure-latitude of zonally average anomaly temperature (difference between day and night) from MCD v6.1 (left) compared to MCS (right). Temperature anomalies are shown for L_s 0°, 90°, 180° and 270° from top to bottom for MY29

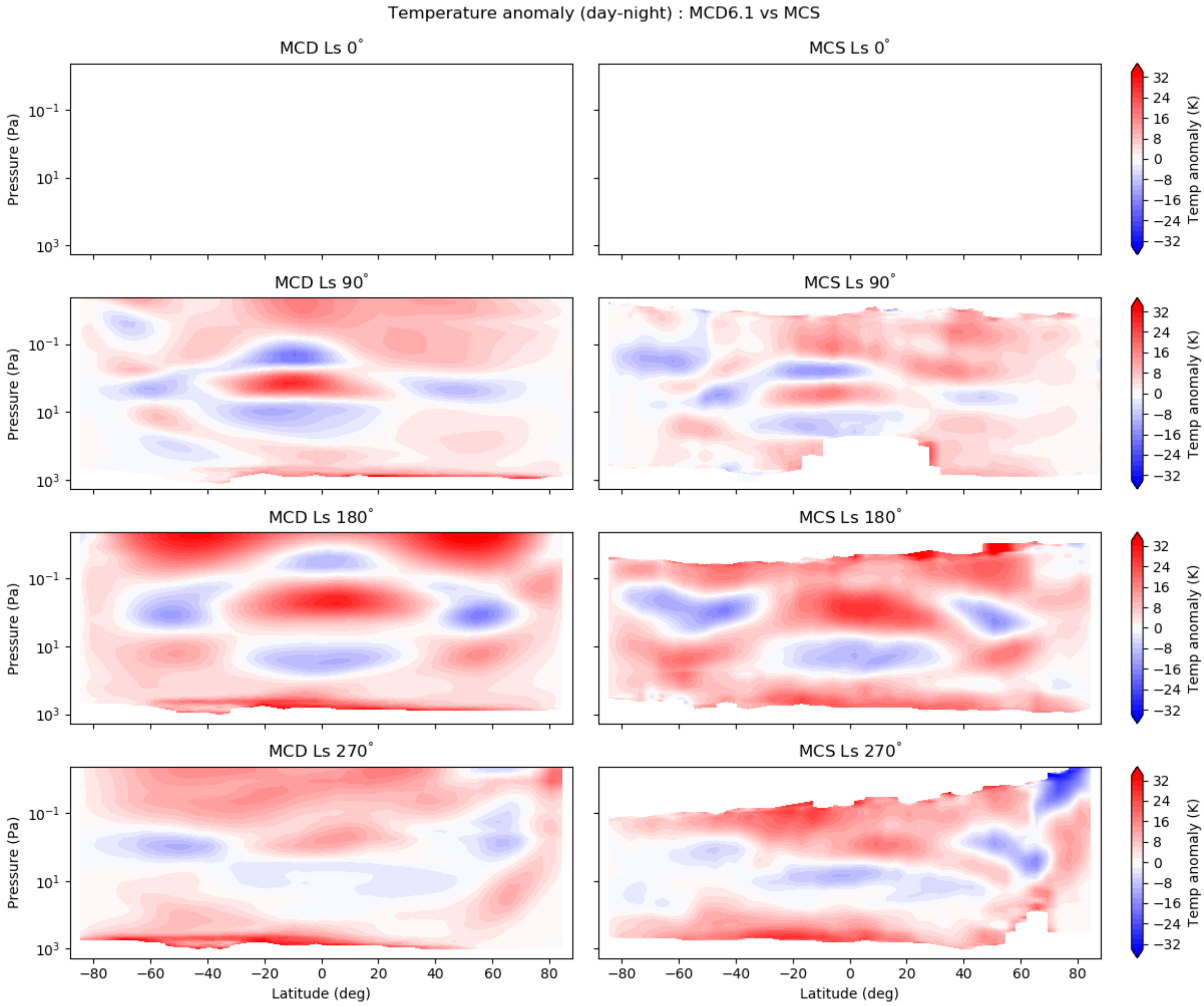

Figure 32: Cross section Pressure-latitude of zonally average anomaly temperature (difference between day and night) from MCD v6.1 (left) compared to MCS (right). Temperature anomalies are shown for L_s 0°, 90°, 180° and 270° from top to bottom for MY30

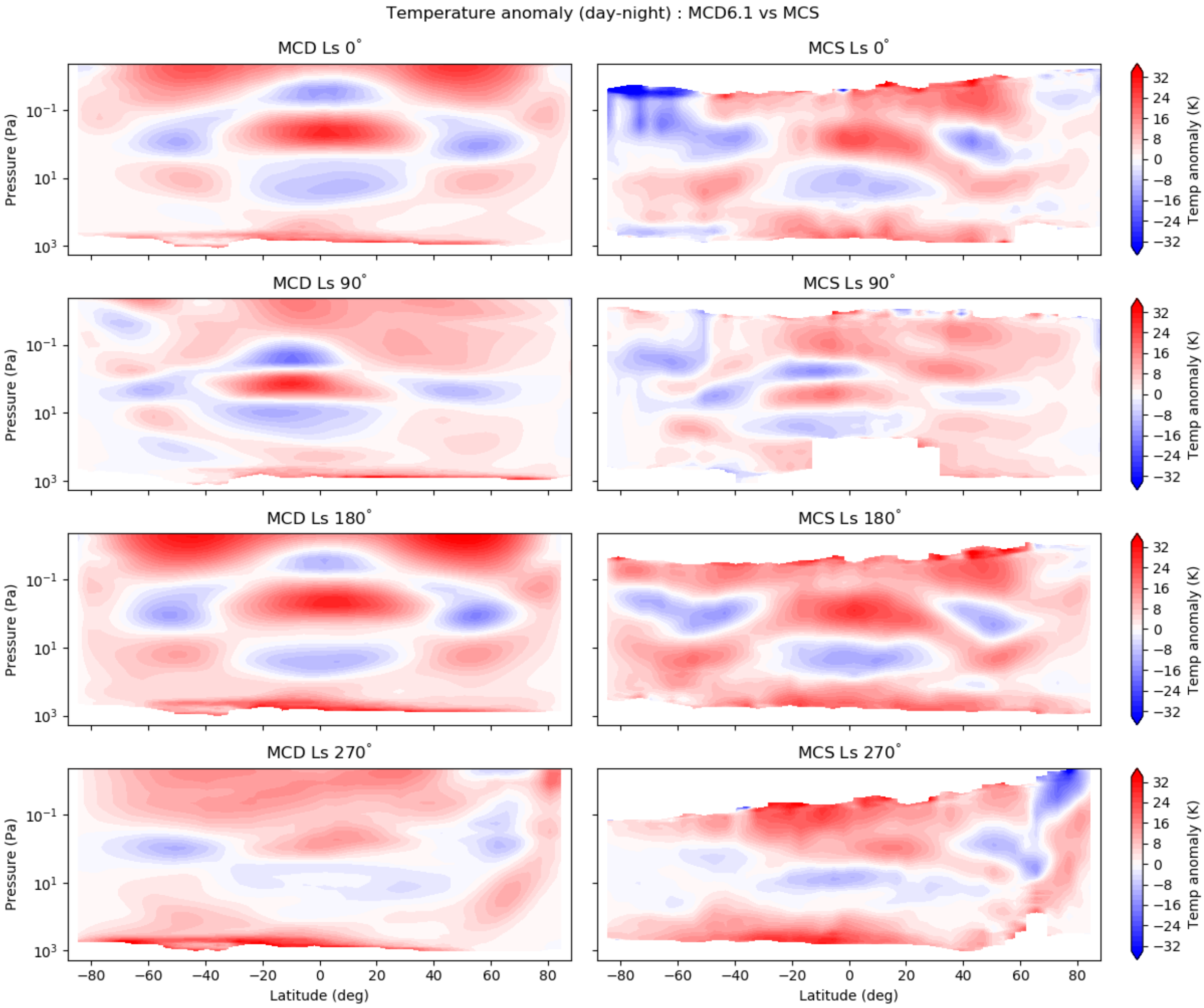

Figure 33: Cross section Pressure-latitude of zonally average anomaly temperature (difference between day and night) from MCD v6.1 (left) compared to MCS (right). Temperature anomalies are shown for L_s 0°, 90°, 180° and 270° from top to bottom for MY31

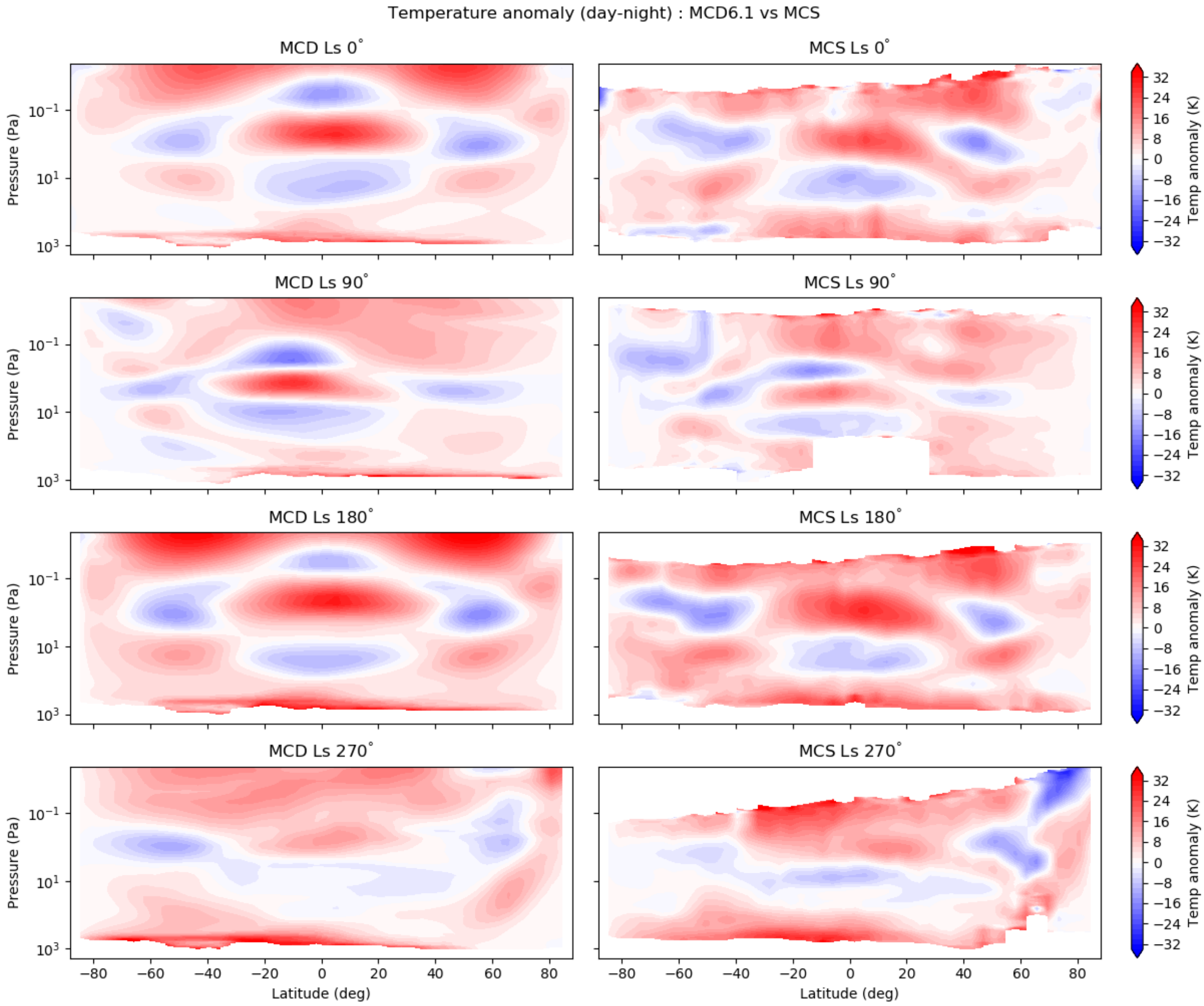

Figure 34: Cross section Pressure-latitude of zonally average anomaly temperature (difference between day and night) from MCD v6.1 (left) compared to MCS (right). Temperature anomalies are shown for L_s 0°, 90°, 180° and 270° from top to bottom for MY32

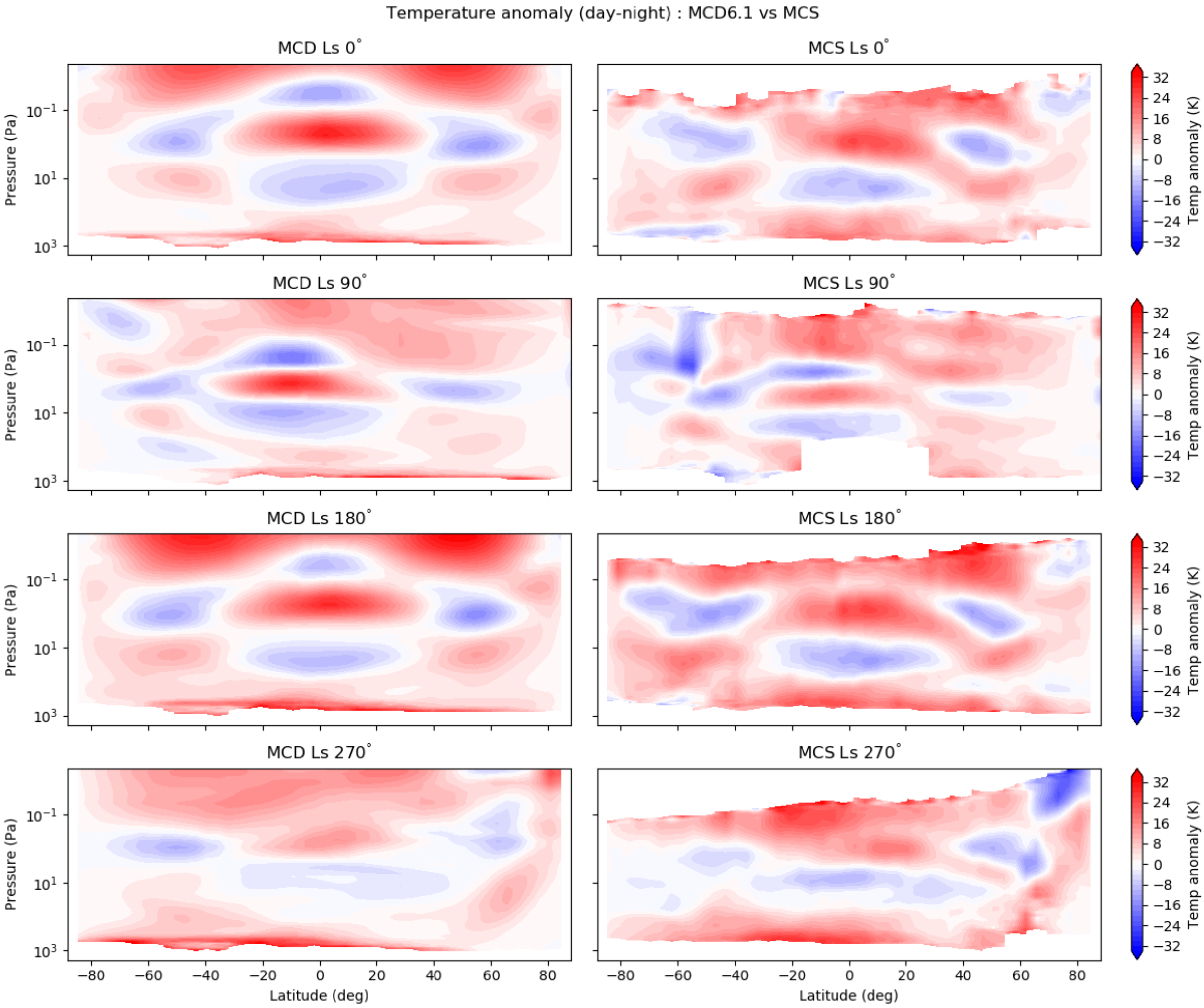

Figure 35: Cross section Pressure-latitude of zonally average anomaly temperature (difference between day and night) from MCD v6.1 (left) compared to MCS (right). Temperature anomalies are shown for L_s 0°, 90°, 180° and 270° from top to bottom for MY33

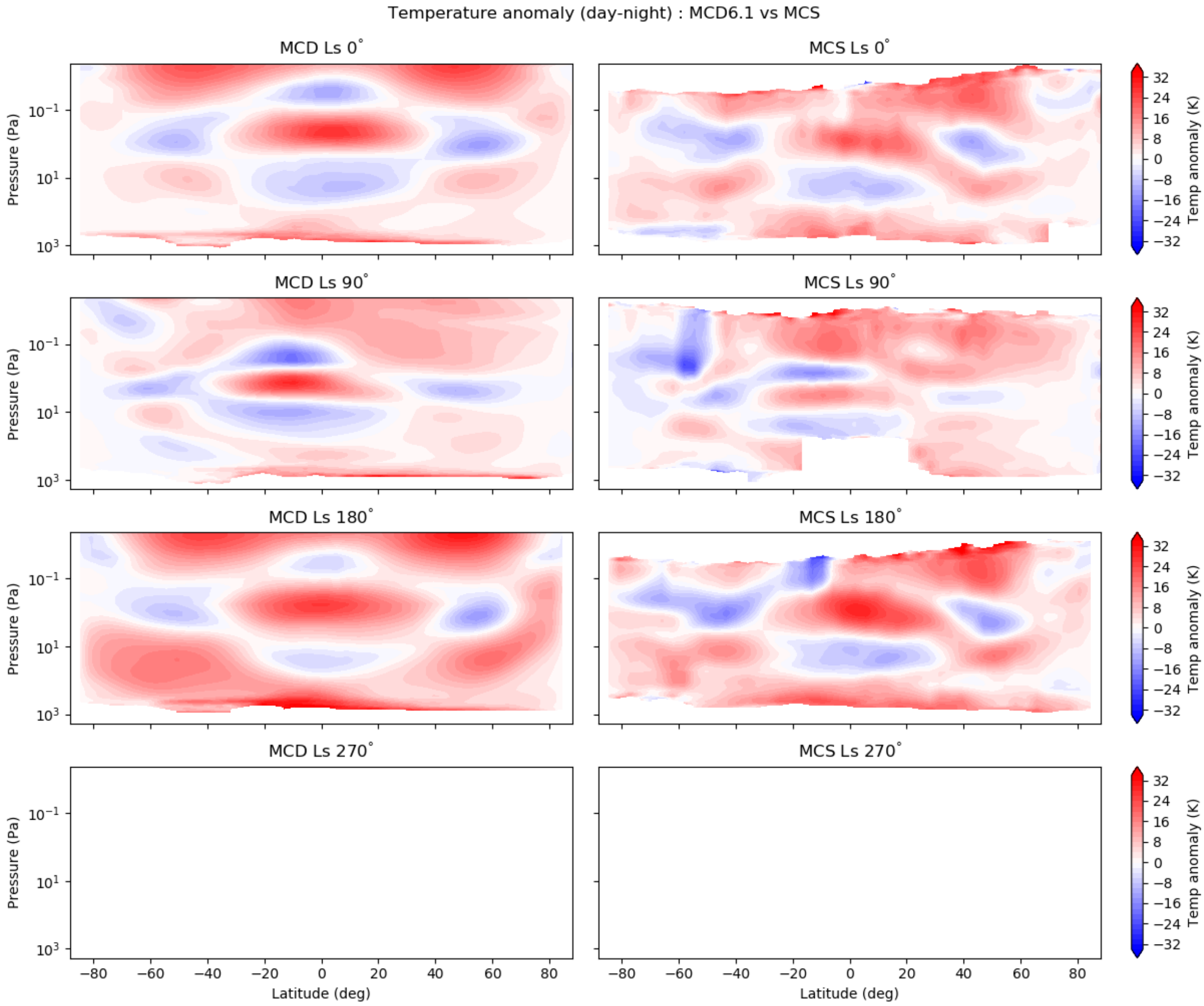

Figure 36: Cross section Pressure-latitude of zonally average anomaly temperature (difference between day and night) from MCD v6.1 (left) compared to MCS (right). Temperature anomalies are shown for L_s 0°, 90°, 180° and 270° from top to bottom for MY34

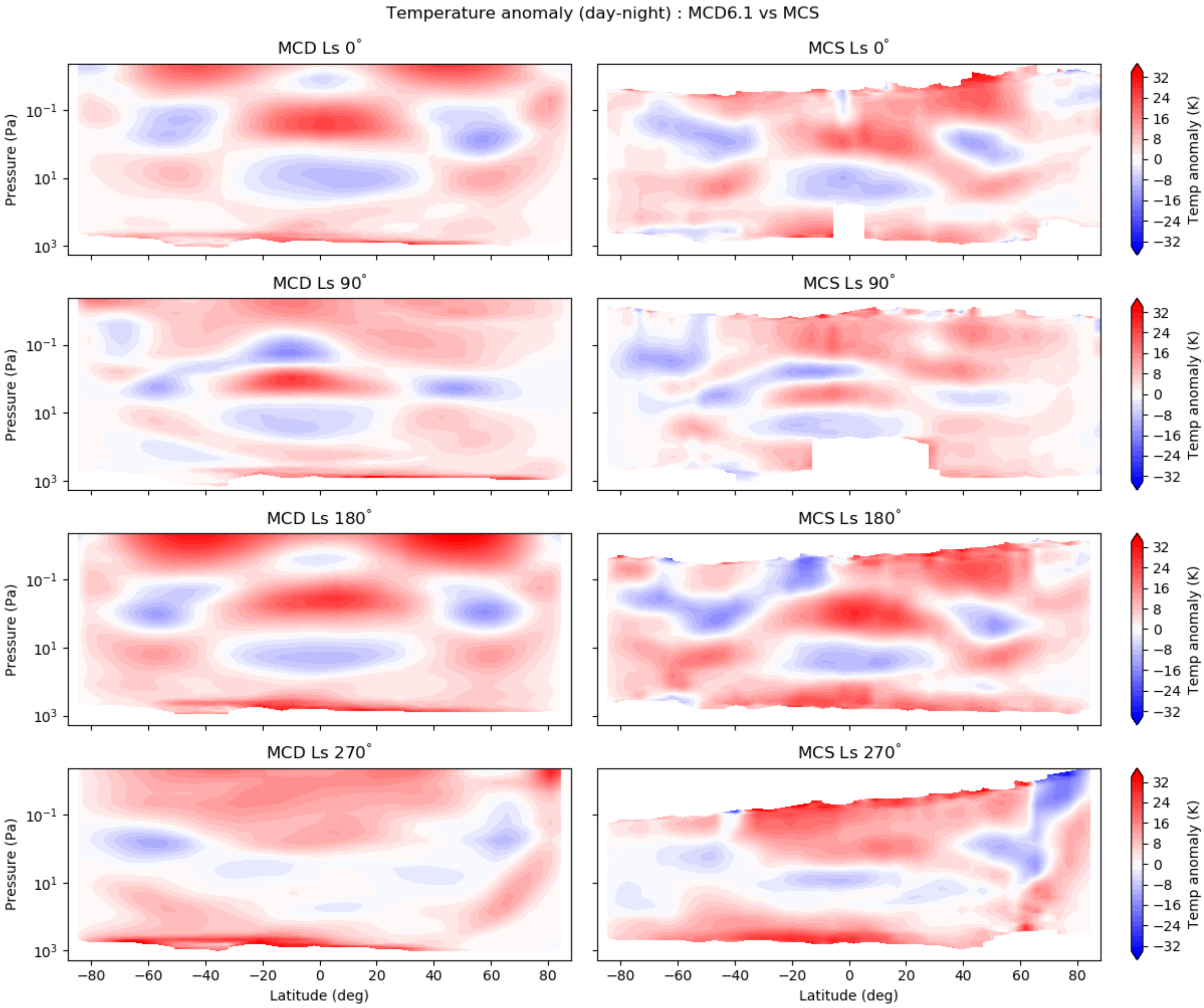

Figure 37: Cross section Pressure-latitude of zonally average anomaly temperature (difference between day and night) from MCD v6.1 (left) compared to MCS (right). Temperature anomalies are shown for L_s 0°, 90°, 180° and 270° from top to bottom for MY35

5.3 TES and MCS : global dust storms

These figures show planetary average (poles removed) of mean temperature during three global dust storms : MY25, MY38 and MY34. MY25 global dust storm is compared to TES data while MY28 and MY34 are compared to MCS data. MY25 and MY34 shows temperature at 100Pa 100Pa (15-20 km) where there are a lot of measurements. At this altitude, there were only few measurements made by MCS during MY28 global dust storm. Therefore it was chosen to show the temperature at 10Pa (roughly to 40km) for MY28 dust storm. The figures show that the MCD clim scenario is too much cold, such as the warm scenario. Indeed these scenario are not made to represent global dust storm. This is why we also show the comparison with the MCD storm case scenario, which is supposed to represent an extreme global dust storm. We see that for MY25 and MY34, the agremeement between the MCD and the observations is really good (less than 1K of difference on average). For MY28, which was a weaker global dust storm than the two others, the storm scenario is much warmer than what MCS measured (MCD 15K warmer than MCS on average).

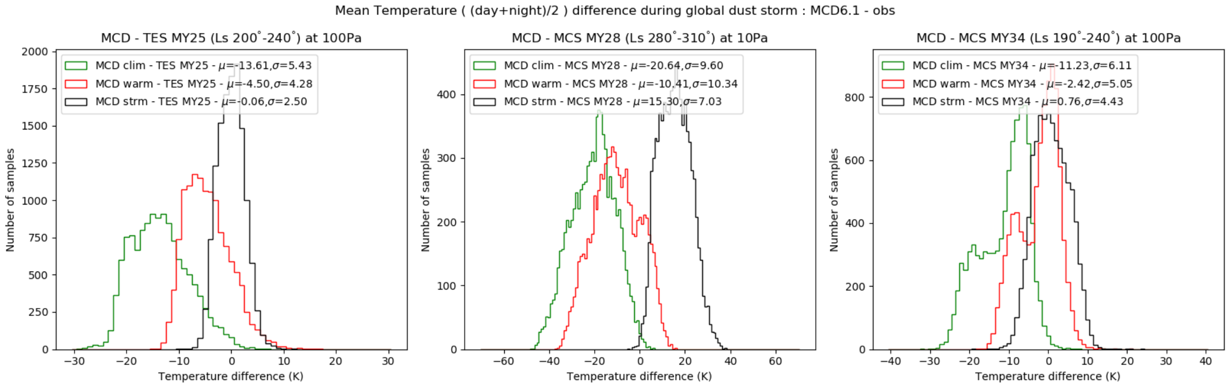

Figure 38: Distribution of atmospheric temperature differences between MCD v6.1 and observations from TES and MCS using bins of 1K for MY25 (left), MY28 (middle) and MY34 (right) global dust storms, temporally averaged for day time and night time, in latitudes (-50,50). The comparison is given for clim, warm and storm scenarios, at 100 Pa for MY25 and MY34 global dust storms and at 10 Pa for MY28 global dust storm.

5.4 EMIRS

The following plots show comparisons of EMIRS and MCD temperature diurnal anomaly binned by 5° of L_s from L_s 47.5° to 267.5°, around equator. Each figure contains an EMIRS panel, a MCD panel and a MCD sampled like EMIRS panel. Note that MY36 being not available in the MCD6.1 scenarios, we use the clim scenario for the MCD data.

The overall pressure-local time structure of the thermal tides is well represented by the MCD. The clear season sees the dominance of the diurnal tide, while the semi-diurnal tide starts to prevail after L_s 215°-220°. Differences still remain, although some could be an effect of the instrument vertical convolution (Fan et al. [2022]) which is not applied to MCD data here (e.g. the hot spot above 40Pa, LT 16h-20h in EMIRS data, Figure 42) and tends among other things to reduce the amplitude of the tides.

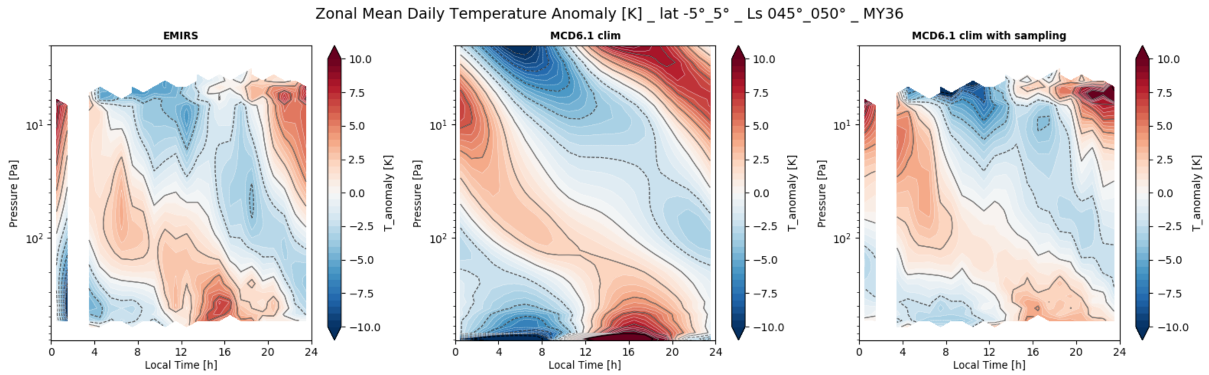

Figure 39: Zonal Mean Daily Temperature Anomaly averaged over latitude (-5,5), L_s 45-50. EMIRS on the left, MCD6.1 without specific sampling in the middle and MCD6.1 with EMIRS sampling on the right.

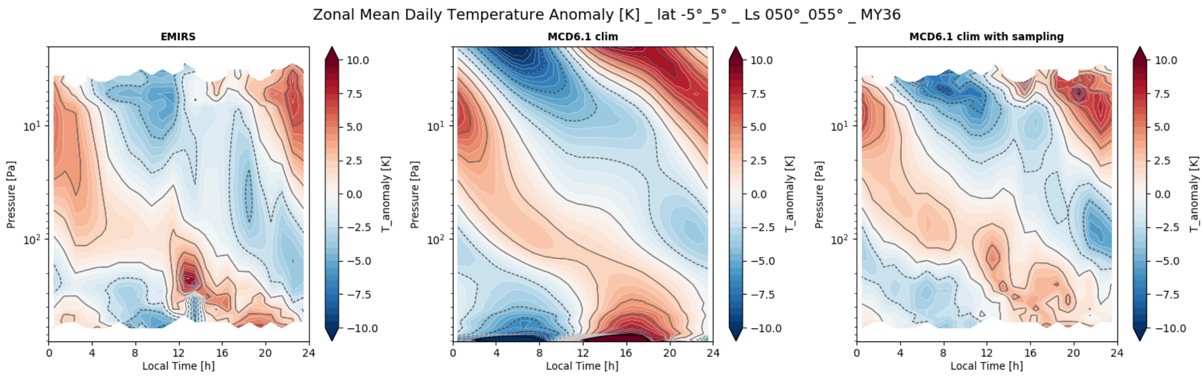

Figure 40: Zonal Mean Daily Temperature Anomaly averaged over latitude (-5,5), L_s 50-55. EMIRS on the left, MCD6.1 without specific sampling in the middle and MCD6.1 with EMIRS sampling on the right.

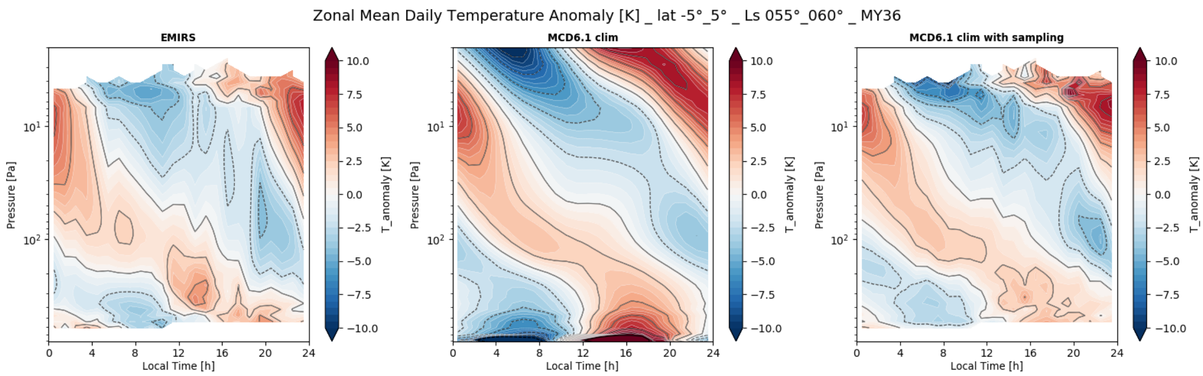

Figure 41: Zonal Mean Daily Temperature Anomaly averaged over latitude (-5,5), L_s 55-60. EMIRS on the left, MCD6.1 without specific sampling in the middle and MCD6.1 with EMIRS sampling on the right.

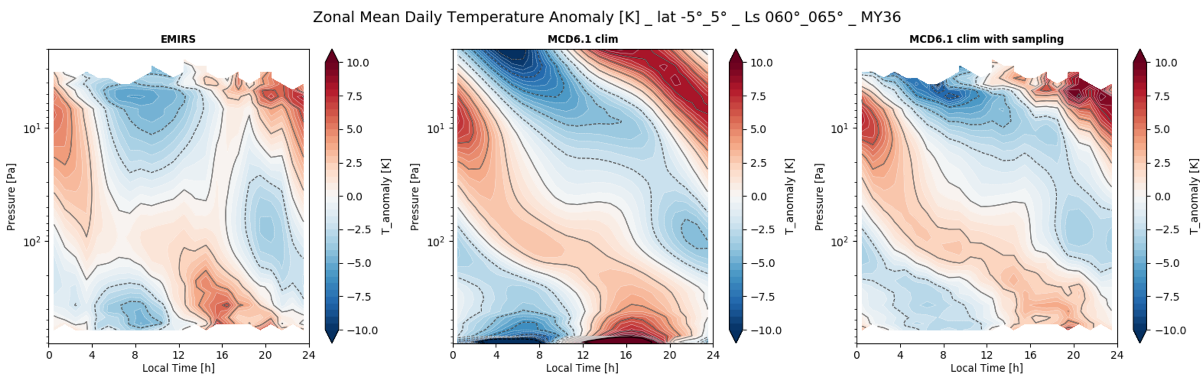

Figure 42: Zonal Mean Daily Temperature Anomaly averaged over latitude (-5,5), L_s 60-65. EMIRS on the left, MCD6.1 without specific sampling in the middle and MCD6.1 with EMIRS sampling on the right.

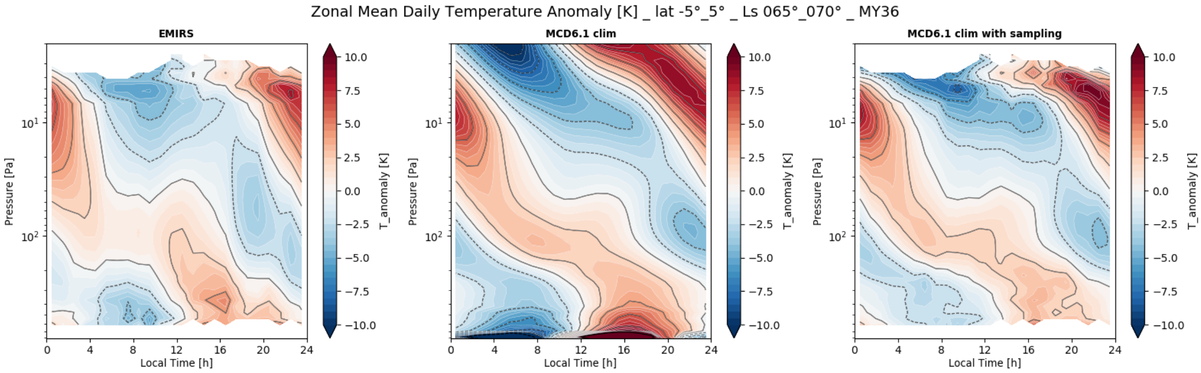

Figure 43: Zonal Mean Daily Temperature Anomaly averaged over latitude (-5,5), L_s 65-70. EMIRS on the left, MCD6.1 without specific sampling in the middle and MCD6.1 with EMIRS sampling on the right.

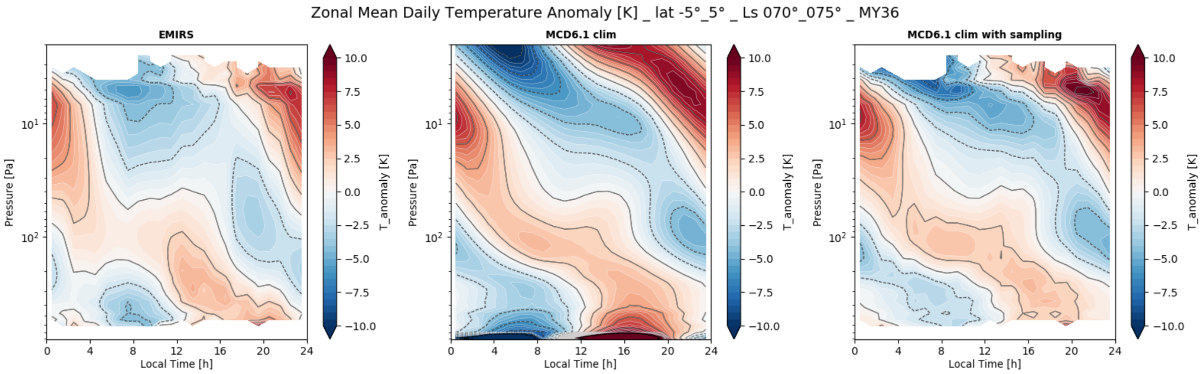

Figure 44: Zonal Mean Daily Temperature Anomaly averaged over latitude (-5,5), L_s 70-75. EMIRS on the left, MCD6.1 without specific sampling in the middle and MCD6.1 with EMIRS sampling on the right.

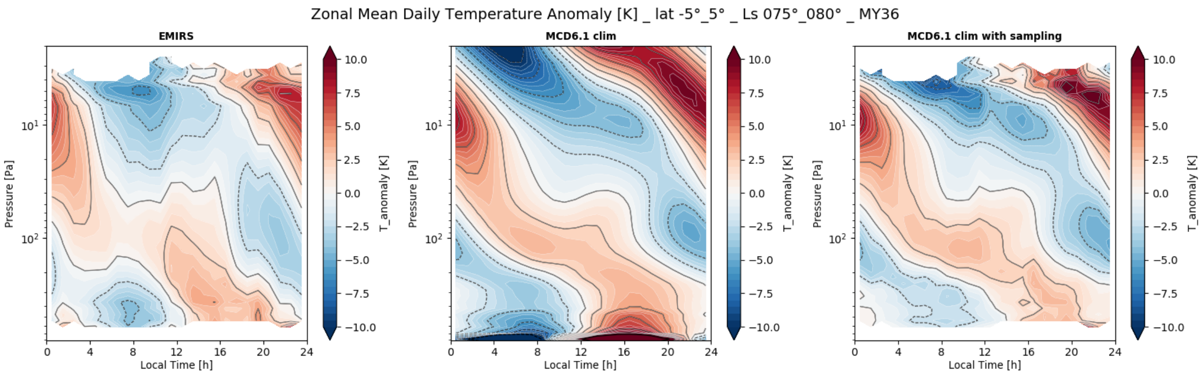

Figure 45: Zonal Mean Daily Temperature Anomaly averaged over latitude (-5,5), L_s 75-80. EMIRS on the left, MCD6.1 without specific sampling in the middle and MCD6.1 with EMIRS sampling on the right.

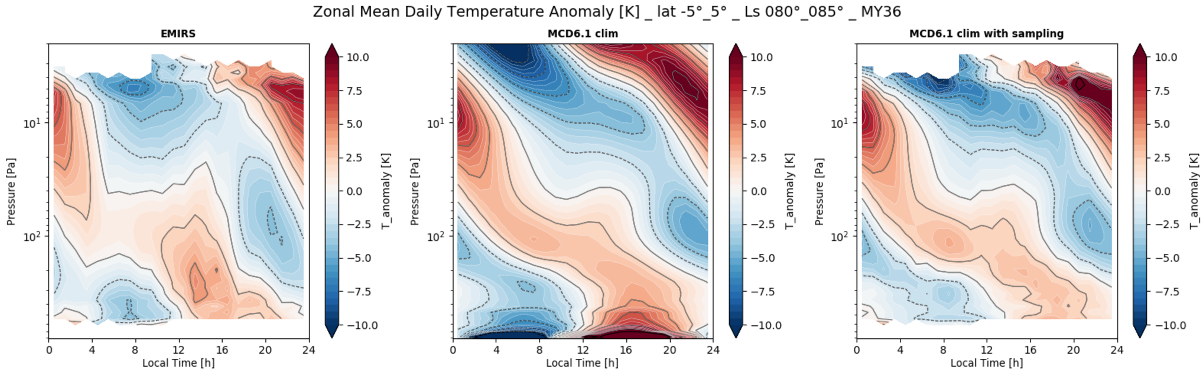

Figure 46: Zonal Mean Daily Temperature Anomaly averaged over latitude (-5,5), L_s 80-85. EMIRS on the left, MCD6.1 without specific sampling in the middle and MCD6.1 with EMIRS sampling on the right.

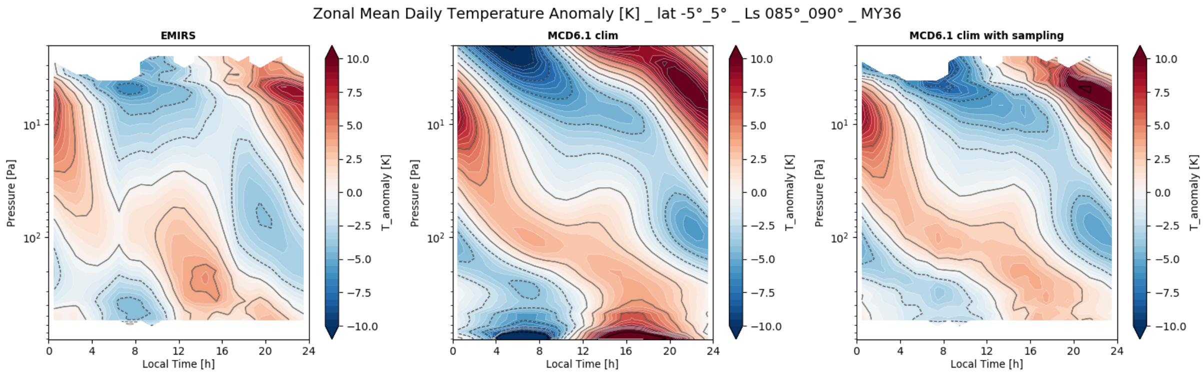

Figure 47: Zonal Mean Daily Temperature Anomaly averaged over latitude (-5,5), L_s 85-90. EMIRS on the left, MCD6.1 without specific sampling in the middle and MCD6.1 with EMIRS sampling on the right.

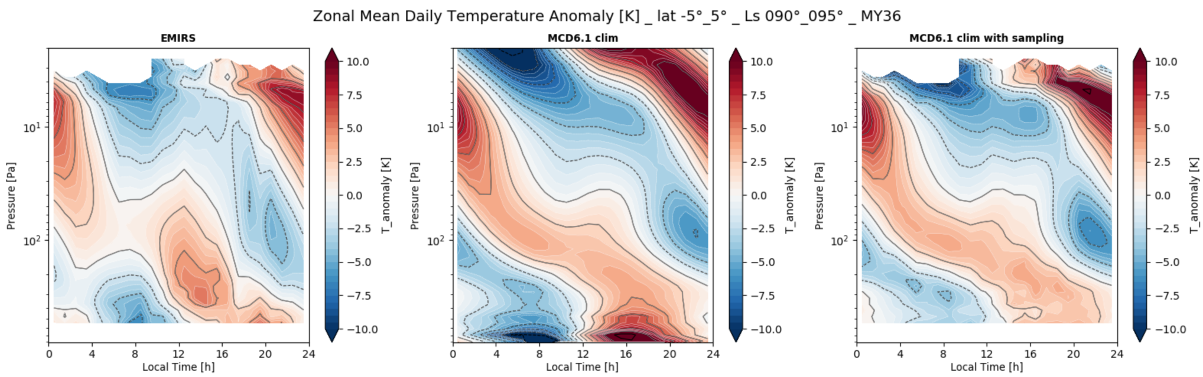

Figure 48: Zonal Mean Daily Temperature Anomaly averaged over latitude (-5,5), L_s 90-95. EMIRS on the left, MCD6.1 without specific sampling in the middle and MCD6.1 with EMIRS sampling on the right.

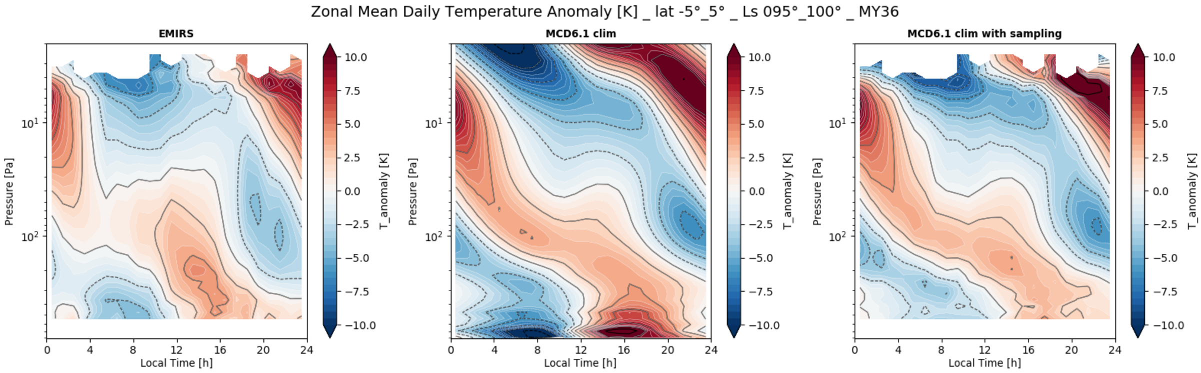

Figure 49: Zonal Mean Daily Temperature Anomaly averaged over latitude (-5,5), L_s 95-100. EMIRS on the left, MCD6.1 without specific sampling in the middle and MCD6.1 with EMIRS sampling on the right.

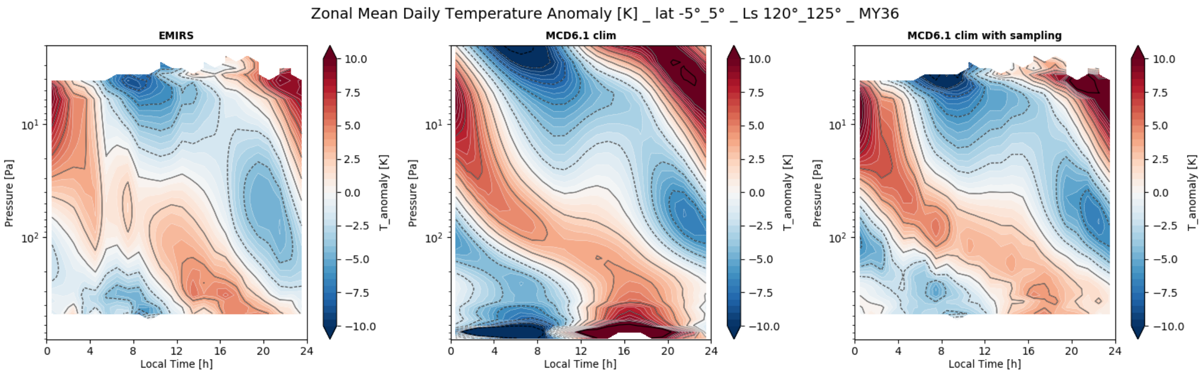

Figure 50: Zonal Mean Daily Temperature Anomaly averaged over latitude (-5,5), L_s 120-125. EMIRS on the left, MCD6.1 without specific sampling in the middle and MCD6.1 with EMIRS sampling on the right.

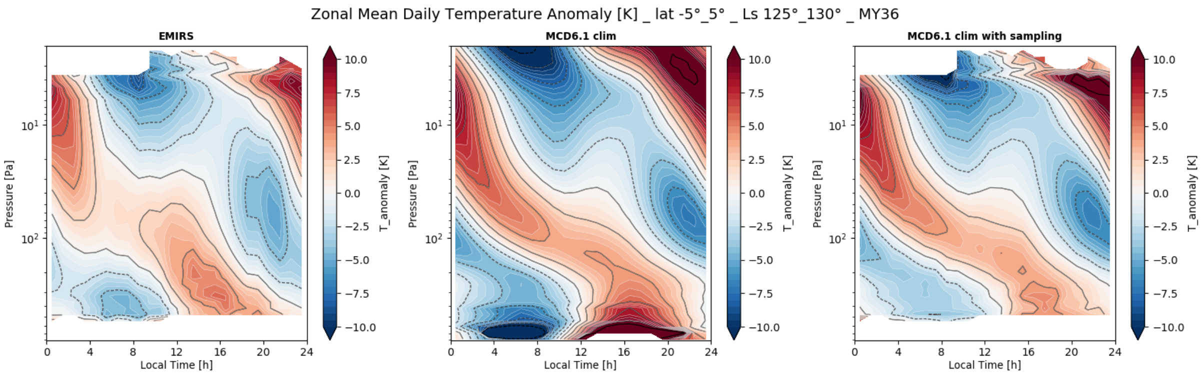

Figure 51: Zonal Mean Daily Temperature Anomaly averaged over latitude (-5,5), L_s 125-130. EMIRS on the left, MCD6.1 without specific sampling in the middle and MCD6.1 with EMIRS sampling on the right.

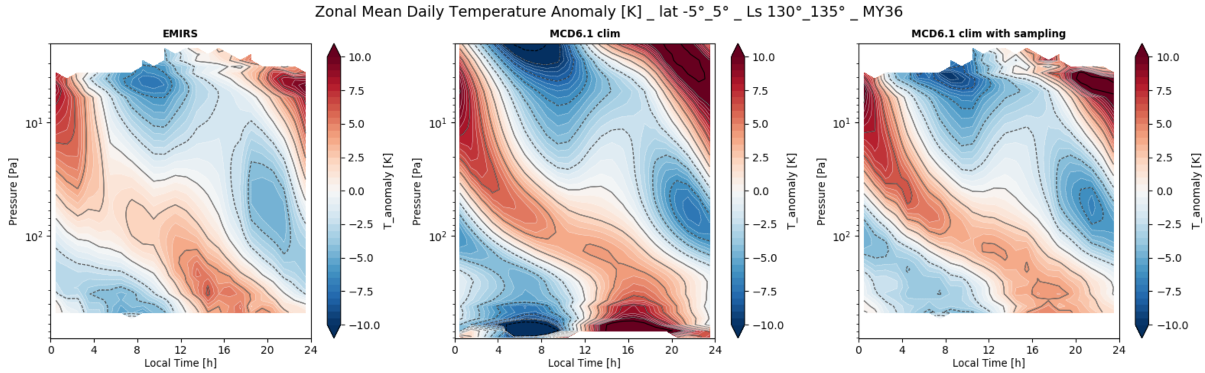

Figure 52: Zonal Mean Daily Temperature Anomaly averaged over latitude (-5,5), L_s 130-135. EMIRS on the left, MCD6.1 without specific sampling in the middle and MCD6.1 with EMIRS sampling on the right.

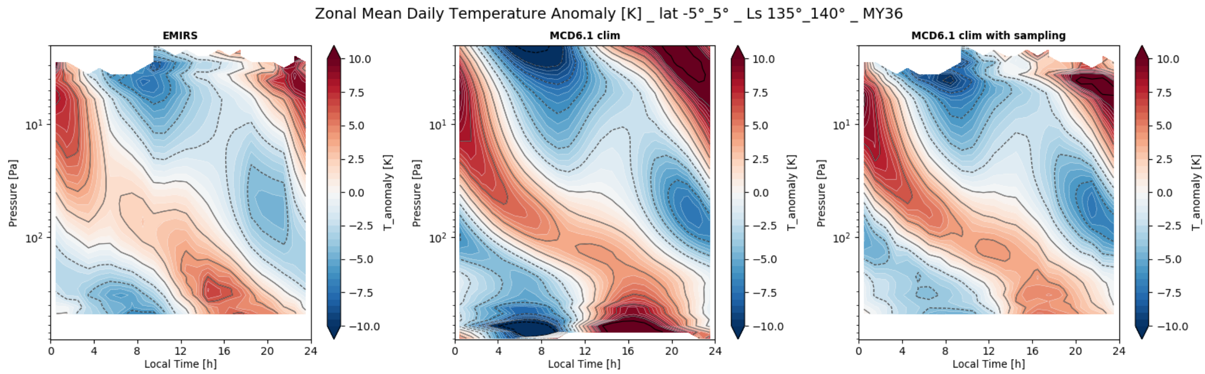

Figure 53: Zonal Mean Daily Temperature Anomaly averaged over latitude (-5,5), L_s 135-140. EMIRS on the left, MCD6.1 without specific sampling in the middle and MCD6.1 with EMIRS sampling on the right.

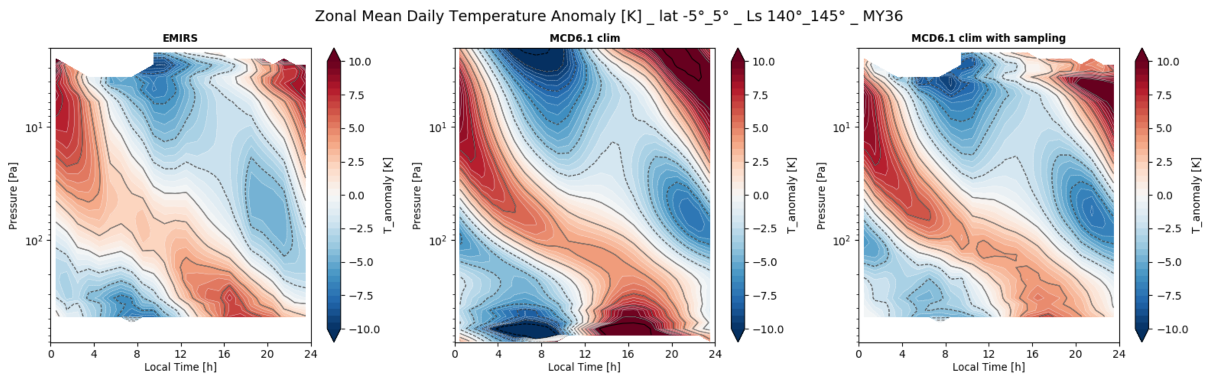

Figure 54: Zonal Mean Daily Temperature Anomaly averaged over latitude (-5,5), L_s 140-145. EMIRS on the left, MCD6.1 without specific sampling in the middle and MCD6.1 with EMIRS sampling on the right.

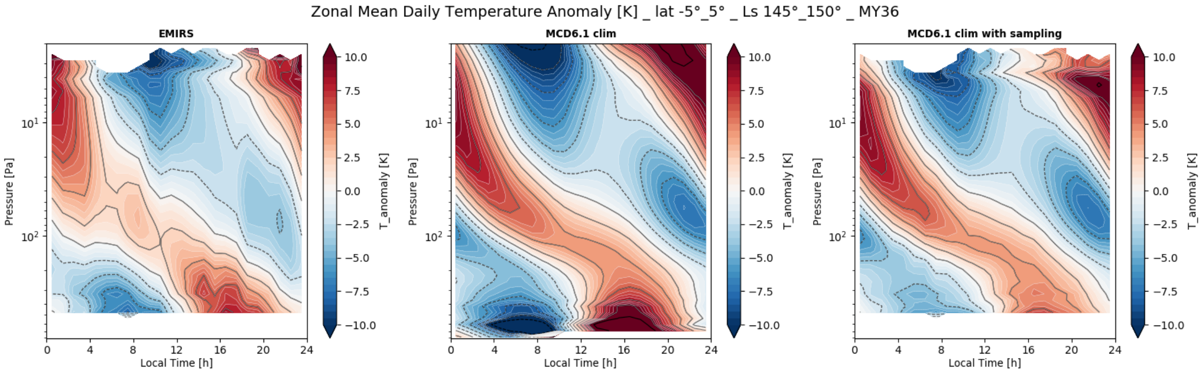

Figure 55: Zonal Mean Daily Temperature Anomaly averaged over latitude (-5,5), L_s 145-150. EMIRS on the left, MCD6.1 without specific sampling in the middle and MCD6.1 with EMIRS sampling on the right.

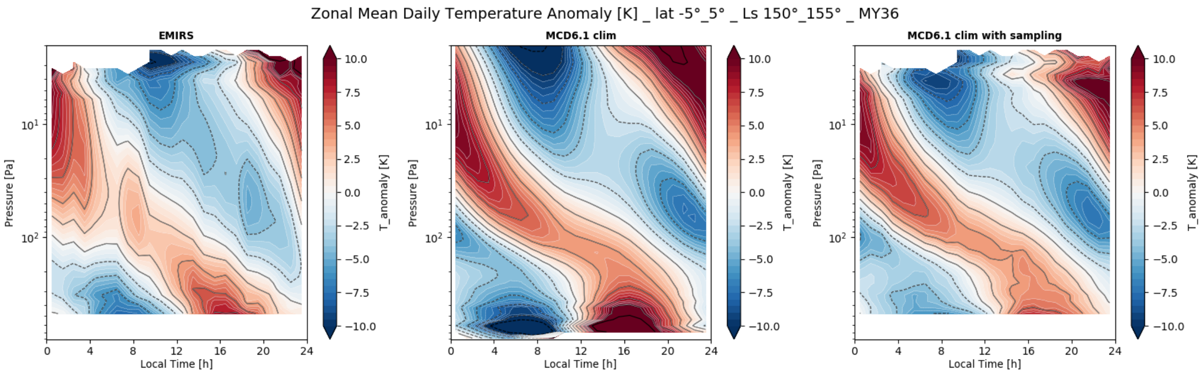

Figure 56: Zonal Mean Daily Temperature Anomaly averaged over latitude (-5,5), L_s 150-155. EMIRS on the left, MCD6.1 without specific sampling in the middle and MCD6.1 with EMIRS sampling on the right.

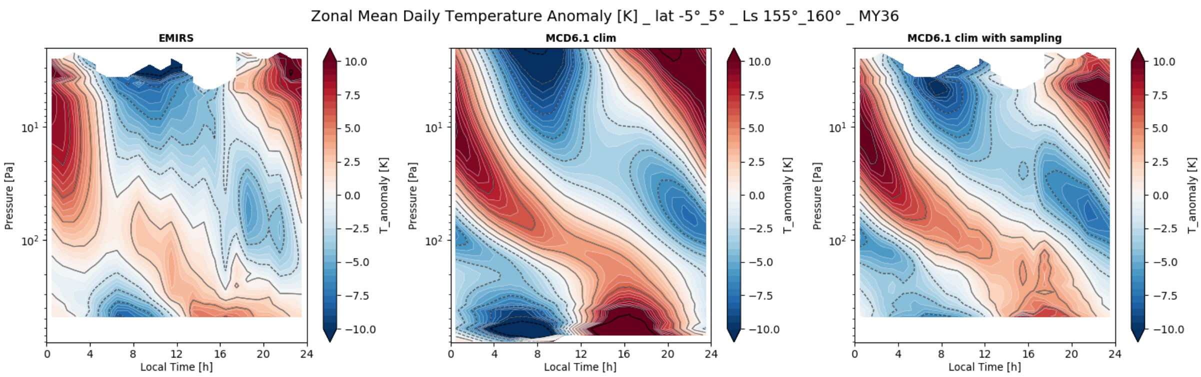

Figure 57: Zonal Mean Daily Temperature Anomaly averaged over latitude (-5,5), L_s 155-160. EMIRS on the left, MCD6.1 without specific sampling in the middle and MCD6.1 with EMIRS sampling on the right.

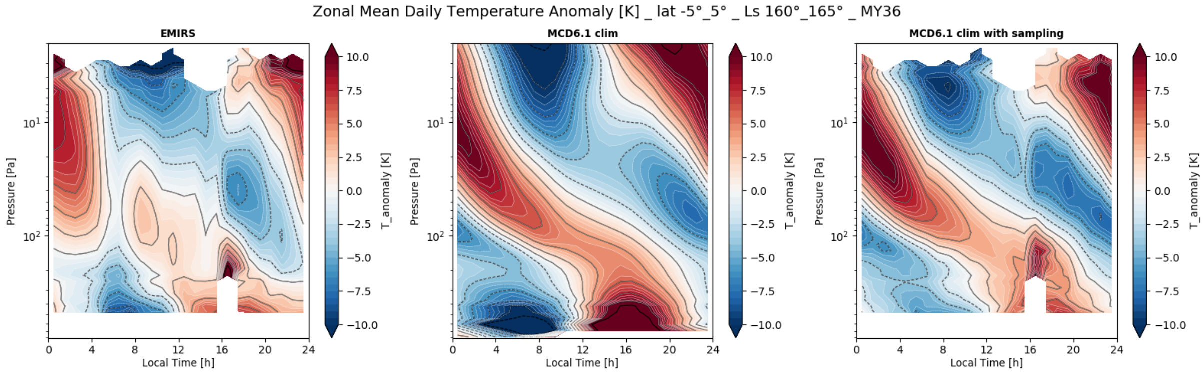

Figure 58: Zonal Mean Daily Temperature Anomaly averaged over latitude (-5,5), L_s 160-165. EMIRS on the left, MCD6.1 without specific sampling in the middle and MCD6.1 with EMIRS sampling on the right.

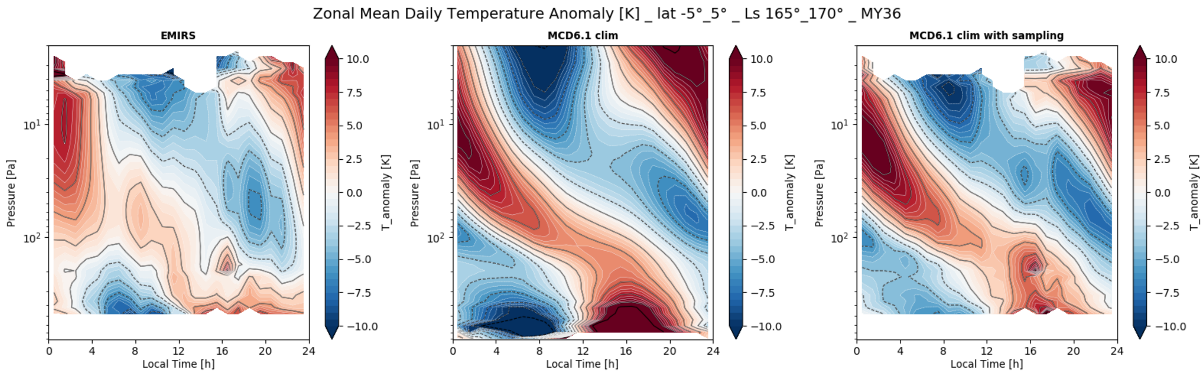

Figure 59: Zonal Mean Daily Temperature Anomaly averaged over latitude (-5,5), L_s 165-170. EMIRS on the left, MCD6.1 without specific sampling in the middle and MCD6.1 with EMIRS sampling on the right.

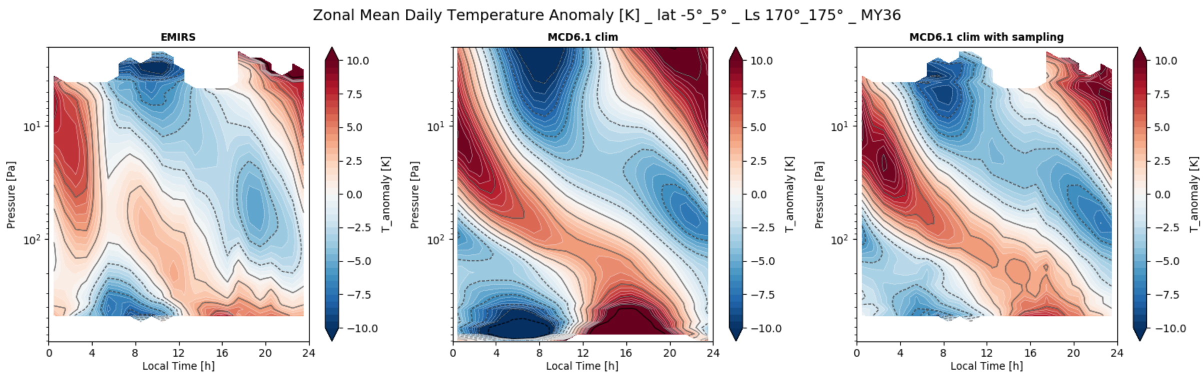

Figure 60: Zonal Mean Daily Temperature Anomaly averaged over latitude (-5,5), L_s 170-175. EMIRS on the left, MCD6.1 without specific sampling in the middle and MCD6.1 with EMIRS sampling on the right.

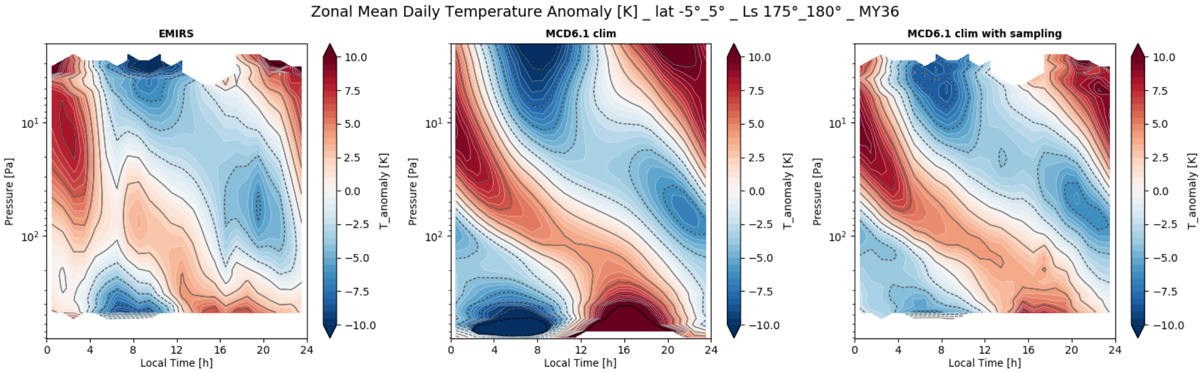

Figure 61: Zonal Mean Daily Temperature Anomaly averaged over latitude (-5,5), L_s 175-180. EMIRS on the left, MCD6.1 without specific sampling in the middle and MCD6.1 with EMIRS sampling on the right.

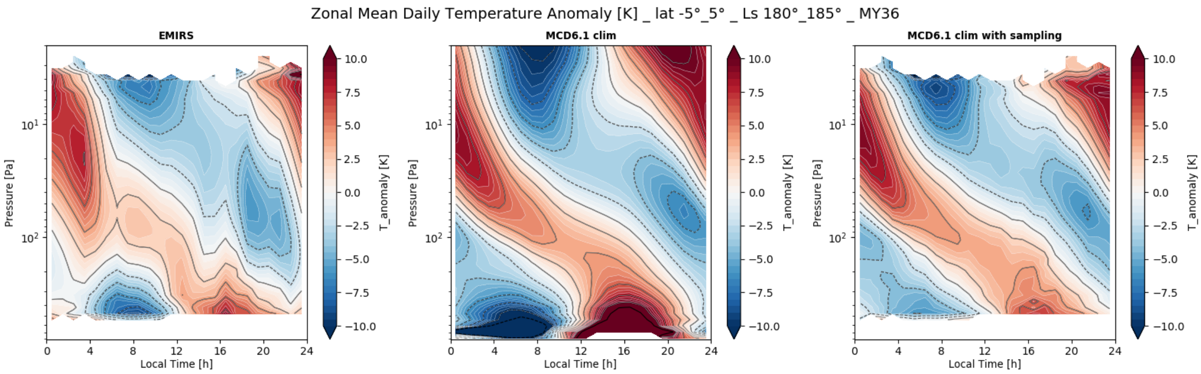

Figure 62: Zonal Mean Daily Temperature Anomaly averaged over latitude (-5,5), L_s 180-185. EMIRS on the left, MCD6.1 without specific sampling in the middle and MCD6.1 with EMIRS sampling on the right.

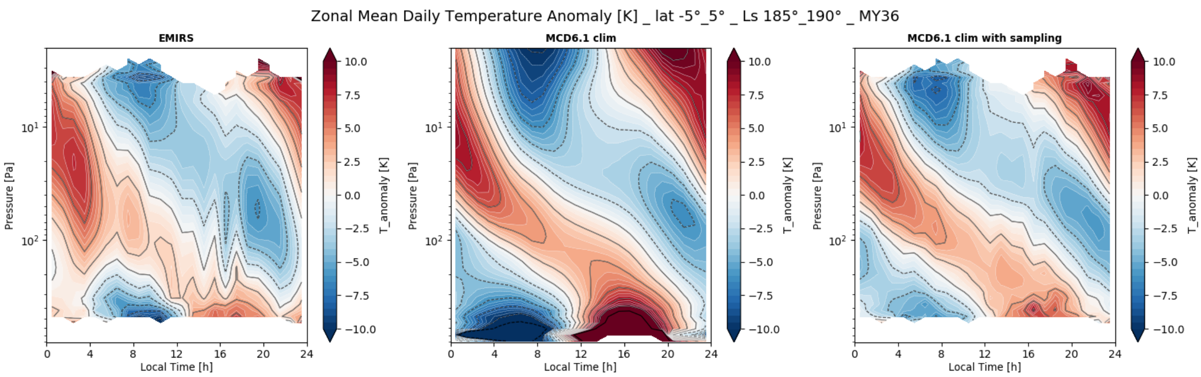

Figure 63: Zonal Mean Daily Temperature Anomaly averaged over latitude (-5,5), L_s 185-190. EMIRS on the left, MCD6.1 without specific sampling in the middle and MCD6.1 with EMIRS sampling on the right.

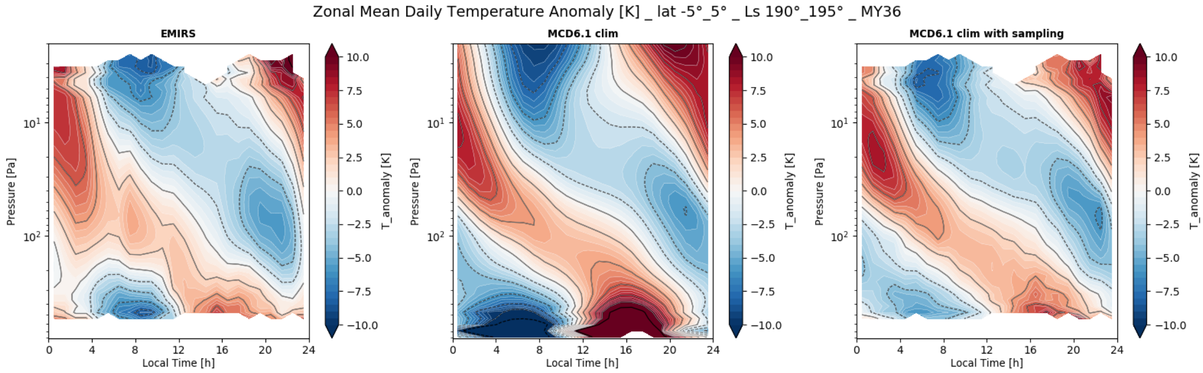

Figure 64: Zonal Mean Daily Temperature Anomaly averaged over latitude (-5,5), L_s 190-195. EMIRS on the left, MCD6.1 without specific sampling in the middle and MCD6.1 with EMIRS sampling on the right.

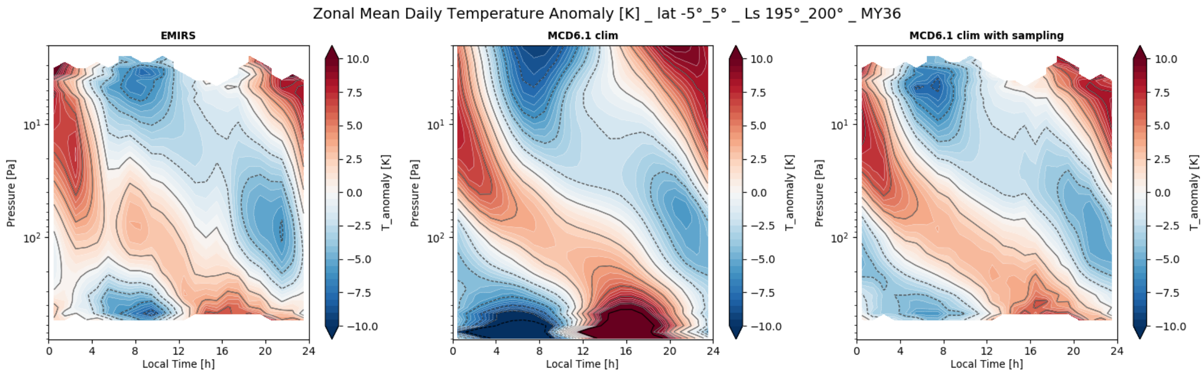

Figure 65: Zonal Mean Daily Temperature Anomaly averaged over latitude (-5,5), L_s 195-200. EMIRS on the left, MCD6.1 without specific sampling in the middle and MCD6.1 with EMIRS sampling on the right.

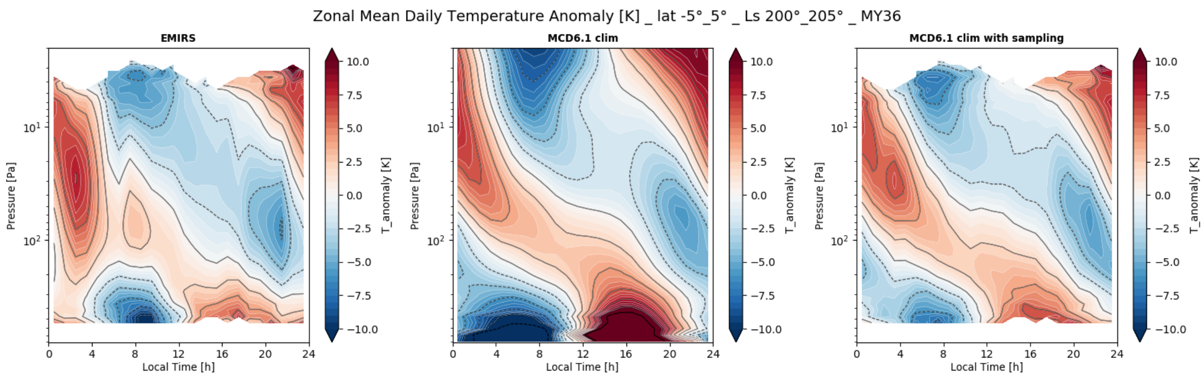

Figure 66: Zonal Mean Daily Temperature Anomaly averaged over latitude (-5,5), L_s 200-205. EMIRS on the left, MCD6.1 without specific sampling in the middle and MCD6.1 with EMIRS sampling on the right.

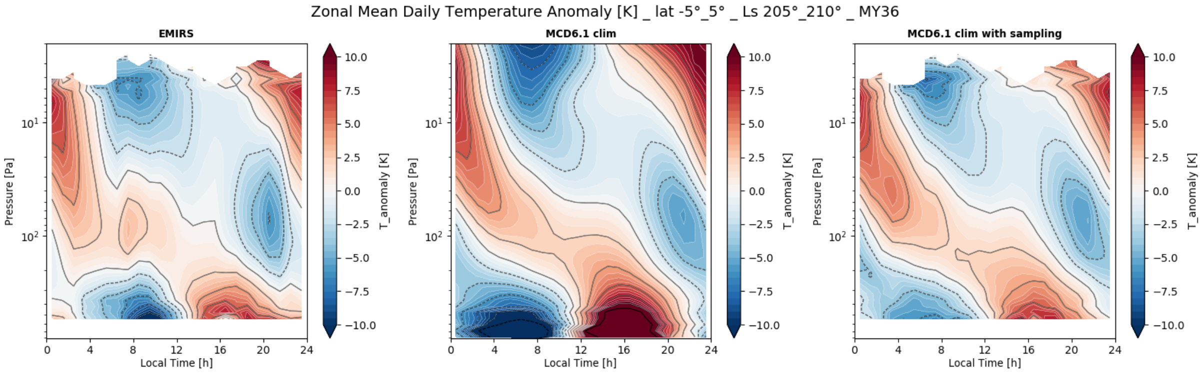

Figure 67: Zonal Mean Daily Temperature Anomaly averaged over latitude (-5,5), L_s 205-210. EMIRS on the left, MCD6.1 without specific sampling in the middle and MCD6.1 with EMIRS sampling on the right.

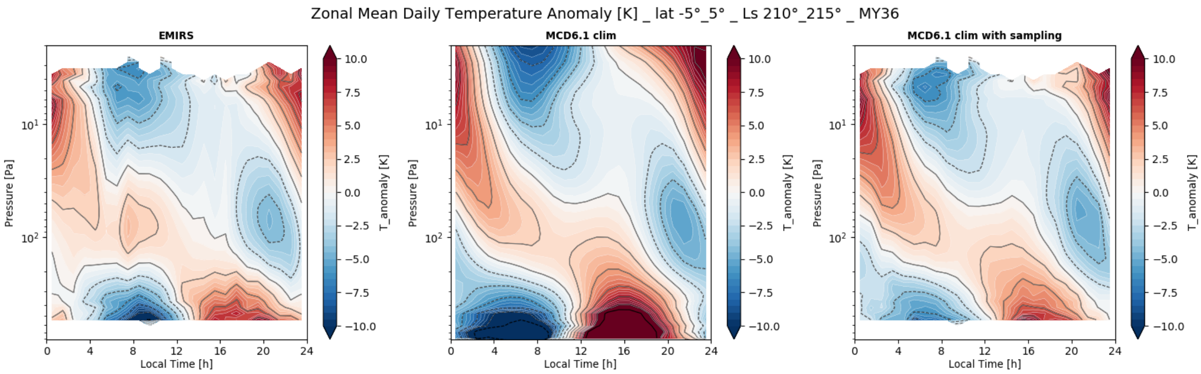

Figure 68: Zonal Mean Daily Temperature Anomaly averaged over latitude (-5,5), L_s 210-215. EMIRS on the left, MCD6.1 without specific sampling in the middle and MCD6.1 with EMIRS sampling on the right.

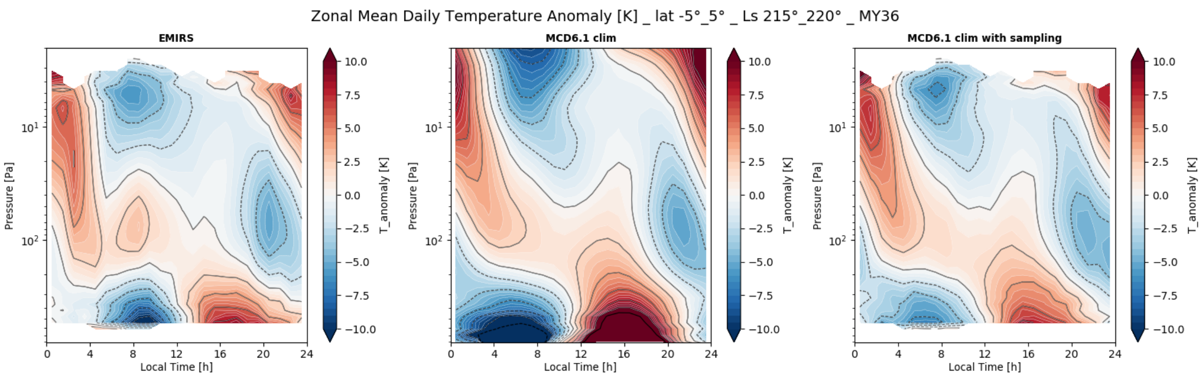

Figure 69: Zonal Mean Daily Temperature Anomaly averaged over latitude (-5,5), L_s 215-220. EMIRS on the left, MCD6.1 without specific sampling in the middle and MCD6.1 with EMIRS sampling on the right.

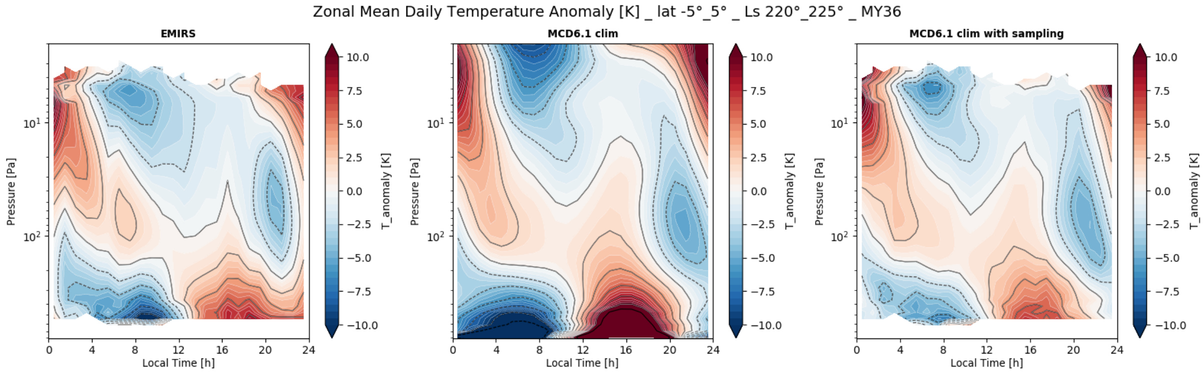

Figure 70: Zonal Mean Daily Temperature Anomaly averaged over latitude (-5,5), L_s 220-225. EMIRS on the left, MCD6.1 without specific sampling in the middle and MCD6.1 with EMIRS sampling on the right.

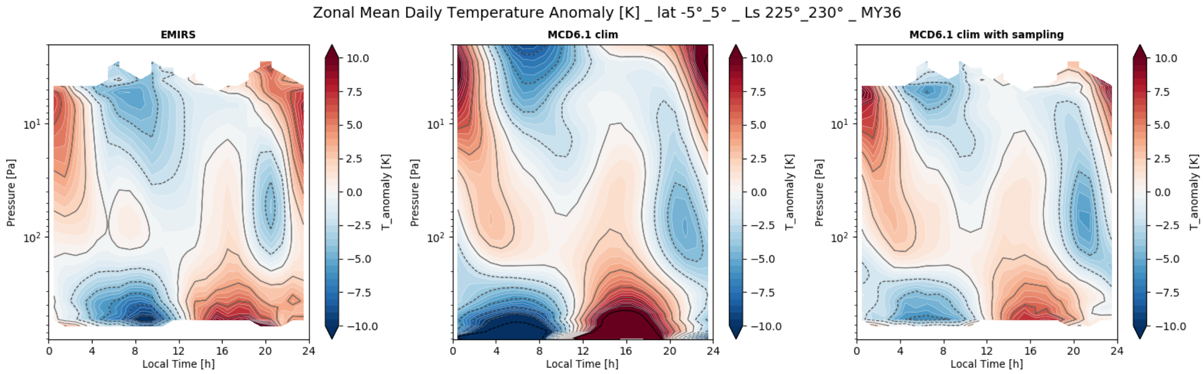

Figure 71: Zonal Mean Daily Temperature Anomaly averaged over latitude (-5,5), L_s 225-230. EMIRS on the left, MCD6.1 without specific sampling in the middle and MCD6.1 with EMIRS sampling on the right.

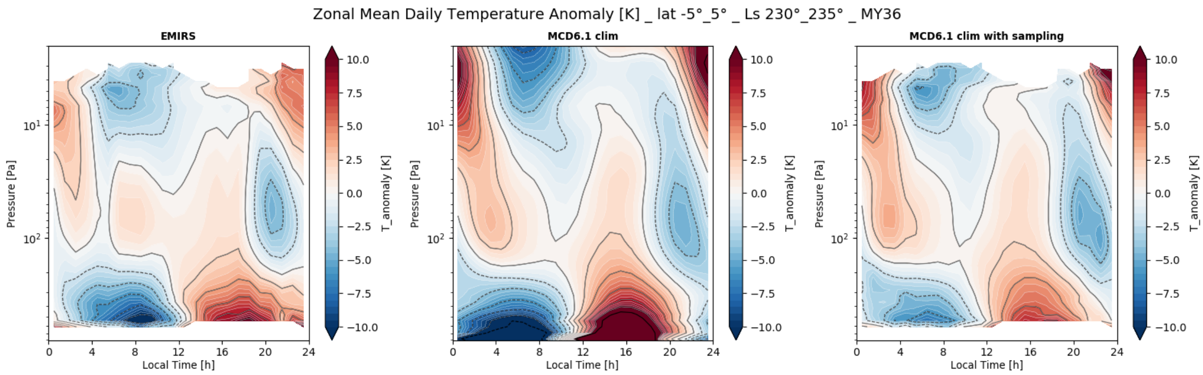

Figure 72: Zonal Mean Daily Temperature Anomaly averaged over latitude (-5,5), L_s 230-235. EMIRS on the left, MCD6.1 without specific sampling in the middle and MCD6.1 with EMIRS sampling on the right.

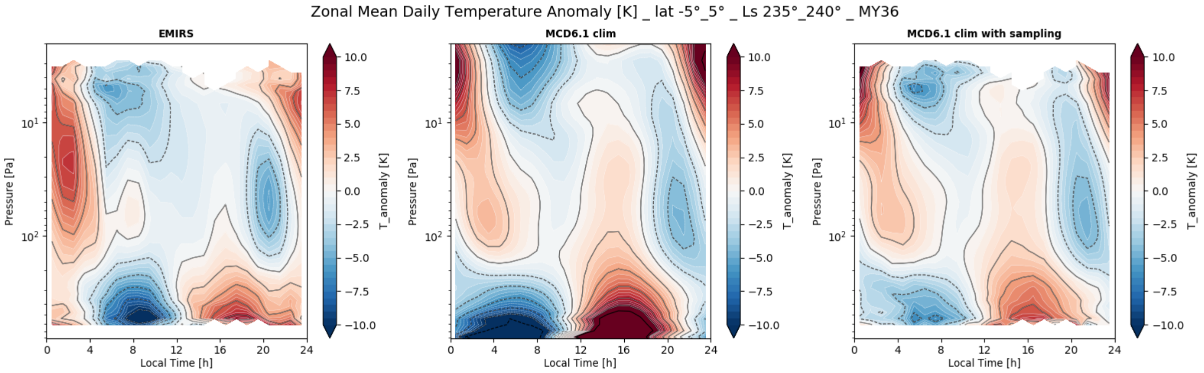

Figure 73: Zonal Mean Daily Temperature Anomaly averaged over latitude (-5,5), L_s 235-240. EMIRS on the left, MCD6.1 without specific sampling in the middle and MCD6.1 with EMIRS sampling on the right.

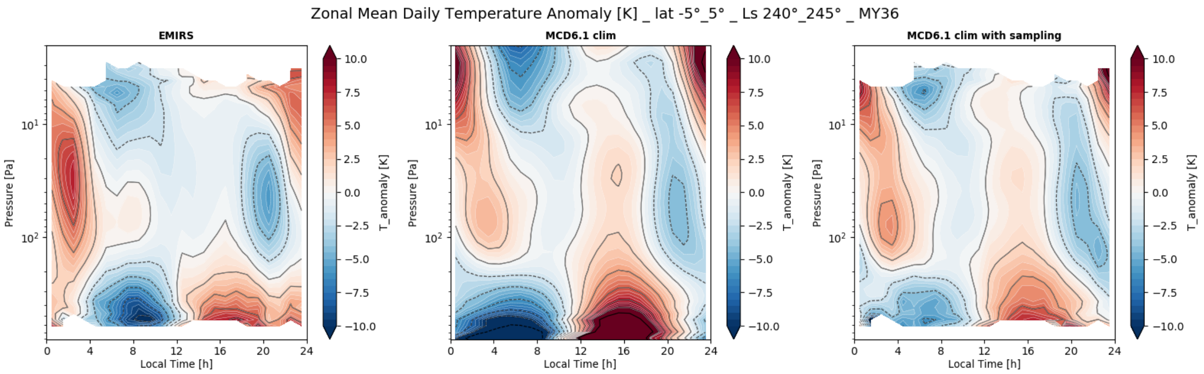

Figure 74: Zonal Mean Daily Temperature Anomaly averaged over latitude (-5,5), L_s 240-245. EMIRS on the left, MCD6.1 without specific sampling in the middle and MCD6.1 with EMIRS sampling on the right.

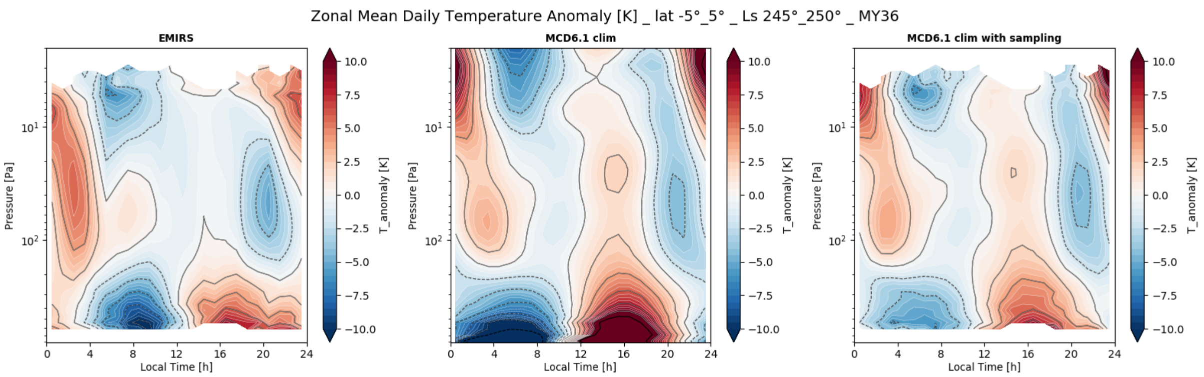

Figure 75: Zonal Mean Daily Temperature Anomaly averaged over latitude (-5,5), L_s 245-250. EMIRS on the left, MCD6.1 without specific sampling in the middle and MCD6.1 with EMIRS sampling on the right.

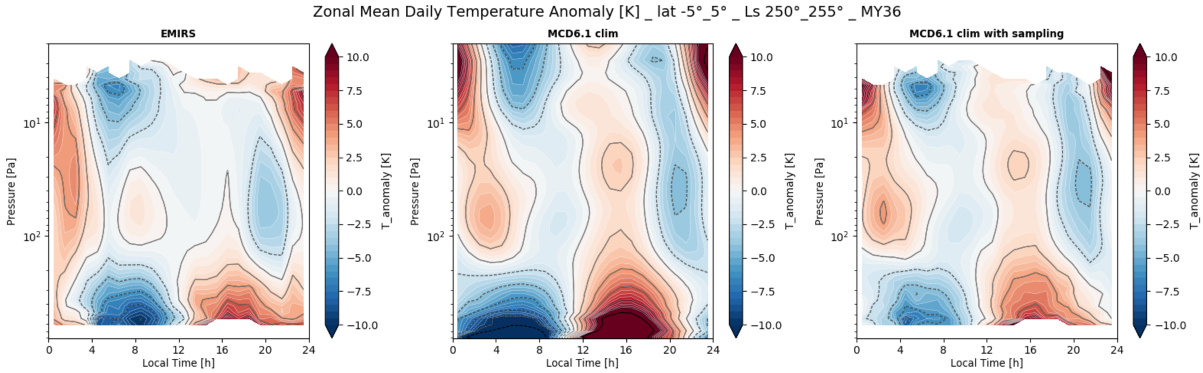

Figure 76: Zonal Mean Daily Temperature Anomaly averaged over latitude (-5,5), L_s 250-255. EMIRS on the left, MCD6.1 without specific sampling in the middle and MCD6.1 with EMIRS sampling on the right.

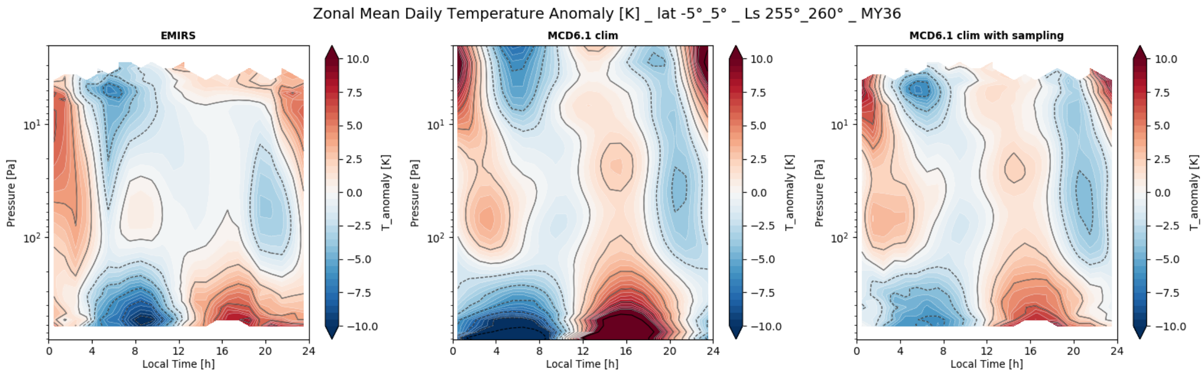

Figure 77: Zonal Mean Daily Temperature Anomaly averaged over latitude (-5,5), L_s 255-260. EMIRS on the left, MCD6.1 without specific sampling in the middle and MCD6.1 with EMIRS sampling on the right.

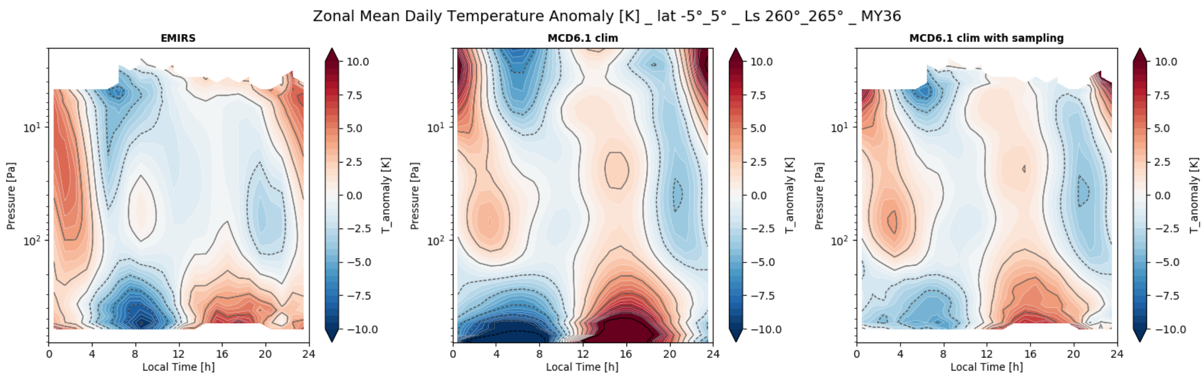

Figure 78: Zonal Mean Daily Temperature Anomaly averaged over latitude (-5,5), L_s 260-265. EMIRS on the left, MCD6.1 without specific sampling in the middle and MCD6.1 with EMIRS sampling on the right.

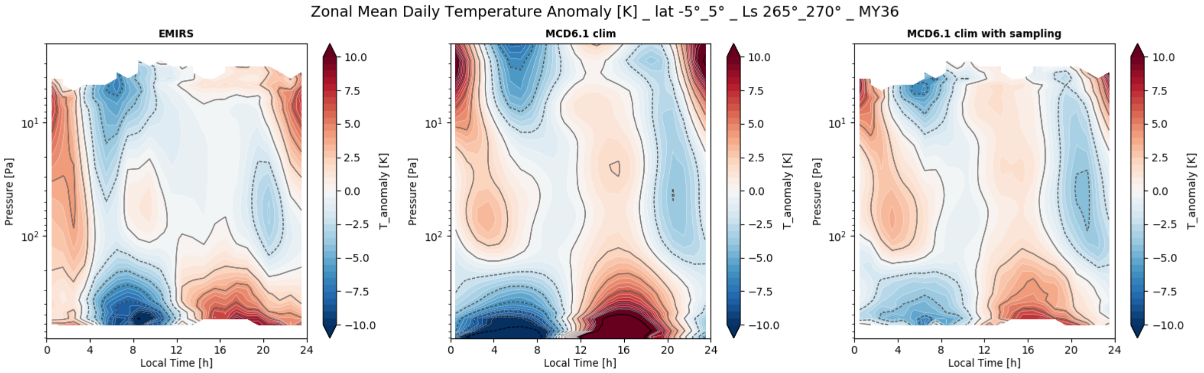

Figure 79: Zonal Mean Daily Temperature Anomaly averaged over latitude (-5,5), L_s 265-270. EMIRS on the left, MCD6.1 without specific sampling in the middle and MCD6.1 with EMIRS sampling on the right.

6 Dust Opacity

6.1 TES

Thanks to its nadir view, TES measured the column-integrated dust optical depth (CDOD) in infrared absorption. The MCD outputs the CDOD in visible extinction, so we use a coefficient of $\frac{1}{2.6}$ here, as assumed by Montabone et al. [2015], to convert this visible extinction to an infrared absorption. We present on Figure 80 these CDOD and their difference, as zonal means at local time 2pm, for Martian Year 24 to 27, in addition to MCD predictions with the clim, warm and cold scenarios.

Before any comparison, one must know that the MCD interpolates its data between times separated by 30° of L_s. Its failure to reproduce the brutal and quick rise of dust opacity at the triggering of the MY25 Global Dust Storm (L_s 200°) is due to this interpolation, which in this unfortunate case takes place between L_s 195° (just before the GDS) and 225° (long after the start of the GDS). This interpolation can also slightly explain the greater amount of dust afterwards in the MCD, although this too slow decay p?ase is mainly a model bias, which even comes to alter the clear season of MY26. The clim scenario, not affected by the MY25, is thus more comparable to TES than the MY26 scenario, as shown by the distributions on Figure 81.

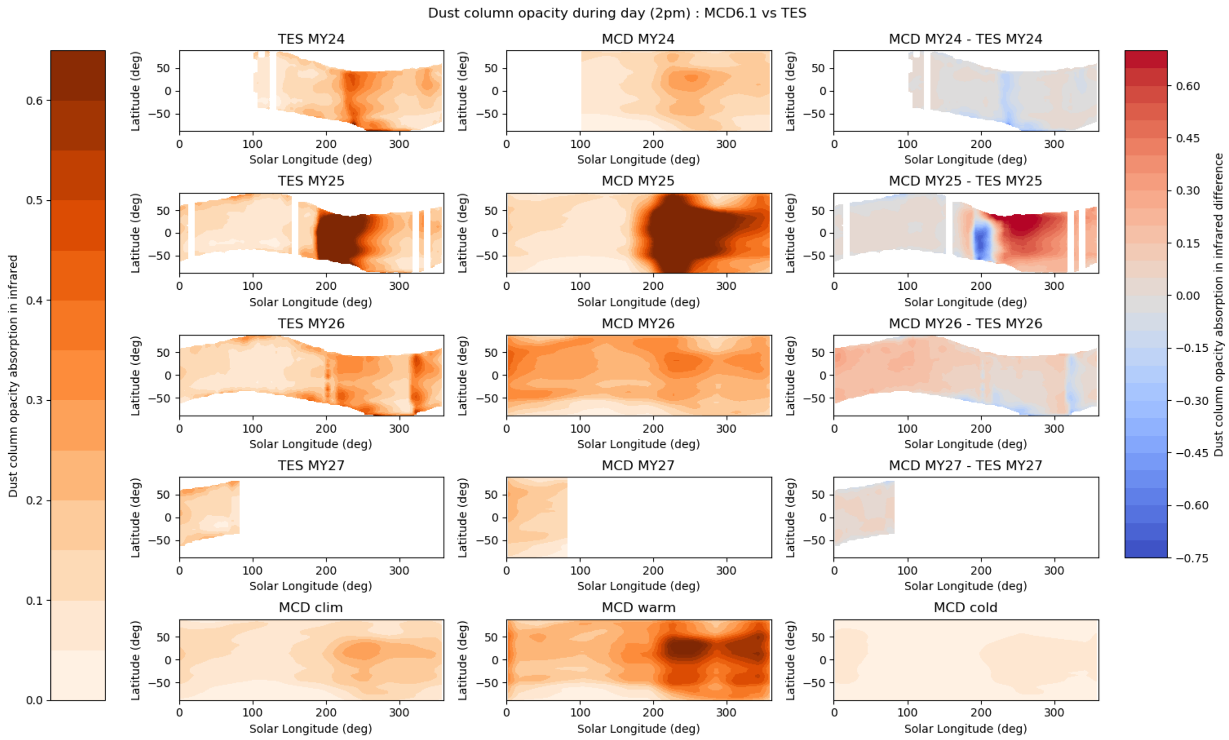

Figure 80: Zonal infrared absorption dust opacity column over solar longitude from MY24 to MY27 (first four lines), at 2 pm (local solar time). Left : TES data. Middle : MCD data. Right : Difference MCD-TES. Last line shows clim, warm and cold scenarios.

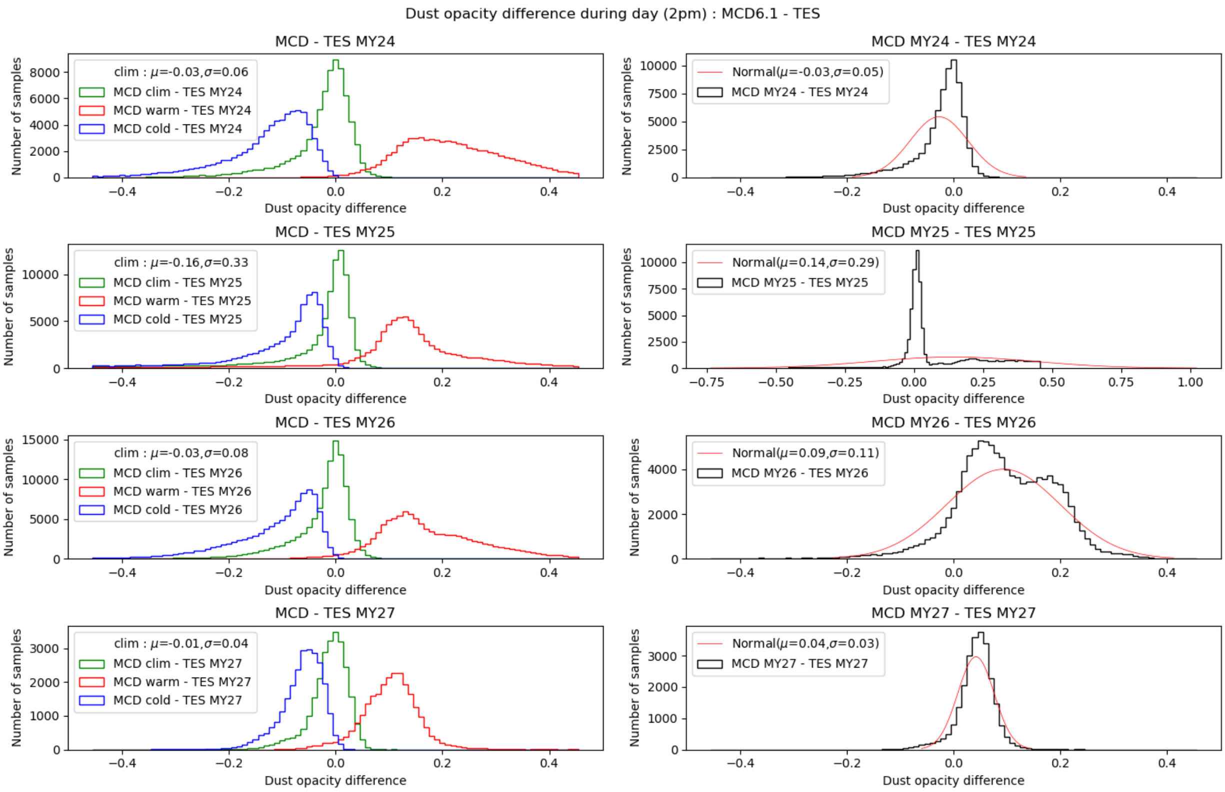

Figure 81: Distribution of infrared absorption dust opacity column differences between MCD v6.1 and TES using bins of 0.01 from MY24 to MY27 (from top to bottom), at 2 pm (local solar time) in latitudes (-50,50). Left : TES compared with MCD for clim, warm and cold scenarios. Right : TES compared with MCD for specific MY scenario. The red curve on the right represents normal distributions of same mean and standard deviation.

6.2 MCS

One of the main modeling focuses for the MCD6.1 was to reproduce the tropical dust detached layers widely observed by MCS (Heavens et al. [2014]).

Figures below represent for each Martian Year the zonal tropical mean density-scaled opacity (DSO) profiles from MCS observations and the MCD, at wavelength of 21.9μm in extinction. For MCS, the DSO $\partial_z \tau / \rho$ [m^2/kg] is computed from the dust opacity $\partial_z \tau$ [1/km], temperature [K] and pressure [Pa] retrievals, using the ideal gas law. For the MCD, we use the dust mass mixing ratio output that we convert into DSO using a $\frac{1}{0.012}$ factor taken from Heavens et al. [2011].

6.2.1 Clear season

In the clear season (L_s 0°-140°), MCS observations during daytime are known to be more difficult to interprete, since a very few of the profiles go down to the altitudes of the detached layers (20-30km, or 200-50Pa). Although the MCD profiles fit well with these daytime observations, this comparison is not very relevant due to the low number of MCS measurements. On the other hand, MCS always observes detached layers during nighttime, which are not reproduced by the MCD.

Only the MY35 scenario exhibits a kind of detached layer, or at least a dust mixing profile. This year is particular since it features an uncommon regional dust storm around L_s 40° near the tropics. Besides, the analysis with and without the MCS sampling on this year shows that sampling on the dayside seems to dampen the "detached layer" shape, while it does accentuate it on the nightside.

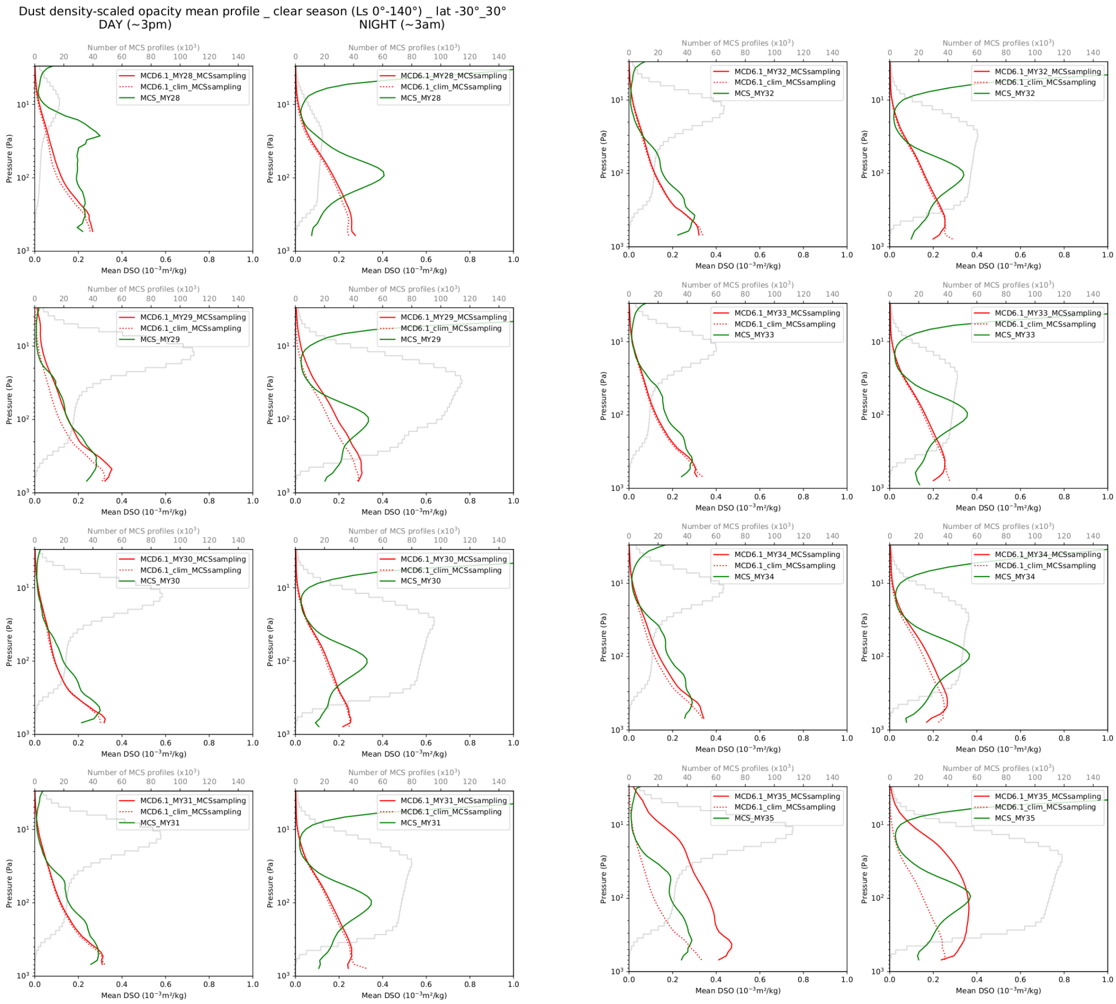

(a) MY28 to MY31 (b) MY32 to MY35

Figure 82: Zonal mean Density-Scaled Opacity profile, averaged in latitude (-30,30) during clear season (L_s 0-140) during day 3pm (left) and during night 3am (right). MCD in red, MCS in green. Number of MCS profiles is also shown as grey steps. Here MCD profiles are calculated using the same sampling than MCS, for clim scenario (dotted curves) and specific scenario (solid curves, from top to bottom: (a) MY28 to MY31 (b) MY32 to MY35)

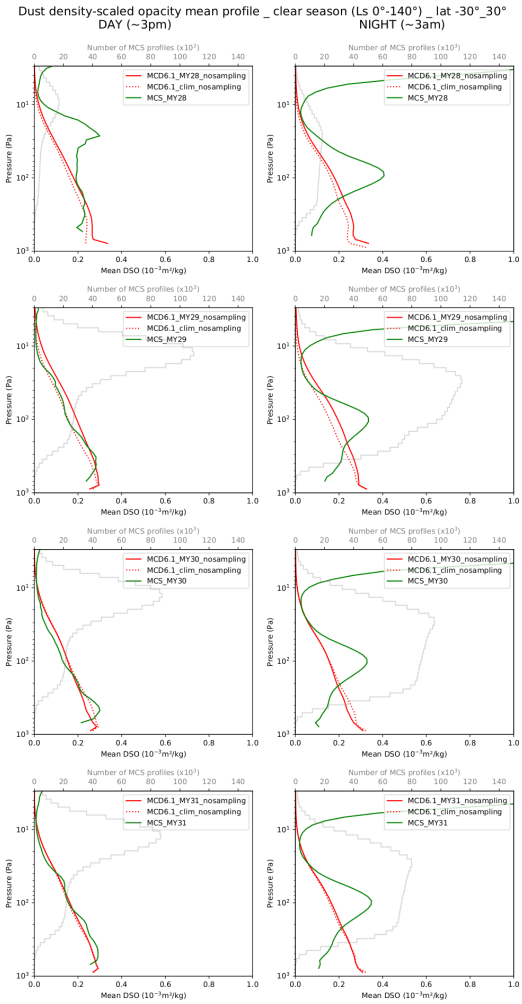

(a) MY28 to MY31

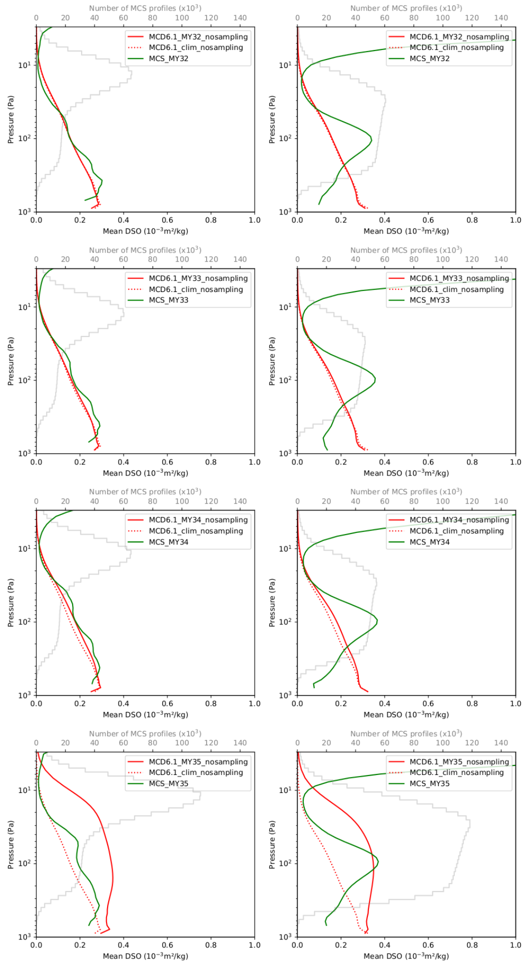

(b) MY32 to MY35

Figure 83: Zonal mean Density-Scaled Opacity profile, averaged in latitude (-30,30) during clear season (L_s 0°-140°) at daytime (left) and nighttime (right). MCD in red, MCS in green. Number of MCS profiles is also shown as grey steps. Here MCD profiles are calculated using no specific sampling, for clim scenario (dotted curves) and specific scenario (solid curves, from top to bottom: (a) MY28 to MY31 (b) MY32 to MY35)

6.2.2 Dusty season

In the dusty season, MCS and the MCD display dust detached layers during both daytime and nighttime. The MCD detached layers lie however slightly below the altitudes of MCS ones. The amplitude of the dust profiles are of the same magnitude.

As already seen for MY35 during the clear season, the MCS sampling strongly emphasizes the ”detached layer” effect : the DSO is increased at the detached layers altitudes, while the near-surface profiles are biased towards lower values than without sampling. This is particularly visible in Martian Years with Global Dust Storms like MY28 and 34. Nonetheless, the profiles without sampling still exhibit some detached layer shape, with a local maximum DSO around 100Pa every year.

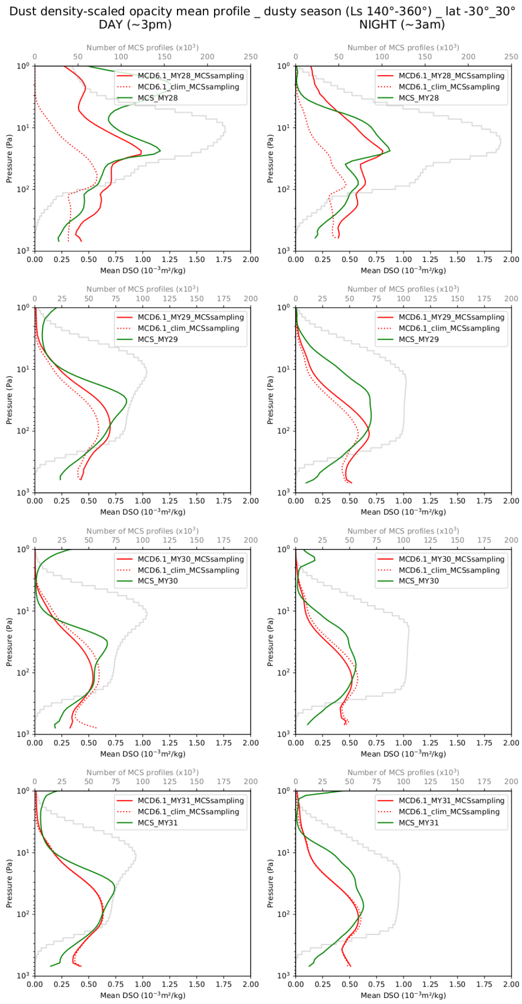

(a) MY28 to MY31

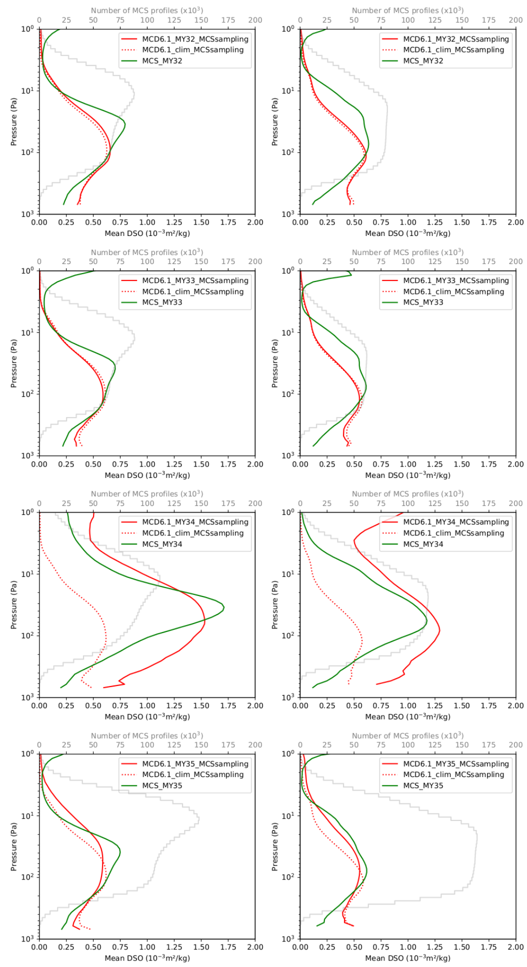

(b) MY32 to MY35

Figure 84: Zonal mean Density-Scaled Opacity profile, averaged in latitude (-30,30) during dusty season (L_s 140°-360°) during day 3pm (left) and during night 3am (right). MCD in red, MCS in green. Number of MCS profiles is also shown as grey steps. Here MCD profiles are calculated using the same sampling than MCS, for clim scenario (dotted curves) and specific scenario (solid curves, from top to bottom: (a) MY28 to MY31 (b) MY32 to MY35)

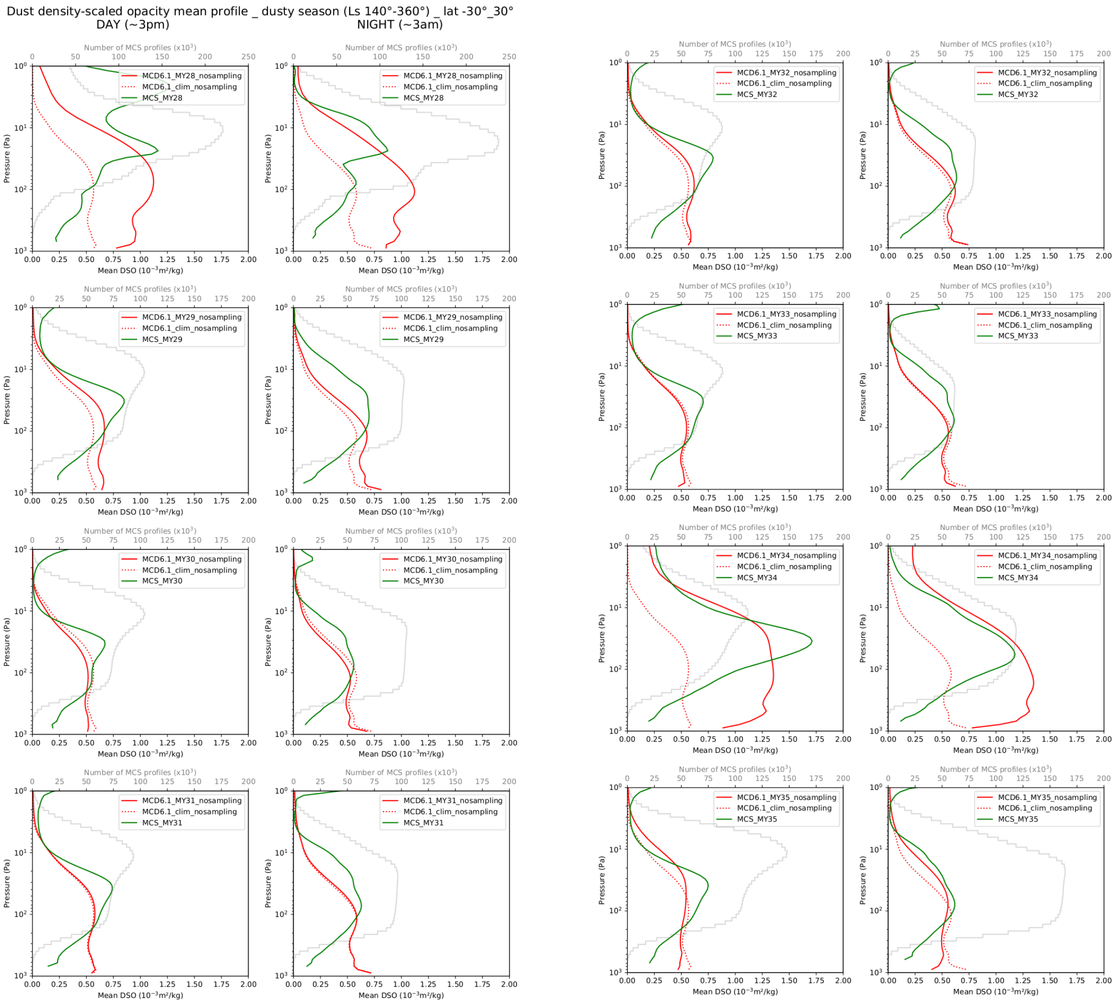

(a) MY28 to MY31

(b) MY32 to MY35

Figure 85: Zonal mean Density-Scaled Opacity profile, averaged in latitude (-30,30) during dusty season (L_s 140°-360°) during day 3pm (left) and during night 3am (right). MCD in red, MCS in green. Number of MCS profiles is also shown as grey steps. Here MCD profiles are calculated using no specific sampling, for clim scenario (dotted curves) and specific scenario (solid curves, from top to bottom: (a) MY28 to MY31 (b) MY32 to MY35)

6.3 EMIRS

In order to compare EMIRS infrared absorption CDOD to the MCD, we convert it into visible extinction like for TES.

There is no MCD scenario that covers the Mars Year 36 during which EMIRS made its observations. We thus use the clim scenario for the comparison, while keeping in mind that some dusty events may not be reproduced by the MCD, especially during the dusty season when the interannual variability is the strongest. This is for example the case when EMIRS witnesses an early regional dust storm around L_s 150°-170°, which was seen only in MY29 and with a lower magnitude before that.

Besides, the overall zonal and diurnal structure is well reproduced by the MCD when the EMIRS sampling is taken into account.

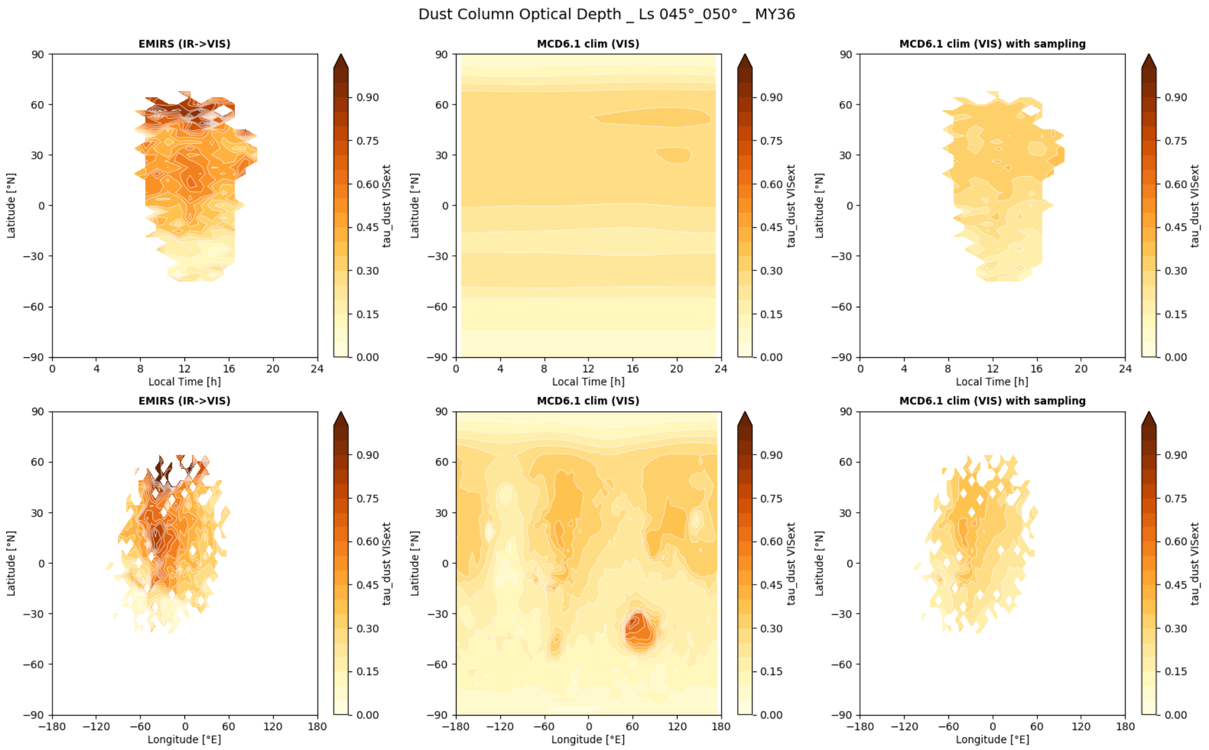

Figure 86: Zonal mean (first row) and diurnal mean (second row) of dust visible extinction column optical depth, L_s 45-50. EMIRS on the left, MCD6.1 without specific sampling in the middle and MCD6.1 with EMIRS sampling on the right.

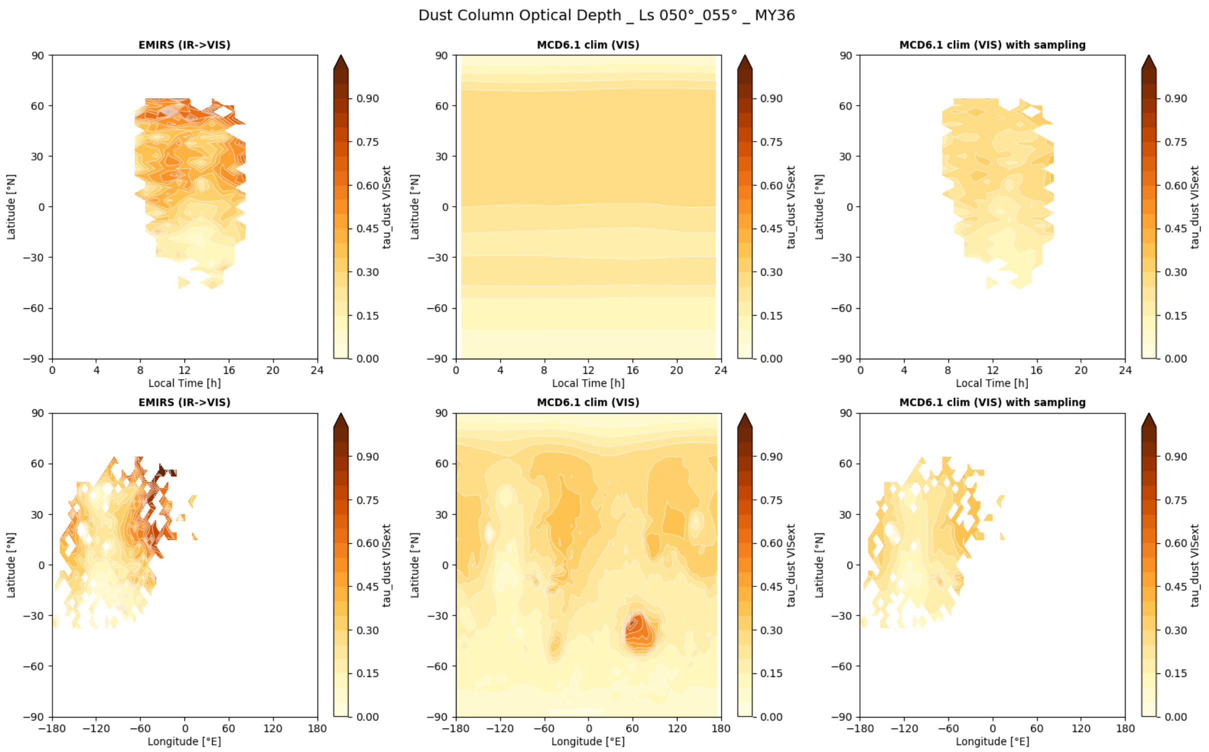

Figure 87: Zonal mean (first row) and diurnal mean (second row) of dust visible extinction column optical depth, L_s 50-55. EMIRS on the left, MCD6.1 without specific sampling in the middle and MCD6.1 with EMIRS sampling on the right.

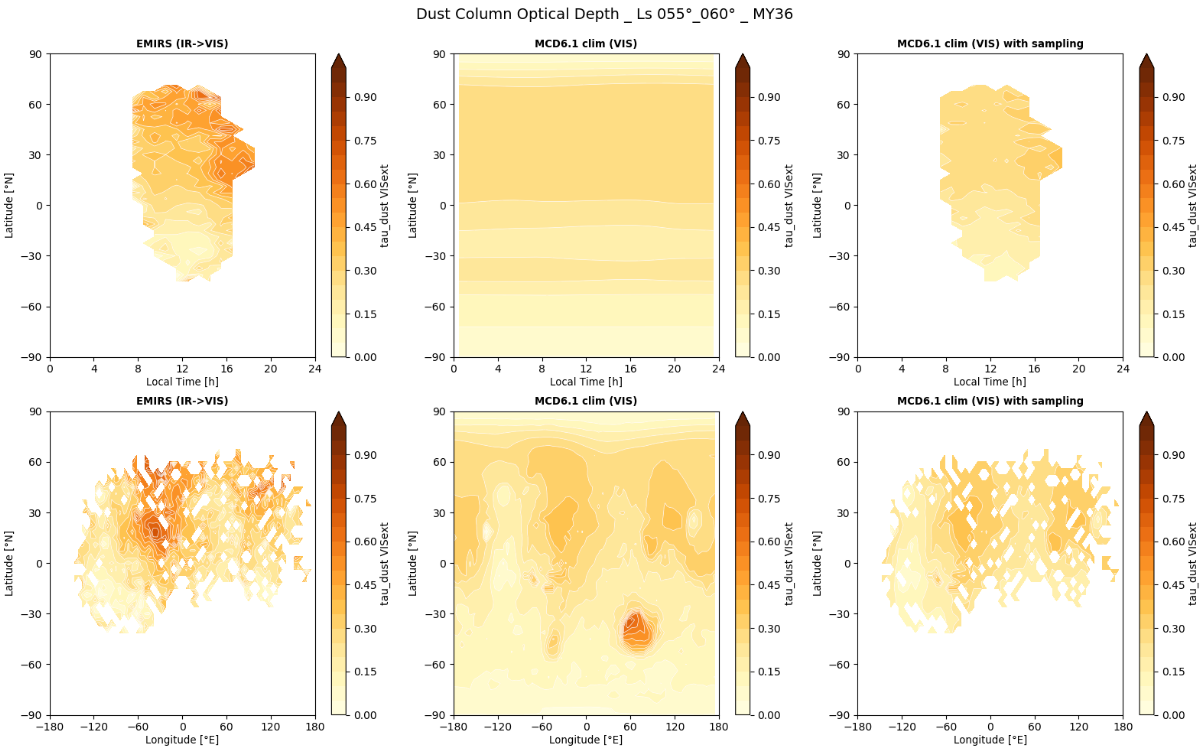

Figure 88: Zonal mean (first row) and diurnal mean (second row) of dust visible extinction column optical depth, L_s 55-60. EMIRS on the left, MCD6.1 without specific sampling in the middle and MCD6.1 with EMIRS sampling on the right.

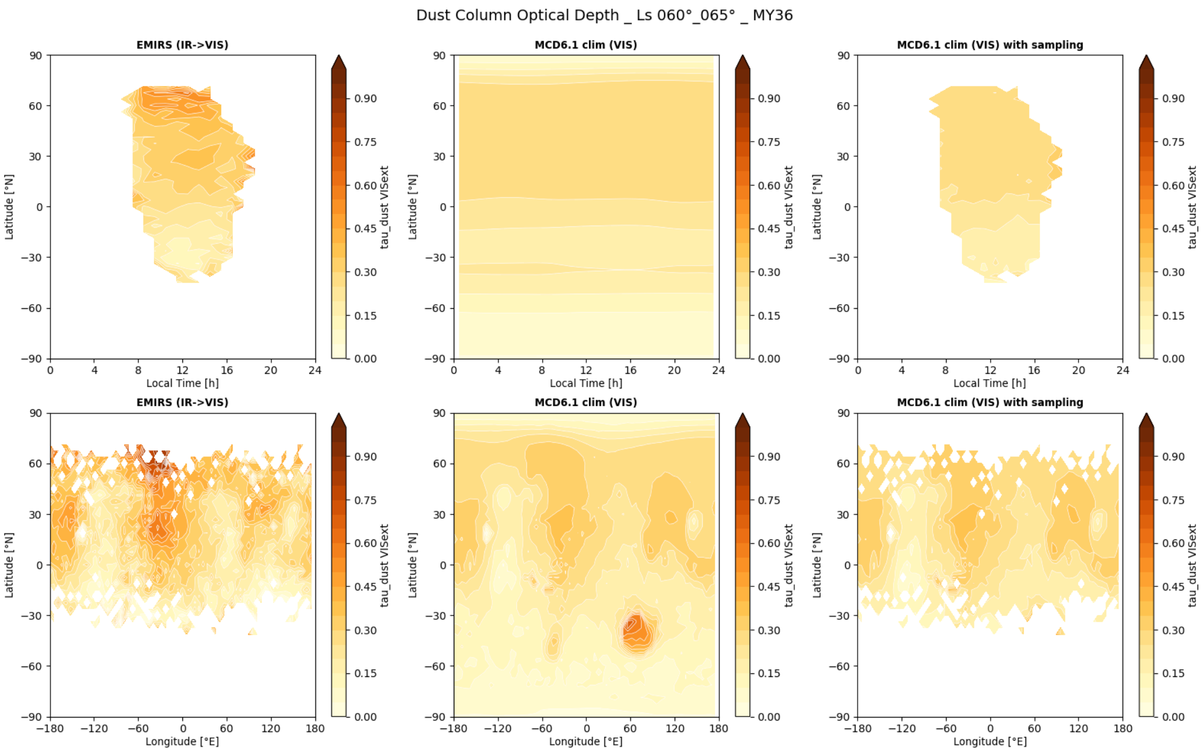

Figure 89: Zonal mean (first row) and diurnal mean (second row) of dust visible extinction column optical depth, L_s 60-65. EMIRS on the left, MCD6.1 without specific sampling in the middle and MCD6.1 with EMIRS sampling on the right.

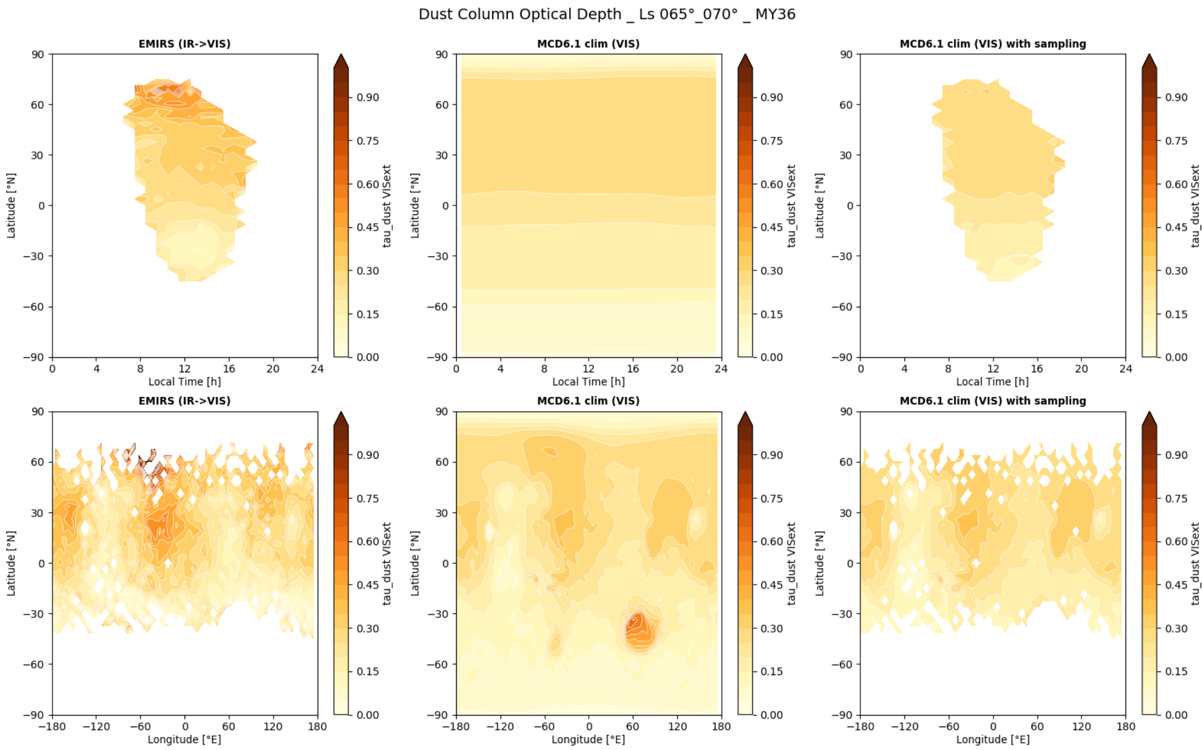

Figure 90: Zonal mean (first row) and diurnal mean (second row) of dust visible extinction column optical depth, L_s 65-70. EMIRS on the left, MCD6.1 without specific sampling in the middle and MCD6.1 with EMIRS sampling on the right.

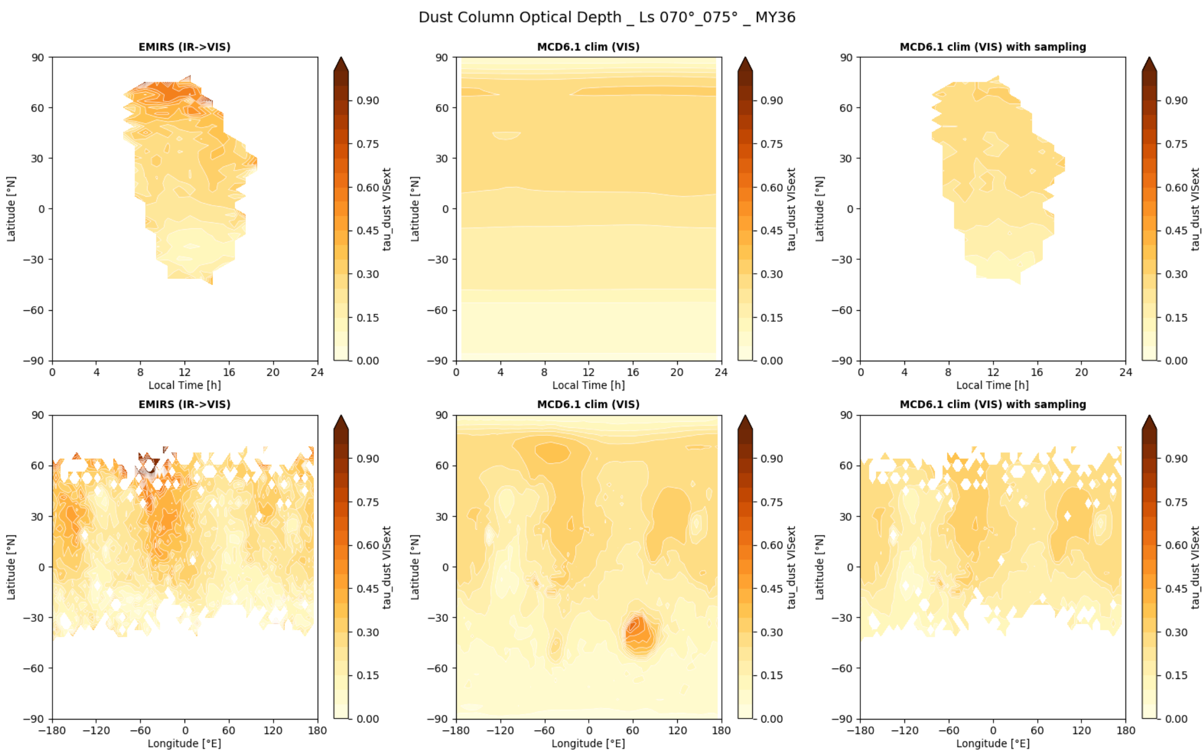

Figure 91: Zonal mean (first row) and diurnal mean (second row) of dust visible extinction column optical depth, L_s 70-75. EMIRS on the left, MCD6.1 without specific sampling in the middle and MCD6.1 with EMIRS sampling on the right.

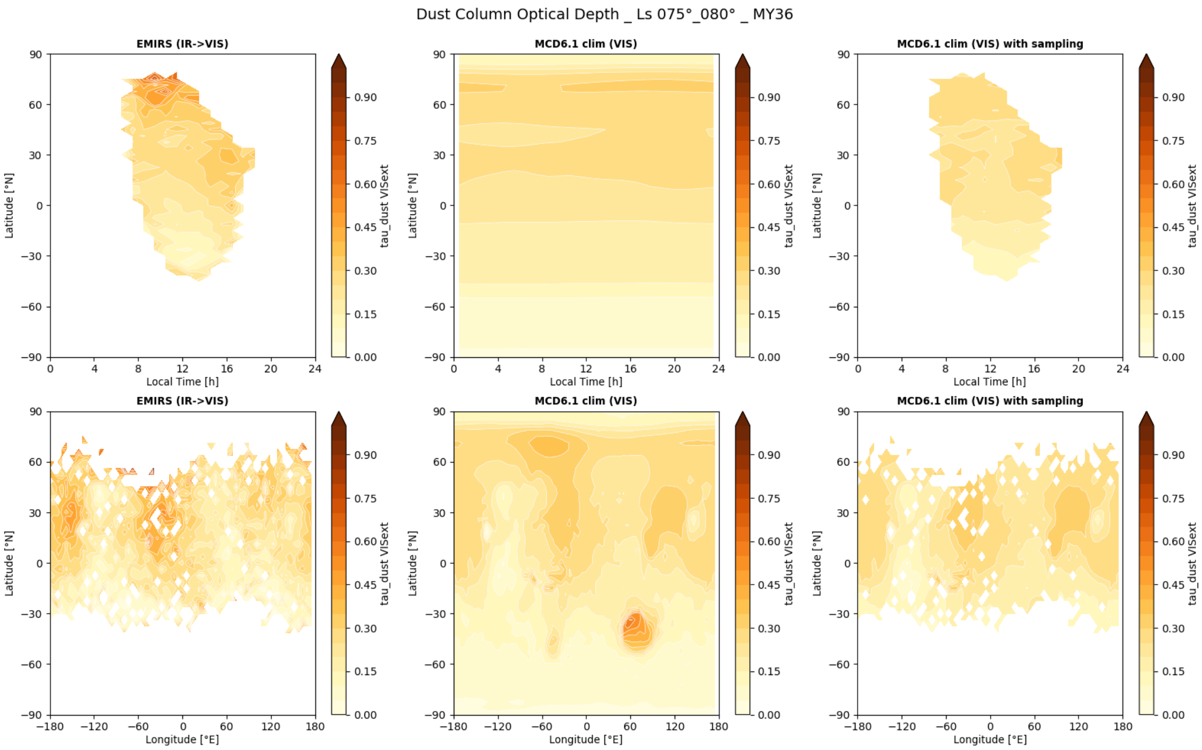

Figure 92: Zonal mean (first row) and diurnal mean (second row) of dust visible extinction column optical depth, L_s 75-80. EMIRS on the left, MCD6.1 without specific sampling in the middle and MCD6.1 with EMIRS sampling on the right.

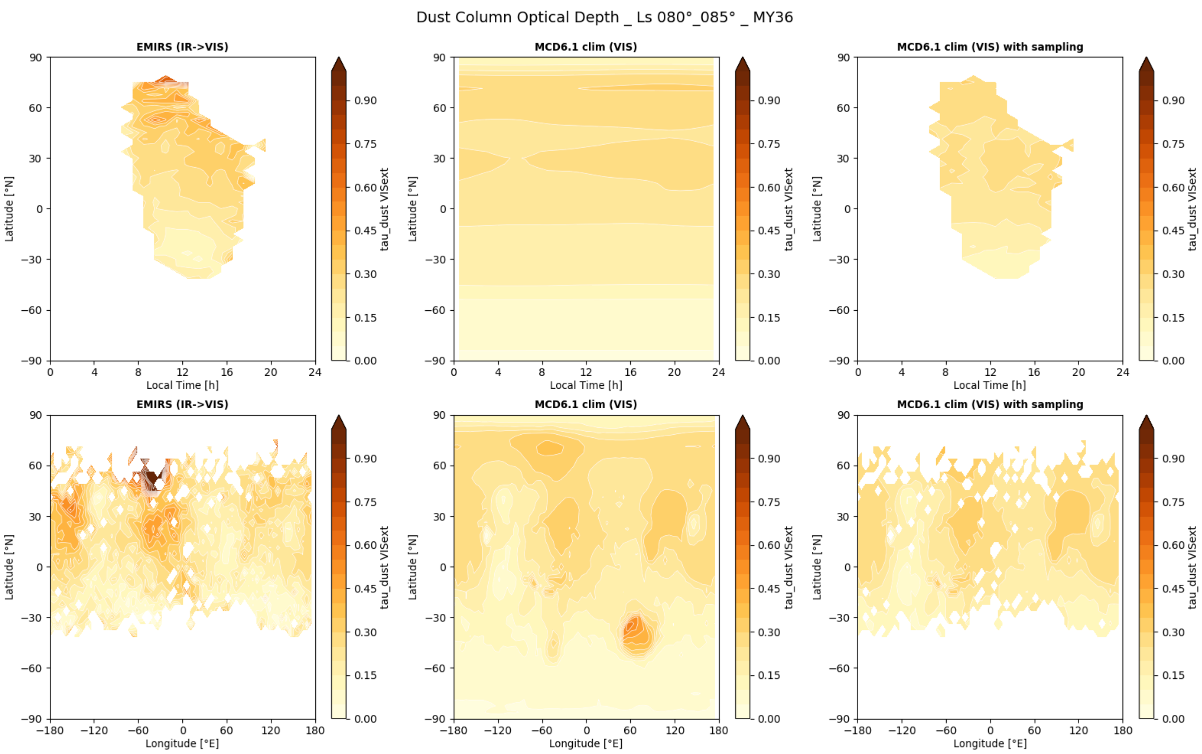

Figure 93: Zonal mean (first row) and diurnal mean (second row) of dust visible extinction column optical depth, L_s 80-85. EMIRS on the left, MCD6.1 without specific sampling in the middle and MCD6.1 with EMIRS sampling on the right.

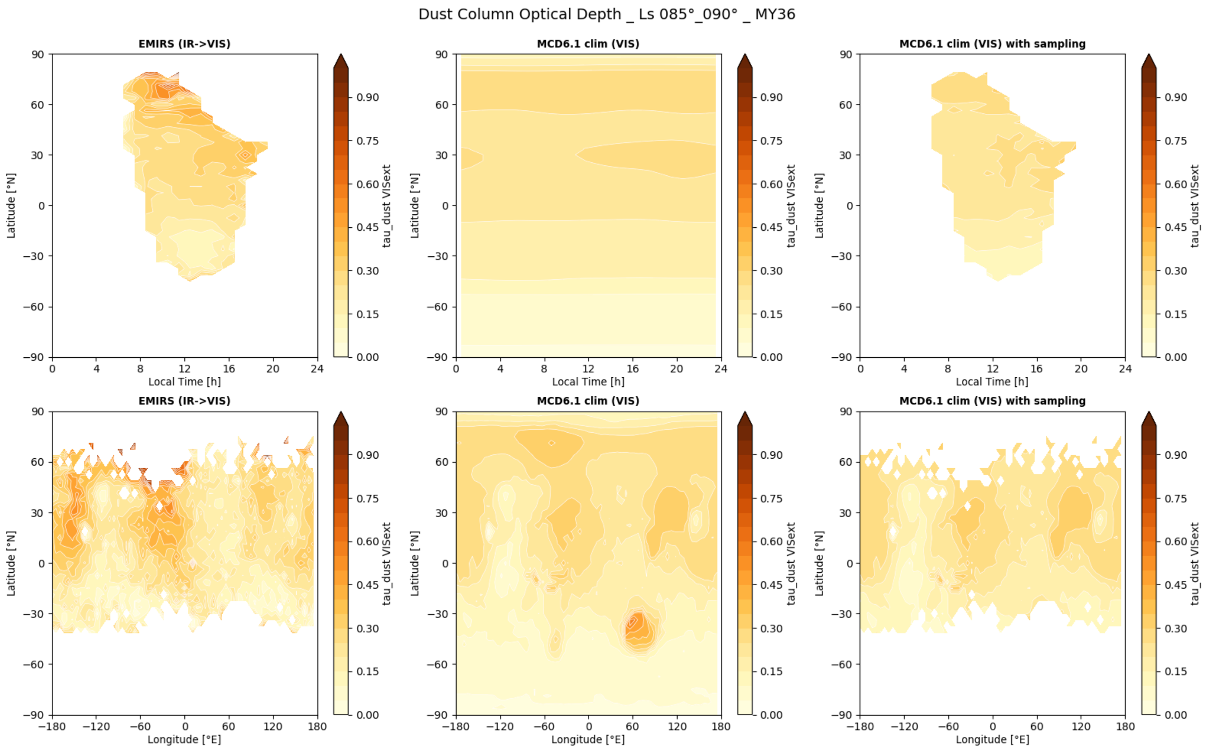

Figure 94: Zonal mean (first row) and diurnal mean (second row) of dust visible extinction column optical depth, L_s 85-90. EMIRS on the left, MCD6.1 without specific sampling in the middle and MCD6.1 with EMIRS sampling on the right.

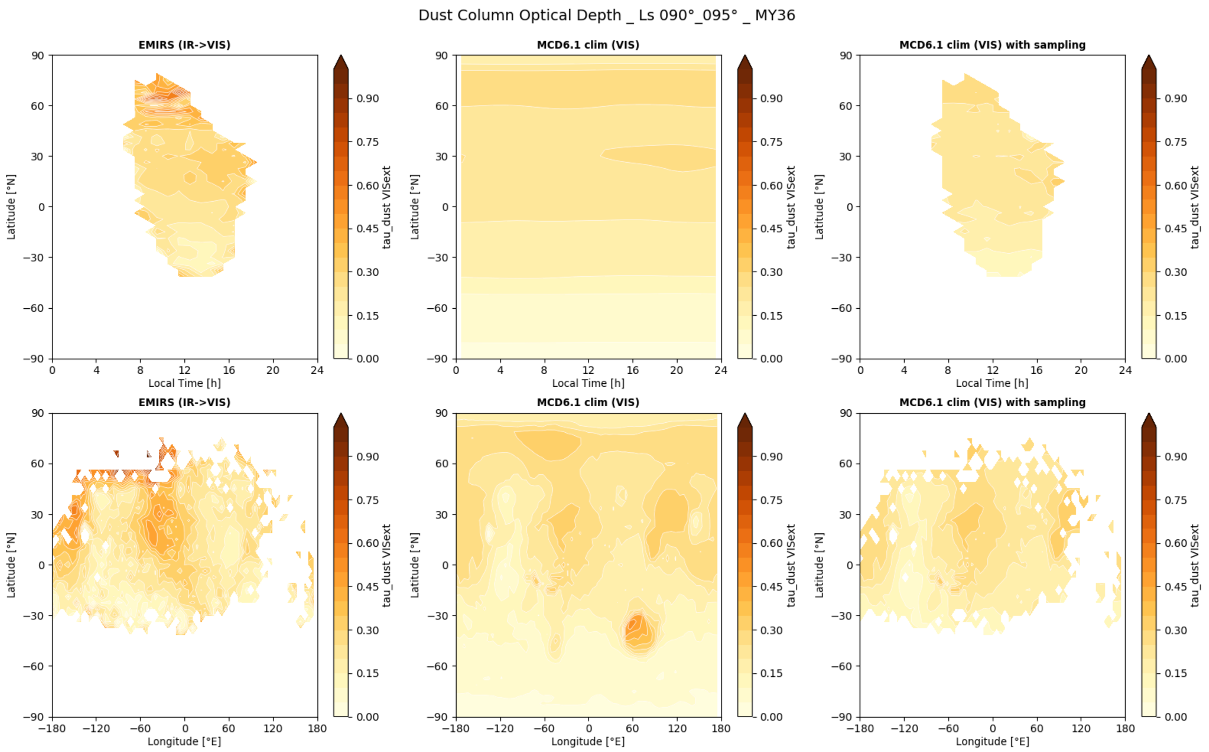

Figure 95: Zonal mean (first row) and diurnal mean (second row) of dust visible extinction column optical depth, L_s 90-95. EMIRS on the left, MCD6.1 without specific sampling in the middle and MCD6.1 with EMIRS sampling on the right.

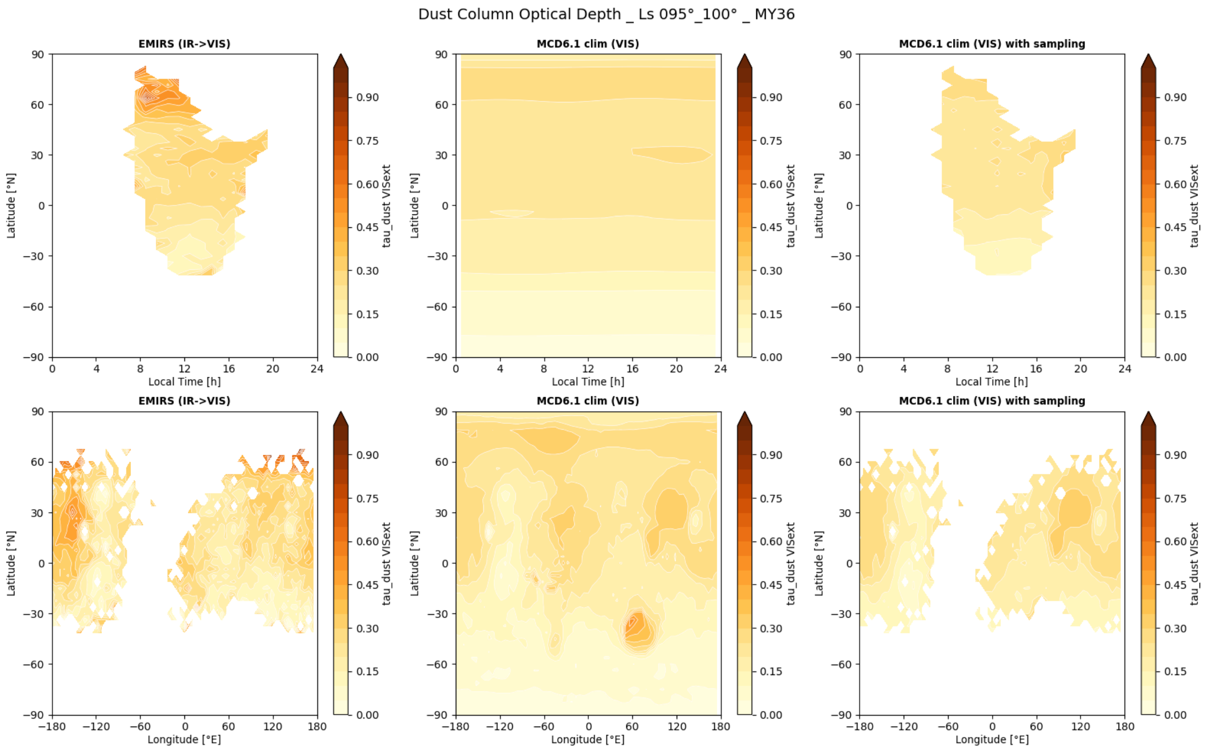

Figure 96: Zonal mean (first row) and diurnal mean (second row) of dust visible extinction column optical depth, L_s 95-100. EMIRS on the left, MCD6.1 without specific sampling in the middle and MCD6.1 with EMIRS sampling on the right.

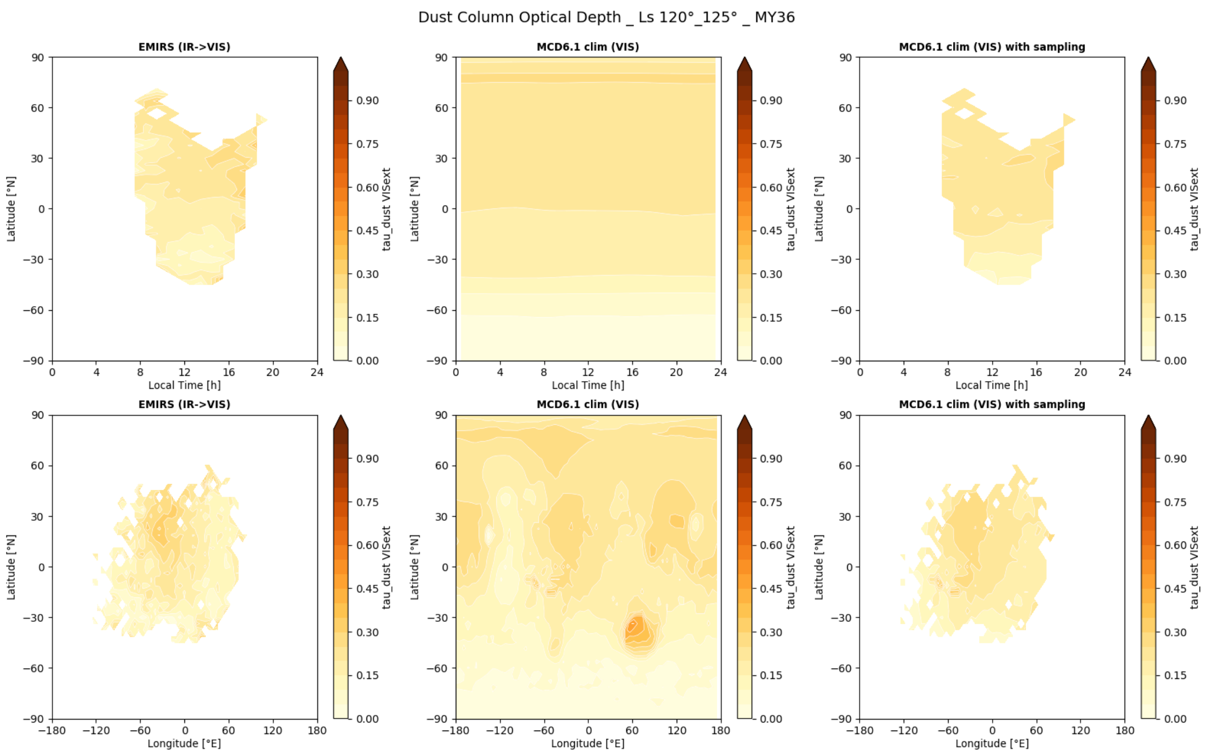

Figure 97: Zonal mean (first row) and diurnal mean (second row) of dust visible extinction column optical depth, L_s 120-125. EMIRS on the left, MCD6.1 without specific sampling in the middle and MCD6.1 with EMIRS sampling on the right.

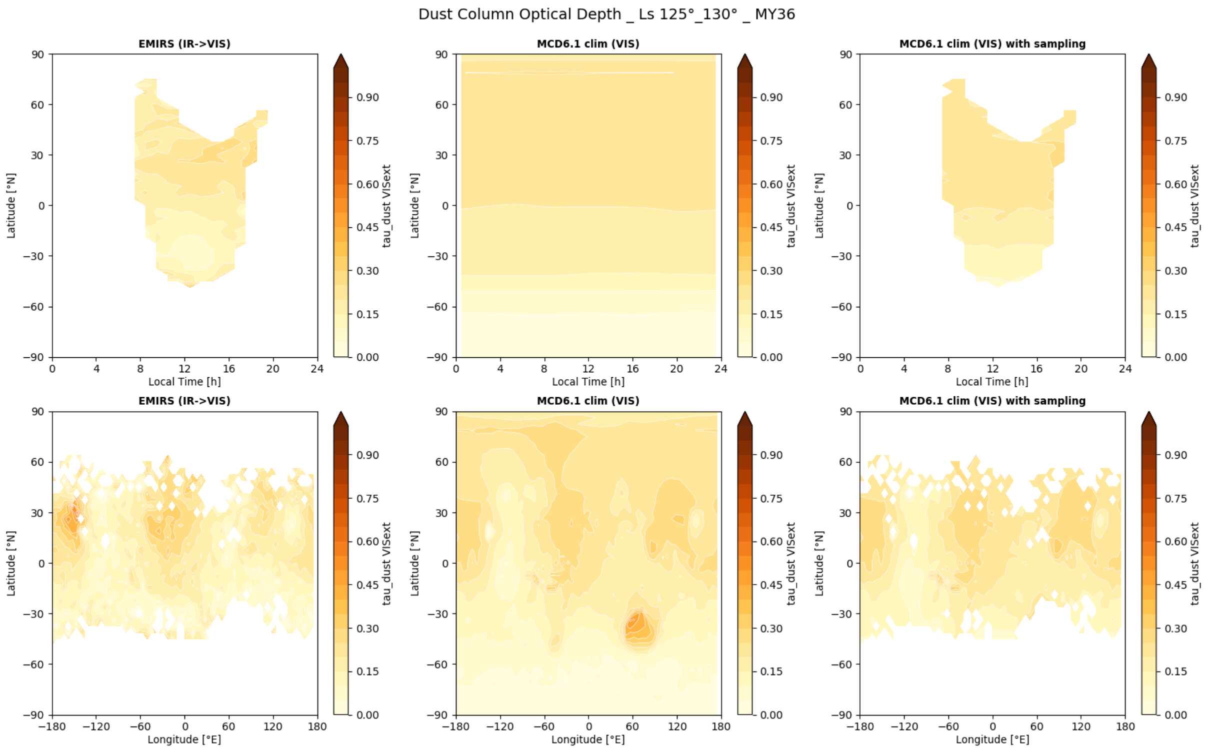

Figure 98: Zonal mean (first row) and diurnal mean (second row) of dust visible extinction column optical depth, L_s 125-130. EMIRS on the left, MCD6.1 without specific sampling in the middle and MCD6.1 with EMIRS sampling on the right.

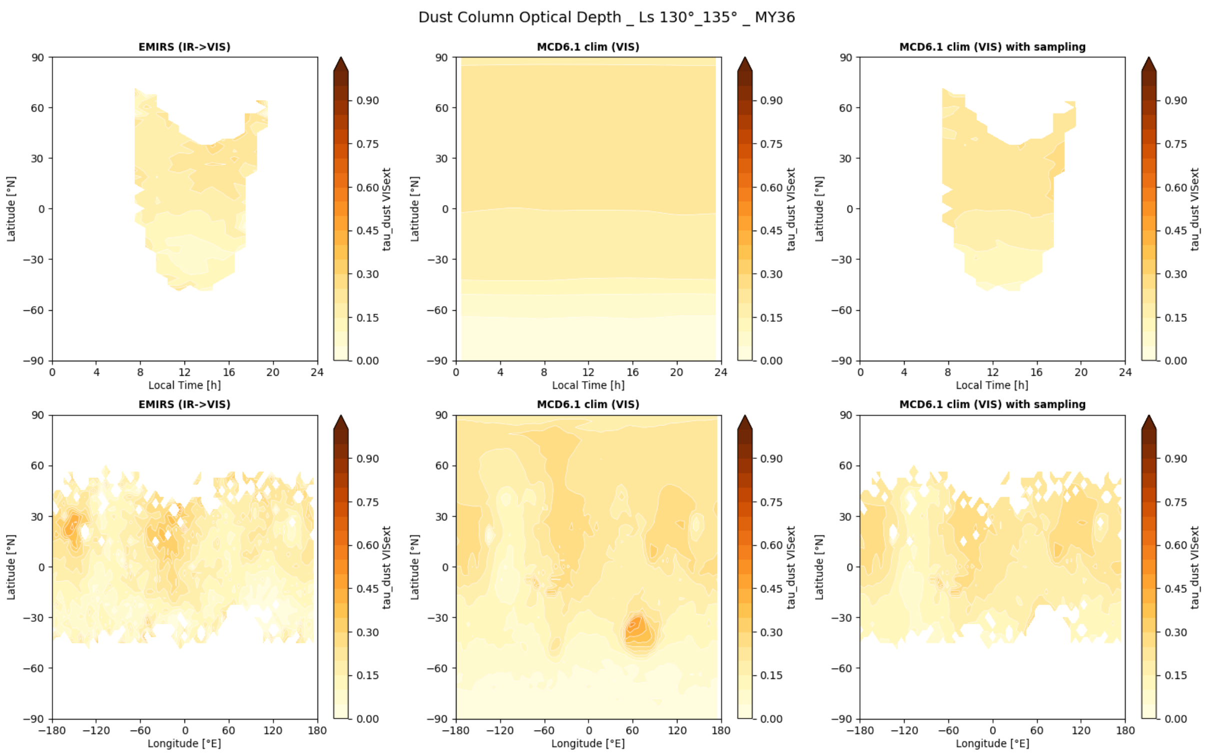

Figure 99: Zonal mean (first row) and diurnal mean (second row) of dust visible extinction column optical depth, L_s 130-135. EMIRS on the left, MCD6.1 without specific sampling in the middle and MCD6.1 with EMIRS sampling on the right.

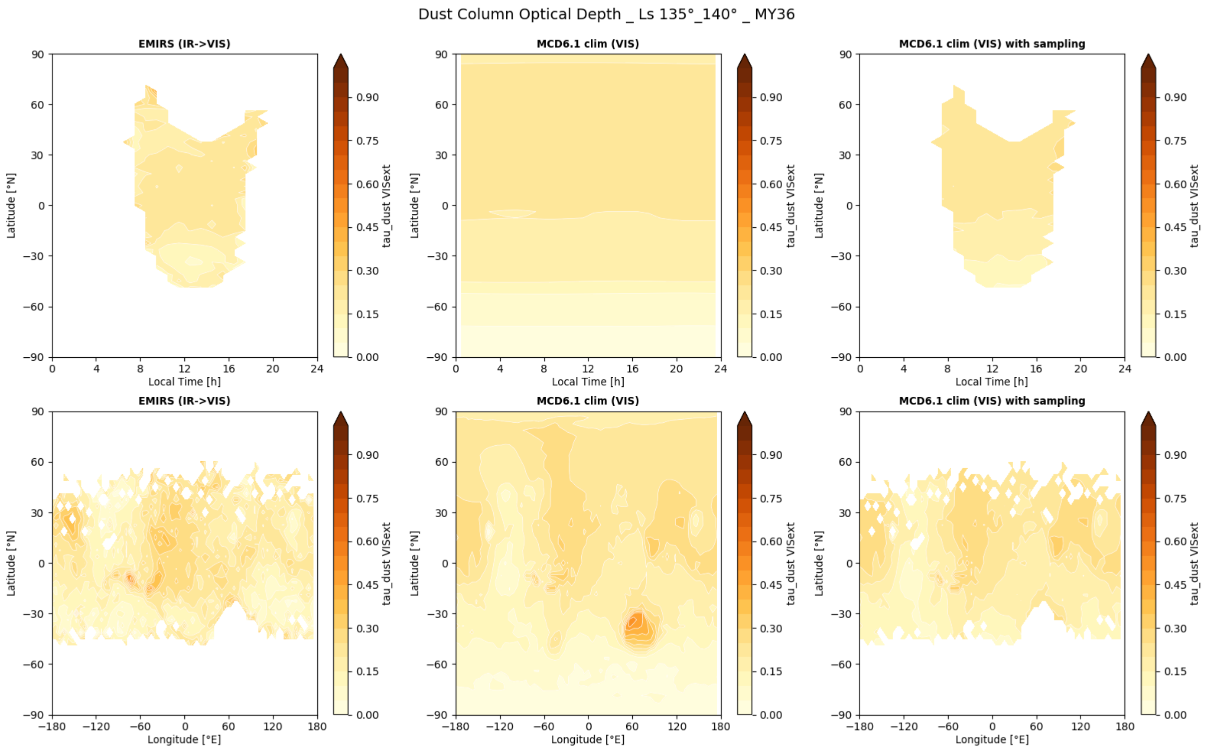

Figure 100: Zonal mean (first row) and diurnal mean (second row) of dust visible extinction column optical depth, L_s 135-140. EMIRS on the left, MCD6.1 without specific sampling in the middle and MCD6.1 with EMIRS sampling on the right.

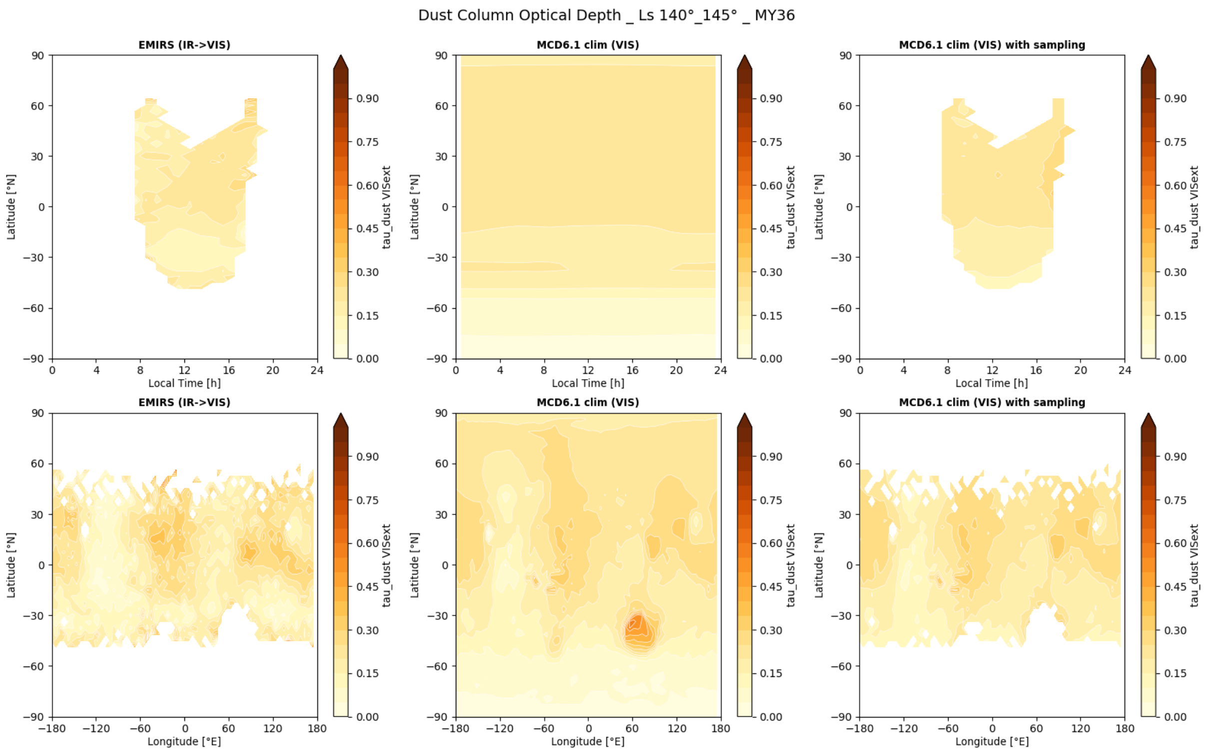

Figure 101: Zonal mean (first row) and diurnal mean (second row) of dust visible extinction column optical depth, L_s 140-145. EMIRS on the left, MCD6.1 without specific sampling in the middle and MCD6.1 with EMIRS sampling on the right.

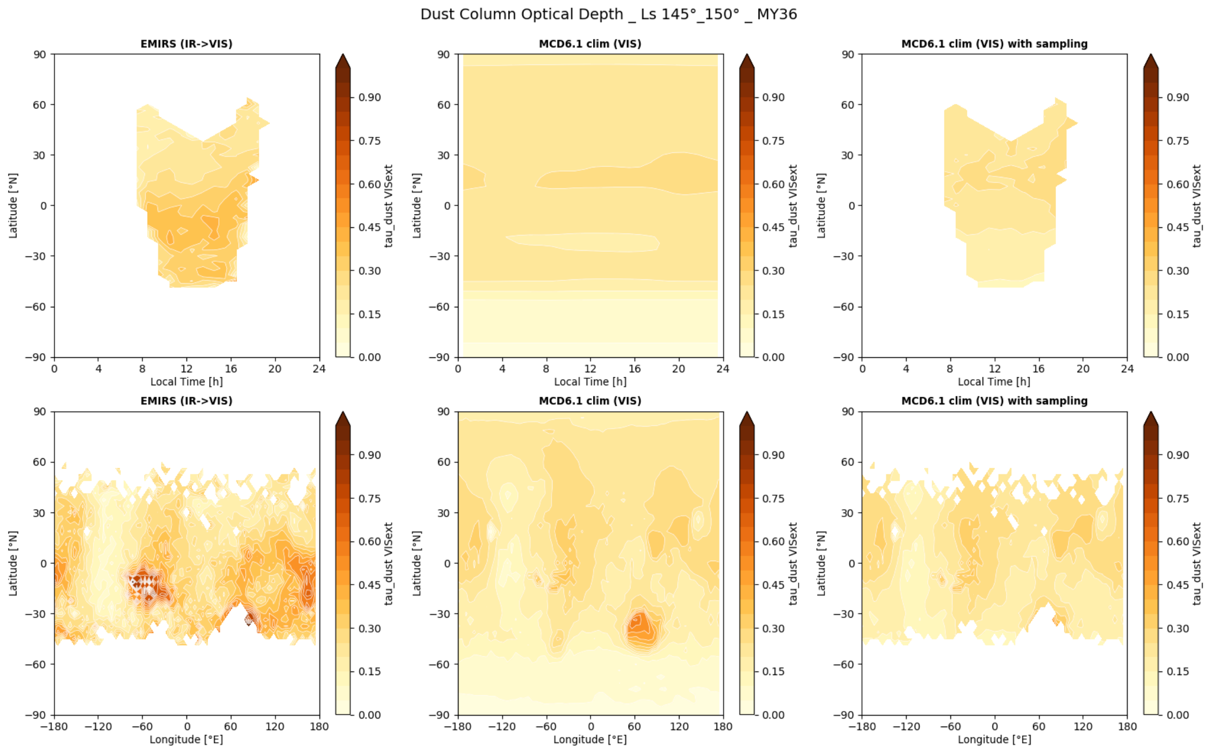

Figure 102: Zonal mean (first row) and diurnal mean (second row) of dust visible extinction column optical depth, L_s 145-150. EMIRS on the left, MCD6.1 without specific sampling in the middle and MCD6.1 with EMIRS sampling on the right.

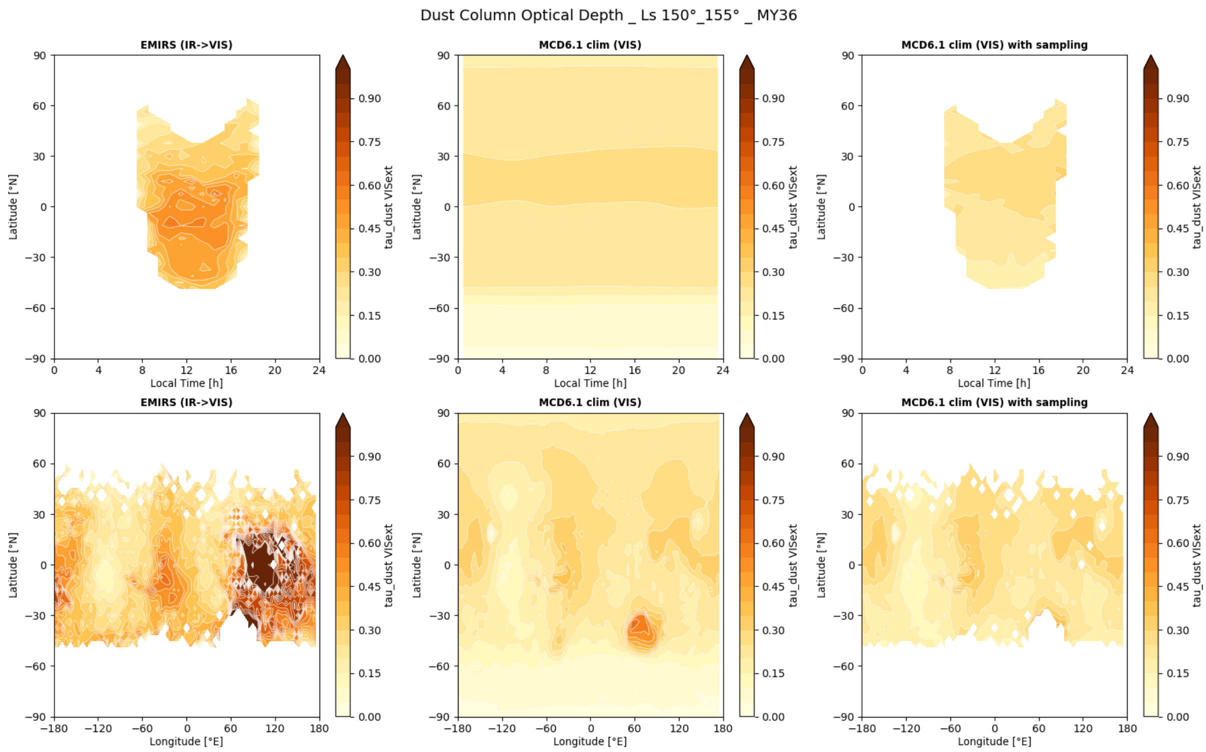

Figure 103: Zonal mean (first row) and diurnal mean (second row) of dust visible extinction column optical depth, L_s 150-155. EMIRS on the left, MCD6.1 without specific sampling in the middle and MCD6.1 with EMIRS sampling on the right.

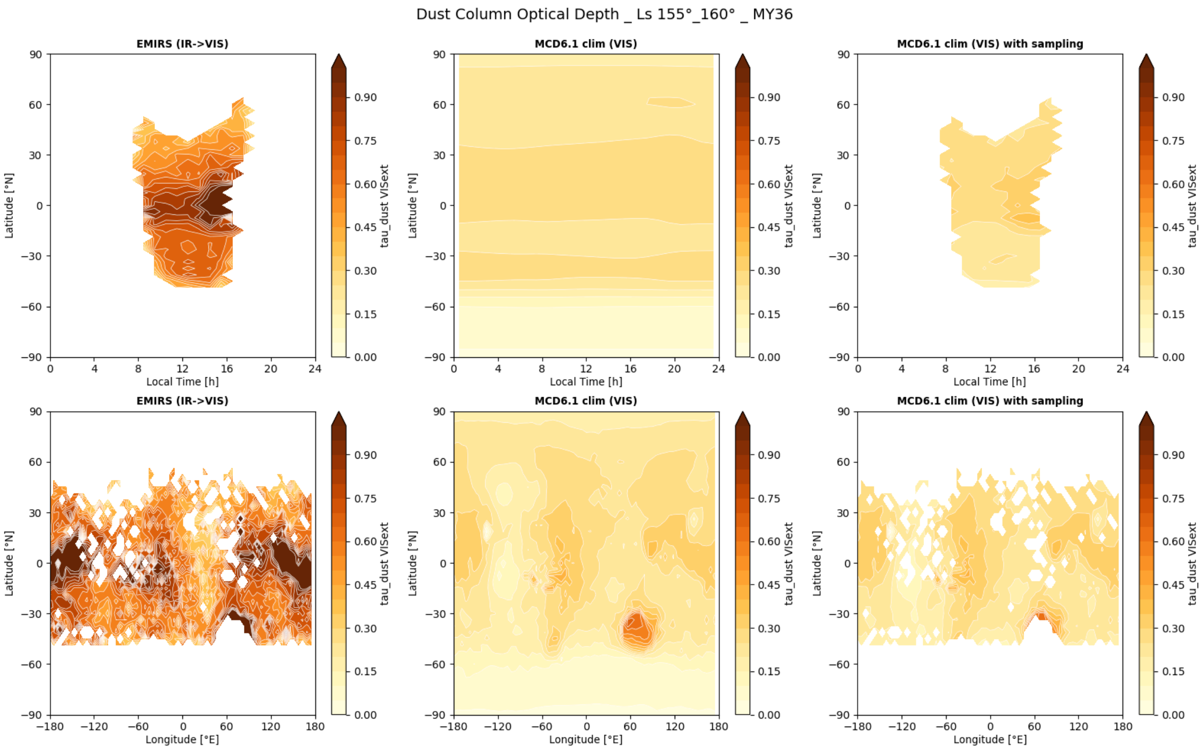

Figure 104: Zonal mean (first row) and diurnal mean (second row) of dust visible extinction column optical depth, L_s 155-160. EMIRS on the left, MCD6.1 without specific sampling in the middle and MCD6.1 with EMIRS sampling on the right.

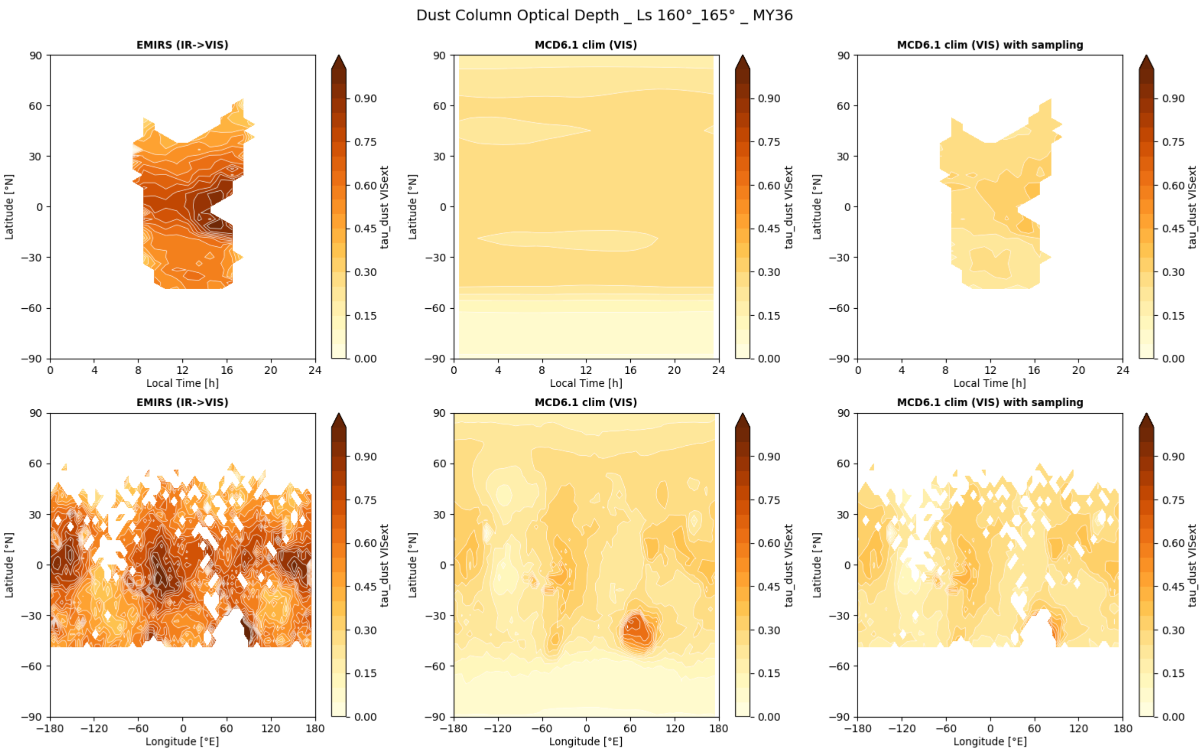

Figure 105: Zonal mean (first row) and diurnal mean (second row) of dust visible extinction column optical depth, L_s 160-165. EMIRS on the left, MCD6.1 without specific sampling in the middle and MCD6.1 with EMIRS sampling on the right.

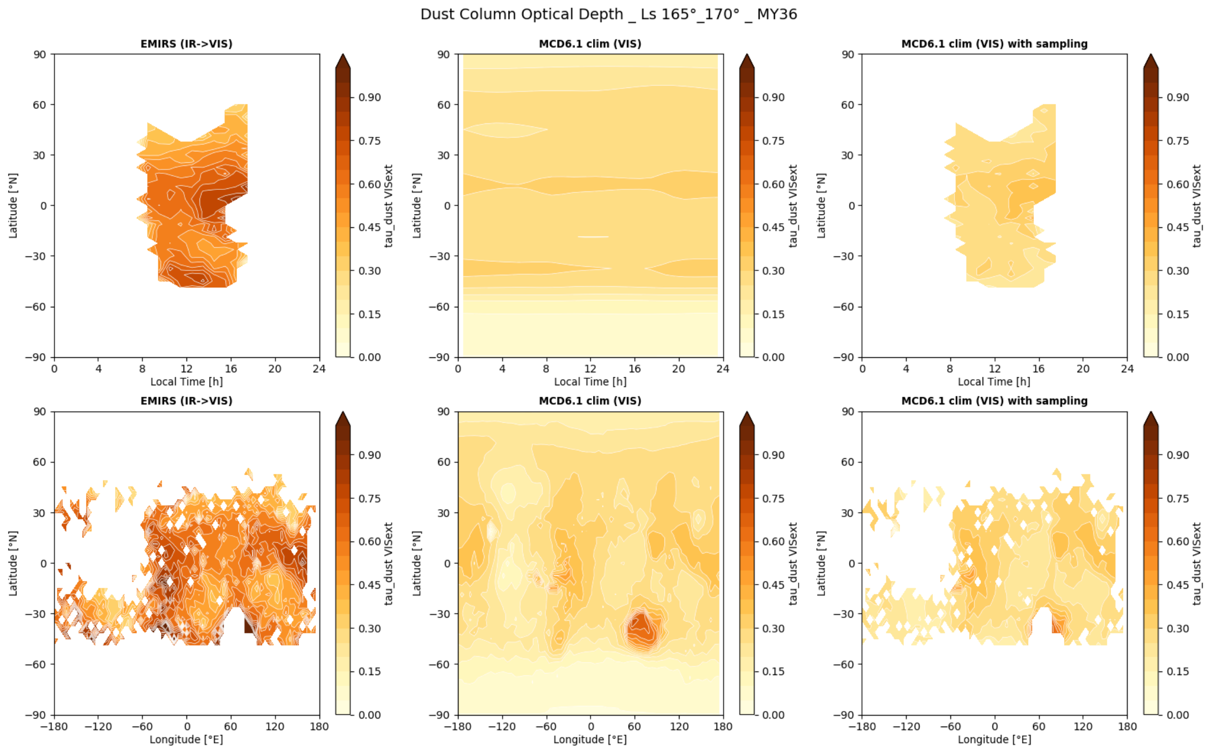

Figure 106: Zonal mean (first row) and diurnal mean (second row) of dust visible extinction column optical depth, L_s 165-170. EMIRS on the left, MCD6.1 without specific sampling in the middle and MCD6.1 with EMIRS sampling on the right.

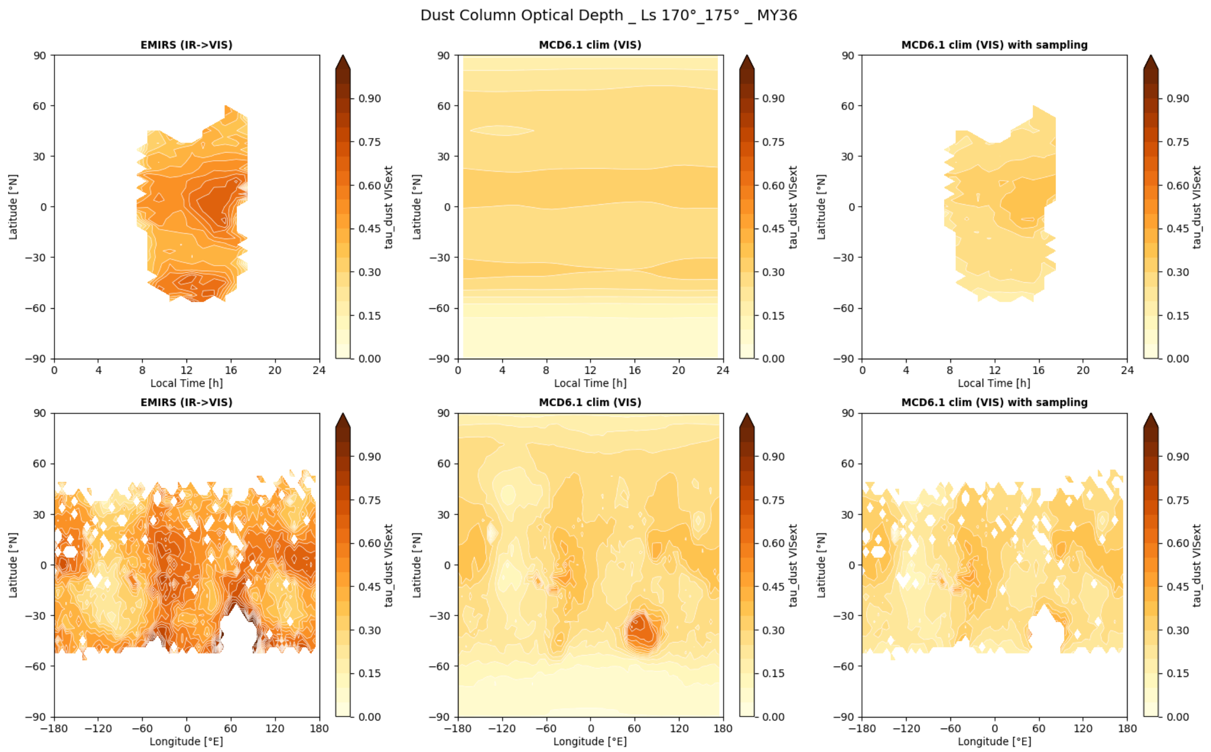

Figure 107: Zonal mean (first row) and diurnal mean (second row) of dust visible extinction column optical depth, L_s 170-175. EMIRS on the left, MCD6.1 without specific sampling in the middle and MCD6.1 with EMIRS sampling on the right.

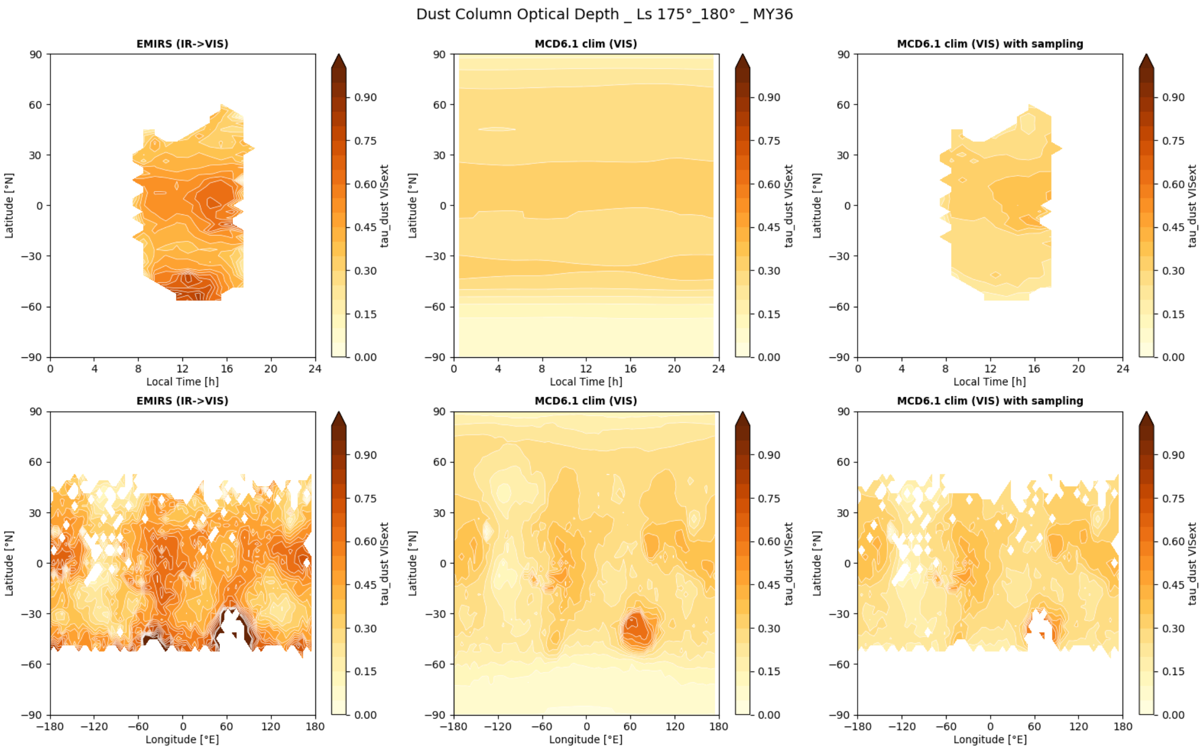

Figure 108: Zonal mean (first row) and diurnal mean (second row) of dust visible extinction column optical depth, L_s 175-180. EMIRS on the left, MCD6.1 without specific sampling in the middle and MCD6.1 with EMIRS sampling on the right.

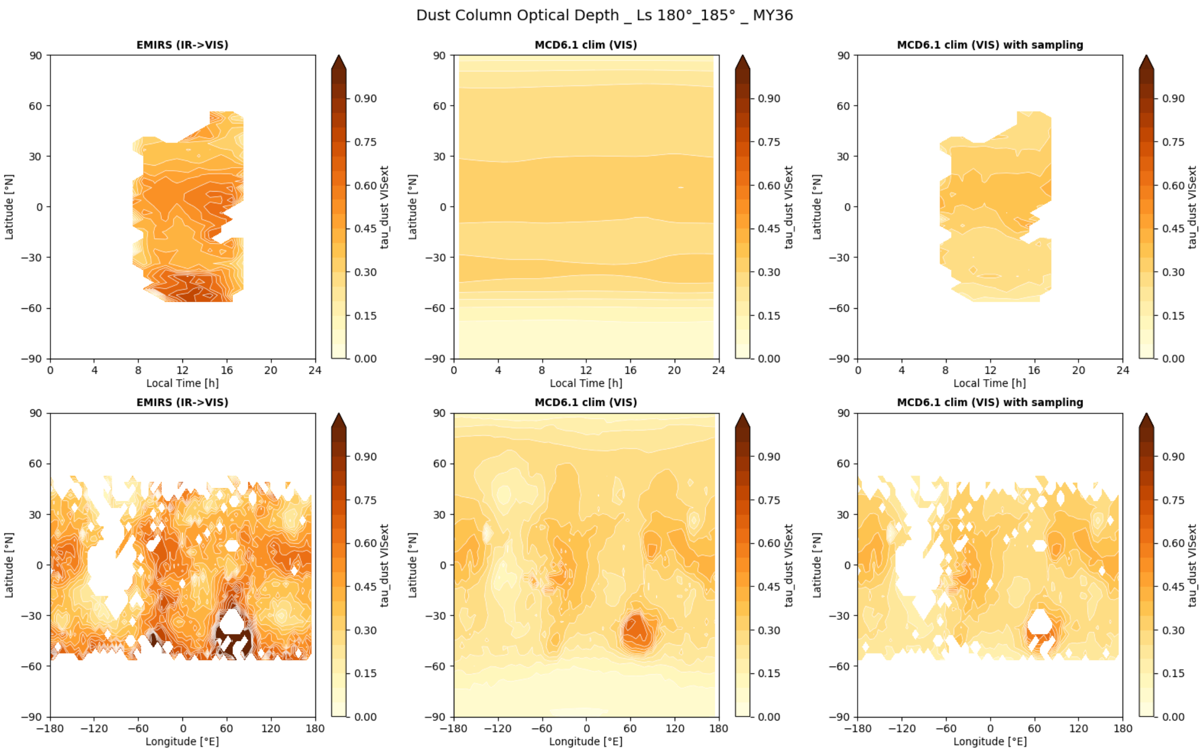

Figure 109: Zonal mean (first row) and diurnal mean (second row) of dust visible extinction column optical depth, L_s 180-185. EMIRS on the left, MCD6.1 without specific sampling in the middle and MCD6.1 with EMIRS sampling on the right.

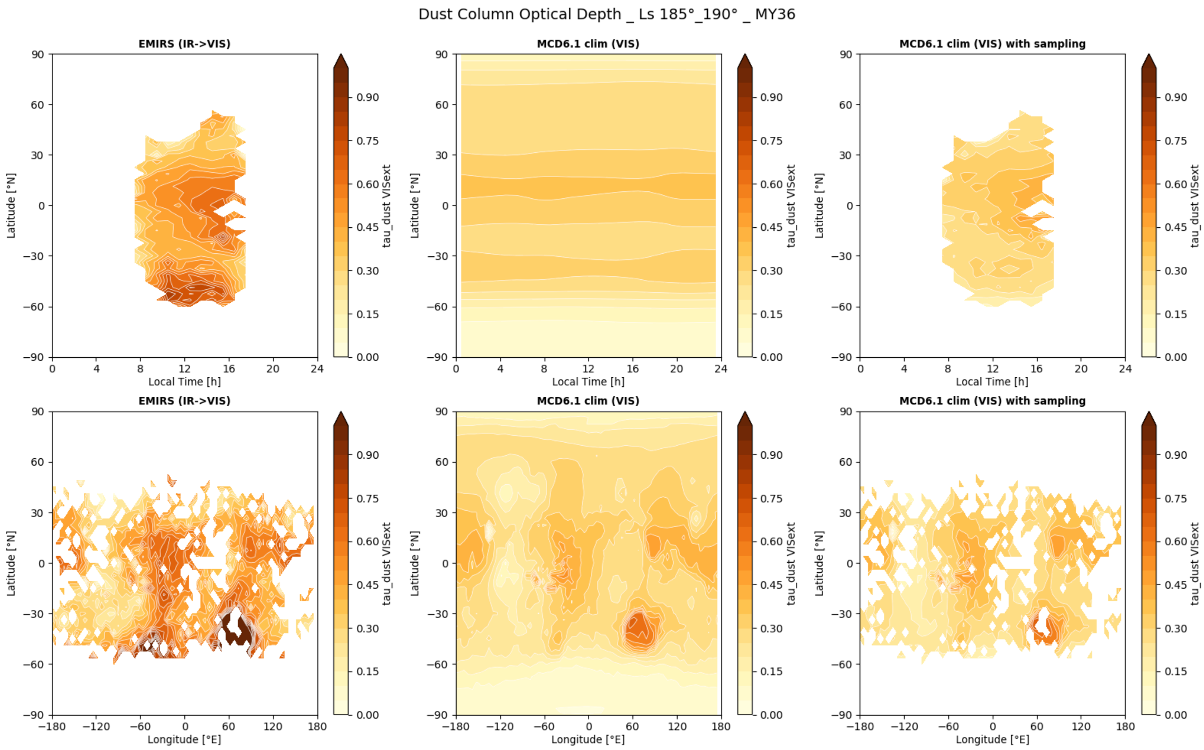

Figure 110: Zonal mean (first row) and diurnal mean (second row) of dust visible extinction column optical depth, L_s 185-190. EMIRS on the left, MCD6.1 without specific sampling in the middle and MCD6.1 with EMIRS sampling on the right.

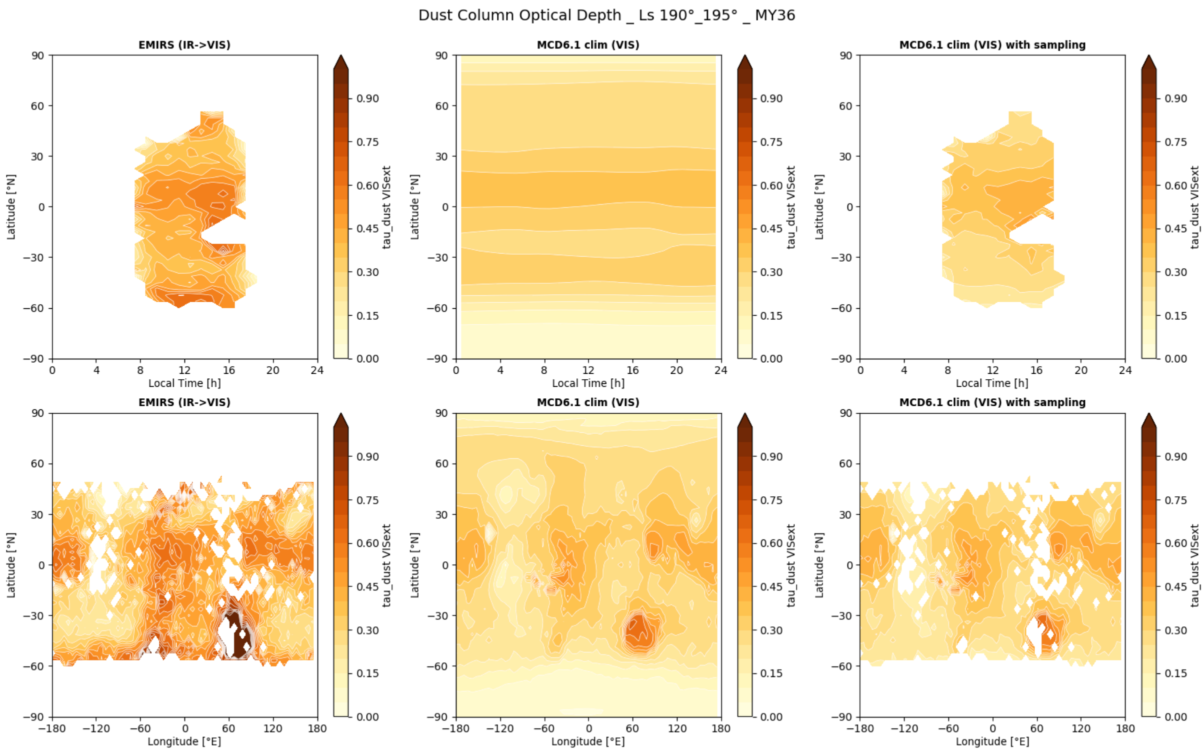

Figure 111: Zonal mean (first row) and diurnal mean (second row) of dust visible extinction column optical depth, L_s 190-195. EMIRS on the left, MCD6.1 without specific sampling in the middle and MCD6.1 with EMIRS sampling on the right.

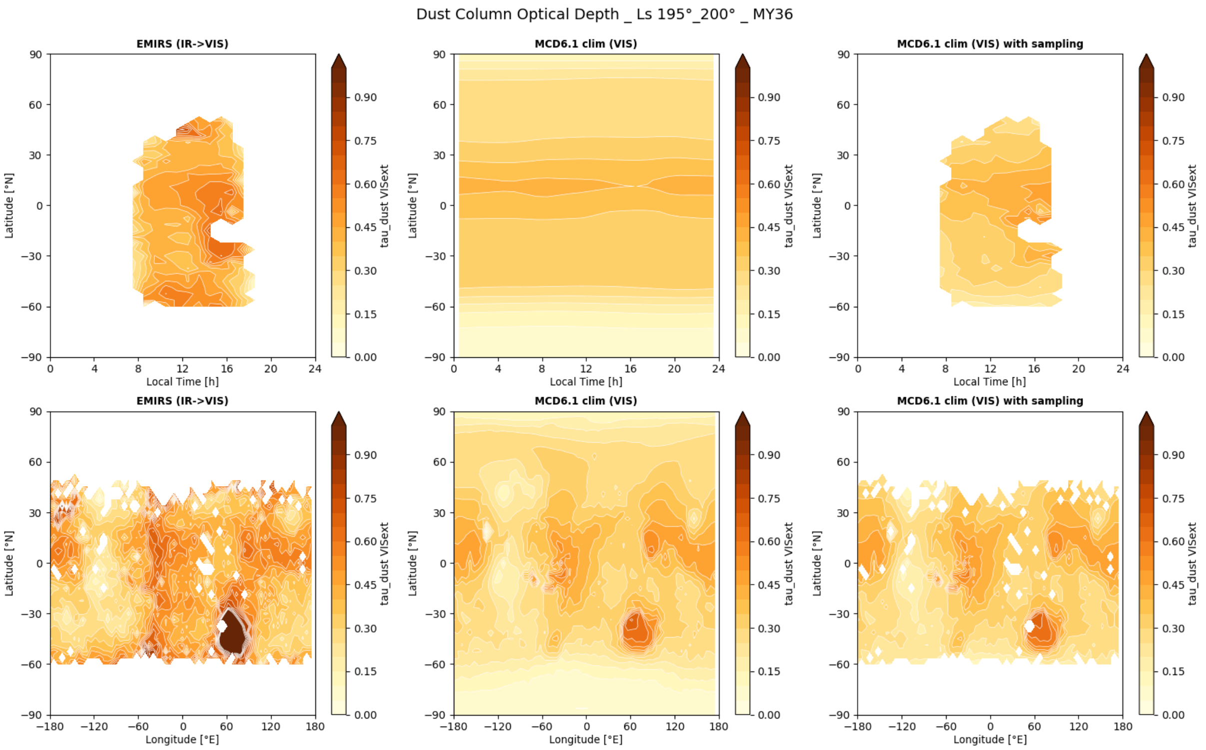

Figure 112: Zonal mean (first row) and diurnal mean (second row) of dust visible extinction column optical depth, L_s 195-200. EMIRS on the left, MCD6.1 without specific sampling in the middle and MCD6.1 with EMIRS sampling on the right.

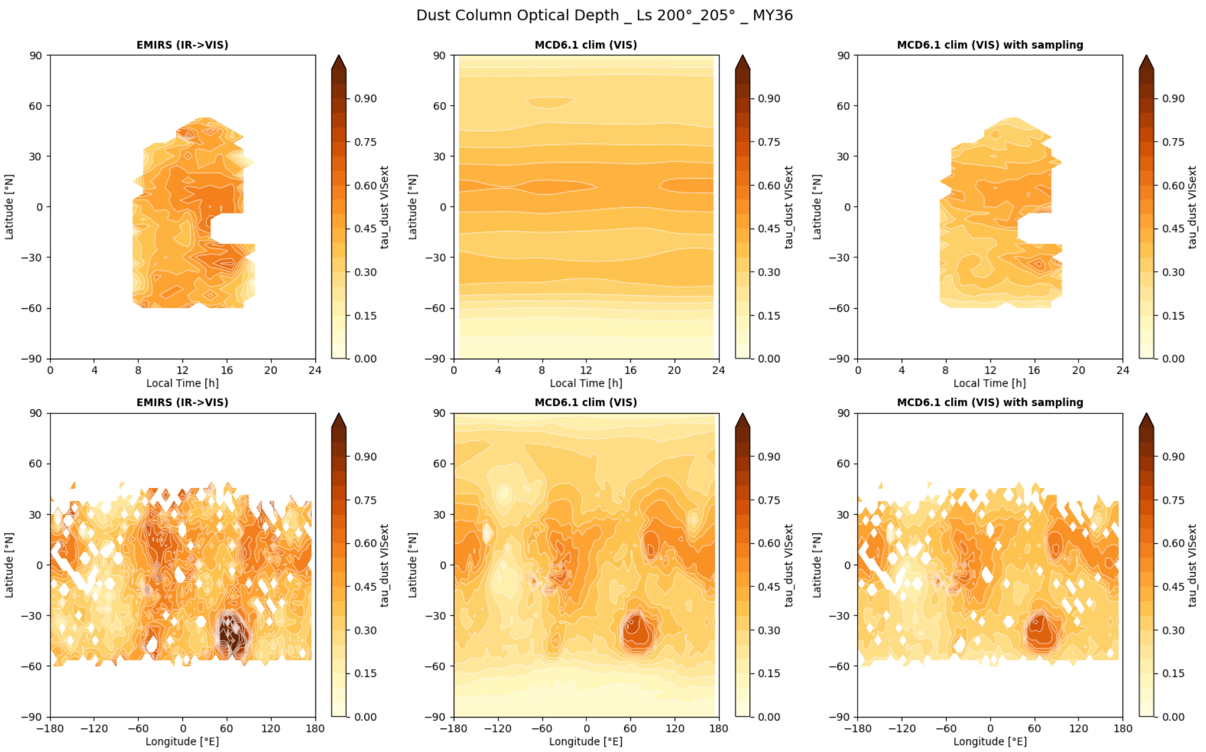

Figure 113: Zonal mean (first row) and diurnal mean (second row) of dust visible extinction column optical depth, L_s 200-205. EMIRS on the left, MCD6.1 without specific sampling in the middle and MCD6.1 with EMIRS sampling on the right.

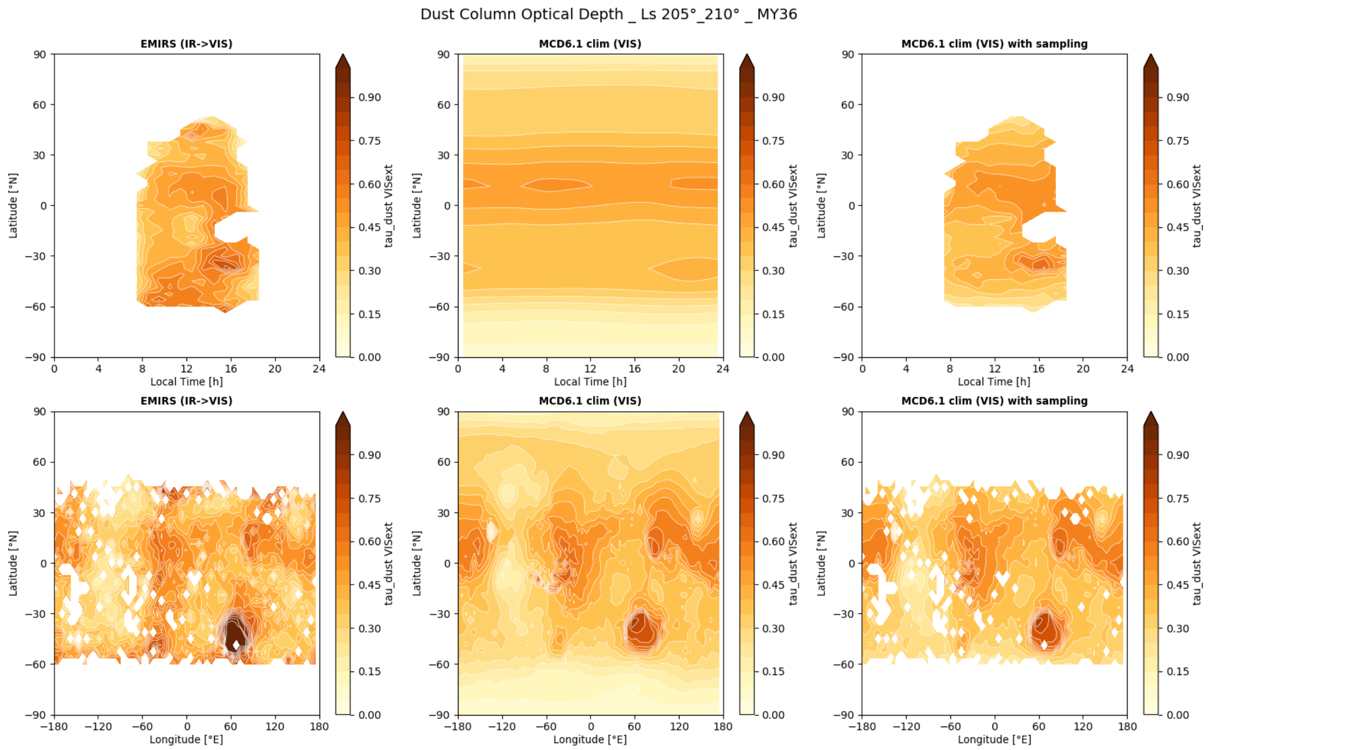

Figure 114: Zonal mean (first row) and diurnal mean (second row) of dust visible extinction column optical depth, L_s 205-210. EMIRS on the left, MCD6.1 without specific sampling in the middle and MCD6.1 with EMIRS sampling on the right.

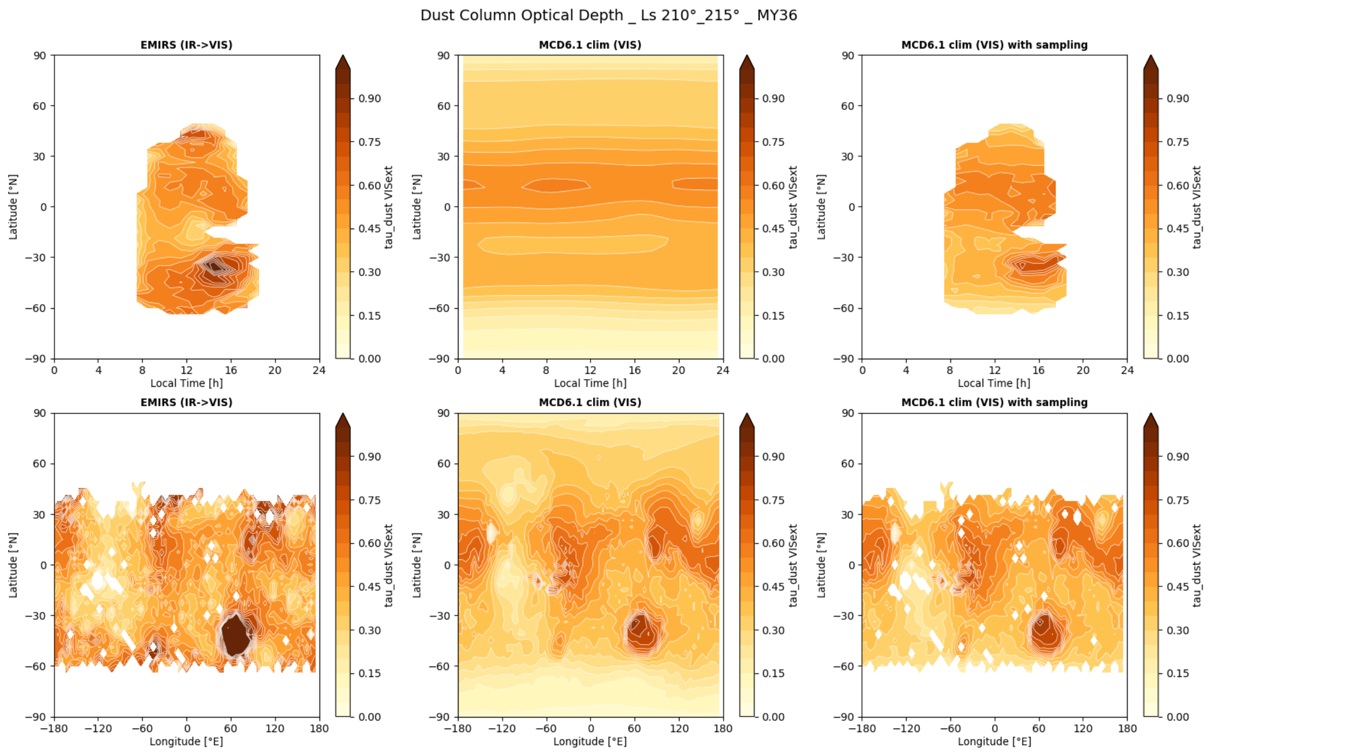

Figure 115: Zonal mean (first row) and diurnal mean (second row) of dust visible extinction column optical depth, L_s 210-215. EMIRS on the left, MCD6.1 without specific sampling in the middle and MCD6.1 with EMIRS sampling on the right.

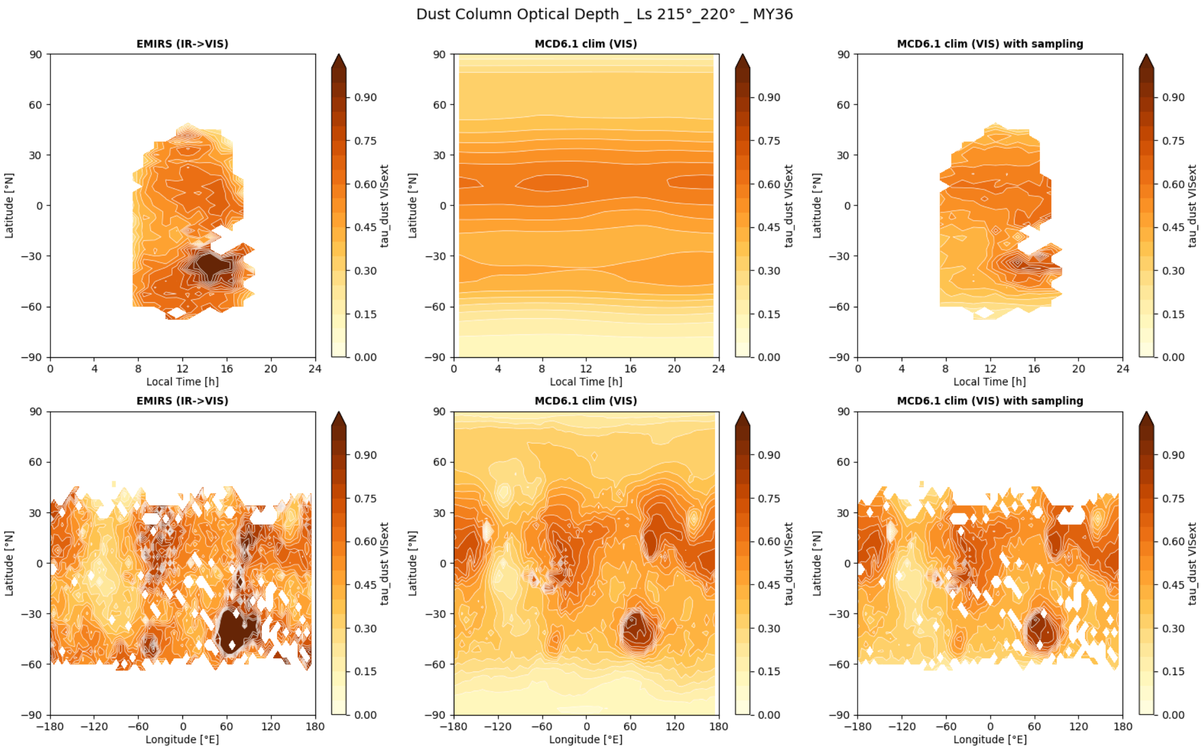

Figure 116: Zonal mean (first row) and diurnal mean (second row) of dust visible extinction column optical depth, L_s 215-220. EMIRS on the left, MCD6.1 without specific sampling in the middle and MCD6.1 with EMIRS sampling on the right.

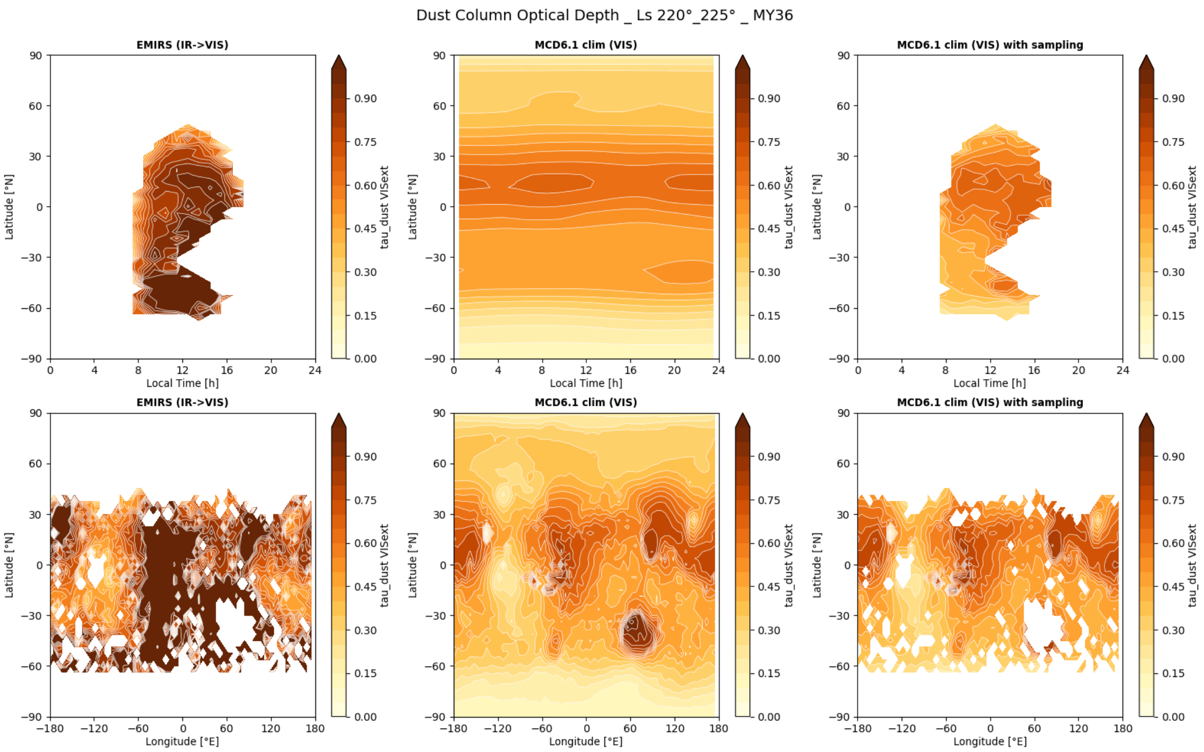

Figure 117: Zonal mean (first row) and diurnal mean (second row) of dust visible extinction column optical depth, L_s 220-225. EMIRS on the left, MCD6.1 without specific sampling in the middle and MCD6.1 with EMIRS sampling on the right.

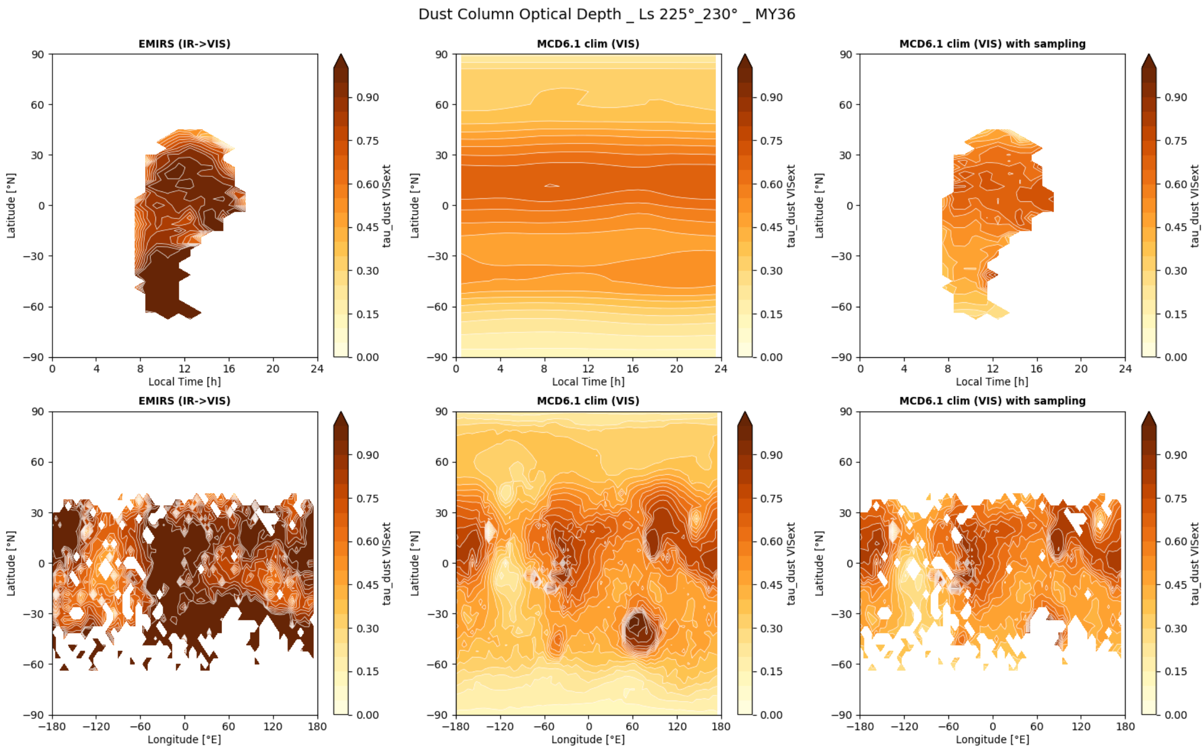

Figure 118: Zonal mean (first row) and diurnal mean (second row) of dust visible extinction column optical depth, L_s 225-230. EMIRS on the left, MCD6.1 without specific sampling in the middle and MCD6.1 with EMIRS sampling on the right.

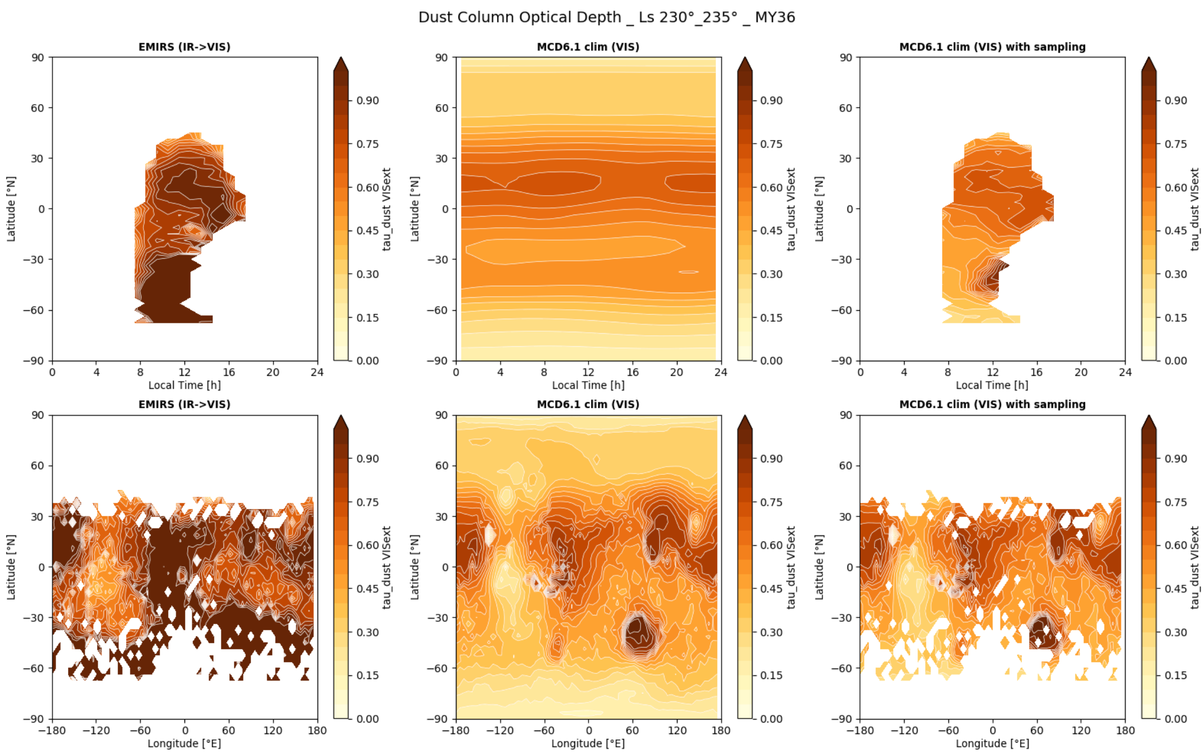

Figure 119: Zonal mean (first row) and diurnal mean (second row) of dust visible extinction column optical depth, L_s 230-235. EMIRS on the left, MCD6.1 without specific sampling in the middle and MCD6.1 with EMIRS sampling on the right.

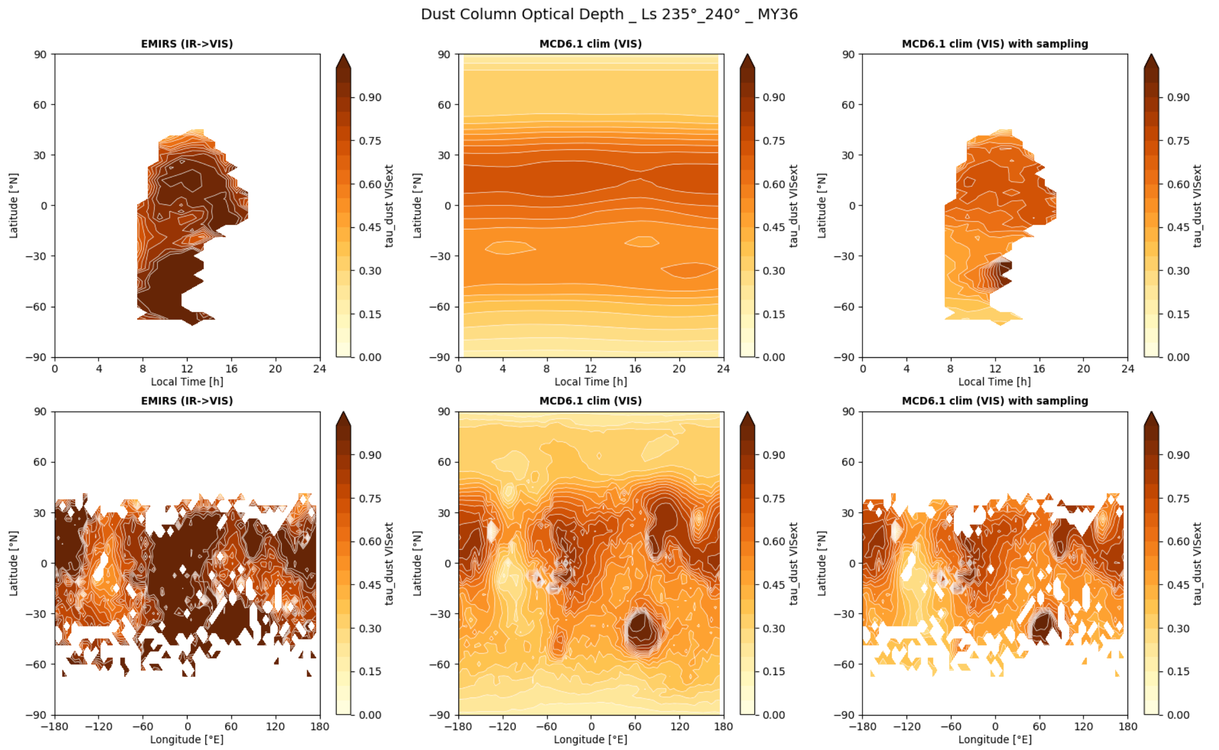

Figure 120: Zonal mean (first row) and diurnal mean (second row) of dust visible extinction column optical depth, L_s 235-240. EMIRS on the left, MCD6.1 without specific sampling in the middle and MCD6.1 with EMIRS sampling on the right.

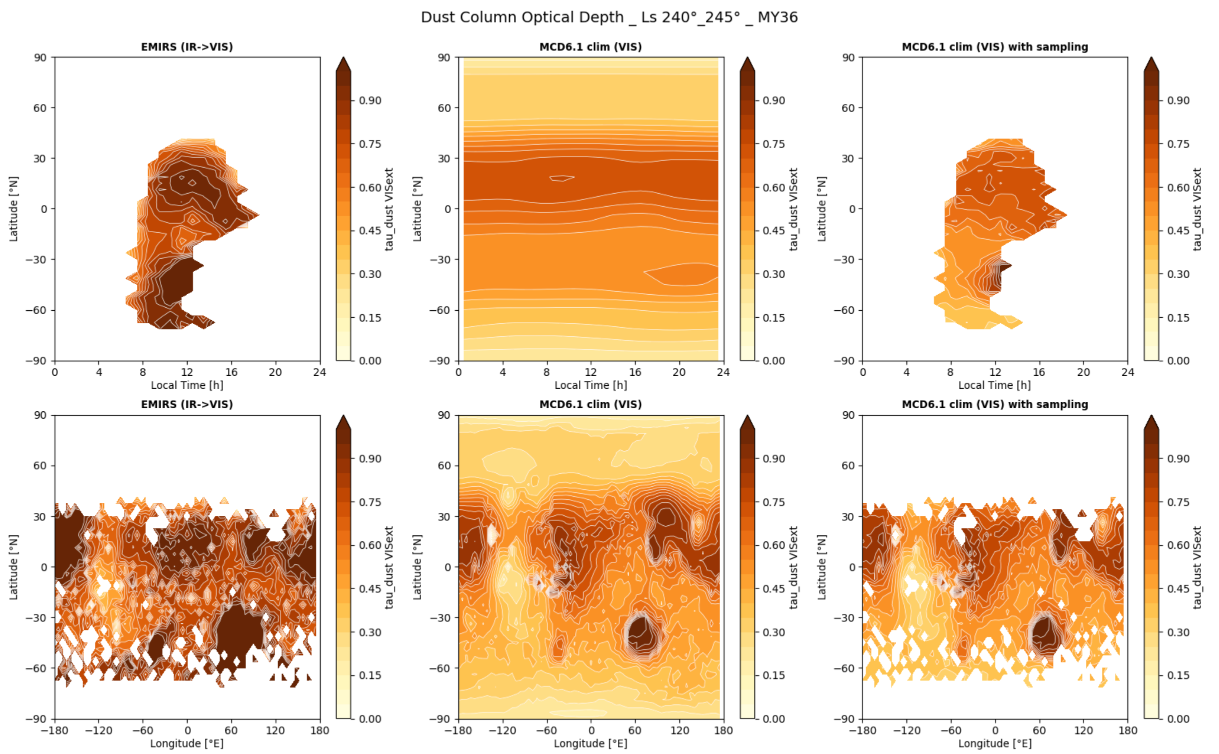

Figure 121: Zonal mean (first row) and diurnal mean (second row) of dust visible extinction column optical depth, L_s 240-245. EMIRS on the left, MCD6.1 without specific sampling in the middle and MCD6.1 with EMIRS sampling on the right.

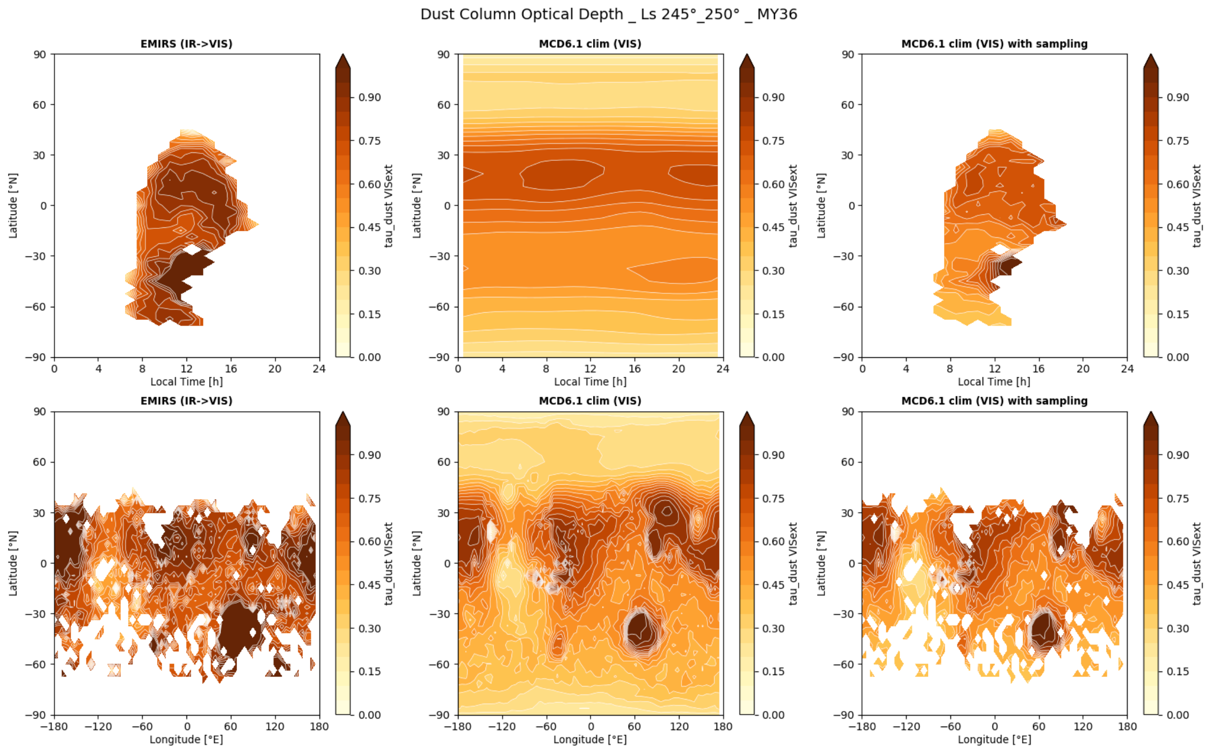

Figure 122: Zonal mean (first row) and diurnal mean (second row) of dust visible extinction column optical depth, L_s 245-250. EMIRS on the left, MCD6.1 without specific sampling in the middle and MCD6.1 with EMIRS sampling on the right.

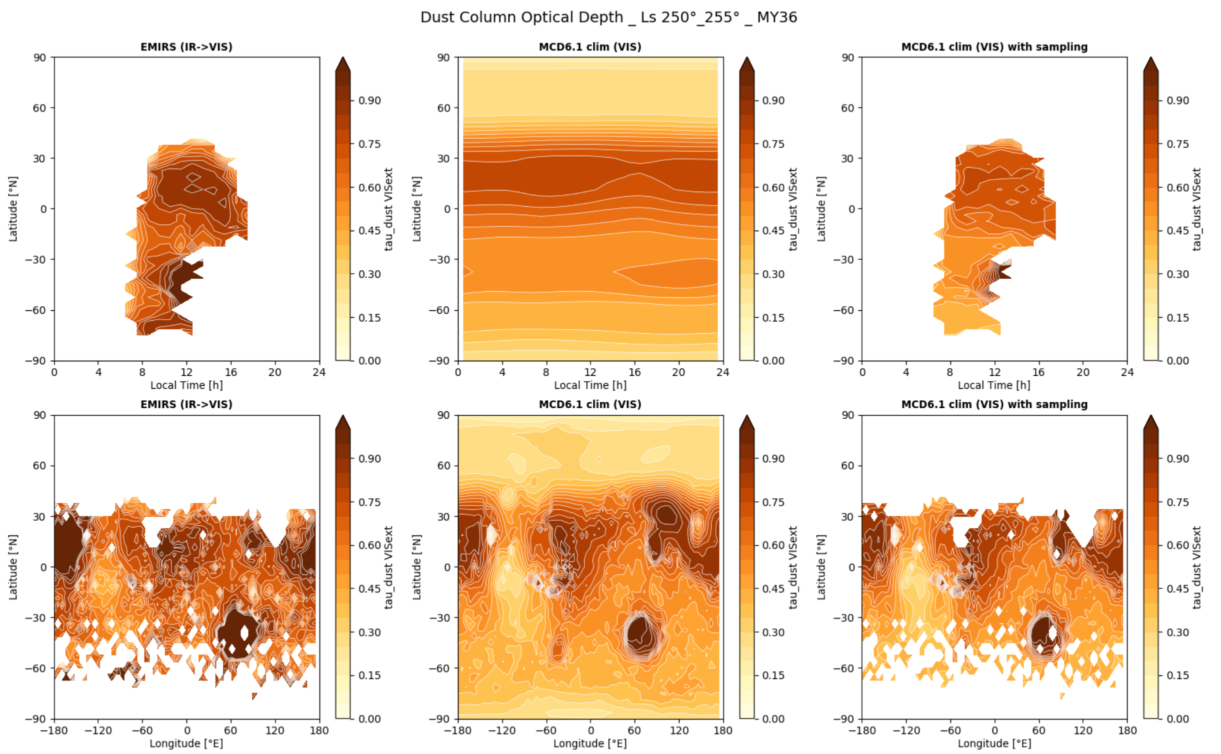

Figure 123: Zonal mean (first row) and diurnal mean (second row) of dust visible extinction column optical depth, L_s 250-255. EMIRS on the left, MCD6.1 without specific sampling in the middle and MCD6.1 with EMIRS sampling on the right.

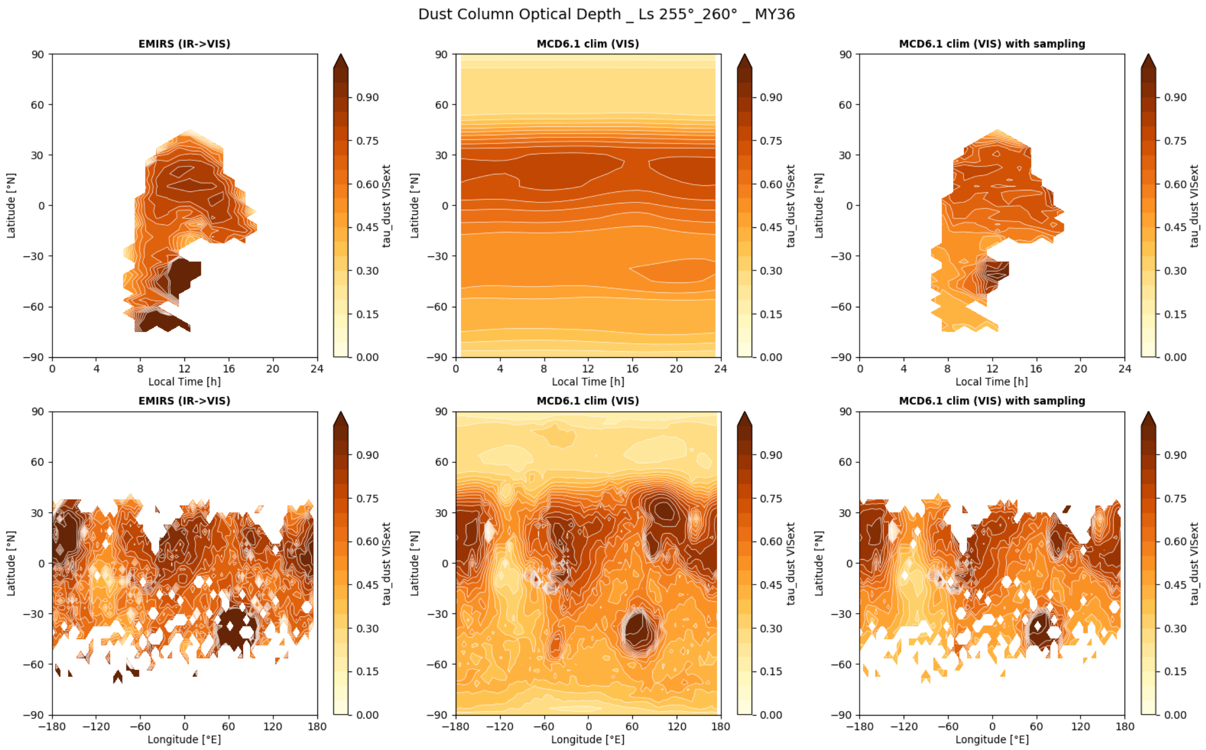

Figure 124: Zonal mean (first row) and diurnal mean (second row) of dust visible extinction column optical depth, L_s 255-260. EMIRS on the left, MCD6.1 without specific sampling in the middle and MCD6.1 with EMIRS sampling on the right.

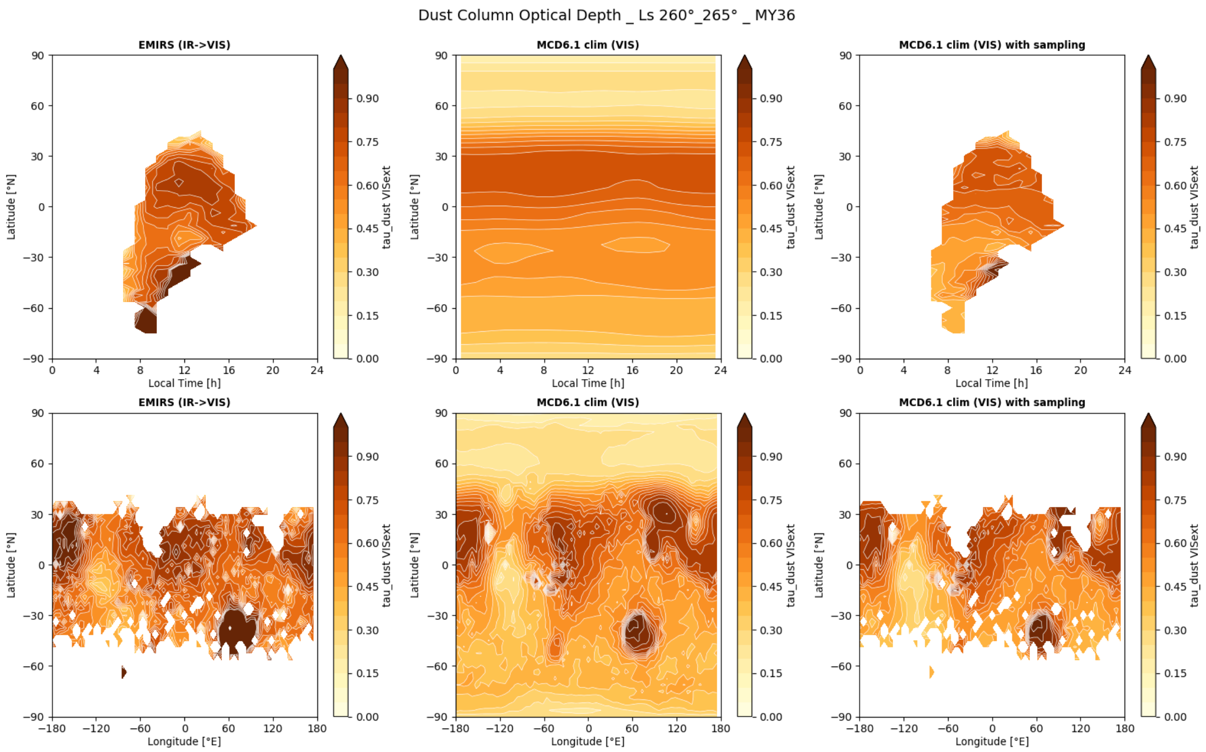

Figure 125: Zonal mean (first row) and diurnal mean (second row) of dust visible extinction column optical depth, L_s 260-265. EMIRS on the left, MCD6.1 without specific sampling in the middle and MCD6.1 with EMIRS sampling on the right.

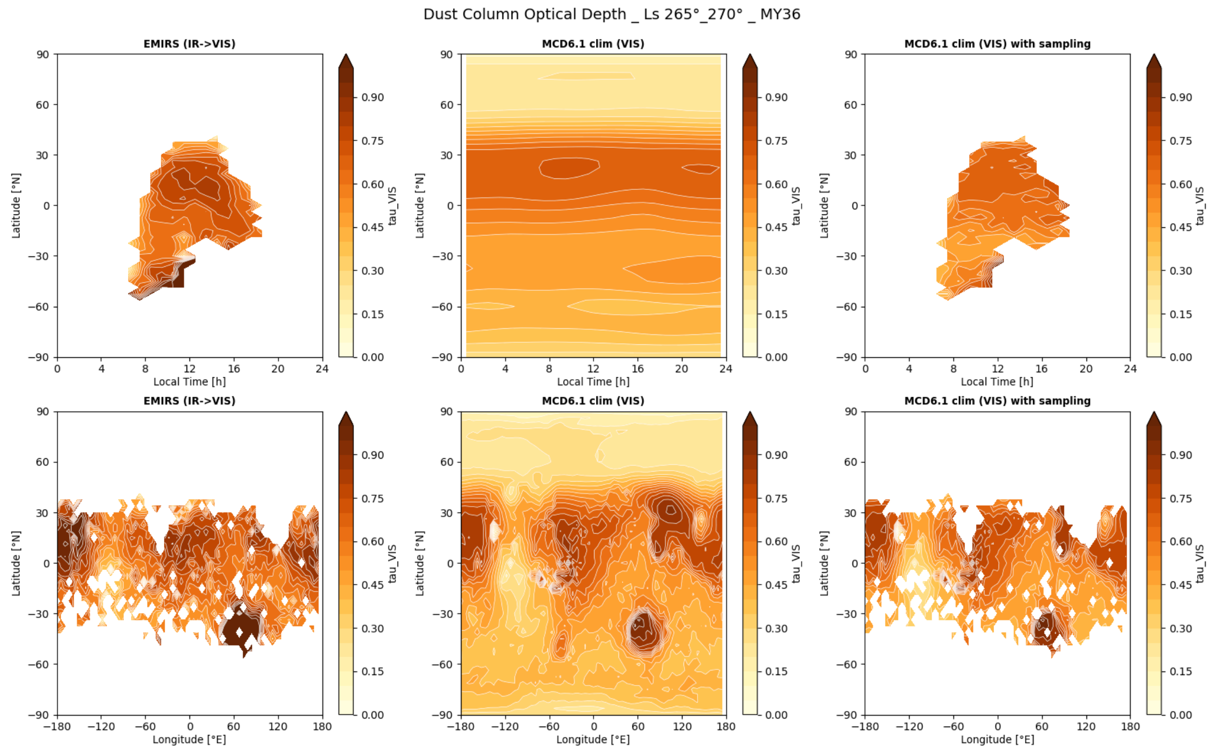

Figure 126: Zonal mean (first row) and diurnal mean (second row) of dust visible extinction column optical depth, L_s 265-270. EMIRS on the left, MCD6.1 without specific sampling in the middle and MCD6.1 with EMIRS sampling on the right.

7 Water vapor

7.1 TES

The MCD directly outputs the water vapor mass column in kg/m^2, that we convert in precipitable microns by dividing by $\rho_{liq} = 1000kg/m^3$ and multiplying by 10^6 before comparing to TES 2pm water vapor column.

Overall, the MCD is slightly drier than the observations, as shown by the seasonal maps on Figure 127 or the annual planetary distributions of the differences on Figure 128. Despite having a strong sublimation peak at the Northern summer, the MCD does not maintain a sufficient humidity in the tropics during the second part of the year, and the dimmer Southern summer sublimation does not compensate for this lack of water vapor.

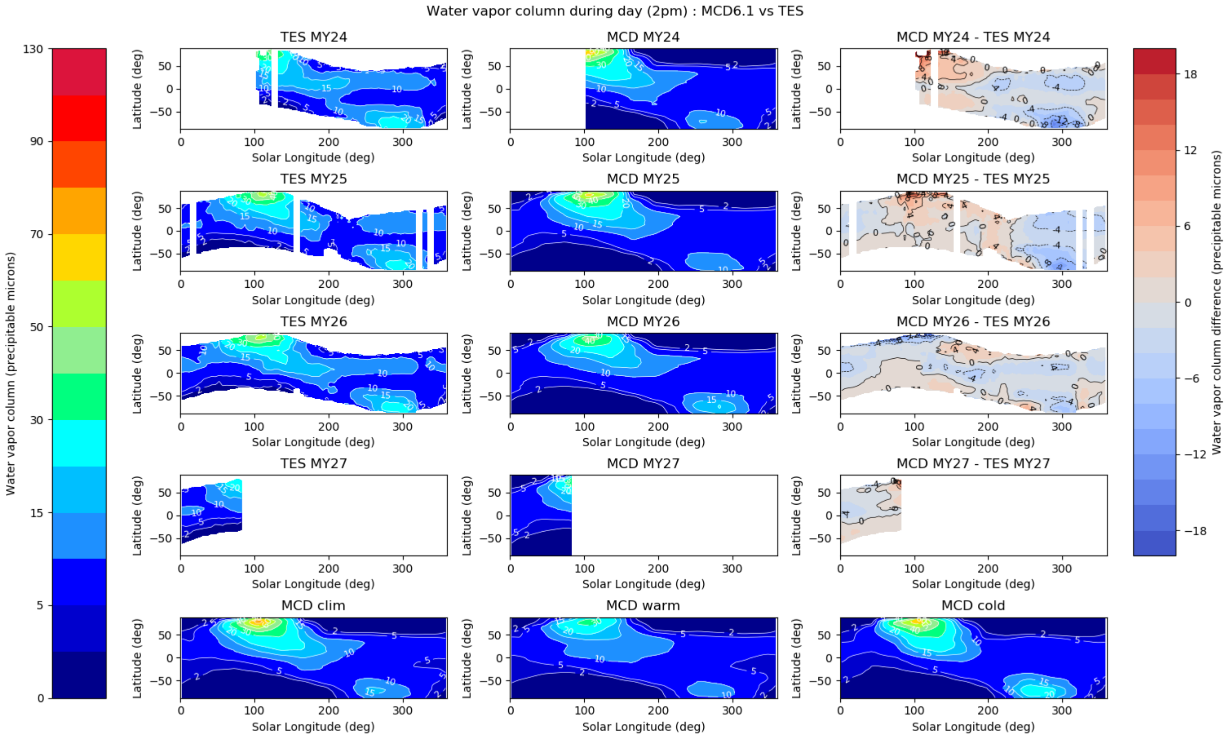

Figure 127: Zonal water vapor column over solar longitude from MY24 to MY27 (first four lines), at 2 pm (local solar time). Left : TES data. Middle : MCD data. Right : Difference MCD-TES. Last line shows clim, warm and cold scenarios.

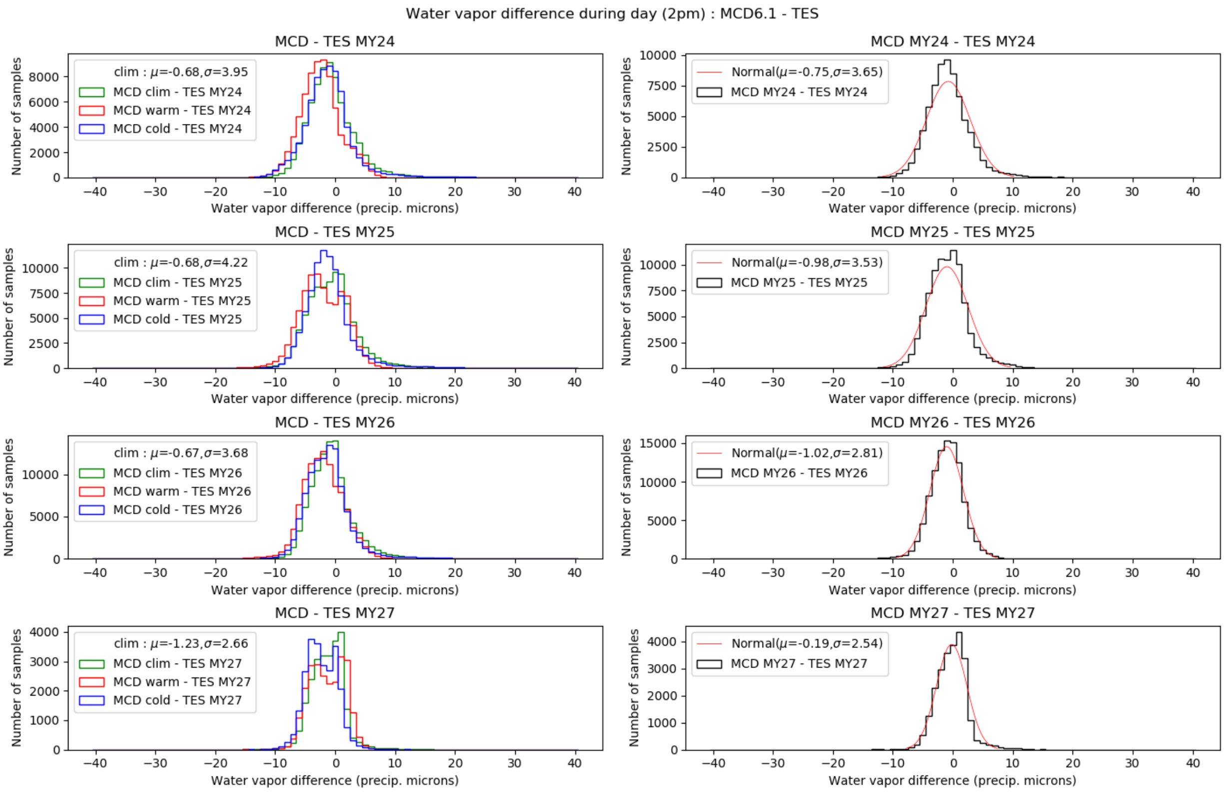

Figure 128: Distribution of water vapor column differences between MCD v6.1 and TES using bins of 1 precip. microns from MY24 to MY27 (from top to bottom), at 2 pm (local solar time) in latitudes (-50,50). Left : TES compared with MCD for clim, warm and cold scenarios. Right : TES compared with MCD for specific MY scenario. The red curve on the right represents normal distributions of same mean and standard deviation.

8 Water ice

The MCD outputs the atmospheric water ice content as a mass column $q_{ice,MCD}$ in kg/m^2. Both TES and EMIRS instruments measure water ice column optical depth in infrared absorption. We thus use the following equation to convert the MCD ice mass into opacity :

$$\tau_{ice,MCD} = \frac{3Q_{abs}}{4r_{eff}\rho_{ice}} q_{ice,MCD} \tag{1}$$

assuming $\rho_{ice} = 920kg/m^3$, and an effective radius $r_{eff} = 5\mu m$ for the ice particles, which corresponds to $Q_{abs} = 1.29$.

8.1 TES

TES measures the water ice clouds optical depth at 2pm, when they are the dimmest, and covers the aphelion cloud belt and the very low edges of the polar nights. The MCD has around 10% less clouds than TES in annual average, as shown on Figure 130. The MCD displays a thicker aphelion cloud belt than the observations near the equator, but present almost none of the thin, sparse, low latitude clouds over the rest of the year.

In the Northern summer, the MCD displays no apparent pause in the polar hood coverage, unlike what TES sees. This presence of clouds is once again due to temporal interpolation in the MCD, which does not appear in the Mars PCM on which the MCD is based on (e.g. Navarro et al. [2014]).

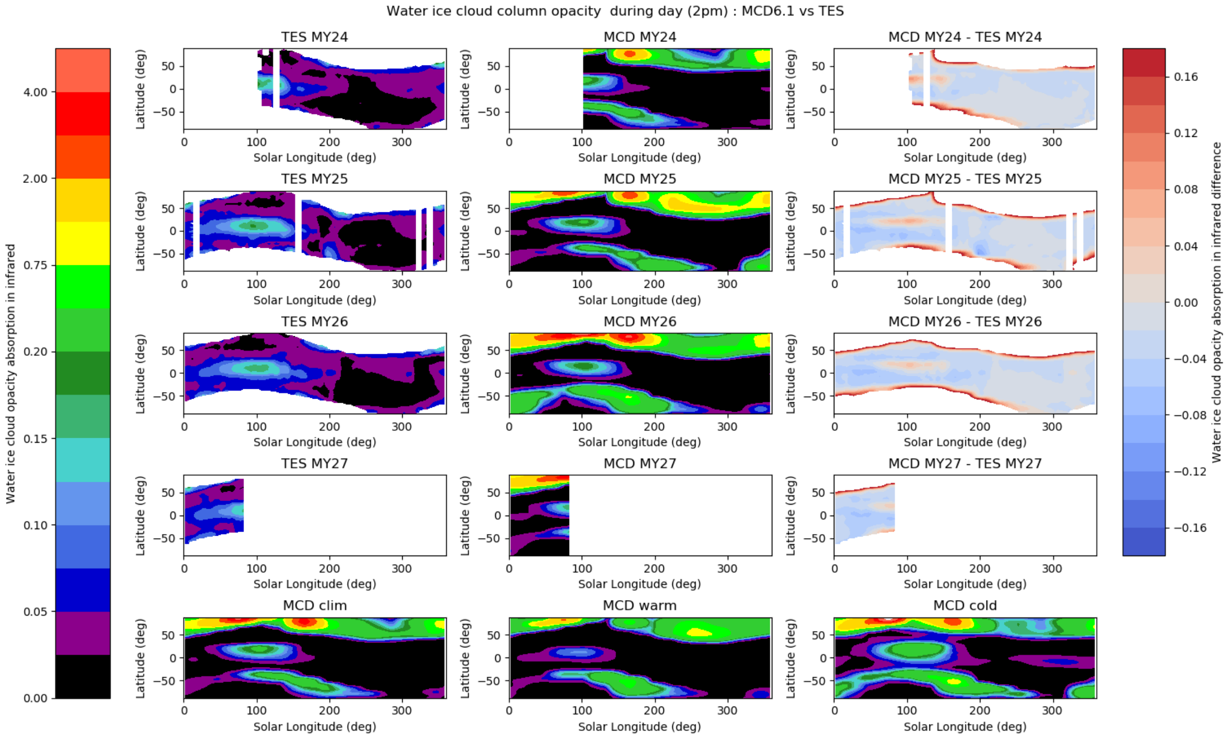

Figure 129: Zonal water ice opacity column over solar longitude from MY24 to MY27 (first four lines), at 2 pm (local solar time). Left : TES data. Middle : MCD data. Right : Difference MCD-TES. Last line shows clim, warm and cold scenarios.

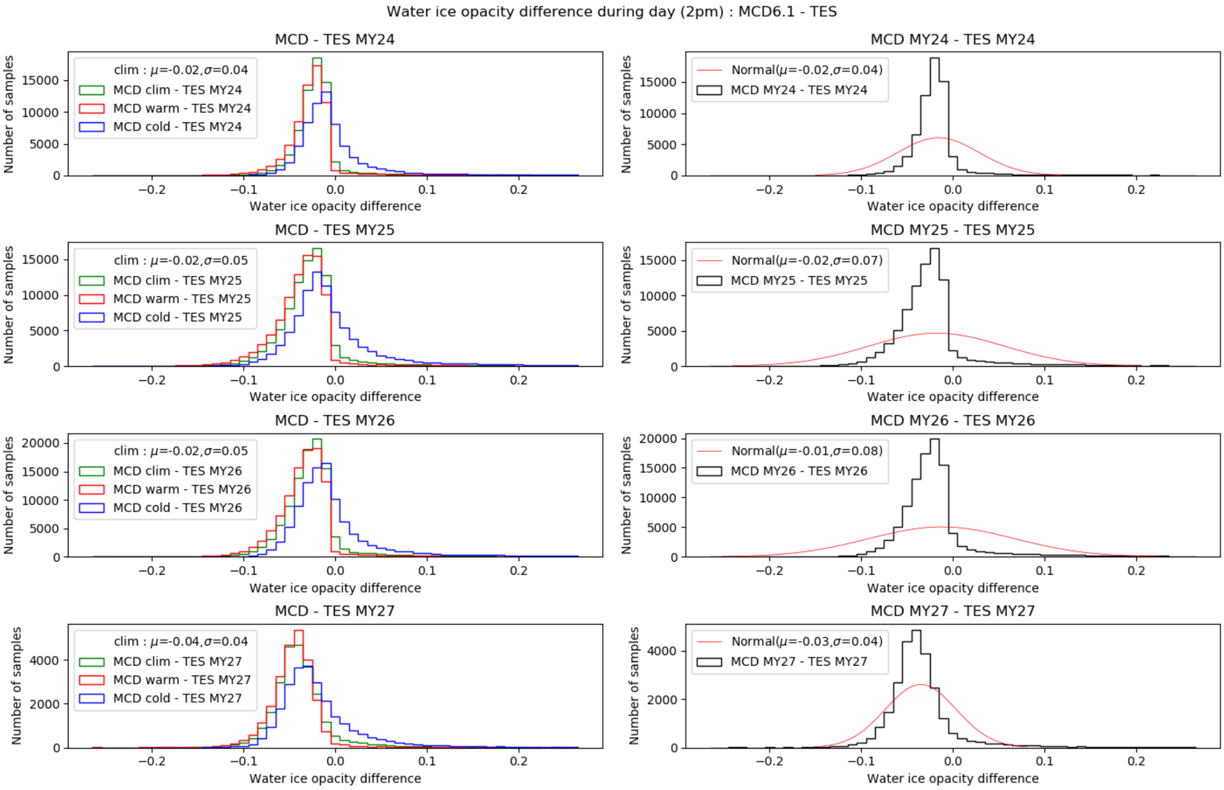

Figure 130: Distribution of water ice opacity column differences between MCD v6.1 and TES using bins of 0.01 from MY24 to MY27 (from top to bottom), at 2 pm (local solar time) in latitudes (-50,50). Left : TES compared with MCD for clim, warm and cold scenarios. Right : TES compared with MCD for specific MY scenario. The red curve on the right represents normal distributions of same mean and standard deviation.

8.2 EMIRS

There is no MCD scenario that covers the Mars Year 36 during which EMIRS made its observations. We thus use the clim scenario for the comparison.

The overall zonal and diurnal structure is well reproduced by the MCD sampled like EMIRS during the first part of the year. Cloud content peaks around terminators while decreasing during daytime. The longitudinal distribution highlights several cloudy regions, such as Tharsis, Utopia Planitia, Argyre and Hellas bassins.

Like TES though, the MCD misses the sparse clouds that appear outside of these regions and during the second part of the year.

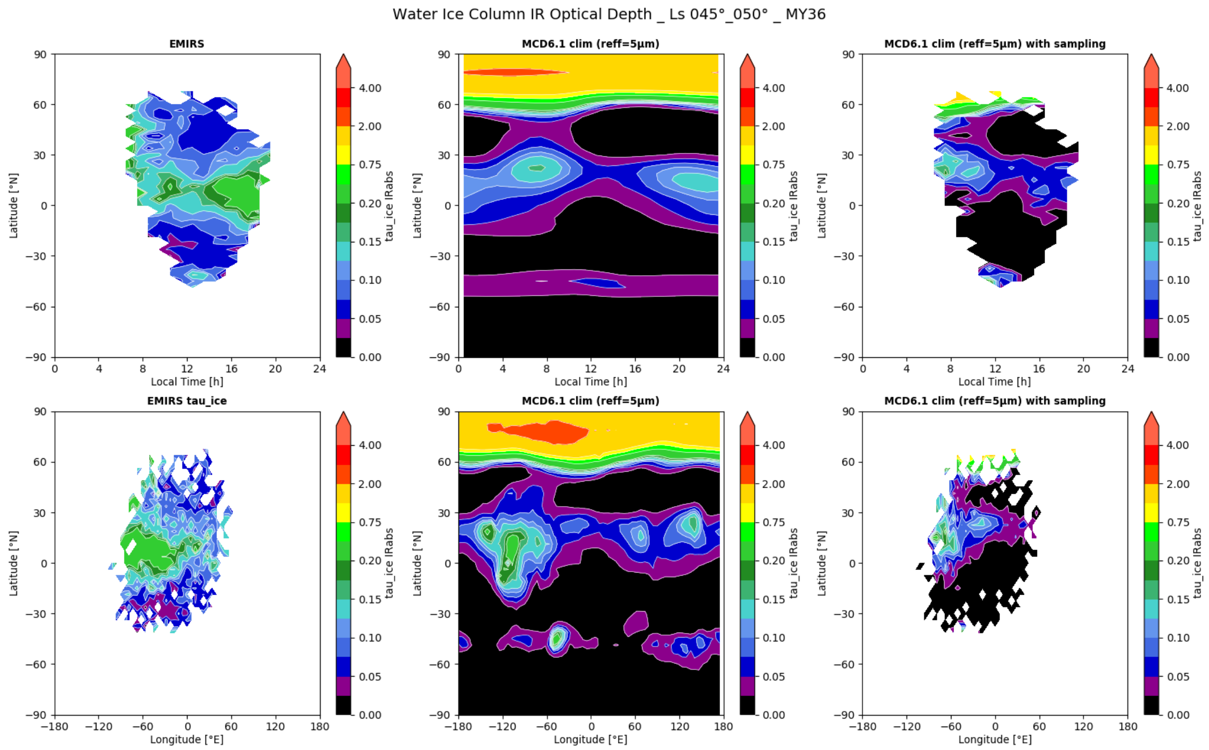

Figure 131: Zonal mean (first row) and diurnal mean (second row) of water ice infrared absorption column optical depth, L_s 45-50. EMIRS on the left, MCD6.1 without specific sampling in the middle and MCD6.1 with EMIRS sampling on the right.

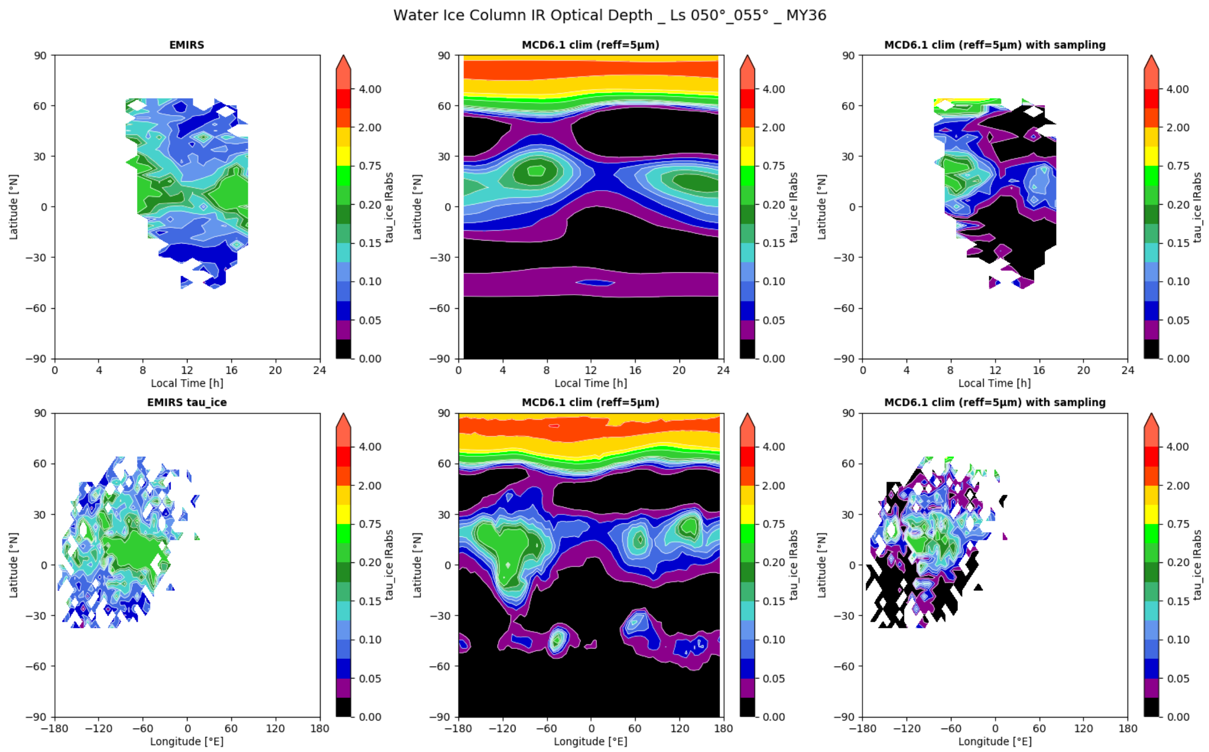

Figure 132: Zonal mean (first row) and diurnal mean (second row) of water ice infrared absorption column optical depth, L_s 50-55. EMIRS on the left, MCD6.1 without specific sampling in the middle and MCD6.1 with EMIRS sampling on the right.

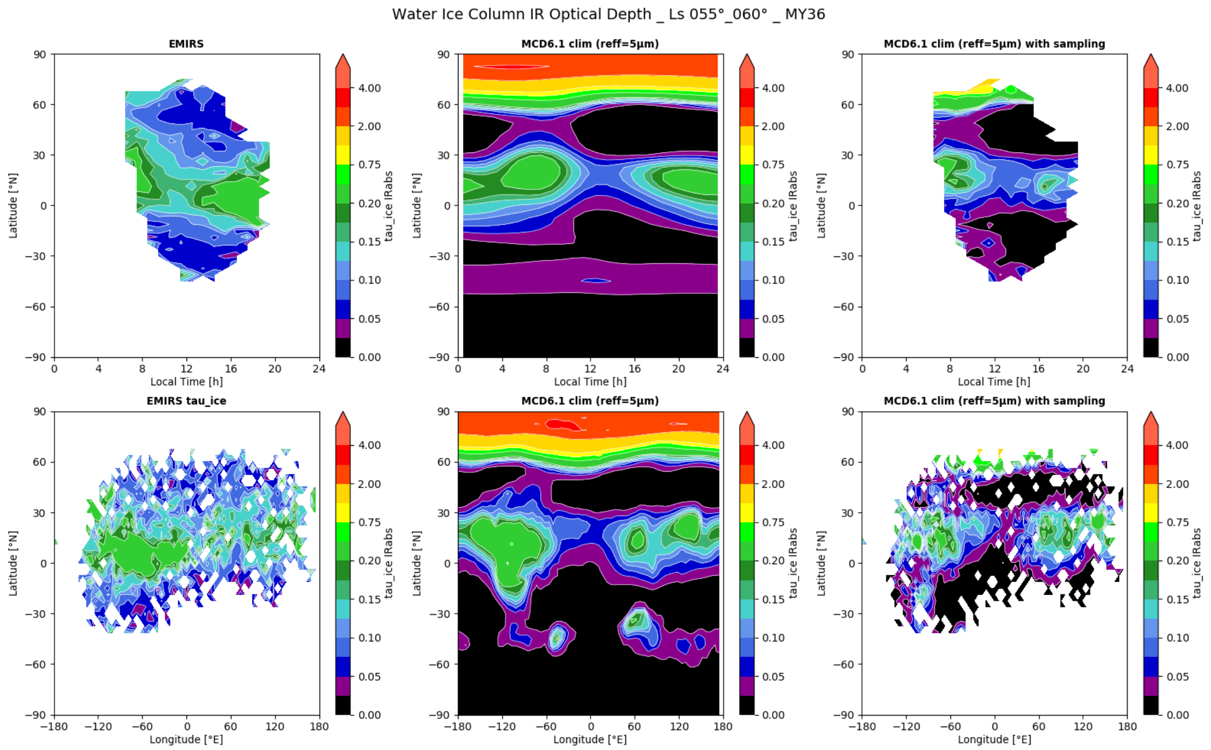

Figure 133: Zonal mean (first row) and diurnal mean (second row) of water ice infrared absorption column optical depth, L_s 55-60. EMIRS on the left, MCD6.1 without specific sampling in the middle and MCD6.1 with EMIRS sampling on the right.

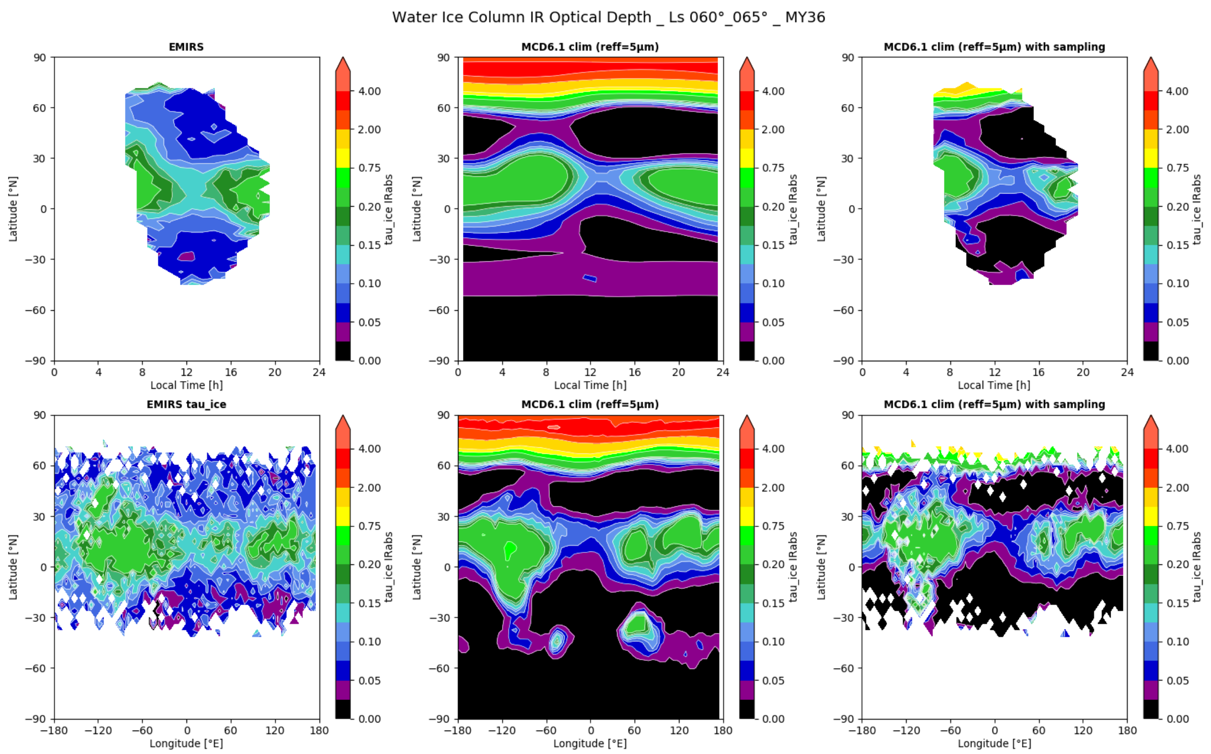

Figure 134: Zonal mean (first row) and diurnal mean (second row) of water ice infrared absorption column optical depth, L_s 60-65. EMIRS on the left, MCD6.1 without specific sampling in the middle and MCD6.1 with EMIRS sampling on the right.

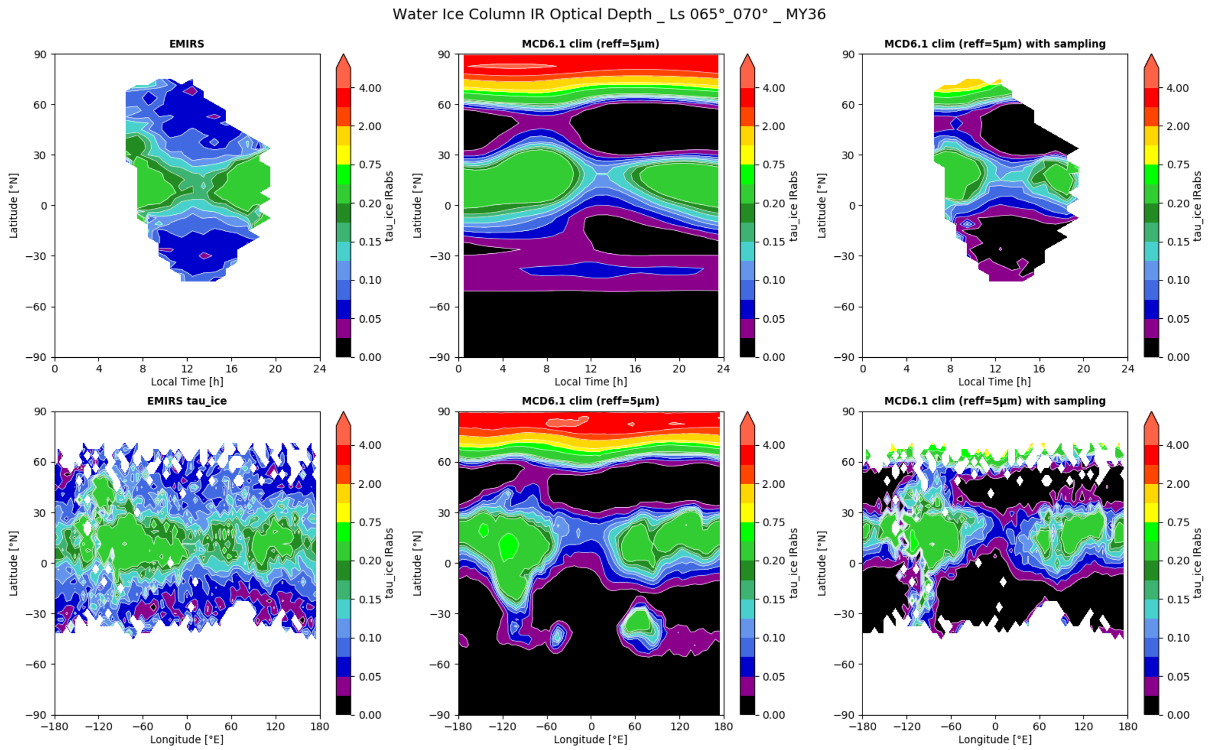

Figure 135: Zonal mean (first row) and diurnal mean (second row) of water ice infrared absorption column optical depth, L_s 65-70. EMIRS on the left, MCD6.1 without specific sampling in the middle and MCD6.1 with EMIRS sampling on the right.

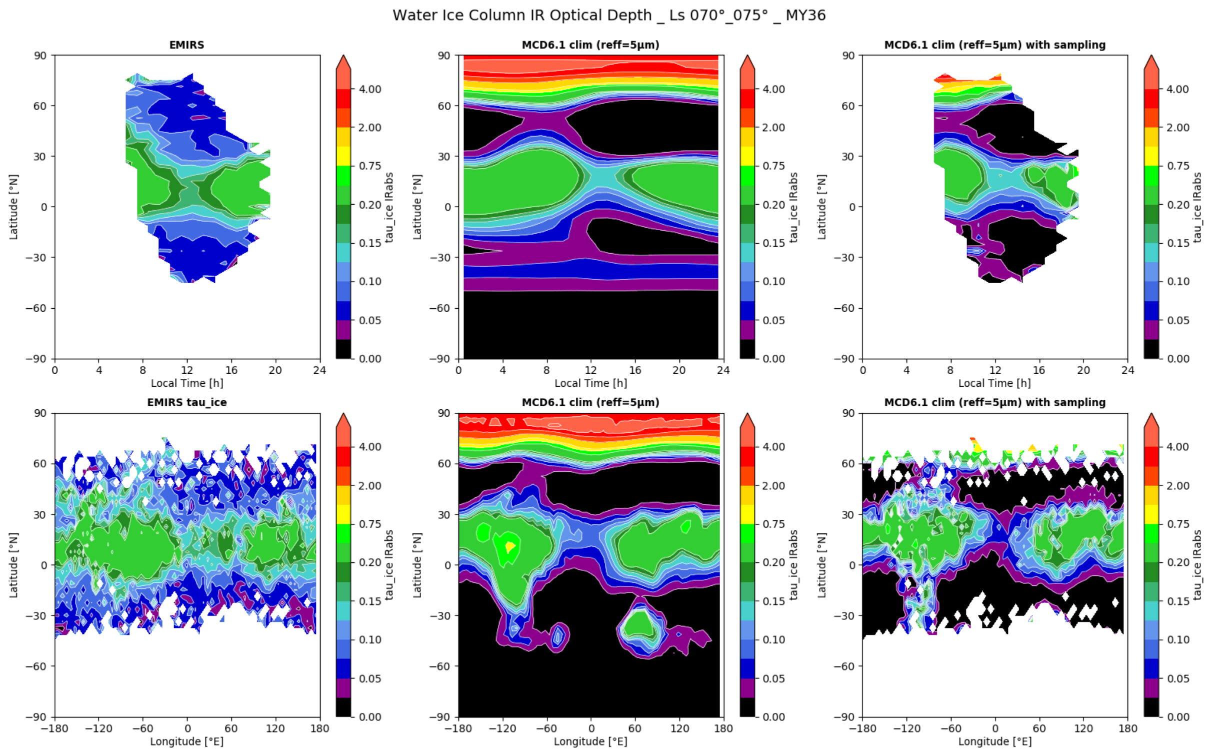

Figure 136: Zonal mean (first row) and diurnal mean (second row) of water ice infrared absorption column optical depth, L_s 70-75. EMIRS on the left, MCD6.1 without specific sampling in the middle and MCD6.1 with EMIRS sampling on the right.

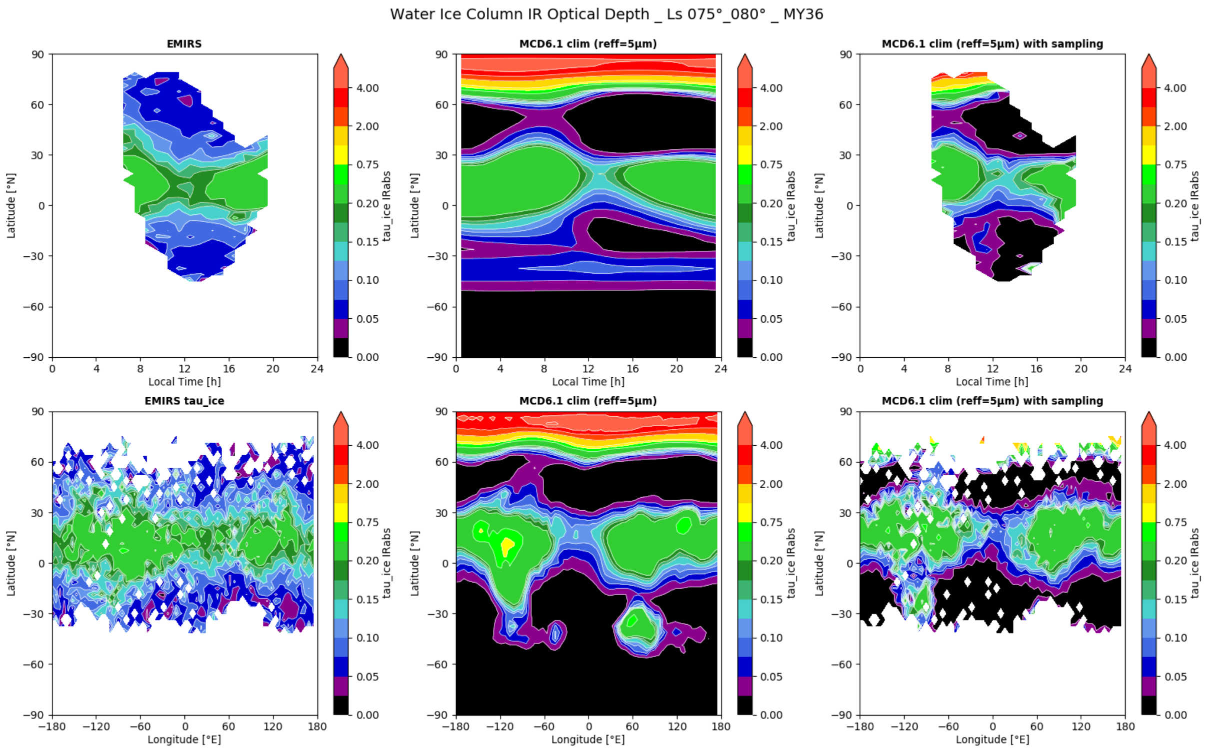

Figure 137: Zonal mean (first row) and diurnal mean (second row) of water ice infrared absorption column optical depth, L_s 75-80. EMIRS on the left, MCD6.1 without specific sampling in the middle and MCD6.1 with EMIRS sampling on the right.

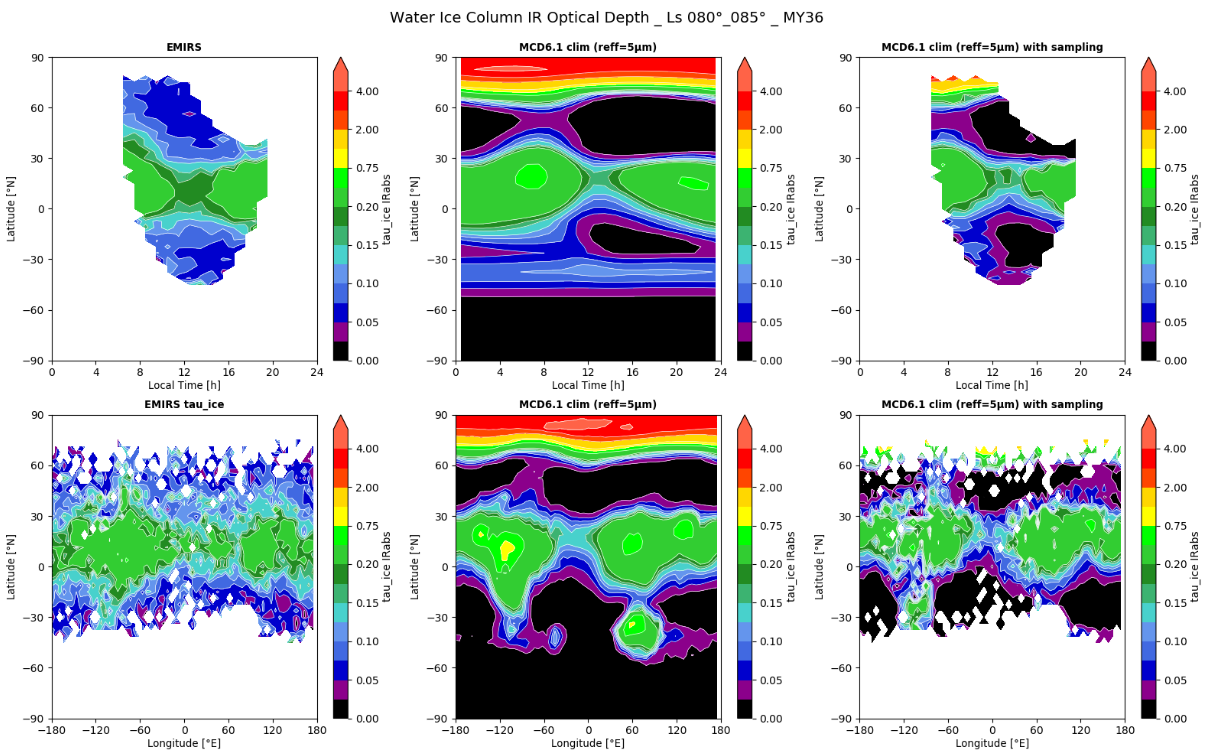

Figure 138: Zonal mean (first row) and diurnal mean (second row) of water ice infrared absorption column optical depth, L_s 80-85. EMIRS on the left, MCD6.1 without specific sampling in the middle and MCD6.1 with EMIRS sampling on the right.

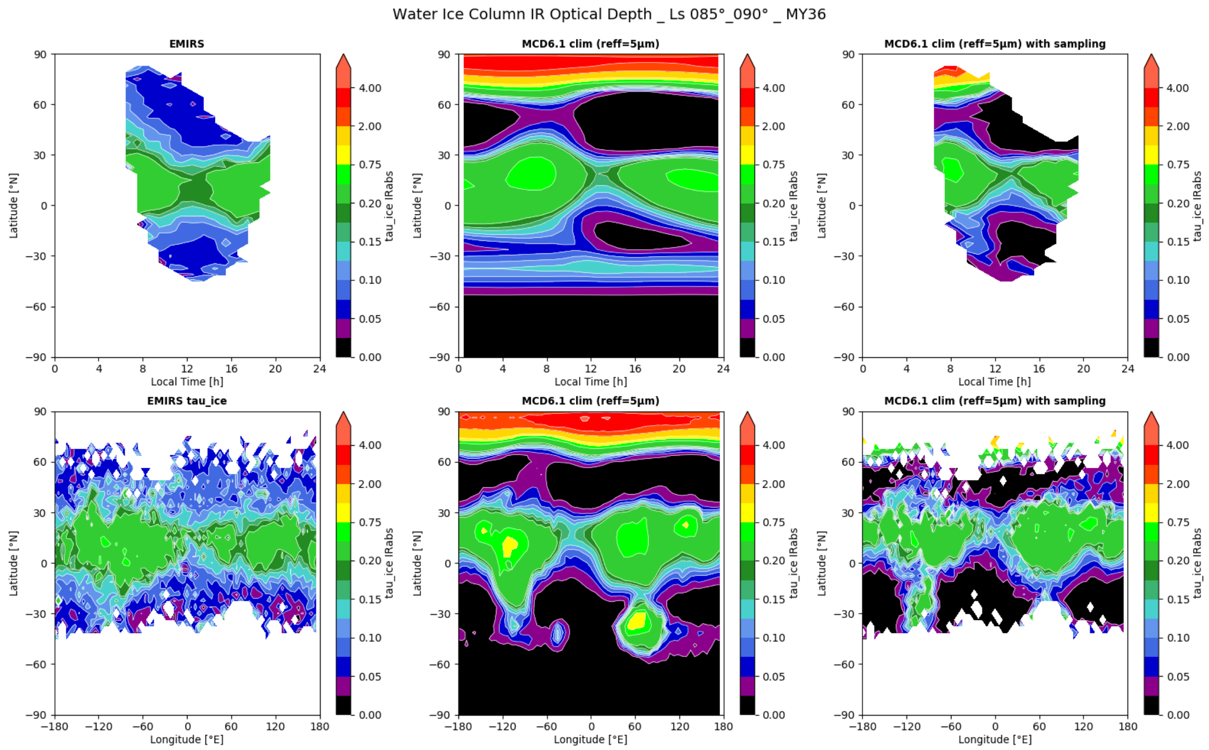

Figure 139: Zonal mean (first row) and diurnal mean (second row) of water ice infrared absorption column optical depth, L_s 85-90. EMIRS on the left, MCD6.1 without specific sampling in the middle and MCD6.1 with EMIRS sampling on the right.

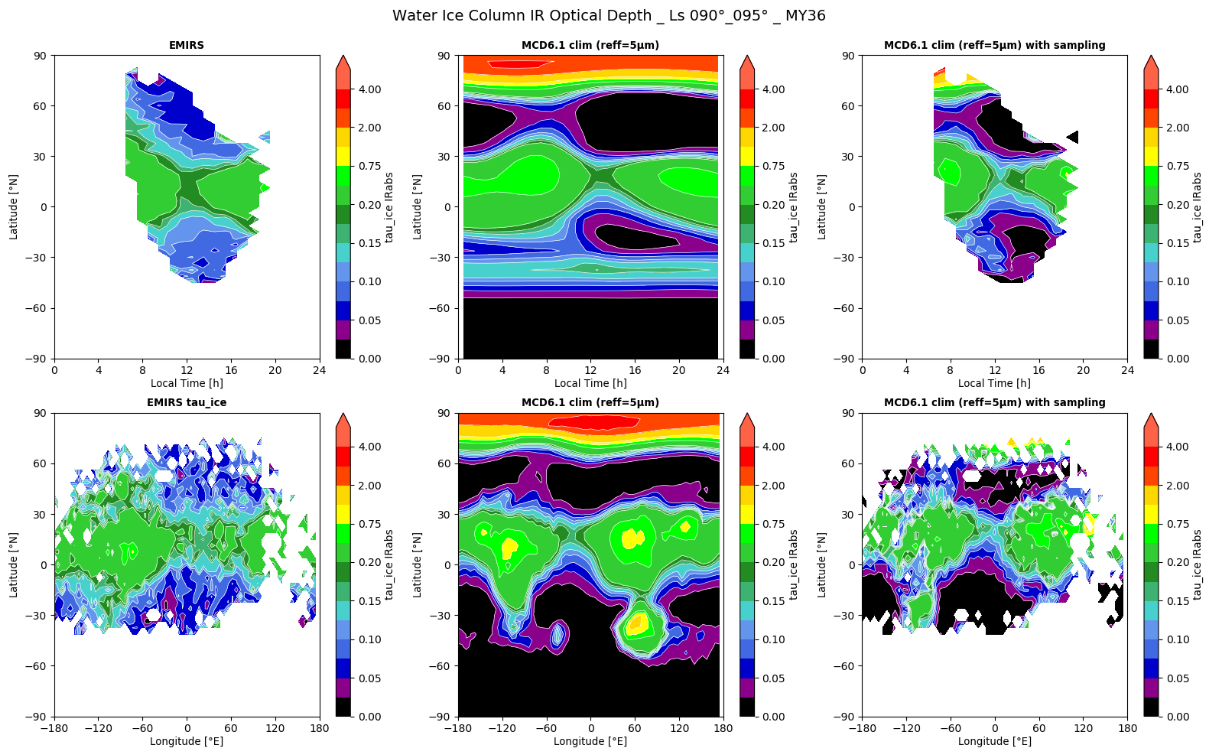

Figure 140: Zonal mean (first row) and diurnal mean (second row) of water ice infrared absorption column optical depth, L_s 90-95. EMIRS on the left, MCD6.1 without specific sampling in the middle and MCD6.1 with EMIRS sampling on the right.

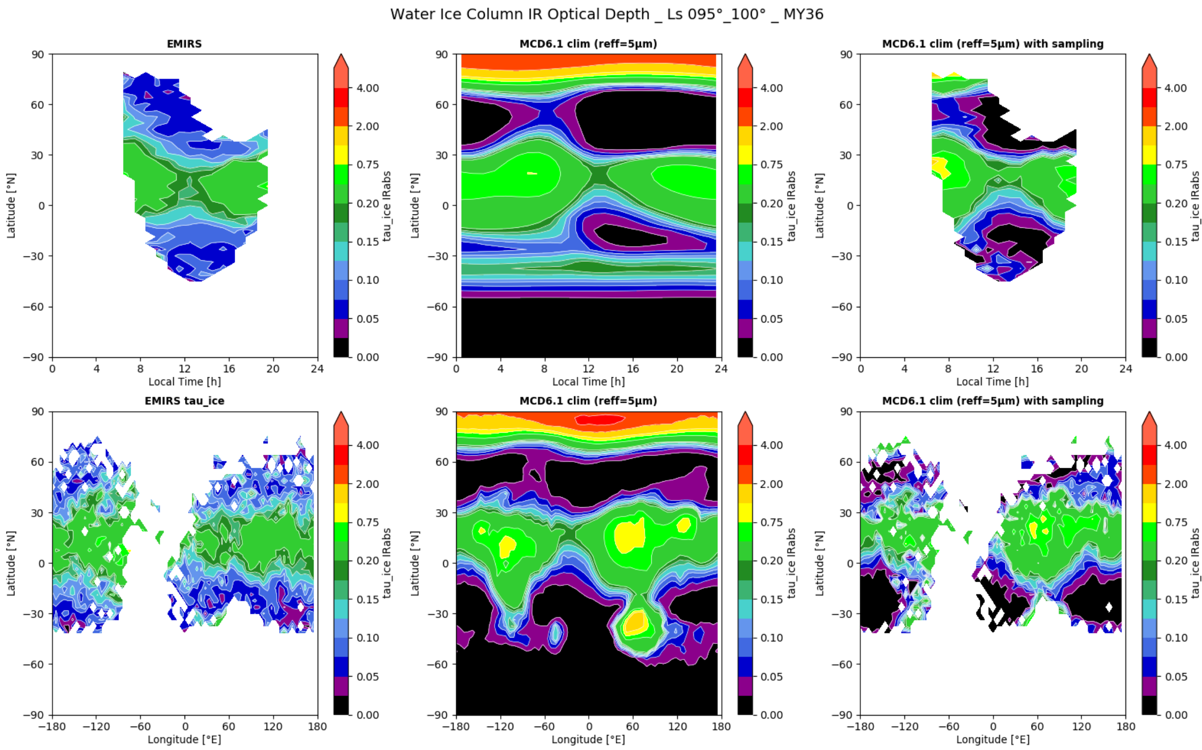

Figure 141: Zonal mean (first row) and diurnal mean (second row) of water ice infrared absorption column optical depth, L_s 95-100. EMIRS on the left, MCD6.1 without specific sampling in the middle and MCD6.1 with EMIRS sampling on the right.

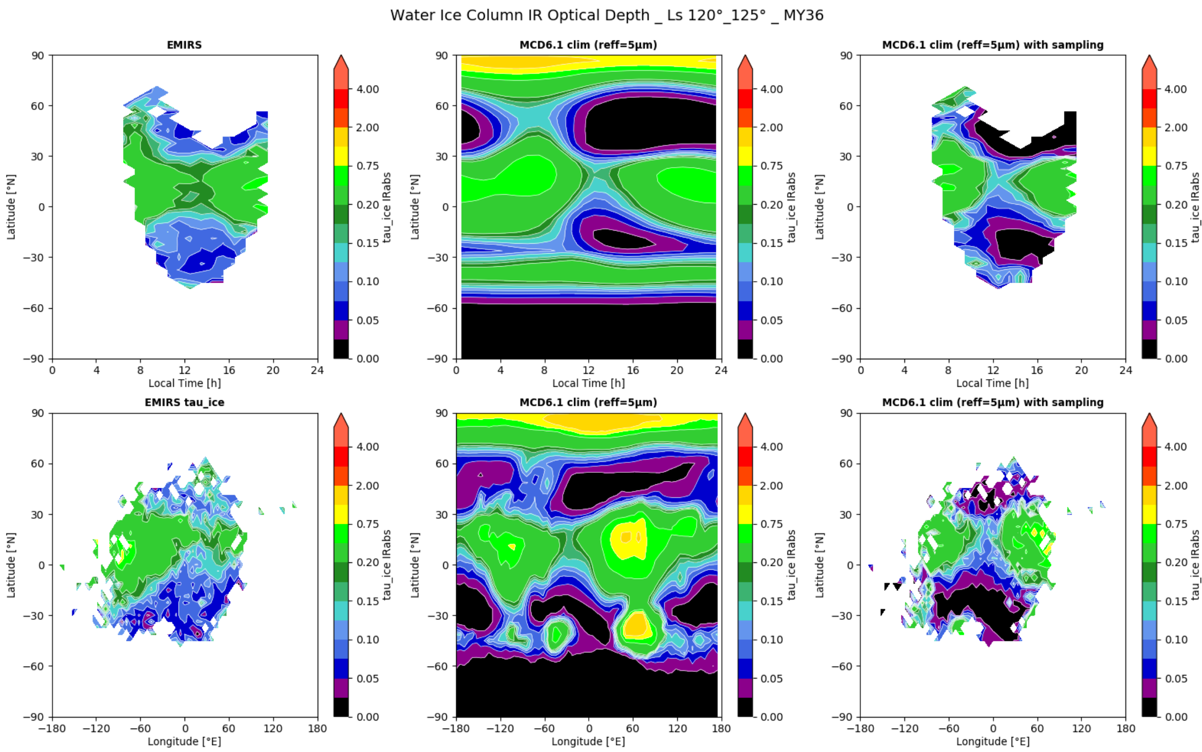

Figure 142: Zonal mean (first row) and diurnal mean (second row) of water ice infrared absorption column optical depth, L_s 120-125. EMIRS on the left, MCD6.1 without specific sampling in the middle and MCD6.1 with EMIRS sampling on the right.

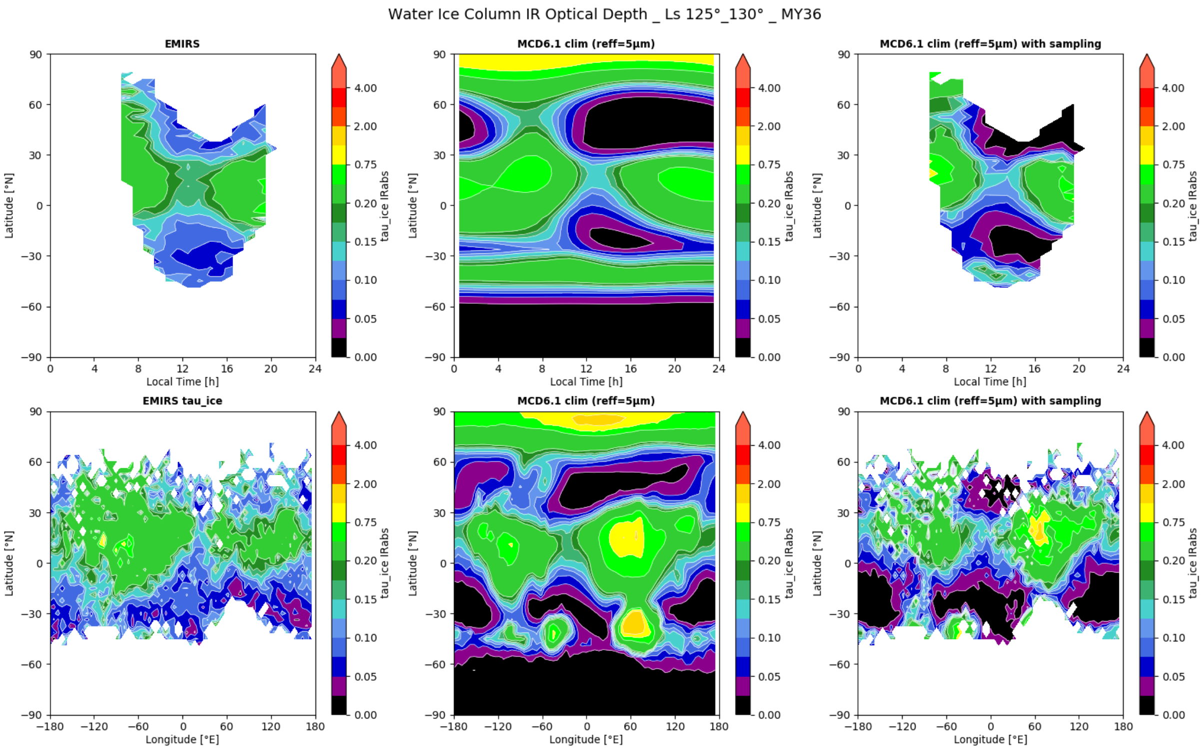

Figure 143: Zonal mean (first row) and diurnal mean (second row) of water ice infrared absorption column optical depth, L_s 125-130. EMIRS on the left, MCD6.1 without specific sampling in the middle and MCD6.1 with EMIRS sampling on the right.

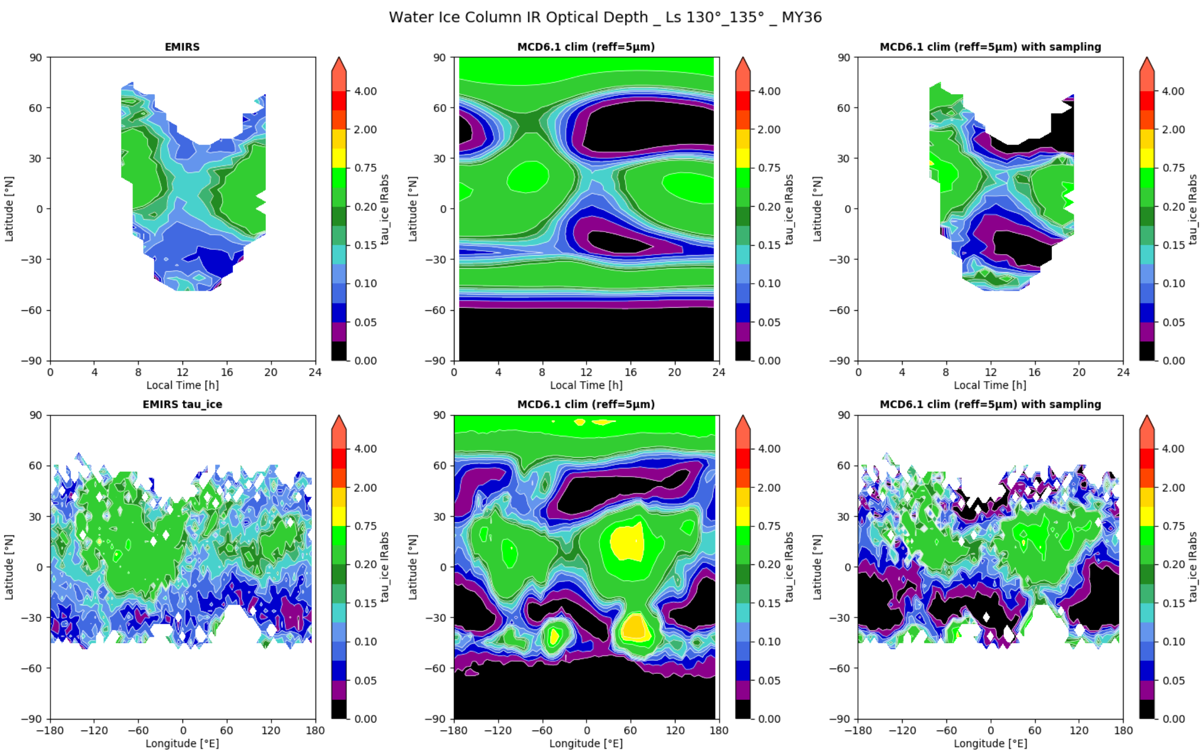

Figure 144: Zonal mean (first row) and diurnal mean (second row) of water ice infrared absorption column optical depth, L_s 130-135. EMIRS on the left, MCD6.1 without specific sampling in the middle and MCD6.1 with EMIRS sampling on the right.

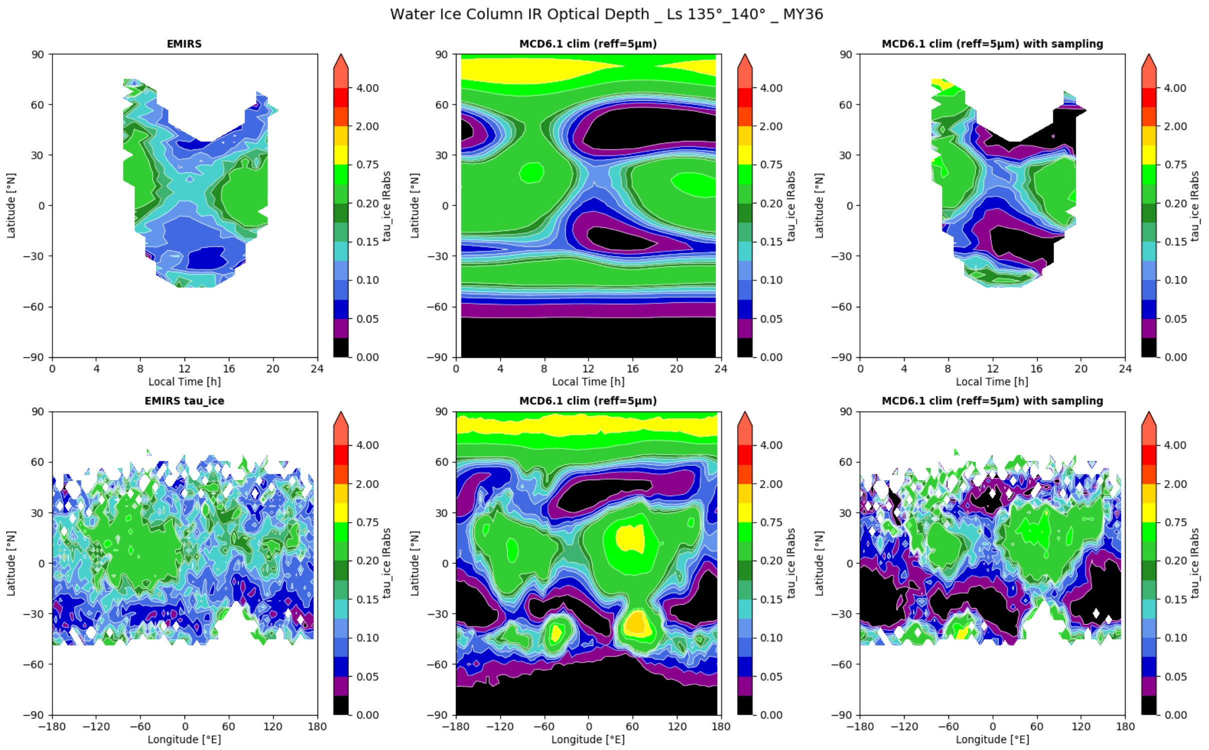

Figure 145: Zonal mean (first row) and diurnal mean (second row) of water ice infrared absorption column optical depth, L_s 135-140. EMIRS on the left, MCD6.1 without specific sampling in the middle and MCD6.1 with EMIRS sampling on the right.

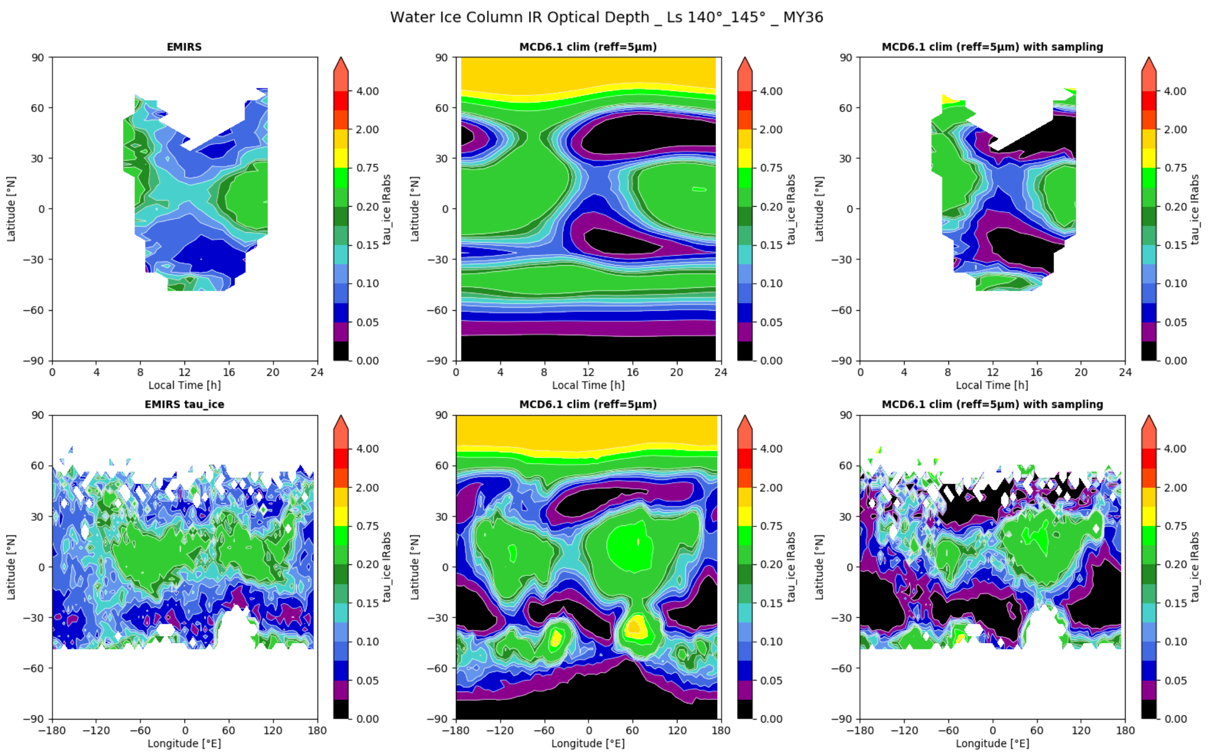

Figure 146: Zonal mean (first row) and diurnal mean (second row) of water ice infrared absorption column optical depth, L_s 140-145. EMIRS on the left, MCD6.1 without specific sampling in the middle and MCD6.1 with EMIRS sampling on the right.

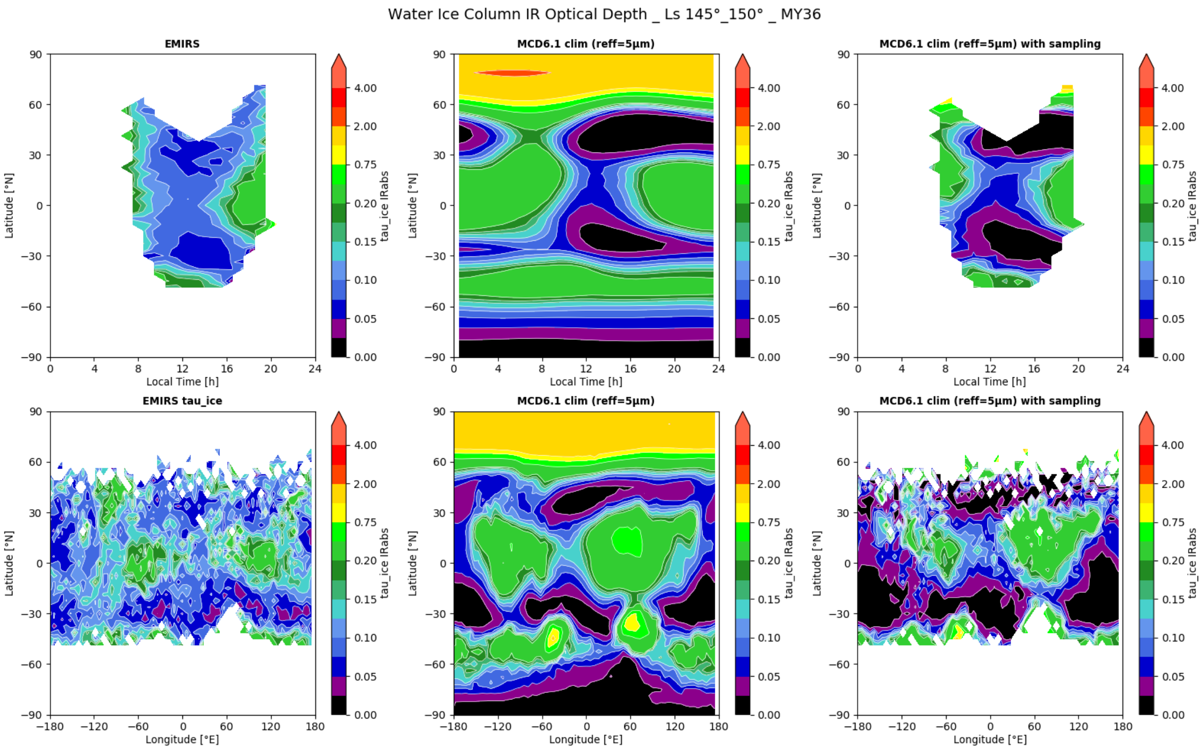

Figure 147: Zonal mean (first row) and diurnal mean (second row) of water ice infrared absorption column optical depth, L_s 145-150. EMIRS on the left, MCD6.1 without specific sampling in the middle and MCD6.1 with EMIRS sampling on the right.

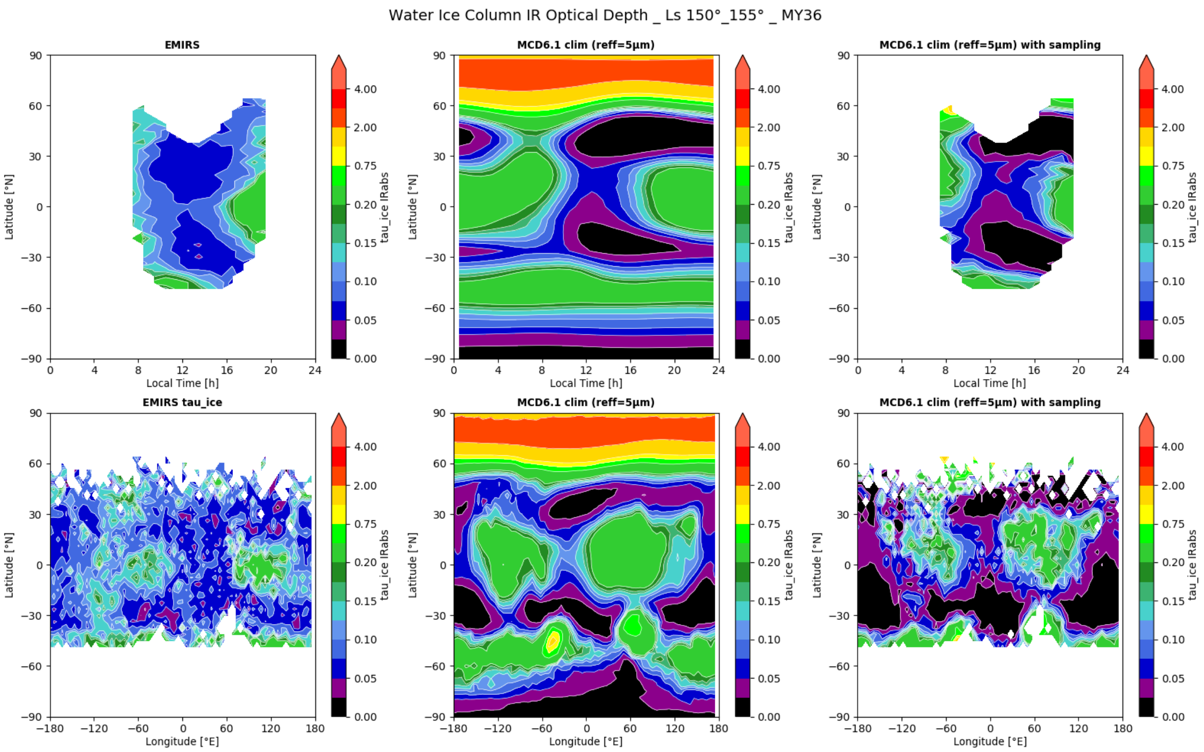

Figure 148: Zonal mean (first row) and diurnal mean (second row) of water ice infrared absorption column optical depth, L_s 150-155. EMIRS on the left, MCD6.1 without specific sampling in the middle and MCD6.1 with EMIRS sampling on the right.

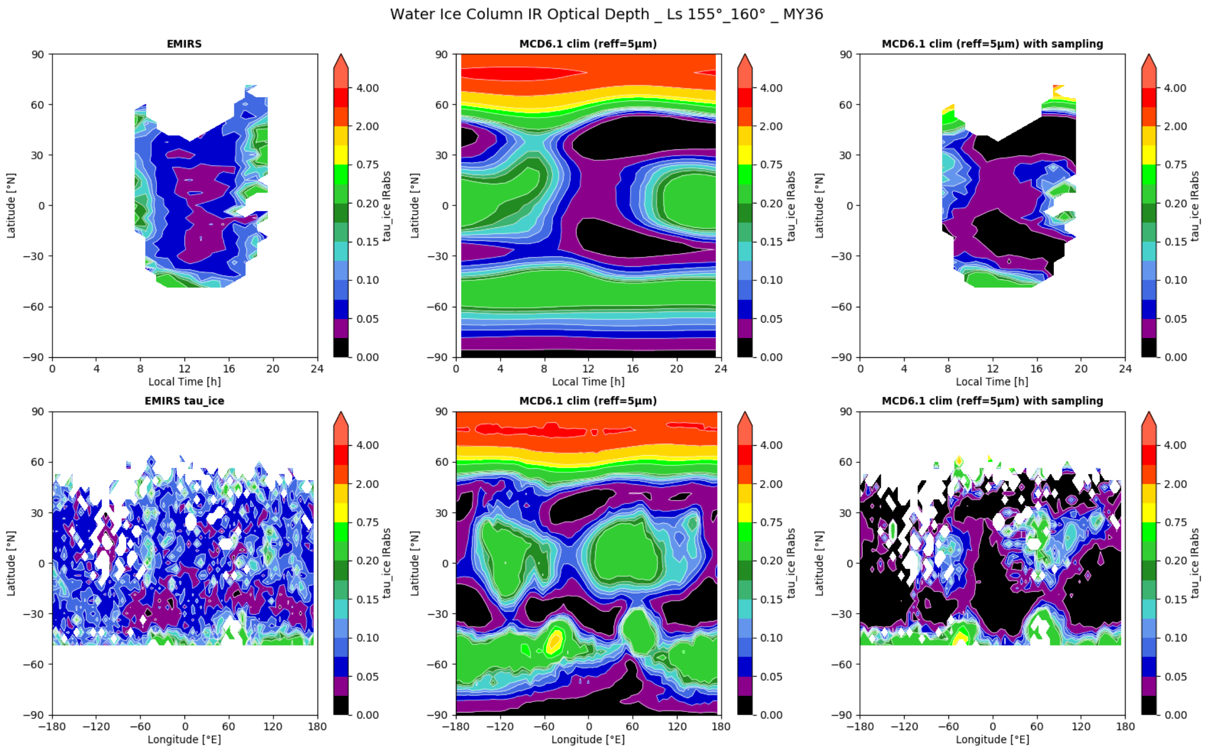

Figure 149: Zonal mean (first row) and diurnal mean (second row) of water ice infrared absorption column optical depth, L_s 155-160. EMIRS on the left, MCD6.1 without specific sampling in the middle and MCD6.1 with EMIRS sampling on the right.

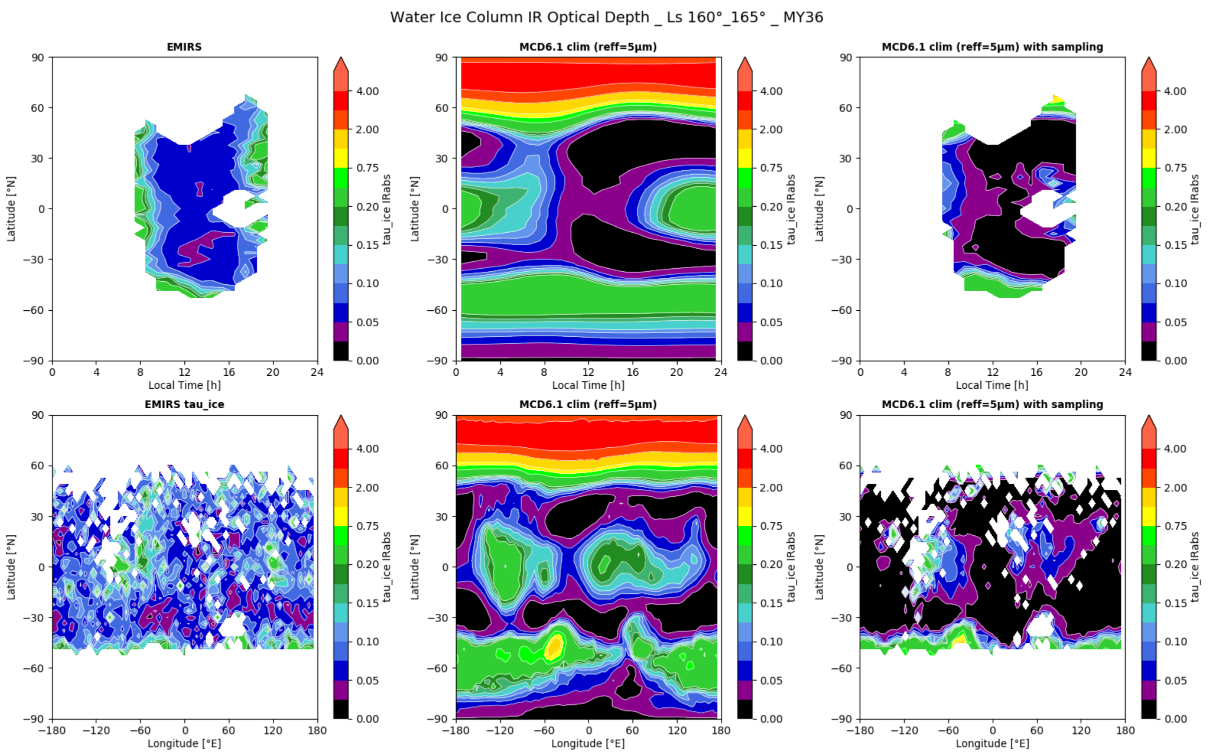

Figure 150: Zonal mean (first row) and diurnal mean (second row) of water ice infrared absorption column optical depth, L_s 160-165. EMIRS on the left, MCD6.1 without specific sampling in the middle and MCD6.1 with EMIRS sampling on the right.

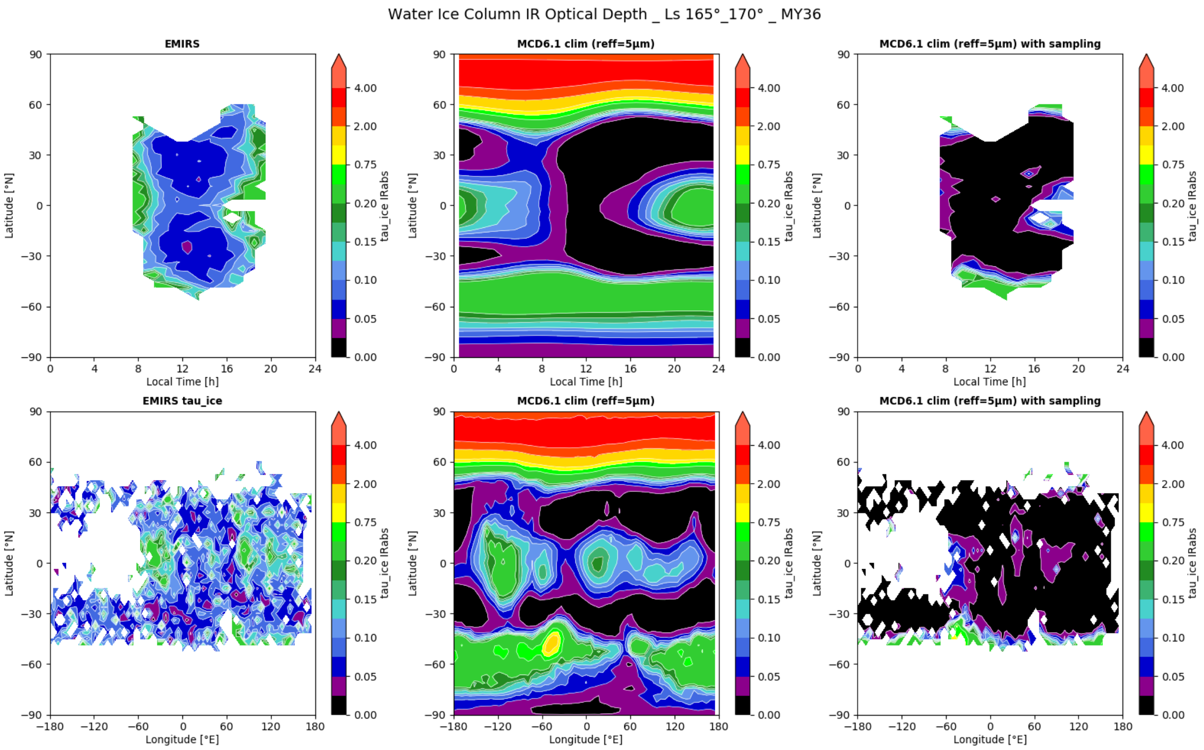

Figure 151: Zonal mean (first row) and diurnal mean (second row) of water ice infrared absorption column optical depth, L_s 165-170. EMIRS on the left, MCD6.1 without specific sampling in the middle and MCD6.1 with EMIRS sampling on the right.

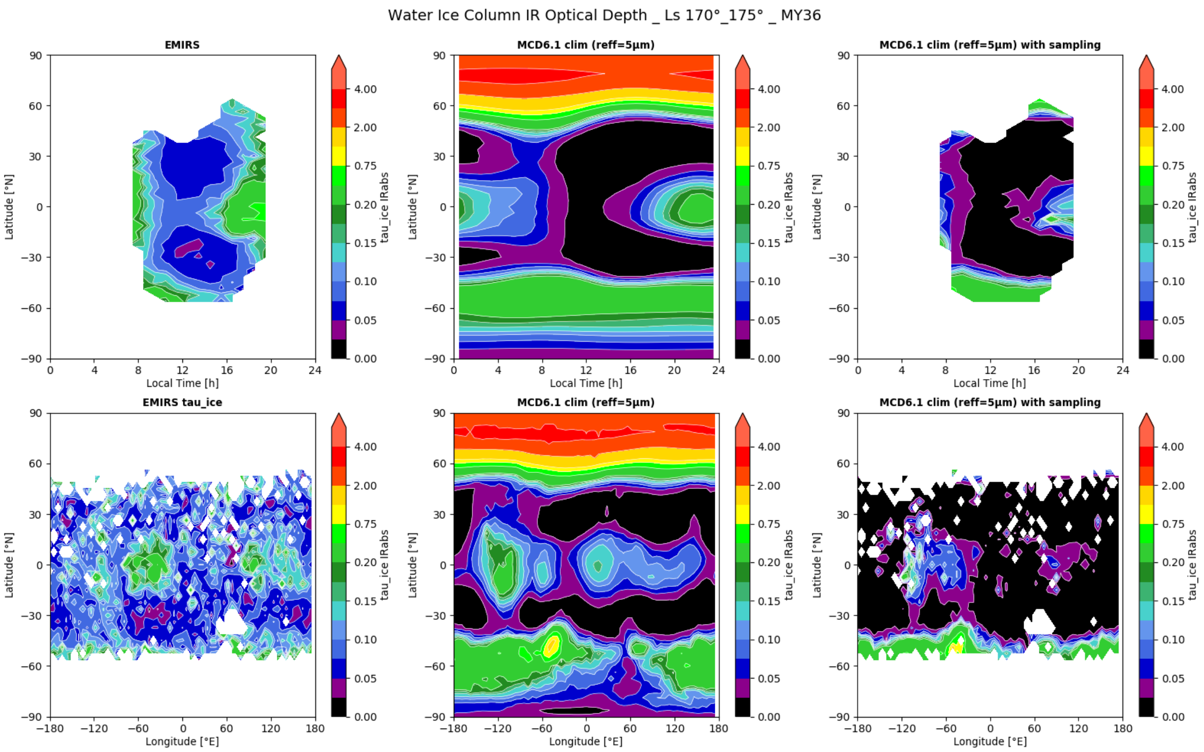

Figure 152: Zonal mean (first row) and diurnal mean (second row) of water ice infrared absorption column optical depth, L_s 170-175. EMIRS on the left, MCD6.1 without specific sampling in the middle and MCD6.1 with EMIRS sampling on the right.

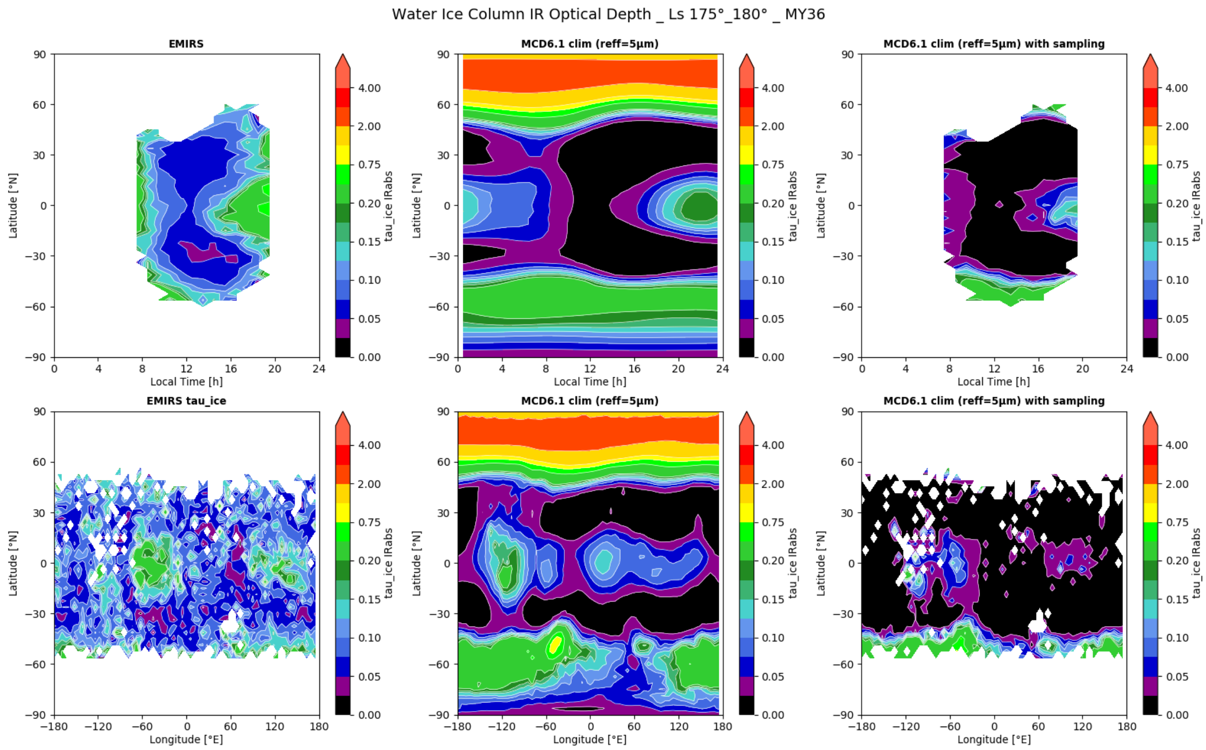

Figure 153: Zonal mean (first row) and diurnal mean (second row) of water ice infrared absorption column optical depth, L_s 175-180. EMIRS on the left, MCD6.1 without specific sampling in the middle and MCD6.1 with EMIRS sampling on the right.

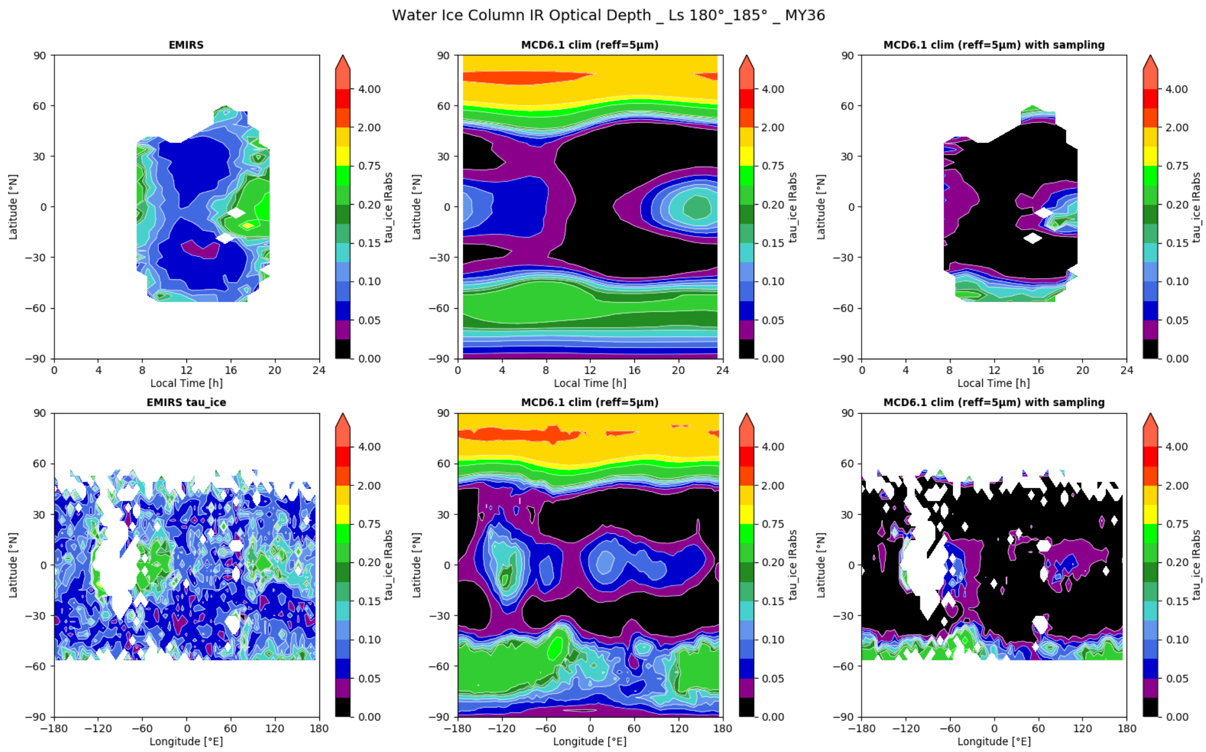

Figure 154: Zonal mean (first row) and diurnal mean (second row) of water ice infrared absorption column optical depth, L_s 180-185. EMIRS on the left, MCD6.1 without specific sampling in the middle and MCD6.1 with EMIRS sampling on the right.

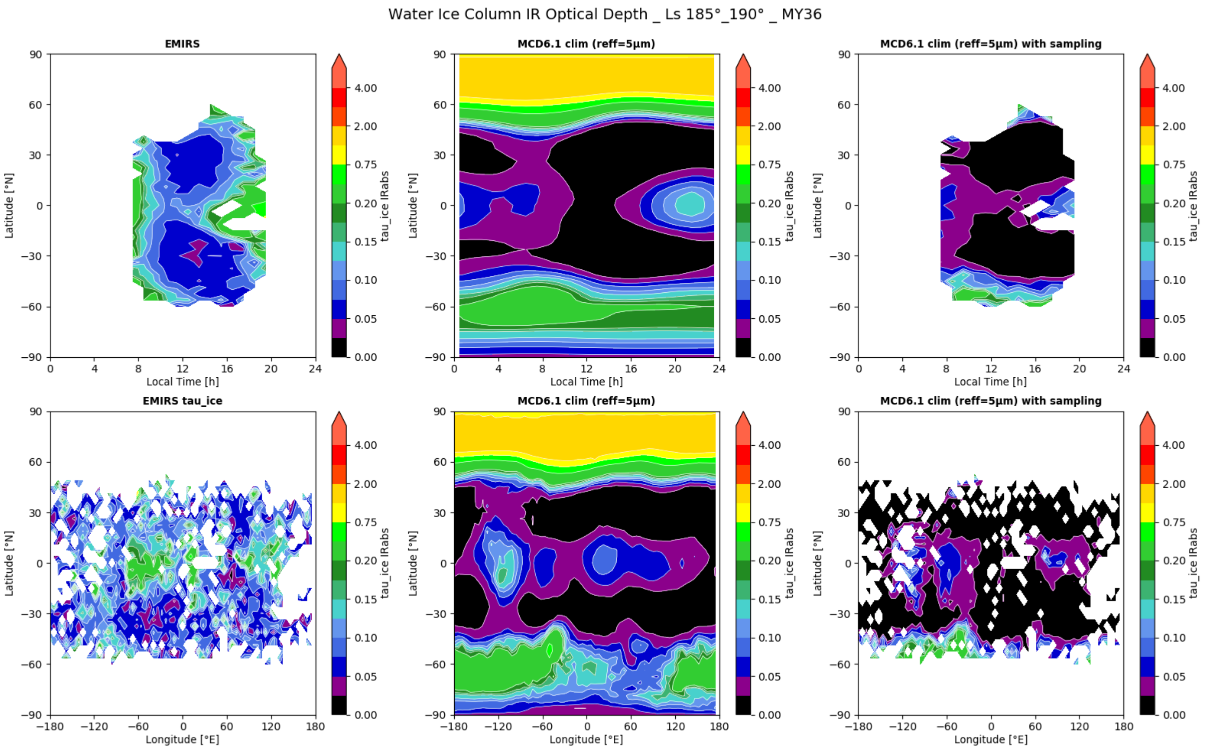

Figure 155: Zonal mean (first row) and diurnal mean (second row) of water ice infrared absorption column optical depth, L_s 185-190. EMIRS on the left, MCD6.1 without specific sampling in the middle and MCD6.1 with EMIRS sampling on the right.

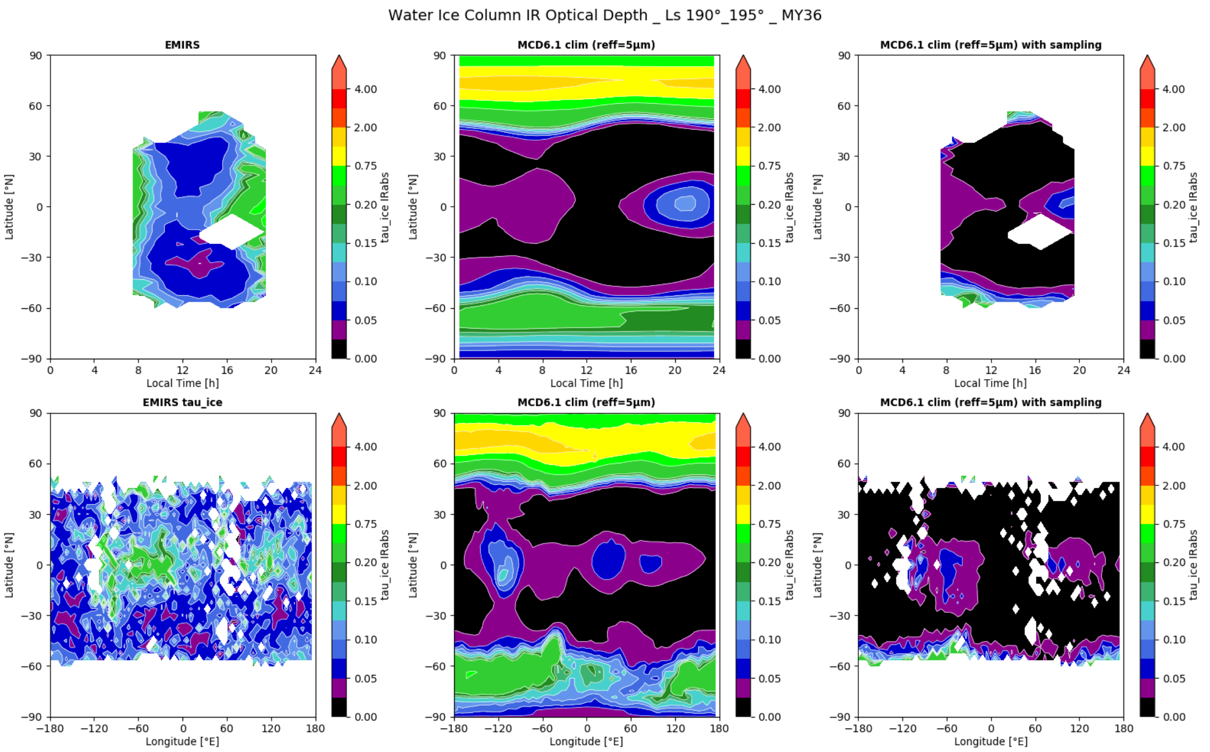

Figure 156: Zonal mean (first row) and diurnal mean (second row) of water ice infrared absorption column optical depth, L_s 190-195. EMIRS on the left, MCD6.1 without specific sampling in the middle and MCD6.1 with EMIRS sampling on the right.

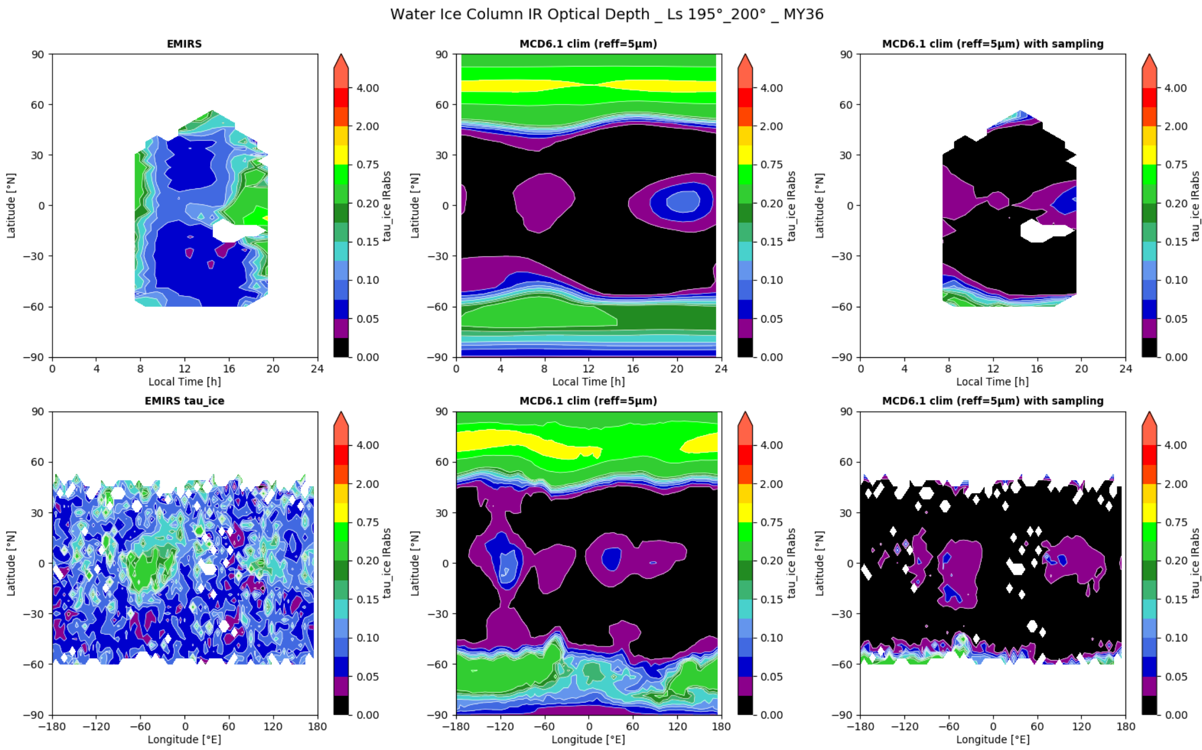

Figure 157: Zonal mean (first row) and diurnal mean (second row) of water ice infrared absorption column optical depth, L_s 195-200. EMIRS on the left, MCD6.1 without specific sampling in the middle and MCD6.1 with EMIRS sampling on the right.

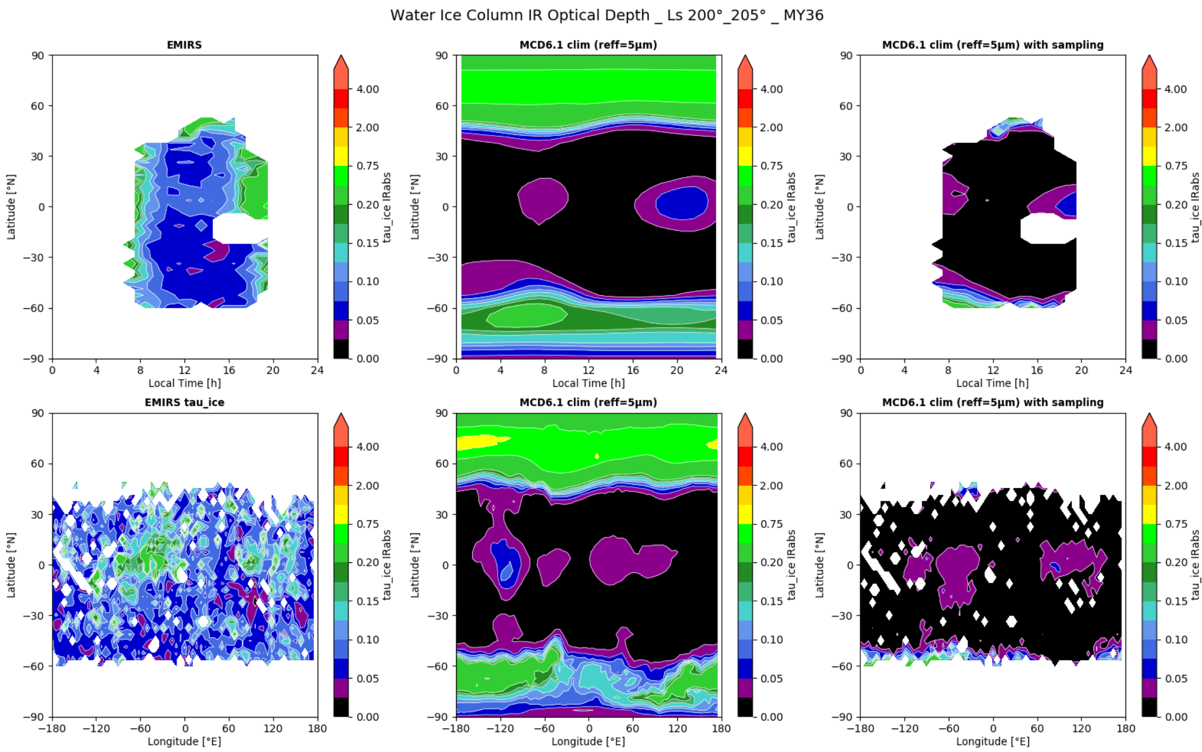

Figure 158: Zonal mean (first row) and diurnal mean (second row) of water ice infrared absorption column optical depth, L_s 200-205. EMIRS on the left, MCD6.1 without specific sampling in the middle and MCD6.1 with EMIRS sampling on the right.

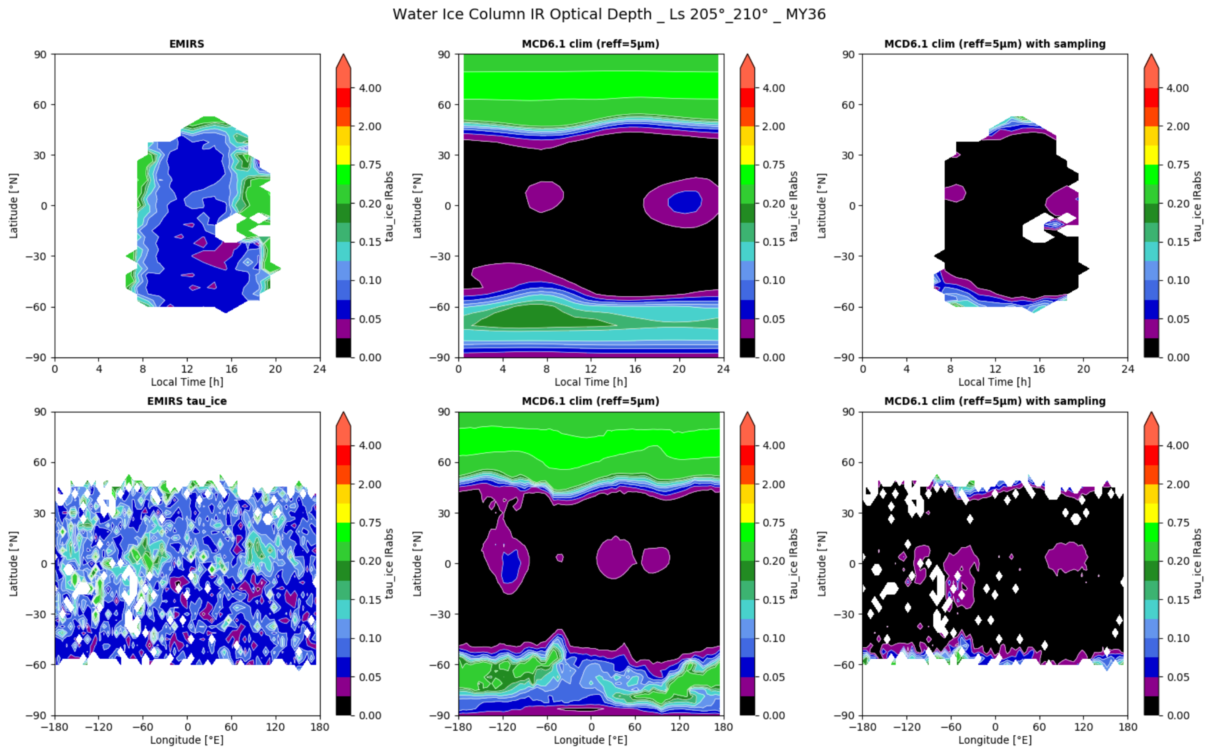

Figure 159: Zonal mean (first row) and diurnal mean (second row) of water ice infrared absorption column optical depth, L_s 205-210. EMIRS on the left, MCD6.1 without specific sampling in the middle and MCD6.1 with EMIRS sampling on the right.

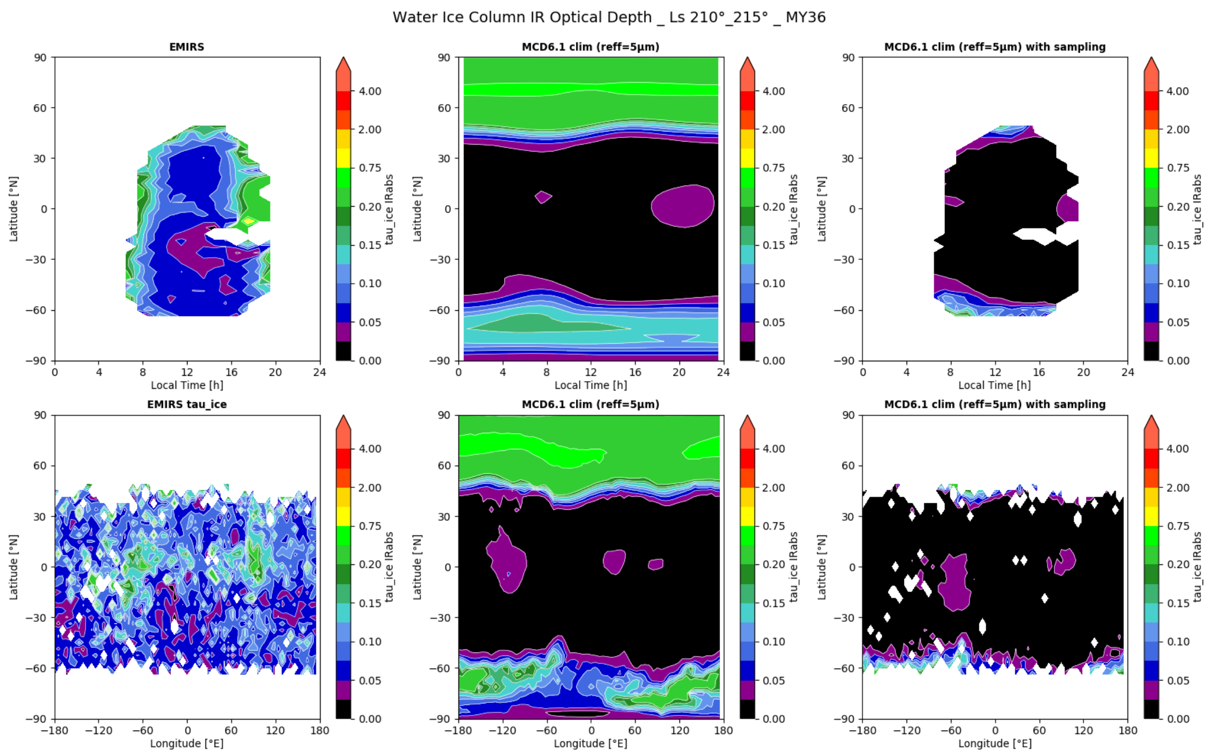

Figure 160: Zonal mean (first row) and diurnal mean (second row) of water ice infrared absorption column optical depth, L_s 210-215. EMIRS on the left, MCD6.1 without specific sampling in the middle and MCD6.1 with EMIRS sampling on the right.

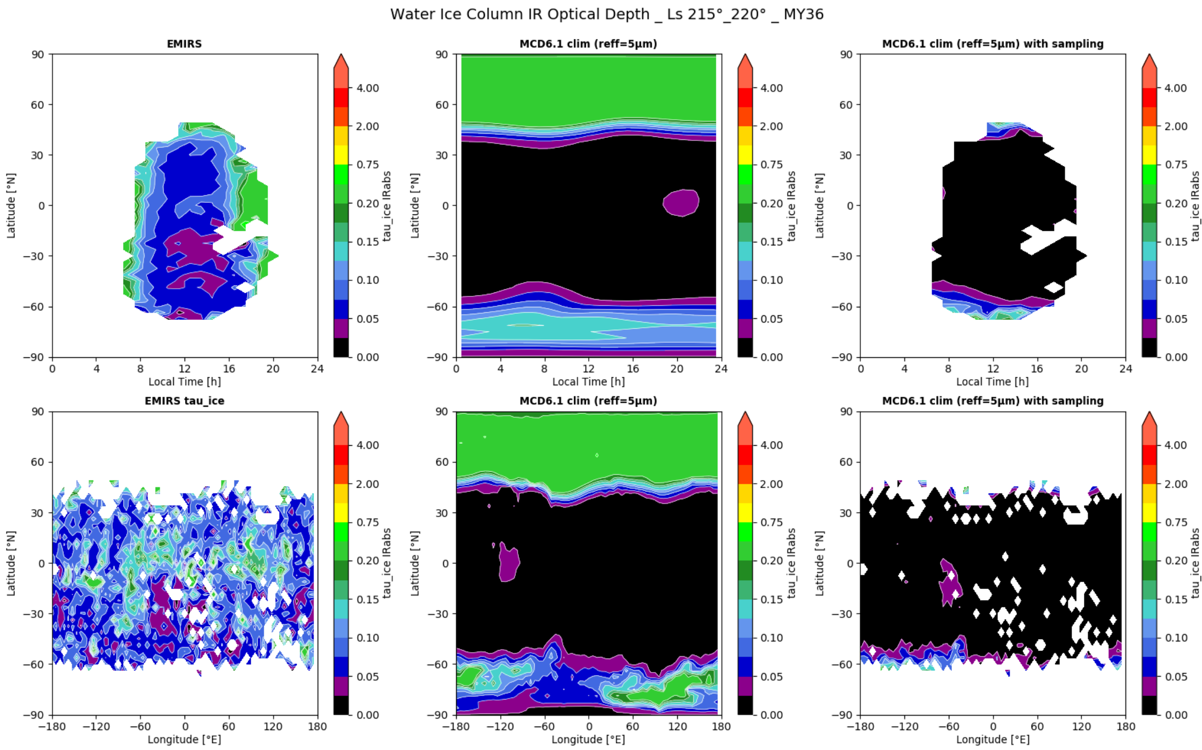

Figure 161: Zonal mean (first row) and diurnal mean (second row) of water ice infrared absorption column optical depth, L_s 215-220. EMIRS on the left, MCD6.1 without specific sampling in the middle and MCD6.1 with EMIRS sampling on the right.

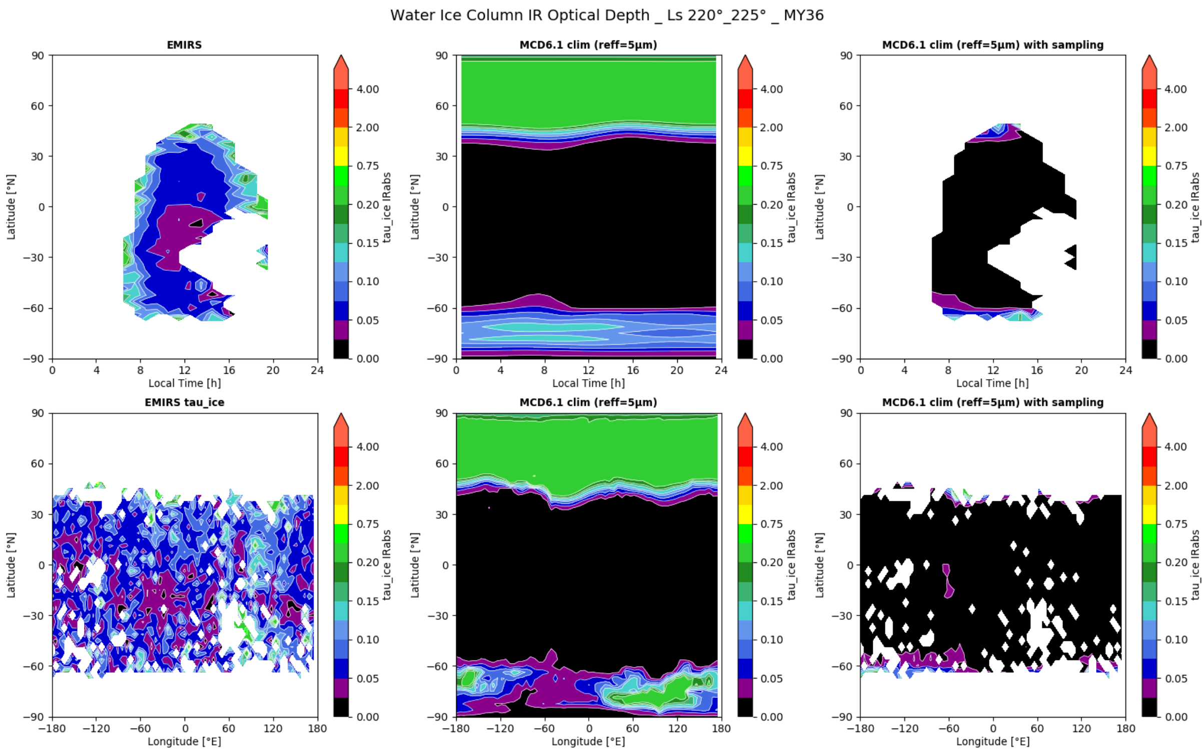

Figure 162: Zonal mean (first row) and diurnal mean (second row) of water ice infrared absorption column optical depth, L_s 220-225. EMIRS on the left, MCD6.1 without specific sampling in the middle and MCD6.1 with EMIRS sampling on the right.

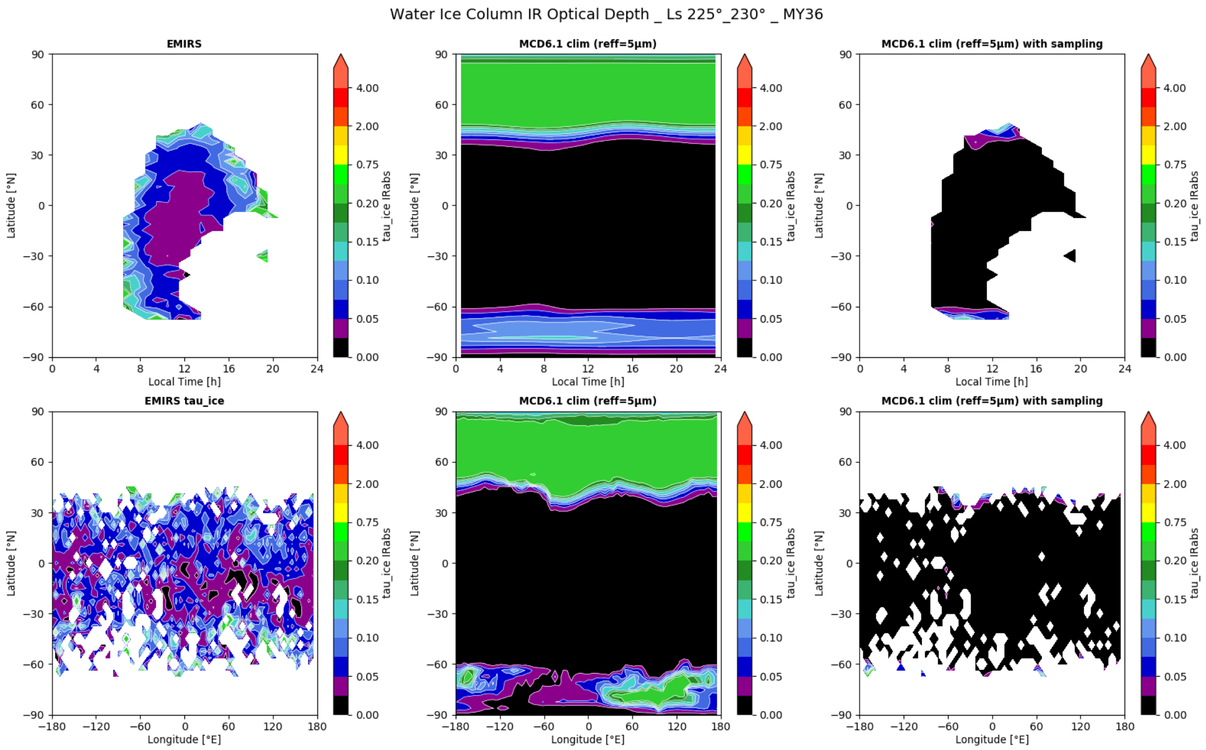

Figure 163: Zonal mean (first row) and diurnal mean (second row) of water ice infrared absorption column optical depth, L_s 225-230. EMIRS on the left, MCD6.1 without specific sampling in the middle and MCD6.1 with EMIRS sampling on the right.

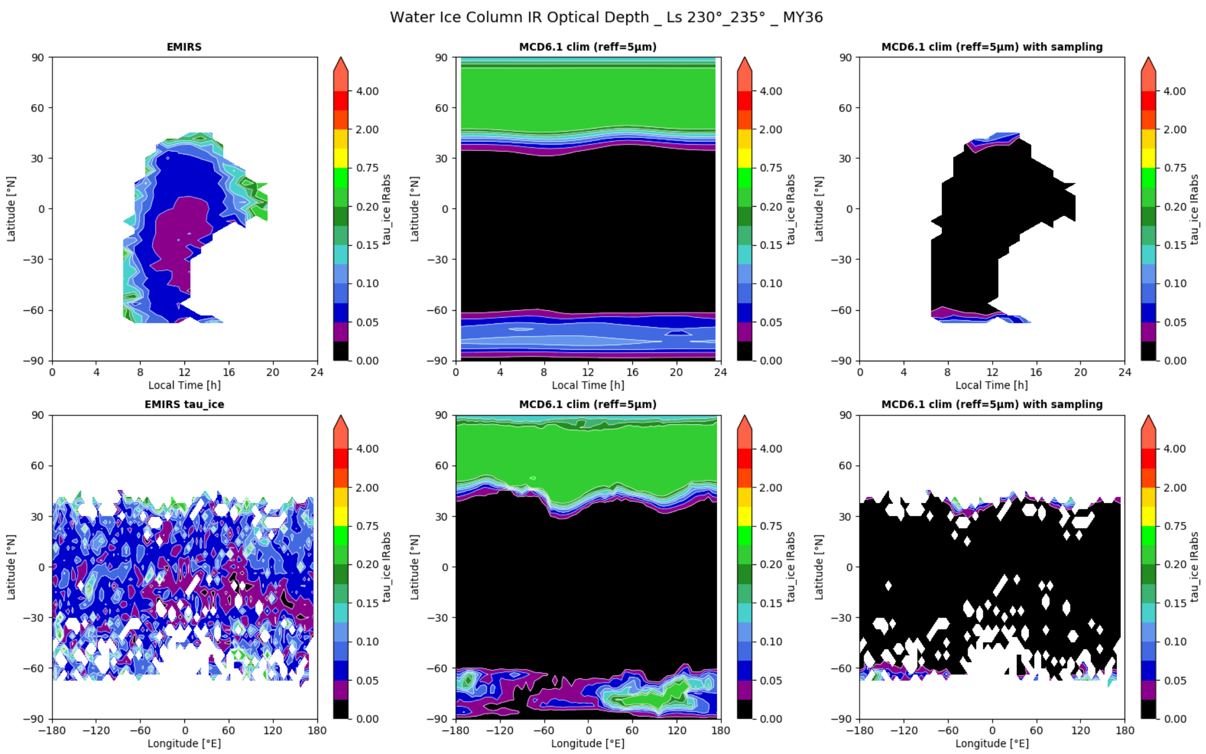

Figure 164: Zonal mean (first row) and diurnal mean (second row) of water ice infrared absorption column optical depth, L_s 230-235. EMIRS on the left, MCD6.1 without specific sampling in the middle and MCD6.1 with EMIRS sampling on the right.

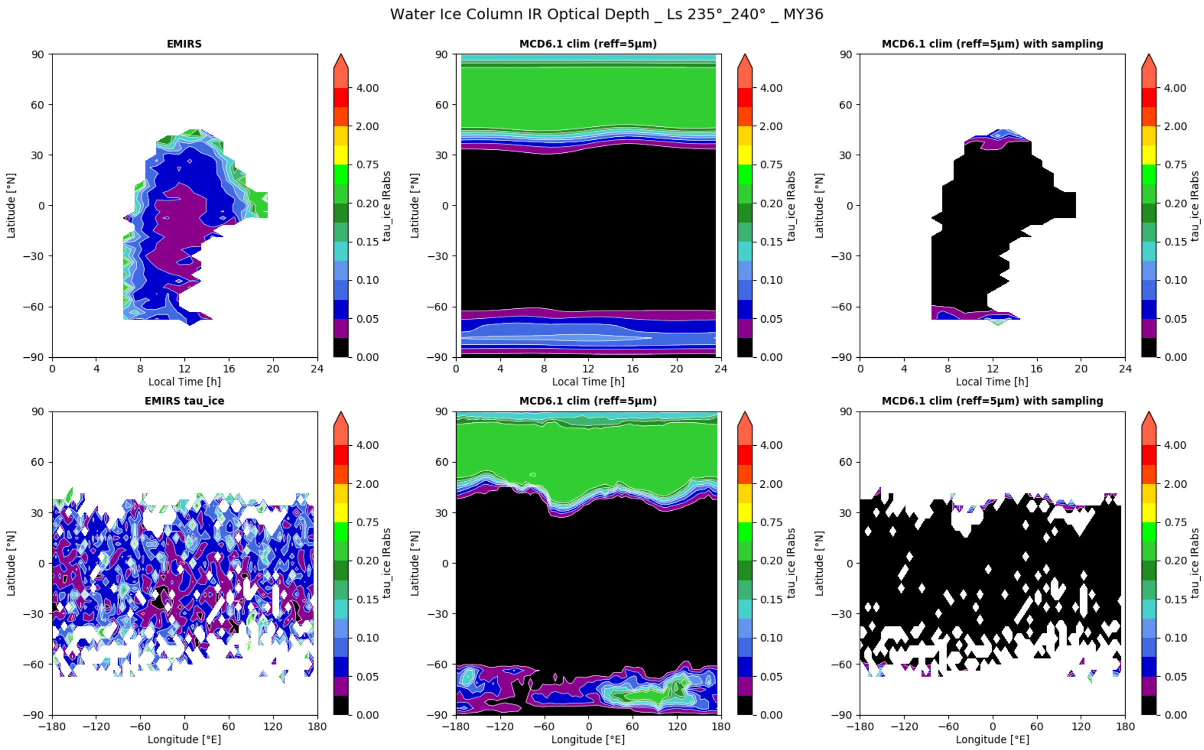

Figure 165: Zonal mean (first row) and diurnal mean (second row) of water ice infrared absorption column optical depth, L_s 235-240. EMIRS on the left, MCD6.1 without specific sampling in the middle and MCD6.1 with EMIRS sampling on the right.

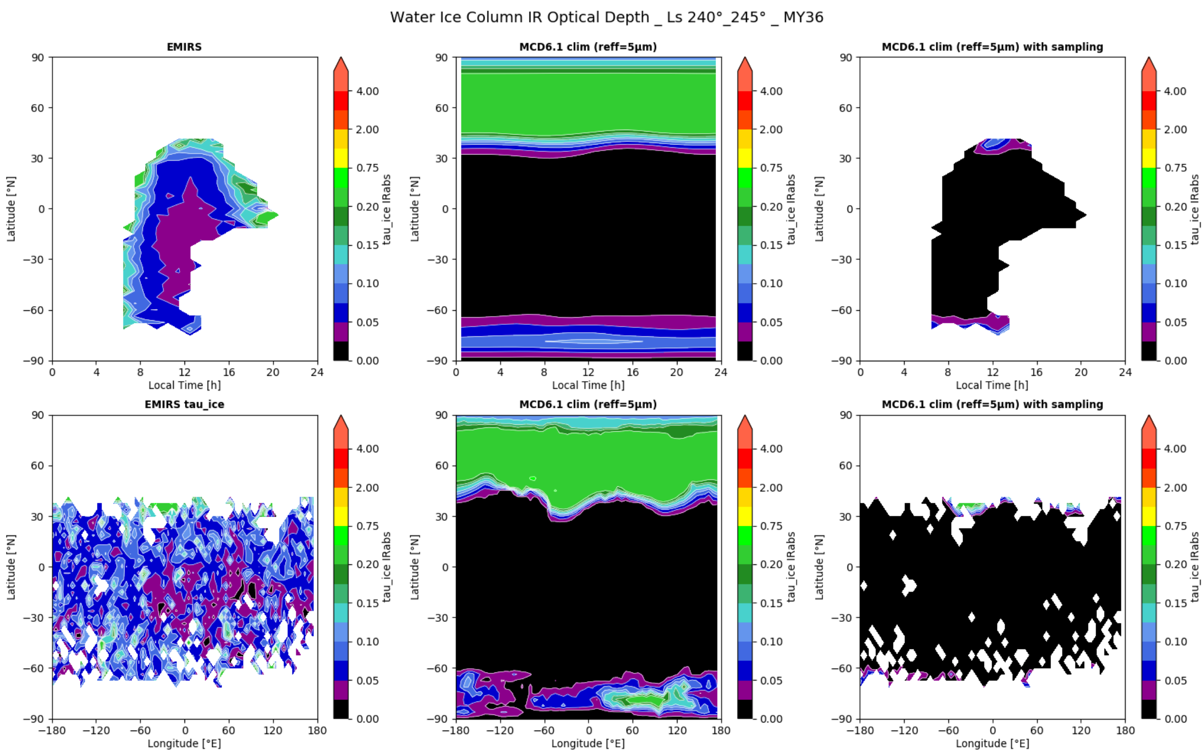

Figure 166: Zonal mean (first row) and diurnal mean (second row) of water ice infrared absorption column optical depth, L_s 240-245. EMIRS on the left, MCD6.1 without specific sampling in the middle and MCD6.1 with EMIRS sampling on the right.

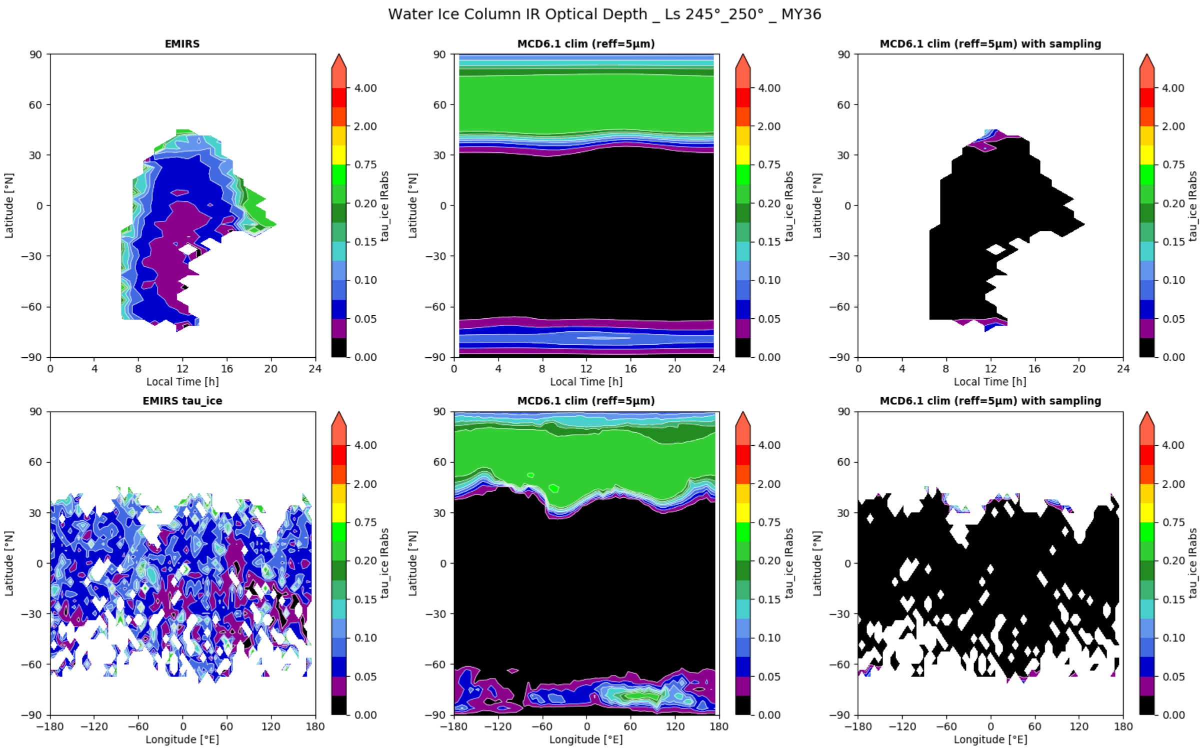

Figure 167: Zonal mean (first row) and diurnal mean (second row) of water ice infrared absorption column optical depth, L_s 245-250. EMIRS on the left, MCD6.1 without specific sampling in the middle and MCD6.1 with EMIRS sampling on the right.

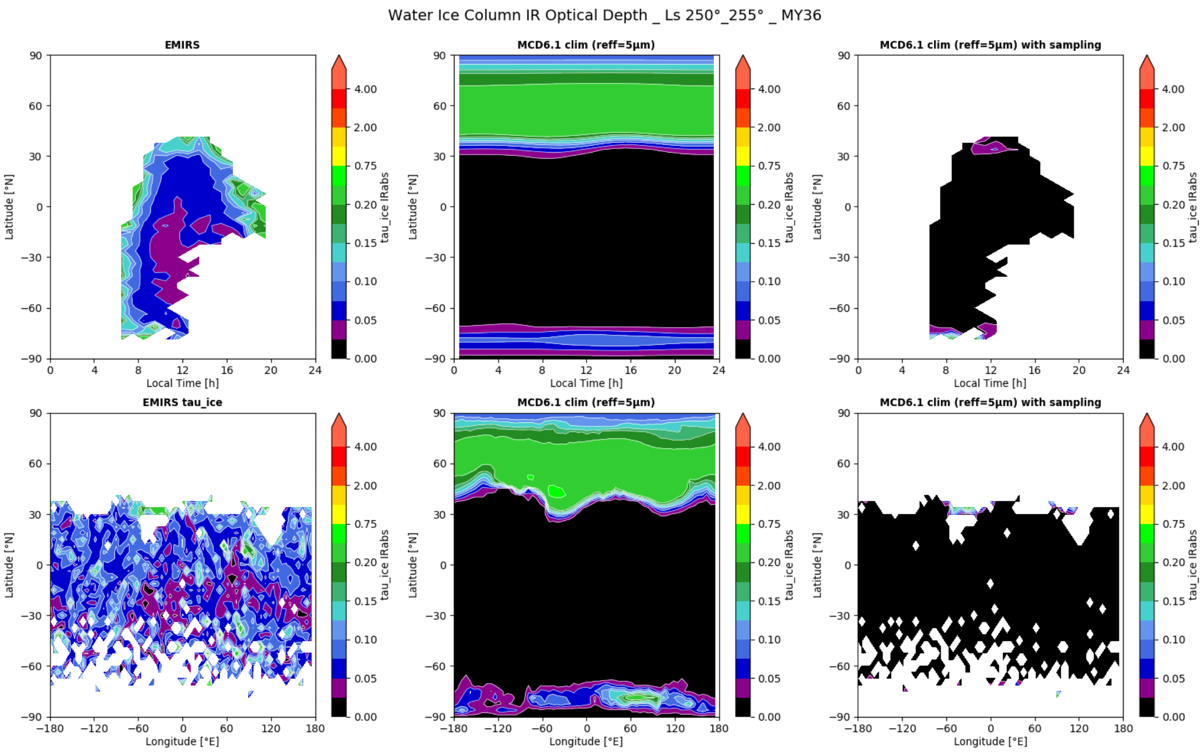

Figure 168: Zonal mean (first row) and diurnal mean (second row) of water ice infrared absorption column optical depth, L_s 250-255. EMIRS on the left, MCD6.1 without specific sampling in the middle and MCD6.1 with EMIRS sampling on the right.

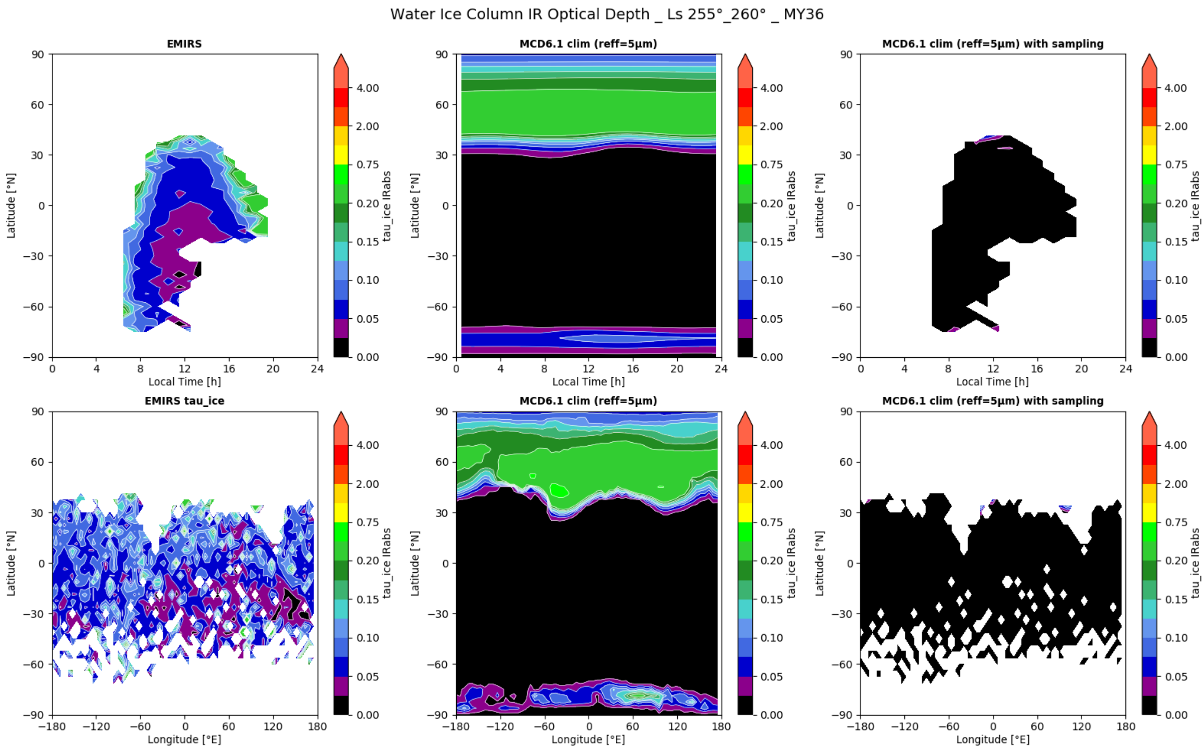

Figure 169: Zonal mean (first row) and diurnal mean (second row) of water ice infrared absorption column optical depth, L_s 255-260. EMIRS on the left, MCD6.1 without specific sampling in the middle and MCD6.1 with EMIRS sampling on the right.

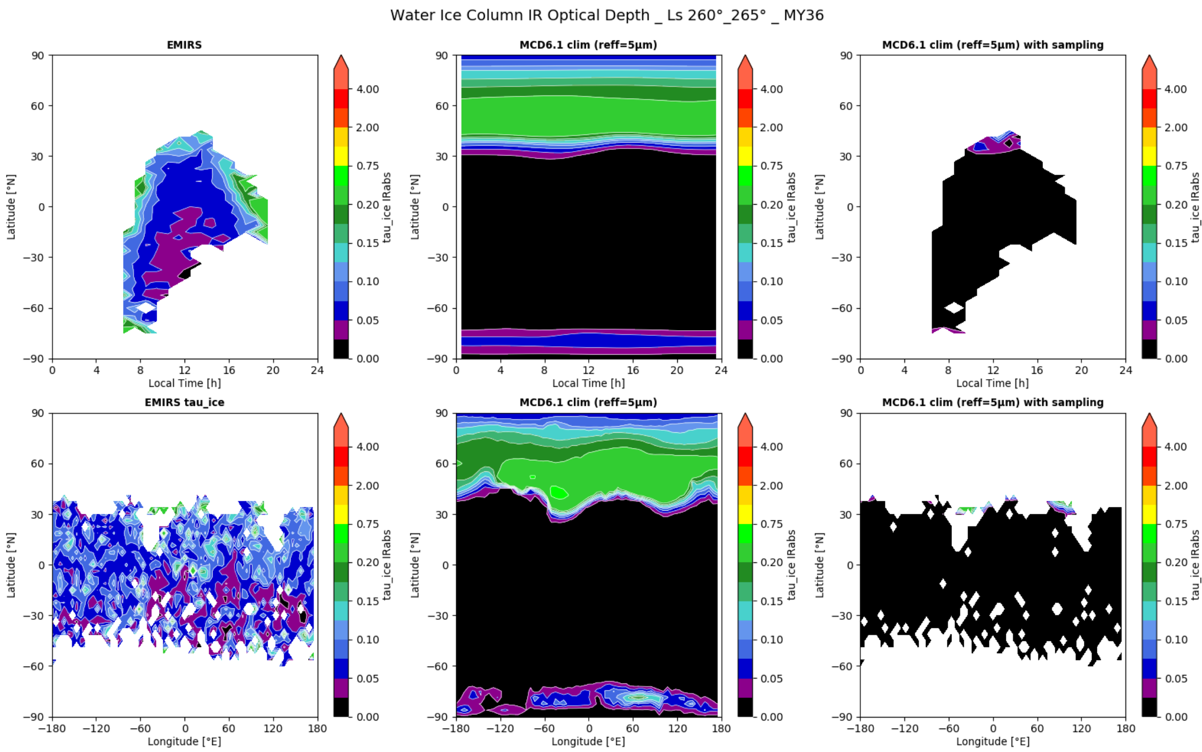

Figure 170: Zonal mean (first row) and diurnal mean (second row) of water ice infrared absorption column optical depth, L_s 260-265. EMIRS on the left, MCD6.1 without specific sampling in the middle and MCD6.1 with EMIRS sampling on the right.

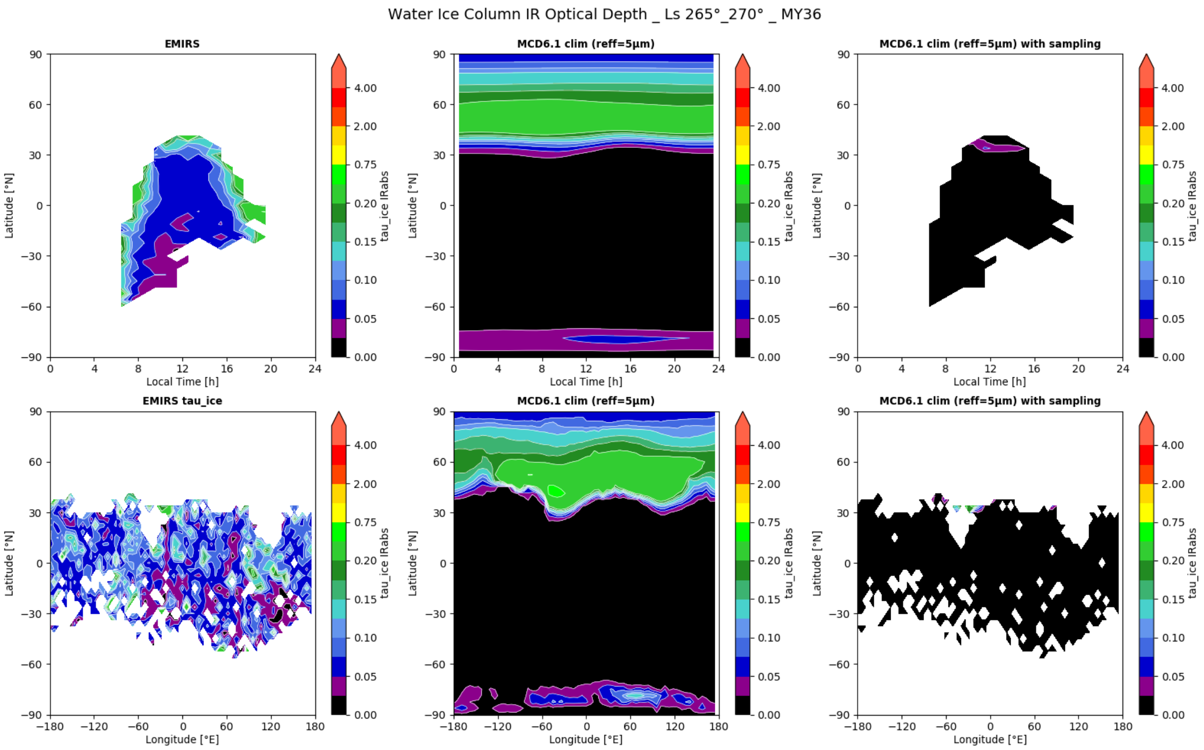

Figure 171: Zonal mean (first row) and diurnal mean (second row) of water ice infrared absorption column optical depth, L_s 265-270. EMIRS on the left, MCD6.1 without specific sampling in the middle and MCD6.1 with EMIRS sampling on the right.

References

Fan, S., Forget, F., Smith, M. D., Guerlet, S., Badri, K. M., Atwood, S. A., Young, R. M. B., Edwards, C. S., Christensen, P. R., Deighan, J., Al Matroushi, H. R., Bierjon, A., Liu, J., and Millour, E. (2022). Migrating Thermal Tides in the Martian Atmosphere During Aphelion Season Observed by EMM/EMIRS. , 49(18):e99494.

Heavens, N. G., Johnson, M. S., Abdou, W. A., Kass, D. M., Kleinböhl, A., McCleese, D. J., Shirley, J. H., and Wilson, R. J. (2014). Seasonal and diurnal variability of detached dust layers in the tropical Martian atmosphere. *Journal of Geophysical Research (Planets)*, 119:1748–1774.

Heavens, N. G., Richardson, M. I., Kleinböhl, A., Kass, D. M., McCleese, D. J., Abdou, W., Benson, J. L., Schofield, J. T., Shirley, J. H., and Wolkenberg, P. M. (2011). The vertical distribution of dust in the Martian atmosphere during northern spring and summer: Observations by the Mars Climate Sounder and analysis of zonal average vertical dust profiles. *Journal of Geophysical Research (Planets)*, 116(E15):4003.

Kleinböhl, A., Schofield, J. T., Kass, D. M., Abdou, W. A., Backus, C. R., Sen, B., Shirley, J. H., Lawson, W. G., Richardson, M. I., Taylor, F. W., Teanby, N. A., and McCleese, D. J. (2009). Mars Climate Sounder limb profile retrieval of atmospheric temperature, pressure, and dust and water ice opacity. *Journal of Geophysical Research (Planets)*, 114:10006.

Lange, L., Forget, F., Banfield, D., Wolff, M., Spiga, A., Millour, E., Viúdez-Moreiras, D., Bierjon, A., Piqueux, S., Newman, C., et al. (2022). Insight pressure data recalibration, and its application to the study of long-term pressure changes on mars. *Journal of Geophysical Research: Planets*, page e2022JE007190.

Montabone, L., Forget, F., Millour, E., Wilson, R. J., Lewis, S. R., Cantor, B., Kass, D., Kleinböhl, A., Lemmon, M. T., Smith, M. D., and Wolff, M. J. (2015). Eight-year climatology of dust optical depth on Mars. *Icarus*, 251:65–95.

Montabone, L., Kass, D., Kleinboehl, A., McCleese, D., and Schofield, J. (2017). NetCDF version (v3.0) of MRO/MCS binned retrievals v5.2 of temperature and dust/water ice opacities. *Internet*.

Navarro, T., Madeleine, J.-B., Forget, F., Spiga, A., Millour, E., Montmessin, F., and Määttänen, A. (2014). Global Climate Modeling of the Martian water cycle with improved microphysics and radiatively active water ice clouds. *Journal of Geophysical Research (Planets)*.

Smith, M. D. (2004). Interannual variability in TES atmospheric observations of Mars during 1999-2003. *Icarus*, 167:148–165.

Smith, M. D., Badri, K., Atwood, S. A., Edwards, C. S., Christensen, P. R., Wolff, M. J., Bertrand, T., Forget, F., Al Tunaiji, E., Wolfe, C., Smith, N., and Anwar, S. (2022). Emirs observations of the aphelion-season mars atmosphere. *Geophysical Research Letters*, 49(15):e2022GL099636. e2022GL099636 2022GL099636.